UNIVERSITÉ DU QUÉBEC À RIMOUSKI

RECONSTITUTION MILLÉNAIRE DES TEMPÉRATURES ESTIVALES DE L'EST DE L'AMÉRIQUE DU NORD À PARTIR DE LA DENSITÉ MAXIMALE DU BOIS FINAL DES CERNES ANNUELS DE CROISSANCE DES ARBRES

THÈSE PRÉSENTÉE

COMME EXIGENCE PARTIELLE

DU DOCTORAT EN BIOLOGIE

EXTENSIONNÉ DE

L'UNIVERSITÉ DU QUÉBEC À MONTRÉAL

PAR

© [FENG WANG]

[NOVEMBRE 2021]

Composition du jury :

[Philippe Gachon], président du jury, [Université du Québec à Montréal]

[Dominique Arseneault], directeur de recherche, [Université du Québec à Rimouski]

[Étienne Boucher], codirecteur de recherche, [Université du Québec à Montréal]

[Trevor Porter], examinateur externe, [University of Toronto-Mississauga]

[Robert Schneider], examinateur interne, [Université du Québec à Rimouski]

Dépôt initial le [19 août 2021] Dépôt final le [24 novembre 2021]

À ma famille

REMERCIEMENTS

Tout d'abord, je tiens à remercier mon directeur, Dominique Arseneault, et mon co-directeur, Étienne Boucher, pour leur support et conseils tout au long du doctorat. Dominique, merci d'avoir organisé les travaux de terrain, structuré mon projet, partagé des discussions académiques constructives et révisé patiemment mes manuscrits. Les aventures dans la forêt boréale dans le lointain nord du Québec et du Labrador avec vous sont inoubliables pour moi, même si j'avais parfois peur des ours noirs que je n'ai jamais rencontré ! Vos décennies de travaux dans des régions éloignées m'ont beaucoup inspiré pour faire face aux difficultés dans mes études et dans ma vie. Étienne, merci d'avoir dirigé le projet PERSISTANCE (numéro de la subvention: RDC 485475-15). Vos conseils sur mes expériences et manuscrits ont été essentiels pour ma thèse. Je vous remercie également de m'avoir gardé optimiste avec vos mots d'humour.

Je voudrais remercier les autres co-auteurs des trois principaux chapitres de cette thèse : Shulong Yu, Tongwen Zhang et Lili Wang, qui m'ont permis et appris à réaliser les mesures de densité au rayon X à l'Institut de Météorologie du Désert de l'Agence Météorologique de Chine ; Fabio Gennaretti qui m'a aidé avec les analyses bayésiennes et l'interprétation des données de reconstitution ; Steeven Ouellet et Gwenaëlle Chaillou qui m'ont aidé pour les traitements chimiques et les analyses ; Anne Delwaide qui m'a permis d'utiliser la scie double lame à l'université Laval ; Nadège Trou-Kechout, Gabrielle Galipaud Gloaguen et Anne Deharte qui ont aidé à mesurer les cernes de croissance des arbres et participé à des discussions utiles au cours de mon étude.

Je tiens à remercier les membres de mon jury de thèse, ainsi que mes deux directeurs de thèse, Philippe Gachon, Trevor Porter et Robert Schneider, pour leur aide précieuse et leurs commentaires constructifs au cours de la dernière étape de mes études doctorales. Je

tiens également à remercier Sergio Rossi, Martin Girardin, Jeannine-Marie St-Jacques, Vézina Francois, Rober Schneider et Dominique Berteaux pour leur assistance durant mon projet de thèse, examen doctoral et séminaire. J'aimerai aussi remercier Nadège, et Pauline Balducci pour leur aide sur le terrain et le partage d'expérience d'étude et de vie au Québec. Un grand merci également à Zahed, Nicolas, Tasneem, Leila et Vincent pour leur aide pendant mes études.

Finalement, je voudrais exprimer mes remerciements à ma famille qui m'a toujours soutenu, encouragé et compris lorsque je me sentais stressé et déprimé au cours de mes études de doctorat ces 5 dernières années.

Ce travail a été soutenu par le projet PERSISTANCE du Conseil de recherches en sciences naturelles et en génie du Canada, Hydro-Québec, Manitoba Hydro et le consortium Ouranos. J'ai également reçu une bourse d'étude de la part du Conseil de bourse de Chine.

ACKNOWLEDGEMENTS

First and foremost, I would like to thank my supervisor, Dr. Dominique Arseneault, and co-supervisor, Dr. Étienne Boucher, for their kind support and guidance throughout the entire PhD process. Dominique, thank you for arranging field works, structuring my project, sharing constructive academic minds, and revising my manuscripts patiently. The adventures in the boreal forests of the far northern Québec and Labrador with you were unforgettable for me, even though I was sometimes afraid of black bears which I've never met! Your decades of works in remote regions have greatly inspired me to deal with difficulties in my studies and life. Étienne, thank you for leading the PERSISTENCE project (grant no. RDC 485475-15). Your advice on my experiments and manuscripts was essential for my thesis. I also thank you for keeping me optimistic with your humorous words.

I would like to thank other co-authors of the three main chapters of this thesis: Shulong Yu, Tongwen Zhang, and Lily Wang who permitted and taught me to undertake X-ray density measurements at the Institute of Desert Meteorology, China Meteorological Administration; Fabio Gennaretti who helped with the Bayesian analysis and the interpretation of the reconstruction data; Steeven Ouellet and Gwenaëlle Chaillou who helped with the chemical treatments and analyses; Anne Delwaide who permitted me to use the twin-blade saw at Université Laval; Nadège Trou-Kechout, Gabrielle Galipaud Gloaguen, and Anne Deharte who helped with tree-ring measurements and participated in useful discussions during my study.

I would like to thank the members of my thesis jury, in addition to my two supervisors, Philippe Gachon, Trevor Porter, and Robert Schneider, for their kind help and constructive comments during the last stage of my PhD study. I would also like to acknowledge Sergio Rossi, Martin Girardin, Jeannine-Marie St-Jacques, Vézina Francois, Robert Schneider, and

Dominique Berteaux for their assistance in my study proposal, doctoral exam, and seminar. I additionally wish to thank Nadège and Pauline Balducci for helping with the field work and sharing study and life experiences in Québec. Many thanks also to Zahed, Nicolas, Tasneem, Leila, and Vincent for their help during my study.

Finally, I would like to express my thanks to my family who always gave me support, encouragement, and understanding when I felt stressed and depressed during my PhD study in the last five years.

This work was supported by the PERSISTENCE project from the Natural Sciences and Engineering Research Council of Canada, Hydro-Québec, Manitoba Hydro, and the Ouranos consortium. I also received a scholarship from the China Scholarship Council.

TABLE OF CONTENTS

REMERCIEMENTS IX

ACKNOWLEDGEMENTS XI

TABLE OF CONTENTS XIII

LIST OF TABLES XVII

LIST OF FIGURES XIX

LIST OF ABBREVIATIONS XXIII

RÉSUMÉ XXVII

ABSTRACT XXXI

GENERAL INTRODUCTION 1

0.1 Purpose of investigation and rationale 1

0.2 Tree rings as temperature proxies 4

0.3 Blue intensity technique 7

0.4 Description of the study region 10

0.5 Objectives and hypotheses 13

CHAPITRE I TEMPERATURE SENSITIVITY OF BLUE INTENSITY, MAXIMUM LATEWOOD DENSITY, AND RING WIDTH DATA OF LIVING BLACK SPRUCE TREES IN THE EASTERN CANADIAN TAIGA 17

1.1 Résumé 18

1.2 Abstract 19

1.3 Introduction 20

1.4 Materials and methods 22
1.4.1 Tree-ring data 22
1.4.2 Temperature data 24
1.4.3 Data analysis 24
1.5 Results 26
1.5.1 Inter-parameter comparison 26
1.5.2 Correlation with temperature 26
1.5.3 Influence of tree replication on the temperature signal 28
1.6 Discussion 28
1.7 Conclusion 31
1.8 Acknowledgements 32
1.9 References 33
1.10 Tables 40
1.11 Figures 42
1.12 Supplementary Materials 48

CHAPITRE II CHEMICAL DESTAINING AND THE DELTA CORRECTION FOR BLUE INTENSITY MEASUREMENTS OF STAINED LAKE SUBFOSSIL TREES 59
2.1 Résumé 60
2.2 Abstract 61
2.3 Introduction 62
2.4 Materials and methods 64
2.4.1 Study sites and staining issue 64
2.4.2 Destaining experiment 65
2.4.3 Dendroclimatic assessment 67
2.4.4 Data analysis 69
2.5 Results 69
2.5.1 Effects of chemical destaining 69
2.5.2 Stain versus iron 70
2.5.3 Comparison of LBI and DBI against MXD chronology 70
2.6 Discussion 71

2.6.1 Causes of stain 71
2.6.2 Chemical destaining versus delta correction 73
2.7 Conclusion 75
2.8 Acknowledgements 75
2.9 References 77
2.10 Tables 83
2.11 Figures 85
2.12 Supplementary Materials 91

CHAPITRE III NORTH AMERICAN MILLENNIAL TEMPERATURES FROM TREE-RING DENSITY DATA 103
3.1 Résumé 104
3.2 Abstract 105
3.3 Introduction 106
3.4 Results and discussion 106
3.5 Materials and methods 110
3.5.1 MXD network and chronology development 110
3.5.2 MJJA temperature reconstruction 111
3.5.3 Historical temperature record 113
3.5.4 Last millennium temperature simulations 113
3.5.5 Correlation analysis and significance test 114
3.5.6 Attribution of cold extremes to volcanic eruptions 114
3.5.7 Superposed epoch analysis (SEA) 115
3.6 Acknowledgments 116
3.7 References 117
3.8 Figures 127
3.9 Supplementary Text 131
3.10 Supplementary Materials 135

GENERAL CONCLUSION 159

REFERENCES 165

LIST OF TABLES

Table 1-1: Description of the standardized tree-ring chronologies at the 17 studied sites. 40

Table 1-2: Correlation coefficients between pairs of regional tree-ring parameters over the 1901–2000 period. 41

Table 2-1: Basic chemical properties of the seven chemical solutions. 83

Table 2-2: Definitions of wood color intensities and tree-ring parameters used in this study. 84

Table 2-S1: Statistics of calibration (1901–1960) and verification (1960–2015) for LBI, DBI and MXD against the May–August temperature target. 91

Table 3-S1. Published millennial MXD chronologies previously used for climate reconstructions. 135

Table 3-S2. Properties of the MXD network. 136

Table 3-S3. Calibration statistics of Bayesian summer temperature reconstructions over the 1905–2006 time period. 137

Table 3-S4. Non-overlapping warmest decades and strongest centennial warming trends reconstructed by 4P-STREC. 138

Table 3-S5. Extremely cold years ($\leqslant$ mean−2SD) in the 4P-STREC and D-STREC reconstructions, and correspondence to volcanic eruptions 139

Table 3-S6. Non-overlapping coldest decades reconstructed by 4P-STREC and correspondence to volcanic eruptions. 140

Table 3-S7. Tropical and NHET volcanic eruptions with peak $SAOD_{NHET} \geqslant 0.03$ 141

Table 3-S8. CMIP5 last-millennium ensemble models and volcanic forcing datasets used..... 142

Table 3-S9. Correlations among sites and MJJA temperatures according to standardization methods. 143

LIST OF FIGURES

Figure 1-1: Locations of the 17 sampling sites (circles) across the eastern Canadian taiga and three nearby meteorological stations (stars). 42

Figure 1-2: Comparison of regional chronologies with MJJA regional mean temperatures (orange) over the 1901–2000 time interval (a–d), and the total number of trees sampled across the 17 sites (e). 43

Figure 1-3: Correlation of LBI, DBI, MXD, and TRW chronologies with corresponding monthly land temperature targets over the 1901–2000 time interval. 44

Figure 1-4: Coherence analysis of the regional LBI, DBI, MXD, and TRW chronologies with MJJA regional mean temperature over the 1901–2000 time interval. 45

Figure 1-5: Spatial correlations of LBI, DBI, MXD, and TRW regional chronologies (a–d), and MJJA regional mean temperatures (averaged from 75ºW–60º W and 50ºN–60º N) (e) against land (CRU TS 4.03) and oceanic (HadISST1) MJJA 1º gridded temperatures for the 1901-2000 time interval. 46

Figure 1-6: Influence of tree replication on the MJJA temperature signals of the LBI, DBI, MXD, and TRW regional chronologies over the 1901–2000 time interval. 47

Figure 1-S1: Relationships between the mean and standard deviation (SD) of LBI, DBI, MXD, and TRW raw measurements before standardization. 48

Figure 1-S2: MJJA temperature signal strength of tree-ring chronologies generated using ratios (blue) and power-transformation plus residuals (red) indexation during the signal-free age-dependent spline standardization. 49

Figure 1-S3: Replication of local tree-ring chronologies at the 17 sites since 1901. 50

Figure 1-S4: Inter-parameter (LBI, DBI, MXD, and TRW) correlation analysis among the 17 local chronologies. 51

Figure 1-S5: Comparisons of local and regional LBI standardized chronologies (blue) against local and regional MJJA temperature targets (red). 52

Figure 1-S6: Comparisons of local and regional DBI standardized chronologies (blue) against local and regional MJJA temperature targets (red). 53

Figure 1-S7: Comparisons of local and regional MXD standardized chronologies (blue) against local and regional MJJA temperature targets (red). 54

Figure 1-S8: Comparisons of local and regional TRW standardized chronologies (blue) against local and regional MJJA temperature targets (red). 55

Figure 1-S9: Comparison of LBI, DBI, and MXD regional chronologies. 56

Figure 2-1: Location of the two studied lakes (a), and frequency of cross-dated LSTs according to staining at L20 (b) and L105 (c). 85

Figure 2-2: Diagram of one chemical destaining experiment for one pair of wood laths from the same subfossil tree in a Falcon® 50mL tube. 86

Figure 2-3: Residual iron (Fe) and wood RGB intensities (see definitions in Table 2-2) of LST laths treated with seven chemical reagents. 87

Figure 2-4: Comparisons of LBI (a, c) and DBI chronologies (b, d) for the MixA, MixB, MixC and Control treatments against the reference MXD chronology. 88

Figure 2-5: Schema of different cross-sectional colors from the buried and exposed cross sections of the same partially buried tree (a), and field observations of cross-sectional color changes after a fresh disc was cut from a buried tree and exposed to air (b). 89

Figure 2-6: Temperature reconstructions using the LBI chronology for the MixC protocol (purple), the Control DBI chronology (blue), and the reference MXD chronology (red) for the 1655–2015 (a, c) and 1901–2015 (b, d) time intervals. 90

Figure 2-S1: A general view of the staining issue of wet LSTs at the site L105. 92

Figure 2-S2: Design of destaining experiments following Section 2.4.2 showing how a subfossil tree replicate (a) and a living-tree replicate (b) were cut into 1mm-thick laths and how these laths were treated using different chemical reagents. 93

Figure 2-S3: Timespans of tree-ring series used for developing LBI, DBI, and MXD chronologies (a–b), and tree replication of the regional chronology (c). 94

Figure 2-S4: Destaining treatments of selected samples used for dendrochronological assessments following Section 2.4.3 showing how a tree replicate was cut into 1mm-thick laths and how these laths were treated using different chemical reagents. 95

Figure 2-S5: Fe dissolution curves during the MixA, MixB, and MixC treatments. 96

Figure 2-S6: Tree-ring structure (a) and an example of tree-ring color intensity measurement using CooRecorder 8.1 (Cybis Dendrochronology) (b). 97

Figure 2-S7: Raw data of LBI, DBI, and MXD of treated (MixA, MixB, and MixC) and untreated (Control) LSTs and living trees.....98

Figure 2-S8: Averaged raw measurements of LBI, DBI, and MXD from five living trees at L20 (untreated with destaining chemicals). 99

Figure 2-S9: MXD regional chronologies for the MixA, MixB, MixC, and Control treatments.....100

Figure 2-S10: Comparisons of LBI (a, c) and DBI (b, d) against MXD data for the MixC treated and Control stained LSTs. 101

Figure 3-1: Millennial MXD network and correlation fields with gridded MJJA temperature of the CRU dataset.....127

Figure 3-2: Reconstructed MJJA temperature anomalies w.r.t. 1905–2006 CE in NENA. 128

Figure 3-3: Superposed epoch analysis for 4P-STREC according to volcanic aerosol forcing.....129

Figure 3-4: Comparison of 4P-STREC with NHET summer temperature reconstructions and simulations.....130

Figure 3-S1: Local MXD chronologies 144

Figure 3-S2: Summary statistics of local and regional MXD series. 145

Figure 3-S3: Tambora (1815 CE) cooling recorded in historical MJJA temperatures, three temperature reconstructions, and the MXD chronologies at four sites.....146

Figure 3-S4: Proxy-level uncertainties of three temperature reconstructions. 147

Figure 3-S5: Timing of cooling maxima occurred within 2 years after tropical (**A**) and NHET (**B**) eruptions in 4P-STREC.....148

Figure 3-S6: Volcanic responses of NHET tree-ring summer temperature reconstructions (**A**, **B**) and climate model simulations (**C**, **D**). 149

Figure 3-S7: Comparison of volcanic responses among three summer temperature reconstructions in NENA. 150

Figure 3-S8: Comparison of 4P-STREC with the single-forcing simulations of NHET land summer temperatures from CESM-LME. 151

Figure 3-S9: Comparison of temperature reconstruction methods. 152

Figure 3-S10: Tree-ring responses to regional mean temperatures from the CRU TS4.03 dataset over the 1905–2006 time period (1905–1989 CE for MXD at Quex). 153

Figure 3-S11: Tests of 4P-STREC responses to volcanic eruptions. 154

Figure 3-S12: Validation of volcanic responses. 155

Figure 3-S13: Validation of the location of the Quex tree-ring dataset. 156

Figure 3-S14: Comparison of standardization methods for MXD ratio chronologies. 157

LIST OF ABBREVIATIONS

BI	Blue intensity.
CE	Common Era.
CESM-LME	Last Millennium Ensemble of Community Earth System Model.
CMIP5	Coupled Model Intercomparison Project Phase 5.
DBI	Delta blue intensity.
D-STREC	Density-based summer temperature reconstruction.
EBI	Earlywood blue intensity.
ECCC	Environment and Climate Change Canada.
EDTA	2% (w/v) solution of disodium ethylenediaminetetraacetate.
EPS	Expressed population signal.
EWD	Earlywood density.
GVP	Global Volcanism Program.
HAc	2% (v/v) solution of acetic acid.

HAsc 2% (v/v) solution of ascorbic acid.

IPCC Intergovernmental Panel on Climate Change.

LBI Latewood blue intensity.

LIA Little Ice Age.

LST Lake subfossil tree.

MCA Medieval Climate Anomaly.

MJJA May to August.

MP-AES Microwave plasma-atomic emission spectrometer.

MXD Maximum latewood density.

NaAsc 2% (w/v) solution of sodium ascorbate.

NENA Northeastern North America.

NHET Northern Hemisphere extratropical.

NSERC Natural Sciences and Engineering Research Council of Canada.

RCS Regional curve standardization.

RSFi Regionally constrained individual signal-free standardization.

SAOD Stratospheric aerosol optical depth at 550 nm.

SEA Superposed epoch analysis.

TRW Total (tree-) ring width.

3P-STREC Three-proxy (ring width, $\delta^{18}O$, and $\delta^{13}C$) summer temperature reconstruction.

4P-STREC Four-proxy (density, ring width, $\delta^{18}O$, and $\delta^{13}C$) summer temperature reconstruction.

RÉSUMÉ

La reconstitution de la variabilité climatique à haute résolution au cours des millénaires passés fournit un contexte historique essentiel pour évaluer l'importance des changements climatiques récents à l'échelle régionale et globale. En se basant sur une compilation de reconstitutions de température à grande échelle, le 5e rapport du Groupe intergouvernemental d'experts sur l'évolution du climat (IPCC, 2013) a mis en évidence l'occurrence d'époques climatiques au cours de l'ère commune (EC), telles que l'anomalie climatique médiévale, le petit âge glaciaire et la période du réchauffement récent. Cependant, les dates et l'amplitude de ces périodes diffèrent selon les reconstitutions et les régions, ce qui souligne la nécessité d'améliorer les reconstitutions climatiques en utilisant de meilleurs enregistrements proxy provenant de divers endroits, ainsi qu'en utilisant des méthodes statistiques avancées.

La densité maximale du bois final (MXD) des conifères des hautes latitudes est largement considérée comme l'indicateur le plus sensible pour la reconstitution des températures avec une résolution annuelle. Cependant, en raison des coûts élevés pour effectuer des mesures densitométriques par rayons X, seulement 12 reconstitutions des températures estivales basées sur la MXD couvrent le dernier millénaire, dont 11 sont regroupées en Eurasie. Ce manque de données a entravé notre compréhension de l'histoire millénaire des températures estivales en Amérique du Nord. Cette thèse de doctorat vise à produire une reconstitution précise et robuste de la température estivale millénaire en utilisant des mesures MXD ou d'intensité du bleu (une alternative à la MXD moins chère mais prometteuse) d'épinettes noires (*Picea mariana* (Mill.) BSP.) vivantes et subfossiles dans la forêt boréale de l'est du Canada. Ces nouvelles données permettront de mieux quantifier la variabilité des températures estivales dans le nord-est de l'Amérique du Nord au cours du dernier millénaire.

Dans le premier chapitre, mon objectif était d'étudier le potentiel de la nouvelle méthode d'intensité de la lumière bleue comme substitut des données de la méthode conventionnelle de densité maximale du bois final basées sur les rayons X. À l'aide de 178 échantillons provenant d'épinettes noires vivantes dans 17 sites de la forêt boréale de l'est du Canada, j'ai démontré que l'intensité du bleu du bois final, l'intensité delta du bleu (i.e. correction delta de l'intensité du bleu) et la densité maximale du bois final répondent de façon très similaire aux températures moyennes du printemps-été à l'échelle régionale. Ces paramètres basés sur la densité sont supérieurs aux mesures de la largeur des cernes et contiennent un signal de température estivale plus fort sur une saison de croissance plus longue. L'intensité du bleu du bois final semble être déformée par des biais de couleur et une faible résolution de mesure. L'intensité delta du bleu possède une cohérence légèrement plus

élevée avec les températures estivales que l'intensité du bleu du bois final en raison de sa capacité à éliminer les biais de couleur en plus d'un signal potentiel de température lié à la largeur des cernes. Cependant, par rapport aux paramètres d'intensité du bleu, la densité maximale du bois final est systématiquement plus robuste et moins sensible aux biais de couleur et au nombre d'arbres mesurés.

L'objectif du deuxième chapitre était de vérifier si les mesures de l'intensité du bleu issues de bois subfossile coloré peuvent être utilisées comme un proxy robuste pour les reconstitutions de la température. J'ai testé sept réactifs chimiques pour éliminer la coloration bleu-gris des arbres subfossiles enfouis dans les sédiments de deux lacs boréaux de l'Est du Canada. Les chronologies résultantes de l'intensité du bleu du bois final ont été comparées à la correction mathématique delta ainsi qu'à la méthode conventionnelle de densité maximale du bois final basée sur les rayons X. Les analyses chimiques ont montré que l'oxydation post-échantillonnage du fer dissous transféré des sédiments aux tissus du bois enfouis est très probablement responsable de la coloration. Cependant, même le meilleur protocole de décoloration chimique n'a pas permis d'obtenir des données non biaisées d'intensité du bleu du bois final en raison d'une décoloration incomplète et de la grande sensibilité des données d'intensité du bleu à la contamination par la couleur. En revanche, la correction delta de l'intensité du bleu (c'est-à-dire l'intensité delta du bleu) a produit une reconstitution de la température très similaire à celle basée sur la densité maximale du bois final dans tout le spectre de fréquences, même lorsqu'elle est mesurée à partir d'échantillons colorés n'ayant subi aucun traitement chimique. Ce résultat indique l'utilité de l'intensité delta du bleu mesuré à partir de subfossiles colorés par le fer pour développer de longues reconstitutions de températures. Cependant, au stade actuel, la MXD est toujours considérée comme le proxy le plus robuste selon les résultats des premier et deuxième chapitres.

L'objectif du troisième chapitre était d'utiliser la densité maximale du bois final pour reconstituer les températures estivales au cours du dernier millénaire dans la forêt boréale de l'est du Canada. J'ai développé un nouveau réseau de données comprenant un nombre sans précédent de mesures de densité de bois final d'épinettes noires vivantes et subfossiles (N = 1249) de trois sites. Ce réseau millénaire a été combiné à un ensemble de données existant plus court (N = 45 arbres) pour reconstituer de la température estivale (mai-août) sur 1300 ans. Cette reconstitution a ensuite été combinée avec les données de largeur de cernes et les données isotopiques du carbone et de l'oxygène disponibles afin de développer une reconstitution de la température encore plus robuste couvrant la période 997-2006 EC. Les résultats indiquent que le nord-est de l'Amérique du Nord a connu des étés chauds pendant l'Anomalie Climatique Médiévale (997-1250 EC ; 0,25 ºC plus chaud par rapport à 1905-2006 EC) suivie par la période froide du Petit Âge Glaciaire (997-1250 EC, -0,27 ºC plus froid que la période 1905-2006 ; en particulier pendant la période 1601-1930 EC), puis par le réchauffement récent contenant la décennie la plus chaude du millénaire en 1997-2006 EC (1,0ºC par rapport à la période 1905-2006 EC), de même que la tendance au réchauffement centennal la plus rapide (1904-2003 EC). La variabilité régionale multidécennale des températures estivales a été synchronisée avec les températures estivales de l'hémisphère

nord par les plus fortes éruptions volcaniques. Bien que les éruptions tropicales et extratropicales de l'hémisphère nord aient conduit à des étés extrêmement froids au cours des 1000 dernières années, les éruptions tropicales ont eu des impacts climatiques plus importants et plus persistants (12 ans contre 1-3 ans) que les éruptions extratropicales.

En résumé, cette thèse met en évidence les avantages de la densité maximale du bois final comme indicateur des températures du passé dans la forêt boréale de l'est du Canada. L'intensité du bleu a un fort potentiel pour se substituer aux données de densité des cernes des arbres issues de bois vivant et de bois subfossile teinté par le fer pour reconstituer le climat dans la région étudiée. La densité et l'intensité du bleu sont supérieures aux mesures de la largeur des cernes en raison de leurs corrélations plus fortes avec les températures estivales et leur faible mémoire biologique. Par conséquent, elles pourraient améliorer la représentation spatiale des reconstitutions climatiques et fournir des informations plus précises sur les variations du climat dans le passé. Les reconstitutions basées sur la densité du bois ont permis de mieux comprendre la variabilité des températures estivales et les mécanismes de forçage externe dans le nord-est de l'Amérique du Nord.

Mots clés : dendroclimatologie ; densité maximale du bois final ; intensité du bleu ; épinette noire ; reconstitutions de la température estivale ; forêt boréale de l'est du Canada ; forçage externe ; changement climatique.

xxx

ABSTRACT

Reconstructing high-resolution climate variability over past millennia provides a critical historical context to assess the importance of the recent climate changes at regional to global scales. Based on a compilation of large-scale temperatures, the 5th Assessment Report of the Intergovernmental Panel on Climate Change (IPCC, 2013) has demonstrated the occurrence of climate epochs over the Common Era (CE), such as the Medieval Climate Anomaly, the Little Ice Age, and the recent warming period. However, the timing and amplitudes of these periods differ by reconstructions and regions, highlighting the need to develop high-quality temperature reconstructions using proxy records from various locations, as well as using advanced statistical methods.

Maximum latewood density (MXD) of high-latitude conifers is widely considered to be the most sensitive proxy for reconstructing temperatures with an annual resolution. However, due to the high costs of conducting X-ray densitometric measurements, only 12 MXD-based summer temperature reconstructions cover the last millennium, and 11 of them are clustered in Eurasia. The resulting geographical data gap has hampered our understanding of North American millennial summer temperatures. This PhD thesis aimed to produce a robust reconstruction of millennial summer temperatures using annually resolved MXD or blue intensity measurements (a less expensive but promising alternative to MXD) of living and subfossil black spruce (*Picea mariana* (Mill.) BSP.) trees in the eastern Canadian boreal forest. These new data will improve the assessment of summer temperature variability in northeastern North America during the last millennium.

In the first chapter, my objective was to investigate the potential of the recent, optical-based blue intensity method as a surrogate for X-ray-based MXD data from living black spruce trees. Using 178 samples collected from 17 sites across the eastern Canadian boreal forest, I demonstrated that latewood blue intensity, delta blue intensity (i.e., delta correction of blue intensity), and MXD respond in very similar ways to spring–summer mean temperatures at the regional scale. These density-based parameters are superior to ring-width measurements because they retain stronger summer temperature signals over a longer growing season. Latewood blue intensity appears to be distorted by color biases and low measurement resolution. Delta blue intensity possesses slightly higher coherence with summer temperatures than latewood blue intensity because of its ability to remove color biases and its potential to retain an additional temperature signal related to ring-width formation. In general, MXD is consistently more robust and less sensitive to color biases and low tree replication compared to blue intensity parameters.

The objective of the second chapter was to test whether blue intensity measurements from stained subfossil wood of black spruce can be used as a robust proxy for temperature reconstructions. I tested seven chemical destaining reagents to remove the blue-gray stain on subfossil trees buried in sediments of two boreal lakes in eastern Canada. The resulting latewood blue intensity chronologies were compared with the mathematical delta correction and conventional X-ray-based MXD data from the same trees. Chemical analyses showed that post-sampling oxidation of dissolved ferrous iron transferred from sediments to buried wood tissues was most likely responsible for the stain. However, even the best chemical destaining protocol could not yield unbiased latewood blue intensity data because the destaining was incomplete and blue intensity measurement is highly sensitive to color contamination. In contrast, the delta correction of blue intensity (i.e., delta blue intensity) produced a temperature reconstruction very close to that based on MXD across the frequency spectrum, even when measured from untreated stained samples. This result indicated the usefulness of delta blue intensity measured from iron-stained subfossil materials for long-term temperature reconstructions. MXD is still considered as the most robust proxy according to the results of the first and second chapters.

The objective of the third chapter was to use MXD to reconstruct summer temperatures during the last millennium in the eastern Canadian boreal forest. I developed a new data network comprising an unprecedented number of latewood density measurements from living and subfossil black spruce trees (N = 1,249) at three sites. This millennial network was combined with an existing shorter dataset (N = 45 trees) to produce a 1300-year reconstruction of summer (May–August) temperatures. This was then combined with available ring-width, and carbon and oxygen isotopic data in order to develop an even more robust temperature reconstruction spanning 997–2006 CE. The results indicated that northeastern North America experienced warm summers during the Medieval Climate Anomaly (997–1250 CE; 0.25 ºC warmer than 1905–2006 CE), followed by the relatively cold Little Ice Age (997–1250 CE), which was 0.27 ºC colder than the 1905–2006 period, especially during 1601–1930 CE. The recent warming includes the warmest decade during 1997–2006 CE (1.0 ºC with respect to (w.r.t.) 1905–2006 CE) and the fastest centennial warming trend (1904–2003 CE) of the last millennium. Regional multidecadal summer temperature variability has been synchronized with Northern Hemispheric summer temperatures by strong volcanic eruptions. Although tropical and Northern Hemispheric extratropical eruptions have led to extremely cold summers over the past 1000 years, the climatic impacts of tropical eruptions were more prominent and persistent (12 years vs 1–3 years) than extratropical eruptions.

In summary, this thesis highlights the advantages of using MXD as a temperature proxy in the eastern Canadian boreal forest. Blue intensity has great potential to produce excellent surrogates for tree-ring density data from living and iron-stained subfossil wood for reconstructing climate in the study region. Density and blue intensity are superior to ring-width measurements due to their stronger correlations with summer temperatures and weaker biological memory. Therefore, they could improve the spatial representation of the

reconstructed climate and reduce potential errors in the reconstruction, providing better constraint and more precise information of climate changes in the past. Finally, the density-derived reconstructions enhanced the understanding of summer temperature variability and external forcing mechanisms in northeastern North America.

Keywords: dendroclimatology; maximum latewood density; blue intensity; black spruce; summer temperature reconstructions; eastern Canadian boreal forest; external forcing; climate change.

GENERAL INTRODUCTION

0.1 Purpose of investigation and rationale

There have been increasing concerns about the Earth's climate changes and associated extreme events since the second half of the 20th century. According to the 5th Assessment Report of the Intergovernmental Panel on Climate Change, the global temperature during 2003–2012 Common Era (CE) has been about 0.78°C warmer than that in the second half of 19th century (1850–1900 CE), and the warming will very likely continue during the 21st century due to increasing greenhouse gases (IPCC, 2013). However, most instrumental temperature observations only began after the mid-19th and even the 20th century (Rennie et al., 2014). Thus, to evaluate climate variability and the forcing mechanisms in a long-term context, we must rely upon climate proxies that span from centuries to millennia (Mann et al., 2008), including historical documentary records and natural archives such as tree rings, ice cores, lake/ocean sediments, and boreholes. While some geological proxies allow reconstructing climate during the Last Glacial Maximum with substantial dating uncertainties (e.g., Masson-Delmotte et al., 2013), high-resolution (annual-to-decadal) temperature reconstructions over the CE have received particular attention (Jones et al., 2009; Christiansen and Ljungqvist, 2017).

Over the last two decades, multiple large-scale millennial temperature reconstructions have been developed to assess the climatic excursions in the last 2000 years (Mann et al., 2008, 2009; PAGES 2k Consortium, 2013; Wilson et al., 2016; Anchukaitis et al., 2017; Neukom et al., 2019), such as the relatively warm Medieval Climate Anomaly (MCA, c.a. 950–1250 CE), and the colder Little Ice Age (LIA, c.a. 1450–1850). Northern Hemisphere reconstructions have also been used to decipher the relative contributions of natural (e.g., solar, volcanic, and orbital) and anthropogenic (e.g., greenhouse gases) forcing agents on the

temperature variability. Such detection and attribution studies have revealed the significant fingerprints of volcanic aerosols throughout historical times and the enhancing influence of greenhouse gases since the industrial period, while the impact of solar forcing is less prominent (Hegerl et al., 2007; Phipps et al., 2013; Schurer et al., 2013, 2014; PAGES 2k Consortium, 2019). Despite these achievements, our understanding of local- to global-scale temperature variations before ~1500 CE is largely constrained by unequal geographical distribution and sparseness of high-quality and high-resolution millennial proxy records (Mann et al., 2008; Masson-Delmotte et al., 2013; Christiansen and Ljungqvist, 2017; Esper et al., 2018; St. George and Esper, 2019), which are keys to data-model comparison over the last millennium (Neukom et al., 2018).

Tree rings, mainly the total tree-ring width (TRW) and maximum latewood density (MXD), of mid-high-latitude conifers are the backbone of temperature reconstructions over the last two millennia (Jones et al., 2009; Büntgen et al., 2013; PAGES 2k Consortium, 2017). Tree rings can record inter-annual climate information (e.g., summer temperatures) because of their accurate dating to calendar years (Schweingruber, 2012). Widespread natural forests and easy sampling procedures (in general using increment borers) further make the annually resolved tree-ring data not only well-replicated (thus reducing uncertainties introduced by individuals) but also more densely distributed in space compared to other types of proxies. As a consequence, tree rings make up more than half (54–91%) of proxy series used for recent global multiproxy temperature reconstructions (Mann et al., 2008; PAGES 2k Consortium, 2013, 2019; Neukom et al., 2019). Numerous tree-ring chronologies have also been individually used to reconstruct summer temperatures at local (Büntgen et al., 2013; Esper et al., 2012, 2020; Gennaretti et al., 2014a; Fuentes et al., 2017) to hemispheric scales (Schneider et al., 2015; Stoffel et al., 2015; Wilson et al., 2016; Anchukaitis et al., 2017; Guillet et al., 2020).

At present, there are only about forty annually resolved, temperature-sensitive tree-ring (TRW and MXD) series extending back to 1000 CE or earlier (Esper et al., 2016), although

thousands of tree ring chronologies have emerged over last few decades. Although millennial tree-ring chronologies are mostly abundant in the mid-high latitude of the Northern Hemisphere, they are clustered in Fennoscandia, the European Alps, Qinghai-Tibetan Plateau, and the western United States. In addition, considering the more robust MXD data compared to TRW (Frank and Esper, 2005; Esper et al., 2015), available datasets are even fewer (only 13), including 11 MXD chronologies from Eurasia (Wang et al., 2001; McCarroll et al., 2013; Esper et al., 2016, 2020). Such spatial coverage, in particular for MXD chronologies, is still far to fully represent the entire globe, hemisphere, or even the North American continent. Several millennial TRW and stable isotope chronologies have been developed in northeastern North America (Arseneault et al., 2013; Gennaretti et al., 2014a, 2017; Naulier et al., 2015), however, there is only one MXD series spanning the last millennium which could not be used for dendroclimatic purposes due to data heterogeneity and low replication (Wang et al., 2001).

This thesis, as a part of the "PERSISTENCE" project supported by the Natural Sciences and Engineering Research Council of Canada (NSERC), Hydro-Québec, Manitoba Hydro, and the Ouranos consortium, focuses on developing a high-quality millennial summer temperature reconstruction for the eastern Canadian boreal forest (i.e., Québec-Labrador Peninsula) using highly replicated MXD data or its blue intensity (BI) surrogates (Campbell et al., 2011; Rydval et al., 2014) measured from black spruce (*Picea mariana* (Mill.) BSP) trees. Previous works have exploited the TRW and isotope data to reconstruct millennial summer temperatures in central Québec (Gennaretti et al., 2014a, 2017; Naulier et al., 2015). However, it was suggested that the high-frequency temperature variations were poorly expressed in these reconstructions (Gennaretti et al., 2017). Therefore, there is a large fraction of unknown (perhaps underestimated) summer temperature variability which has yet to be reconstructed using MXD data. This work is intended to improve our understanding of the regional temperature history using the more robust MXD data over the last 1000 years. Simultaneously, our MXD network will fulfill an important spatiotemporal gap that currently exists in the global high-resolution temperature proxy database.

0.2 Tree rings as temperature proxies

Tree-ring parameters

A variety of tree-ring parameters have been found sensitive to summer temperatures, such as tree-ring width, density, and stable isotope ratios of cell walls (Schweingruber, 2012). Among them, only a handful of temperature-sensitive tree-ring stable isotope measurements (carbon, hydrogen, and oxygen) have been used to reconstruct temperature variability (Gagen et al., 2007; Liu et al., 2014; Porter et al., 2014; Naulier et al., 2015), and even no tree-ring isotope series were included in a recent global database of temperature proxies (PAGES 2k Consortium, 2017). In this section, we will thus focus on TRW and MXD, the two most important tree-ring proxies that are widely used in temperature reconstructions.

Total tree-ring width is the most frequently used tree-ring proxy because it can be easily measured using instruments such as the LINTAB system (Rinntech) as well as image analysis software (e.g., CooRecorder developed by Cybis Dendrochronology). However, in general, temperature signals recorded in TRW are relatively weak, and species- and site-specific (Briffa et al., 2002; Frank and Esper, 2005). In regions where a unique limiting factor is not dominant, TRW growths can be governed by temperatures in several discontinuous seasons (Chen et al., 2012; Wang et al., 2019). Moreover, TRW exhibits exceptionally strong biological persistence (or memory effect) which most likely arises from utilization and remobilization of carbohydrates stored from precedent growing years (Esper et al., 2015; Frank et al., 2007). The resulting high autocorrelation (above the level of instrumental temperature records, see Esper et al., 2015) could thus lead to delayed and attenuated TRW responses to pulse-like cooling episodes (Esper et al., 2014, 2015; Wang et al., 2020), for example following large explosive volcanic eruptions which are important drivers of the Earth's climate variability (Robock, 2000). Some studies also reported spectral biases related to strong autocorrelations of TRW series, which may inflate the low-frequency variability (Frank et al., 2007; Franke et al., 2013).

Maximum density in the latewood portion of tree rings is widely accepted as a more sensitive proxy for reconstructing summer temperatures than TRW (Björklund et al., 2019). In general, MXD responds more strongly to summer temperatures over broader seasons (Briffa et al., 2002; Frank and Esper, 2005). For example, the average correlation with summer (June–August) temperatures is 0.55 for MXD compared to 0.33 for TRW according to analyses on multi-century series from 11 sites in extratropical Northern Hemisphere (Esper et al., 2015). Summer temperature signals recorded in MXD are more independent of species and site ecology than TRW (Frank and Esper, 2005). Biological persistence of MXD is also weaker, such that the autocorrelation of MXD is similar to instrumental (Esper et al., 2015) and simulated temperature series (Lücke et al., 2019). MXD is thus capable of precisely recording inter-annual summer temperature variations and abrupt post-volcanic summer cooling episodes (Esper et al., 2013, 2015), although a few studies have argued that MXD overestimates volcanic cooling as this parameter can be light-sensitive (Stine and Huybers, 2014; Tingley et al., 2014). A two-millennium MXD-based temperature reconstruction in Northern Scandinavia has further demonstrated the superiority of MXD data to record long-term (millennial) cooling signatures induced by orbital forcing, a pattern which is largely absent in TRW chronologies developed from the same area (Esper et al., 2012).

These advantages have increased calls for producing more high-quality MXD series in order to improve the robustness of tree-ring reconstructions from local to global scales and to fill the spatiotemporal gaps in the current temperature proxy network, in particular, in North America (Wilson et al., 2016; Anchukaitis et al., 2017; Esper et al., 2018; St. George and Esper, 2019; Büntgen et al., 2020; Zhu et al., 2020). However, the development of MXD series lags far behind that of TRW data, because it is constrained by the high cost of the conventional X-ray densitometric methods (e.g., X-ray radiography and computed tomography; Jacquin et al., 2017) and the lack of facilities (Rydval et al., 2014; Wilson et al., 2014, 2019). In recent years, researchers have attempted to develop less expensive alternatives, such as the optical-based blue intensity (BI) approach (Campbell et al., 2007) as well as anatomical density methods (Björklund et al., 2019, 2020a).

Tree-ring standardization

In practical reconstructions, most tree-ring data need to be standardized (or detrended) to remove growth patterns that do not vary with climate (Helama et al., 2017). Although this has been debated for the tree-ring isotopes (Duffy et al., 2019; Arosio et al., 2020; Nakatsuka et al., 2020), there is a consensus that non-climatic growth trends are evident in TRW and MXD series (see Young et al., 2011; Schweingruber, 2012). The principal idea of standardization is to fit the tree-ring growth pattern using suitable functions (e.g., modified negative exponential functions, slope lines, and smoothing splines), and subsequently remove this fitted curve from raw measurements using either subtraction or division (Fritts, 1976). Traditional approaches proceed by fitting curves on a tree-by-tree basis and consequently set the mean of every standardized series to 1.0. Consequently, variability at wavelengths exceeding the lengths of tree-ring series cannot be retained in the standardized chronologies (i.e., the "segment length curse" issue), in particular when developing (millennial) long chronologies that combine subfossil materials with living trees for short living species (Cook et al., 1995).

In the early 1990s, regional curve standardization (RCS) was introduced to mitigate the low-frequency losses resulting from traditional standardization methods in dendrochronology (Briffa et al., 1992). The RCS method basically relies on constructing one growth curve for one species in a region (i.e., regional curve) using averaged growth patterns of multiple tree-ring series aligned according to cambial ages (Briffa and Melvin, 2011; Helama et al., 2017). Pith offset data are generally needed for RCS, though some work suggested insignificant effects if not using pith offsets (Esper et al., 2008). Individual raw series are subsequently standardized using the regional curve by division or subtraction, such that the resulting mean of standardized series is not forced to be 1.0. This approach provides an effective way to preserve more long-term variations (Jones et al., 2009; Helama et al., 2017). However, there are several potential problems associated with the RCS method (see details in Briffa and Melvin, 2011). For example, insufficient samples which cannot fully

represent a wide range of growth rates will very likely lead to biased regional curves. Thus, RCS may not be suitable to standardize small sets of tree-ring data. Another issue occurs with chronologies which only consist of living trees because some common climate signals will remain in the regional curve and be ultimately removed by the RCS procedure. This, however, appears to be ideally resolved by the signal-free approach (Melvin and Briffa, 2008). Moreover, the RCS method is quite sensitive to data inhomogeneity, such as the cases where (1) trees largely exhibit distinct growth rates (Melvin and Briffa, 2014), (2) samples are collected from varying heights with different growth patterns (Autin et al., 2015), and (3) trees have been randomly disturbed (e.g., by fires and insects) in different periods (Björklund et al., 2013). A number of modifications of RCS have been proposed in specific situations (see details in Helama et al., 2017). Attention should thus be given when choosing methods or modifications of RCS to appropriately retain the low-frequency climate variability in tree-ring chronologies and subsequent climate reconstructions.

0.3 Blue intensity technique

Blue intensity (BI) or blue reflectance (McCarroll et al., 2002) is a promising method to produce surrogates for X-ray density measurements. The optical-based BI technique only requires commercial flatbed scanners and affordable image analysis software (e.g., CooRecorder, Cybis Dendrochronology). Although pioneering works focused on the normal (visible) light brightness of tree rings (Sheppard et al., 1996; Sheppard, 1999), systematic comparisons among different types of light reflectance (red, green, blue, ultraviolet, and infrared) suggested that blue light reflectance is most similar to X-ray density (McCarroll et al., 2002). The term “blue intensity” was subsequently introduced in dendrochronology to represent the tree-ring light reflectance in the blue channel of the RGB space (Campbell et al., 2007). From earlier results, variations of lignin content in cell walls were assumed to be a key factor that links BI to density variation (McCarroll et al., 2002). However, more recent anatomical studies demonstrate that both BI and X-ray densitometric methods reflect cell

wall proportions (Björklund et al., 2017, 2019, 2020a), rather than cell wall components (e.g., lignin; Björklund et al., 2020b).

There have been sustained efforts to explore the dendroclimatic potentials of the BI technique since the establishment of standard measuring protocols (Campbell et al., 2011; Rydval et al., 2014). Excellent correlations ($r > 0.8$, often > 0.9) have been reported between latewood BI (LBI) and MXD for a number of coniferous species (mostly pine and spruce) at mid-high-latitude sites in Europe (McCarroll et al., 2002; Campbell et al., 2007; Rydval et al., 2014; Österreicher et al., 2015; Kaczka et al., 2018) and western North America (Wilson et al., 2014). Another set of works revealed stronger temperature signals in LBI than TRW measured from temperate conifers in both Northern (Wiles et al., 2019; Wilson et al., 2019; Harley et al., 2020) and Southern Hemispheres (Brookhouse and Graham, 2016; Blake et al., 2020). BI parameters have been recently shown to record informative climate signals in subtropical and tropical regions as well (Buckley et al., 2018; Cao et al., 2020). In addition to its dendroclimatic significance, LBI can facilitate the dating of archaeological wood samples (Wilson et al., 2017a) and the detection of ecological disturbances (Arbellay et al., 2018; Rydval et al., 2018).

In fact, the optical-based BI method is facing great challenges that are mainly related to discolorations of different wood samples. Any color irrelevant to climate variations will introduce biases in BI measurements (Wilson et al., 2019), in particular in the low-frequency domains (Björklund et al., 2014; Rydval et al., 2014). The most-widely-known issue is the color differences between sapwood and heartwood of many tree species (e.g., pine and larch) (Sheppard, 1999; Björklund et al., 2014; Rydval et al., 2014), a phenomenon resulting from accumulation of extractives in the inner portion of trees (Kampe and Magel, 2013). Discoloration may also be caused by external reasons during tree growth or after death, such as injury (Björklund et al., 2014), fungal growth (Rydval et al., 2014), decay (Wilson et al., 2014), and weathering. Another less-documented discoloration issue occurs frequently with subfossil trees preserved in lakes (hereafter lake subfossil trees, LSTs). Overcoming these

issues is important to ensure unbiased and reliable BI data for climate reconstructions, given the high potential of the cheap BI to produce surrogates of MXD. In particular, resolving color biases associated with LSTs is critically needed because LSTs are ideal materials that can be combined with living trees to form well-replicated chronologies for reconstructing the climate over the last 1–2 millennia (Esper et al., 2012; Arseneault et al., 2013; Gennaretti et al., 2014a).

Several chemical and mathematical solutions have been proposed to reduce color biases in BI data. Chemical methods aim at homogenizing the sapwood-heartwood colors using chemical reagents. Conventional organic solvents such as ethanol and acetone could not fully extract non-structural substances deposited in heartwood (Sheppard, 1999), even after a treatment of 144 hours (Rydval et al., 2014). Sheppard and Wiedenhoeft (2007) concluded that hydrogen peroxide beaching is effective to remove the heartwood color, although earlier works showed that bleaching tended to degrade the inter-annual variability of cell-wall brightness by altering some of their components (Sheppard, 1999). By contrast, the mathematical correction calculating the difference between LBI and earlywood BI (EBI) (i.e., the delta BI, hereafter referred to as DBI) appears to be a more promising approach (Björklund et al., 2014, 2015). The efficiency of DBI is not limited to the sapwood-heartwood issues but also to a variety of discolorations since DBI mathematically uses the EBI counterpart as a baseline to correct for the color-related low-frequency biases (Björklund et al., 2014). However, it was also pointed out that DBI might still contain low-frequency biases (Björklund et al., 2014, 2015), and an MXD-based adjustment was proposed (Björklund et al., 2015). Another approach combines the high-frequency components of LBI with the low-frequency TRW data (Rydval et al., 2017a).

In recent years an increasing number of LBI, including DBI measurements, have been used to reconstruct local (Dolgova, 2016; Wilson et al., 2017b; Heeter et al., 2020; Parfitt et al., 2020; Seftigen et al., 2020), regional (Trachsel et al., 2012; Linderholm et al., 2015; McCarroll et al., 2013; Rydval et al., 2017b; Heeter et al., 2021a, b), and hemispheric climate

(Wilson et al., 2016; Anchukaitis et al., 2017), although BI is still an immature method (Wilson et al., 2019). LBI and DBI series could potentially densify the millennial tree-ring network in order to improve our understanding of the pre-1500 climate changes. However, discoloration issues should be dealt with properly.

0.4 Description of the study region

This study encompasses a region between 50ºN and 58ºN, and 60ºW and 77ºW in the eastern Canadian boreal forest which covers a large part of the Québec-Labrador Peninsula. The entire study region is governed by the subarctic climate, characterized by long, cold winters and short, mild summers. According to the 1981–2010 climate normals of three nearby meteorological stations (Kuujjuarapik A, La Grande Rivière A, and Sept-Iles A; obtained from Environment and Climate Change Canada (ECCC) 2020) (Figure 1-1), the average annual temperature is −2 ± 2.6ºC (mean ± standard deviation (SD)), and the lowest and highest monthly mean temperatures reach −20.6 ± 4.6ºC and 13.5 ± 1.7ºC in January and July, respectively. Albeit cold, the eastern Canadian boreal forest receives relatively abundant precipitations (including rainfall and snowfall) throughout the year, about twice higher than the central and western boreal forest of Canada (D'Orangeville et al., 2016), due to moisture transportation by multiple storm tracks (Stralberg et al., 2020) influenced by the North Atlantic Ocean. The mean annual precipitation is about 826 ± 255 mm averaged from the three weather stations. Snowfall makes up 34.4% of the total precipitation and mostly accumulates from October to May. Accordingly, there are sufficient water supplies for trees to initiate and sustain their growth during the early growing season. Summer temperatures thus become a vital limiting factor for the regional forest productivity (Boucher et al., 2017). The study region is also covered by numerous lakes (more than half a million in Québec Province; Québec: Ministère de l'Environnement, 2002) which serve as important water resources for ecosystems as well as Québec's hydroelectric productions.

The eastern Canadian boreal forest can be divided into three major latitudinal subdomains, including spruce-moss woodlands, spruce-lichen woodlands, and forest-tundra from south to north (Saucier et al., 2003). Black spruce is the most dominant coniferous species over all these domains, while other tree species, such as eastern larch (*Larix laricina* (Du Roi) Koch), balsam fir (*Abies balsamea* L.), jack pine (*Pinus banksiana* Lamb.), and poplars (*Populus balsamifera* and *P. tremuloides*) are found at lower densities (Payette, 1993). Human activity is low, particularly in the north (White et al., 2017). By contrast, wildfire is the primary disturbance that alters forest ecosystems. Sedimentary charcoal-based reconstructions of fire history (Cyr et al., 2009; Hély et al., 2010) and dendrochronological studies (Gennaretti et al., 2014b, 2014c) have all suggested that the mean fire-return interval varies between 100–500 years and increase eastward. Consequently, black spruce forest is often young and even-aged (Bergeron and Fenton, 2012). Even though, several millennium-length tree-ring chronologies have been successfully developed in our study region because the regional landscape (abundant black spruce, lakes, and peatlands) is favorable for long-term preservations of wood remains that have randomly fallen in water, especially in sectors that have repeatedly escaped fires over several centuries (Arseneault and Payette, 1997; Wang et al., 2001; Payette and Delwaide, 2004; Arseneault et al., 2013; Gennaretti et al., 2014a).

Dendrochronological studies in the eastern Canadian taiga emerged in the 1980s. In particular, a range of tree-ring series were constructed from TRW, MXD, anatomical features, and light rings (tree rings with thin-walled latewood) of black spruce growing around the subarctic tree line in the Boniface River area (Payette et al., 1985, 1989; Filion et al., 1986; Arseneault and Payette, 1997; Lavoie and Payette, 1997; Wang et al., 2001, 2002; Payette and Delwaide, 2004). While these works were mostly designed to investigate long-term forest dynamics from an ecological perspective, a few studies have attempted to exploit the dendroclimatic potential of black spruce tree rings by matching the diagnostic light rings to large explosive volcanic eruptions (Filion et al., 1986) and by examining tree-ring-climate relationships (Wang et al., 2001, 2002). No climate reconstructions have been developed in

the Boniface River area, despite the availability of long TRW and MXD chronologies (Arseneault and Payette, 1997; Wang et al., 2001; Payette and Delwaide, 2004; Delwaide et al., 2021). Arseneault et al. (2013) presented the potential of constructing well-replicated, millennial TRW chronologies using LSTs buried in lakes in Caniapiscau region, central Québec. This work has triggered several summer temperature reconstructions based on millennial TRW and stable isotope data (Gennaretti et al., 2014a, 2017; Naulier et al., 2015). The TRW chronology of the Caniapiscau region was recently extended over the entire Common Era and has been included in a Northern Hemisphere reconstruction of summer temperatures (Büntgen et al., 2020).

Although instrumental climate records are very sparse and short (mostly starting after 1950; see historical climate data of ECCC: https://www.canada.ca/en/environment-climate-change/services/climate-change/science-research-data/climate-trends-variability/adjusted-homogenized-canadian-data.html), proxy-based reconstructions have expanded our understanding of past climate changes in our study region over centuries to millennia. Multiple pollen and chironomid records from lake sediments allowed reconstructing postglacial summer temperatures for the Québec-Labrador Peninsula, revealing a very warm period from about 7–5k yr BP, as well as the evidence of the MCA and LIA (Kerwin et al., 2004; Viau and Gajewski, 2009; Bajolle et al., 2018). It was concluded that the regional summer temperatures during the MCA were, at least, as warm as the present-day level (Viau et al., 2012; Bajolle et al., 2018). This is, in general, consistent with the findings of millennial summer temperature reconstructions based on tree rings in central Québec (Gennaretti et al., 2014a, 2017; Naulier et al., 2015). In addition, these tree-ring reconstructions have shown an evident millennial summer cooling trend before the recent warming. The multi-proxy approach integrating TRW, $\delta^{18}O$, and $\delta^{13}C$ data improved the regional low-frequency temperature variability over the last millennium, however, the high-frequency domain was poorly expressed due to the lack of millennial MXD data (Gennaretti et al., 2017). There are also numerous tree-ring- and sediment-based reconstructions that provide insights of

hydroclimatic and drought variability during the last 500 years in our study region (Girardin et al., 2004; Dinis et al., 2019; Gagnon-Poiré et al., 2020; Nasri et al., 2020).

0.5 Objectives and hypotheses

Given the robustness of MXD and the fact that millennial MXD chronologies are exceptionally sparse, this thesis aims to provide a more comprehensive understanding of millennial summer temperature variability for the eastern Canadian boreal forest by developing a new network of robust millennial MXD chronologies or the BI surrogates (i.e., LBI and DBI) measured from living and subfossil samples of black spruce samples. To achieve this goal, three chapters were planned:

Chapter I: *Temperature sensitivity of blue intensity, maximum latewood density, and ring width data of living black spruce trees in the eastern Canadian taiga*

The BI technique shows great potential as a cheaper alternative to the X-ray densitometric method to generate surrogates of MXD. Although climate signals in LBI and DBI were examined for living-tree samples of several coniferous species growing in Eurasia and North America, no such investigation has yet been conducted using black spruce growing in the eastern Canadian boreal forest. Comparing BI parameters (LBI and DBI) with traditional tree-ring parameters (TRW and MXD) measured from living black spruce trees provides a basis for understanding the suitability of LBI and DBI for summer temperature reconstructions. This chapter helped us to select the more robust parameter for our final reconstruction in Chapter III.

Objective I: Assess the temperature sensitivity of BI parameters (LBI and DBI), MXD, and TRW over the instrumental period.

Hypothesis I: Across the eastern Canadian boreal forest, the four tree-ring parameters of black spruce respond significantly to the summer temperatures of the current year. LBI and DBI are as temperature-sensitive as MXD and more robust than TRW.

Hypothesis II: DBI is more strongly correlated to summer temperatures than LBI because DBI can reduce potential biases caused by wood discoloration.

Objective II: Test and compare the summer temperature signal strength depending on the sample replication for the four parameters.

Hypothesis III: Summer temperature signal of TRW is more dependent on tree replication compared to LBI, DBI, and MXD.

Chapter II: *Chemical destaining and the delta correction for blue intensity measurements of stained lake subfossil trees*

Staining or discoloration issues are the largest challenge when applying the promising BI technique for climate reconstructions. Subfossil trees buried in lakes from the eastern Canadian boreal forest are frequently stained with different intensities of gray and blue colors after being sampled and exposed to air. Some chemical and mathematical approaches have been proposed to resolve discoloration biases (mostly the sapwood-heartwood issue) in BI measurements, however, no work has particularly focused on the staining problem of LSTs. It is thus critical to understand the causes of the stains on LSTs and explore suitable protocols to remove such stains in order to produce unbiased BI data from LSTs of black spruce for future climate reconstructions.

Objective I: Study the causes of the staining problem of LSTs buried in lake sediments in the eastern Canadian boreal forest.

Hypothesis I: The stain of LSTs is mainly caused by oxidation of iron transferred to wood from sediments, which can be removed using some antioxidant reagents.

Objective II: Compare the LBI and DBI measured from chemically treated samples with the X-ray-based MXD measurements over the last 400 years to verify the effect of chemical destaining and mathematical correction.

Hypothesis II: Chemical destaining protocol and DBI can greatly improve BI-based temperature reconstructions that are comparable to MXD-based reconstructions.

Chapter III: *North American millennial temperatures from tree-ring density data*

MXD of conifers growing in cool environments is a superior proxy for reconstructing summer temperatures than TRW. Because MXD more precisely captures the inter-annual temperature variability, it is considered as a suitable proxy to study the cooling effects of large volcanic eruptions, an important natural forcing of summer temperature variability (Robock, 2000; Sigl et al., 2015). In the eastern Canadian boreal forest, a region sensitive to volcanic eruptions (Gennaretti et al., 2014a), there is no MXD-based millennial temperature reconstruction although some have used TRW and tree-ring stable isotopes. Developing a network of well-replicated millennial MXD series in this region would not only improve the understanding of the temperature variability over the last 1000 years as well as the volcanic effects, but also will fill an important gap in the global network of millennial MXD chronologies.

Objective I: Reconstruct millennial summer temperatures with two approaches: (1) using only MXD chronologies and (2) integrating MXD series and the existing TRW, $\delta^{18}O$, and $\delta^{13}C$ chronologies to compose a four-proxy reconstruction.

Hypothesis I: The two new millennial summer temperature reconstructions are more strongly calibrated against instrumental targets compared to the reconstructions based on TRW only

or assembling TRW, $\delta^{18}O$, and $\delta^{13}C$ data. The four-proxy reconstruction better records the regional temperature variability than the MXD-only reconstruction because it includes multiple temperature proxies such that the individual sources of error of each proxy are largely reduced.

Hypothesis II: The two reconstructions are important complements to pervious TRW and isotope-based reconstructions in high-frequency domain for summer temperatures in eastern Canada.

Hypothesis III: Low-frequency patterns (the MCA, LIA and the recent warming) revealed by our two new reconstructions are consistent with previously published temperature reconstructions and climate model simulations over the last millennium.

Objective II: Explore the fingerprints of large-scale climate forcings superimposed in our two millennial summer temperature reconstructions.

Hypothesis IV: The two new reconstructions are able to record forcing signals related to large volcanic eruptions as well as from others forcing agents (e.g., solar activities, orbital, and anthropogenic influences).

CHAPITRE I

TEMPERATURE SENSITIVITY OF BLUE INTENSITY, MAXIMUM LATEWOOD DENSITY, AND RING WIDTH DATA OF LIVING BLACK SPRUCE TREES IN THE EASTERN CANADIAN TAIGA

Feng Wang[a,b*], Dominique Arseneault[a,b], Étienne Boucher[c], Gabrielle Galipaud Gloaguen[a,d], Anne Deharte[a,d], Shulong Yu[e], Nadège Trou-kechout[a,b]

a. Département de Biologie, Chimie et Géographie, Université du Québec à Rimouski, Rimouski, G5L 3A1, Canada

b. Centre d'Études Nordiques, Université du Québec à Rimouski, Rimouski, G5L 3A1, Canada

c. Département de Géoscience, GEOTOP, and Centre d'Études Nordiques, Université du Québec à Montréal, Montréal, H3A 0B9, Canada

d. Département de Biologie et Géoscience, Université Toulouse III-Paul Sabatier, 31062 Toulouse Cedex 9, France

e. Key Laboratory of Tree-ring Ecology of Uigur Autonomous Region and Key Laboratory of Tree-ring Physical and Chemical Research, Institute of Desert Meteorology, China Meteorological Administration, Urumqi, 830002, China

Published in Dendrochronologia 2020

1.1 Résumé

Le premier chapitre de ma thèse, intitulé « *Sensibilité à la température de l'intensité du bleu, de la densité maximale du bois final et de la largeur des cernes des épinettes noires vivantes dans la taïga de l'est du Canada* », a été rédigé par Feng Wang, Dominique Arseneault, Étienne Boucher, Gabrielle Galipaud Gloaguen, Anne Deharte, Shulong Yu et Nadège Trou-kechout. J'ai participé à la planification de l'expérience, à la collecte et l'analyse des données et j'ai été le principal rédacteur du manuscrit. Mon directeur et mon co-directeur de recherche, les professeurs Dominique Arseneault et Étienne Boucher, ont supervisé la recherche et ont révisé le manuscrit. Gabrielle Galipaud Gloaguen, Anne Deharte, Shulong Yu et Nadège Trou-kechout ont toutes été impliquées dans la collecte des échantillons ou des données et dans les discussions connexes. Dans ce chapitre, nous avons étudié le potentiel dendroclimatique des mesures d'intensité du bleu (LBI et DBI) sur 178 épinettes noires vivantes via des comparaisons avec des données de densité maximale du bois final et de largeur des cernes annuels de croissance des arbres. En examinant l'effet de la réplication des données sur la robustesse des signaux de température fournis par ces paramètres dendrochronologiques, ce chapitre permet également d'évaluer nos reconstitutions dendroclimatiques dans le troisième chapitre de la thèse.

La technique de l'intensité du bleu (BI) offre un substitut peu couteux à la mesure de la densité des cernes pour reconstituer les températures estivales dans les régions de haute latitude. Dans cette étude, nous comparons la BI du bois final (LBI) et le delta BI (DBI), avec des données conventionnelles de densité maximale de bois final obtenues par la méthode des rayons X (MXD) et des données de largeur de cerne (TRW) pour 178 spécimens vivants d'épinette noire (*Picea mariana* (Mill.) BSP) provenant de 17 sites de la taïga du Québec-Labrador. Les chronologies régionales de la LBI et du DBI sont fortement corrélées à celles de MXD (Pearson's r = 0,97 et 0,92, respectivement), tandis que le DBI est en plus corrélé aux données de TRW (Pearson's r = 0,67). La LBI et le DBI répondent plus fortement aux températures de mai à août que le TRW, et ce pour des échelles temporelles et spatiales plus

étendues. Cependant, seul le DBI est aussi bien corrélé aux températures estivales que le MXD pour les échelles de temps interannuelles à décennales. Les signaux de basses fréquences du LBI sont probablement déformés par des problèmes de coloration du bois, ainsi que par la résolution des mesures plus faible, ce qui conduit à une sensibilité à la température inférieure par rapport au MXD. Une expérience de ré-échantillonnage suggère qu'une réplication minimale de 10 arbres est nécessaire pour conserver ≥90% du signal de température contenu dans les données du MXD, de la LBI et du DBI, alors qu'un minimum de 20 arbres est requis pour les données du TRW.

1.2 Abstract

The first chapter of my thesis, entitled *Temperature sensitivity of blue intensity, maximum latewood density, and ring width data of living black spruce trees in the eastern Canadian taiga*, was written by Feng Wang, Dominique Arseneault, Étienne Boucher, Gabrielle Galipaud Gloaguen, Anne Deharte, Shulong Yu, and Nadège Trou-kechout. I participated in experiment design, the collection and analysis of the data, and was the principal writer of the manuscript. My supervisor and co-supervisor, professors Dominique Arseneault and Étienne Boucher supervised the research and revised the manuscript. Gabrielle Galipaud Gloaguen, Anne Deharte, Shulong Yu, and Nadège Trou-Kechout were all involved in sample or data collection and related discussions. In this chapter, we investigated the dendroclimatic potential of blue intensity measurements (LBI and DBI) of 178 living black spruce trees via comparisons with maximum latewood density and tree-ring width data. By examining the effect of data replication on the robustness of the temperature signals provided by these dendrochronological parameters, this chapter also allows us the evaluate our dendroclimatic reconstructions in the third chapter of this thesis.

The blue intensity (BI) technique provides opportunities to obtain surrogates to tree-ring density for reconstructing summer temperatures in high-latitude regions. In this study, we compare latewood BI (LBI) and delta BI (DBI), with the conventional X-ray maximum

latewood density (MXD) and tree-ring width (TRW) data using 178 living trees of black spruce (*Picea mariana* (Mill.) B.S.P.), one of the most dominant species of conifers in the Northern Hemisphere, from 17 sites across the eastern Canadian taiga. The regional LBI and DBI chronologies are highly correlated to that of MXD (Pearson's r = 0.97 and 0.92, respectively), while DBI is also similar to TRW (Pearson's r = 0.67). Both LBI and DBI exhibit stronger responses to the May–August temperatures than TRW over larger time and spatial scales. However, only DBI is comparable to MXD data from inter-annual to decadal timescales. Low-frequency components of LBI data are likely distorted by color biases even if no obvious discoloration is present, as well as by the potentially low measurement resolution, leading to an overall weaker temperature sensitivity compared to the MXD data. A resampling experiment suggests that a minimum replication of 10 trees is needed to retain ≥90 % of the optimal temperature signal for MXD, LBI, and DBI data, and a minimum of 20 trees is required for TRW data.

1.3 Introduction

Annually resolved tree rings are important archives of climate that extend our knowledge of climate change back to pre-instrumental times. For decades, a range of climate-sensitive tree-ring properties (i.e., width, density, stable isotope ratios, and anatomical features) have been widely used to reconstruct the centennial to millennial climate, particularly the tree-ring width (TRW) and maximum latewood density (MXD) parameters (Schweingruber, 2012). The MXD of conifers in temperature-limited regions is the most powerful proxy for reconstructing summer temperatures (Esper et al., 2014, 2015, 2017a; Frank and Esper, 2005; Rydval et al., 2014), because it captures stronger temperature signal over a longer growing season (Frank and Esper, 2005; Tuovinen et al., 2009), and is less influenced by biological persistence in the time series than TRW (Esper et al., 2015, 2017b). However, compared to TRW, fewer long MXD series have been developed, particularly in North America (Anchukaitis et al., 2017; St. George and Esper, 2019), mostly due to the need

for costly X-ray densitometric facilities (Björklund et al., 2014; Rydval et al., 2014; Wilson et al., 2017a).

In the last two decades, the blue intensity (BI) method has been developed as a cheaper surrogate to the traditional X-ray densitometric technique (Kaczka et al., 2018; McCarroll et al., 2002; Rydval et al., 2014). Instead of measuring the wood density, BI measures the blue light reflectance of tree rings using affordable commercial flatbed scanners and image analysis software. Latewood BI (hereafter referred to as LBI) is found to correlate strongly with MXD for several coniferous tree species in Europe (Campbell et al., 2007; Kaczka et al., 2018; Österreicher et al., 2015; Rydval et al., 2014) and North America (Parfitt et al., 2020; Wilson et al., 2014). Therefore, BI data are being used increasingly for regional temperature (Dolgova, 2016; Heeter et al., 2019; Parfitt et al., 2020; Wilson et al., 2019) and precipitation reconstructions (Seftigen et al., 2020), tree-ring dating (Wilson et al., 2017b), as well as the detection of ecological disturbances (Arbellay et al., 2018; Rydval et al., 2018).

Yet, BI-based climate reconstructions can be distorted by color biases, such as sapwood-heartwood color differences and colors related to the incomplete extraction of resins and other extractives (Björklund et al., 2014). The delta BI (DBI) was developed to overcome these problems, by differencing the earlywood BI (EBI) and LBI values of each tree ring (Björklund et al., 2014, 2015). DBI can reduce low-frequency biases caused by color contaminations (Björklund et al., 2014, 2015; Wang et al., 2020; Wilson et al., 2017a). However, the use of DBI data for climate reconstructions has been less frequently assessed compared to LBI (Fuentes et al., 2017; Heeter et al., 2019; Wilson et al., 2017a).

Black spruce (*Picea mariana* (Mill.) B.S.P.) is a dominant species across the North American boreal forest and one of the most dominant conifers of the Northern Hemisphere. In the eastern Canadian taiga, MXD of black spruce is more sensitive to spring–summer temperatures than TRW (Boucher et al., 2017; Wang et al., 2001, 2002). Although the potential of BI as a surrogate to MXD has been assessed on stained black spruce subfossil stems (Wang et al., 2020), the temperature sensitivity of BI in black spruce remains poorly

understood because previous work only used a few living-tree stems. In this paper, we performed extensive assessments to test the temperature sensitivity of BI parameters (i.e., LBI and DBI) based on a dataset composed of 178 living trees. Our hypothesis is that LBI and DBI of living black spruce trees are as temperature-sensitive as MXD and more robust than TRW.

1.4 Materials and methods

1.4.1 Tree-ring data

We used a network of 178 living black spruce trees growing at 17 sites across a vast region (74ºW to 60º W, 50ºN to 56º N) in the eastern Canadian taiga (Fig. 1-1; Table 1-1). Stem discs were sampled from dominant trees during several field campaigns from 2002 to 2017. According to three nearby meteorological stations (Fig. 1-1; Environment Canada, 2020), the annual average temperature (1981–2010) of the study region is approximately -2 ºC, with the coldest and warmest mean monthly temperatures reaching -20.6 ºC and 13.5 ºC in January and July, respectively. Total annual precipitation averages about 826 mm, with minimum and maximum precipitations of 38 mm and 109 mm in February and September, respectively. Regional forests are strongly dominated by black spruce, along with some minor coniferous and deciduous species such as balsam fir (*Abies balsamea* L.), eastern larch (*Larix laricina* (Du Roi) K. koch), and aspen (*Populus tremuloides*) (Payette, 1993).

Selected samples showed no apparent color anomalies (e.g., reaction wood, decay, and heterogeneous colors between sapwood and heartwood). MXD data from 14 sites had been measured previously to investigate forest productivity changes (Table 1-1; Boucher et al., 2017). We added three new sites (i.e., L105, L134, and L20) to improve the spatial representation and tree replication. Wood blocks were extracted from stem discs along 1–2 radii and transversely cut into 1 mm-thick laths using a twin-blade saw (Dendrocut2003, Walesch Electronic). The laths were then pretreated with 95 % ethanol in Soxlet extractors for 48 h to remove resins and other extractives. The MXD measurements were taken using

the DendroXray2 and Dendro2003 systems (Walesch Electronic) following the standard protocol (Schweingruber, 2012).

The BI and TRW data were measured from the same laths as used for MXD measurements or from duplicate laths from the same wood block. Finely polished laths (1000 grit) along with an IT8.7/2 calibration target were scanned as RGB images using SilverFast 8.0 software (LaserSoft Imaging) and an Epson V800 scanner covered by a black plastic box (Rydval et al., 2014). The actual resolution of images is about 2580×1825 dpi according to the USAF-1951 resolution target. The image analysis software CooRecorder 8.1 (Cybis Dendrochronology) was used to calibrate images and measure the BI and TRW data. We selected the semi-automatic "Seasonwood" mode to separate measurements of earlywood and latewood. The raw LBI was defined as average of the darkest 30 % of the pixels in latewood and the EBI was defined as average of 100 % of the pixels in earlywood. We inverted the LBI and EBI by subtracting the raw BI values from 256 to make BI series positively correlated with wood density values (Rydval et al., 2014). The DBI was automatically calculated by differencing the raw EBI and LBI measurements in CooRecorder. Details of the density and BI measurements can be found in *Section 2* of Wang et al (2020). In subsequent analysis, we kept only the tree-ring series with measured values for LBI, DBI, MXD, and TRW and raw measurements were averaged by tree when more than one radius was available.

Tree-ring series were individually standardized by site and parameter (LBI, DBI, MXD, and TRW) using the RCSigFree program (Cook et al., 2014) and signal-free age-dependent spline smoothing, a method that more naturally fits tree-ring growth (Melvin et al., 2007). This was consistently the most suitable approach for all parameters among multiple smoothing methods, showing optimal correlations with the MJJA mean temperatures (not shown). We indexed series as ratios and power-transformation plus residuals (Cook and Peters, 1997), since MXD and TRW exhibited evident heteroscedastic variance (Supplementary Fig. 1-S1) according to the relationships between mean and

variance of raw, unstandardized tree-ring data (Cook and Kairiukstis, 2013; Helama et al., 2008). We chose ratio chronologies (hereafter chronologies or chronology) of all parameters for this study due to their stronger temperature signals at local (≥11 of 17 sites) and regional scales, even for LBI and DBI which are not heteroscedastic (Supplementary Fig. 1-S2). Ratio indexation of LBI and DBI allowed direct comparisons with MXD and TRW series. Standardized series were averaged by site using Tukey's bi-weight robust mean to form local chronologies, which were later truncated to ensure a replication of ≥5 trees since 1901 (a minimum of two trees was used for site POOL due to poorly replicated MXD data) (Supplementary Fig. 1-S3). Subsequently, a regional chronology for each parameter was arithmetically averaged from the corresponding 17 local chronologies and was considered for the time interval 1901–2000. Expressed population signal (EPS; Wigley et al., 1984) was computed for local and regional chronologies using the "dplR" R package (Bunn, 2008). We also developed one EBI chronology using the same approach, but this parameter was used only to interpret inter-parameter relationships.

1.4.2 Temperature data

We used the CRU TS 4.03 0.5° gridded monthly mean temperature dataset (Harris et al., 2014) since there are few meteorological stations providing long instrumental records in the study region. Data from the four closest gridded points to each site were averaged to generate 17 local temperature targets. We also computed a regional temperature target covering the entire study region between 75º W–60º W and 50º N–60º N. The CRU data were obtained from the KNMI Climate Explorer (https://climexp.knmi.nl/).

1.4.3 Data analysis

We used the "treeclim" R package (Zang and Biondi, 2015) to calculate the Pearson's correlation coefficients (Pearson's *r* or *r*) between monthly temperature targets and the corresponding LBI, DBI, MXD, and TRW chronologies. Pearson's *r* was also used to assess the May–August (MJJA) temperature signal strength of the regional tree-ring series as well as the 10-year high-pass and low-pass filtered series generated using the Butterworth filter

provided in the "dplR" R package (Bunn, 2008). In addition, in order to study the frequency-dependent relations of tree-ring parameters with the MJJA mean temperatures, we applied multi-taper coherence analysis with adaptive weighting (Thomson, 1982) and bias correction, using the Matlab functions developed by Huybers (2020). We calculated the coherency, rather than the squared coherency to make results comparable to Pearson's *r*. Spatial domains of the four regional tree-ring chronologies were assessed on the KNMI Climate Explorer (https://climexp.knmi.nl/), using MJJA mean temperatures from the CRU TS 4.03 (land) and HadISST1 (ocean; Rayner et al., 2003) temperature datasets (resolution of 1°).

We designed a random resampling experiment to study the influence of tree replication on the temperature signal. For each parameter, N samples were randomly taken with replacement from the available 178 standardized tree-ring series, with a sample size of 5–100 trees, by steps of 5. After each draw, a chronology was averaged from sampled series using the Tukey's bi-weight robust mean and was correlated against the regional MJJA mean temperatures (averaged from 75ºW–60º W and 50ºN–60º N). This procedure was repeated 1000 times for each sample size. The replication of 100 trees was set as the optimal target replication because it systematically yielded the highest median temperature correlation for each parameter. Using two-sample, one-sided Wilcoxon rank sum tests, we compared Pearson's *r* distributions obtained from resampling at lower replications to the target replication. By incrementally increasing replication, we determined when the median correlation reached or exceeded 90 % of the median correlation coefficient calculated from the optimal replication (N=100). We also compared the resampling results of DBI and MXD using the same procedure. Temperature correlations of DBI and MXD were considered identical when the difference of their Pearson's *r* was less than 0.005.

1.5 Results

1.5.1 Inter-parameter comparison

The regional LBI, DBI, MXD, and TRW chronologies (Fig. 1-2), were fairly robust according to the EPS statistics (Table 1-1). Although local chronologies were less robust due to lower replication, their respective EPS values were generally above 0.8 (Table 1-1). TRW chronologies at seven sites showed EPS < 0.8, demonstrating that TRW contains the weakest climate signals compared to LBI, DBI and MXD, all of which had only 1–3 sites with an EPS smaller than 0.8.

Regional LBI and MXD chronologies, averaged across sites, were almost perfectly correlated ($r = 0.97$) compared to Pearson's r of 0.82 ± 0.12 (mean ± SD) across the 17 pairs of local chronologies (Supplementary Fig. 1-S4). Correlation coefficients between DBI and MXD were also very high ($r = 0.92$ at regional scale), though slightly lower than LBI (Table 1-2; Supplementary Fig. 1-S4), because the DBI is a function of both LBI and EBI. In addition, DBI had a higher correlation with TRW at regional ($r = 0.67$) and local scales (r = 0.62 ± 0.16), than was observed between TRW and LBI or MXD. Correlation analyses using first-differenced series showed similar results (Table 1-2). Although the regional EBI chronology was positively correlated with the four other parameters, its correlation with TRW was negative ($r = -0.25$, $p < 0.05$) when using first-differenced data (Table 1-2).

1.5.2 Correlation with temperature

Local LBI, DBI, and MXD chronologies responded more strongly to temperatures of the current summer than the TRW chronologies (Fig. 1-3). Correlations with temperatures were significant ($p < 0.01$) and positive over the entire MJJA season at most sites for LBI, DBI, and MXD, with several sites also showing significant correlations in April and September. MXD is the only parameter that was significantly correlated with MJJA temperatures at site CEA, where tree replication and EPS values are low (Table 1-1; Fig. 1-3). In contrast, TRW data correlated significantly to temperatures during a single or a few

summer months and only at 12 sites. TRW also showed some negative correlations ($p < 0.01$) with temperatures of the previous MJJA season at a few sites, particularly in August (Fig. 1-3). At the regional scale, the MXD chronology was the most related to MJJA mean temperatures ($r = 0.72$), followed by DBI ($r = 0.71$), LBI ($r = 0.68$), and TRW ($r = 0.48$). The corresponding 10-year low-pass filtered chronologies showed the same result, while DBI high-pass filtered data showed a slightly higher Pearson's *r* than that of the MXD chronology (Fig. 1-2). Site-by-site correlations with MJJA temperatures can be found in Supplementary Figures 1-S5–1-S8.

Although coherencies of DBI and MXD with MJJA temperatures were comparable when averaged across all frequencies (0.73 vs 0.74, respectively), some differences were found among frequency domains. Coherencies of LBI, DBI, and MXD were similar in the high-frequency domain (periods < 3 years; Fig. 1-4), in line with the Pearson's *r* between high-passed time series (Fig. 1-2). However, DBI exhibited higher coherency for intermediate periods of 3–8 years, whereas MXD was consistently the most temperature-coherent parameter in the lower-frequency domain (periods > 8 years; Fig. 1-4). Compared to DBI and MXD, coherency of LBI tended to gradually decrease from high to low frequencies. In contrast, coherency between TRW and summer temperatures was weak for very high (periods < 2 years) and intermediate frequencies (4–15 years), but increased markedly to be significant at periods of 2–4 years and > 15 years (Fig. 1-4).

Spatial domains of MJJA temperature correlations were larger for LBI, DBI, and MXD than for TRW, particularly over the mainland (Fig. 1-5). Positive correlations ($r \geq 0.25$) with MJJA land temperatures covered the entire Quebec-Labrador Peninsula and extended westward up to the Rocky Mountains. These patterns, including the oceanic domain, were similar to the spatial correlation derived from our regional temperature target (averaged from 75ºW–60º W and 50ºN–60º N; Fig. 1-5). In contrast, the spatial domain of correlations ($r \geq 0.25$) for TRW showed limited extension to central Canada (Fig. 1-5d).

1.5.3 Influence of tree replication on the temperature signal

The resampling experiment confirmed that DBI and MXD are more sensitive to MJJA mean temperatures than LBI and TRW (Fig. 1-6). However, DBI depended more strongly on tree replication than MXD. The temperature signal became nearly identical (difference of Pearson's *r* less than 0.005) for DBI and MXD when tree replication was greater than 20. In addition, MXD, LBI, and DBI needed a minimum of 10 trees to retain at least 90% of their optimal temperature signal, while TRW required a minimum of 20 trees.

1.6 Discussion

Our results indicate that the LBI and DBI of black spruce are sensitive temperature proxies similar to MXD that is generated using the X-ray densitometric method (see Supplementary Fig. 1-S9 for a direct comparison). In addition, because DBI corrects for the color biases in LBI using the BI data from the earlywood as a background for the LBI counterpart (Björklund et al., 2014), DBI preserves most of the LBI signal as well as the corresponding association with temperatures.

Two hypotheses have been proposed to explain the similarity between LBI and MXD. Earlier works attributed such high correlations to the lignin content of the latewood cell walls (McCarroll et al., 2002). Yet few evidences support direct co-variations of lignin content and LBI (or MXD). Gindl et al. (2000) reported a non-significant correlation between latewood lignin content and density, though based on only ten-year tree-ring series of Norway spruce (*P. abies*). Moreover, latewood lignification was in fact related to temperatures at the end of the growing season, i.e., September to October (Gindl et al., 2000; Piermattei et al., 2015), whereas MXD was mainly regulated by temperatures in earlier months. In addition, a more recent study revealed an offset of lignin content between the sapwood and heartwood of *Larix gmelinii* (Lu et al., 2020). This suggests that cell wall lignin may not be the predominant driver of the density variation (e.g., MXD) as density measurements generally do not show the sapwood-heartwood distinction (Bjorklund et al., 2014, 2015). Nevertheless, as a key

component of cell walls, lignin content may affect the variation of density to some extent. It is thus reasonable to obtain the most temperature-sensitive light intensity parameter in the blue channel (i.e., lignin absorbs shortwave lights) compared to the red and green ones (McCarroll et al., 2002). A more likely explanation for the similarity of LBI and MXD is that both parameters reflect the variations of cell wall proportions in the latewood, as demonstrated by excellent correlations between LBI (or MXD) and structural anatomical features (Björklund et al., 2017, 2019, 2020).

Although highly correlated with MXD, LBI exhibited increasingly weaker temperature responses on the low frequency spectrum (Fig. 1-4). As a direct measure of blue light reflectance, LBI is sensitive to color contaminations such as darker heartwood than sapwood or staining caused by fungi invasion (Björklund et al., 2014, 2015; Rydval et al., 2014), as well as postsampling oxidation of Fe in subfossil wood buried in lake sediments (Wang et al., 2020). In this study, we carefully chose 178 living-tree samples without apparent color issues, in addition to the fact that black spruce generally shows indistinguishable sapwood-heartwood color difference (Yang, 2007). Nevertheless, some color biases may still be present in our samples, for example due to incomplete resin extraction, and distort the low-frequency variability of LBI. In addition, it was suggested that the climate signal strength of density data (LBI, MXD, and anatomical density) depends strongly on the measurement resolution, particularly when TRW are narrow (Björklund et al., 2019). For the BI method, the lower image resolution imposed by flatbed scanners compared to other techniques could degrade the temperature sensitivity of LBI series (Björklund et al., 2019). Similar results were reported for Norway spruce whose LBI correlates with temperature in a more unstable manner than MXD (Kaczka et al. 2018). Our resampling experiment (Fig. 1-6) further demonstrates that such loss of temperature signal relative to MXD is inherent to LBI and less likely to be compensated by increasing replication. These results add to the well-documented difficulties of generating unbiased LBI data in the low-frequency domain.

In contrast to LBI, the summer temperature signal of DBI is almost identical to MXD. Two main reasons explain the excellent temperature sensitivity of DBI. First, DBI is efficient in reducing color biases that may distort LBI data (Björklund et al., 2014, 2015), resulting in a stronger signal strength and more stable temperature correlations across a larger range of frequencies (Fig. 1-4). Second, the DBI of black spruce also contains the temperature signal carried by TRW data due to the fairly good correlation between these two parameters (r = 0.67). This phenomenon may apply to several coniferous species where earlywood density (EWD; or EBI) negatively co-vary with TRW (Björklund et al., 2017). A significant (p < 0.05) Pearson's r of -0.25 based on the first-differenced series confirmed that such negative co-variations between TRW and EBI (and likely EWD) occurs also for black spruce (Table 1-2). Similar findings have been reported for silver pine (*Manoao colensoi*) in New Zealand (Blake et al., 2020). In fact, under warm temperatures, trees produce more tracheids with larger lumens to increase the hydraulic conductivity in the early growing season. EWD (or EBI) is lower due to the larger cells in the earlywood, and larger cells in the meantime coincide with wider rings. Hence, EBI correlates negatively with TRW. As a consequence, temperature-dependent variations of TRW can be partially transferred to DBI (Supplementary Fig. 1-S10).

In theory, the temperature sensitivity of DBI also depends on the climate signal recorded in the EBI. The temperature signal of DBI can thus be degraded when EBI is well synchronized with LBI, as reported for yellow cedar (*Callitropsis nootkatensis*) in Alaska (Wiles et al., 2019). However, the EWD of black spruce (equivalent to EBI) contains weak climate information even at the northern treeline (Boucher et al., 2017; Wang et al., 2001, 2002), explaining why most of the climatic information is preserved in the calculation of DBI from LBI and EBI.

We found that temperature sensitivity of TRW is weaker than that of MXD, LBI or DBI in black spruce, in agreement with previous studies on the other species (Björklund et al., 2017; Esper et al., 2015; Frank and Esper, 2005; Wilson et al., 2014, 2017a). The main

explanation for this result is the strong biological persistence of TRW data (Esper et al., 2015; St. George and Esper, 2019). In contrast to latewood density which mainly depends on photosynthates accumulated during the current growing season (Conkey, 1986), TRW also depends on photosynthates from previous seasons (Miina, 2000; St. George and Esper, 2019; Wang et al., 2019). For example, we found that compared to other parameters, TRW expressed stronger temporal autocorrelations (Supplementary Fig. 1-S11) as well as a ~two-year delayed response to an abrupt cooling event in 1956 (Fig. 1-2), in addition to negative correlations with the temperature of the previous summers (Fig. 1-3). However, the lower-frequency (period > 15 years) variability of TRW can likely benefit from the smoothing effect of biological persistence and thus display improved correlations with temperature (Fig. 1-4).

1.7 Conclusion

This study confirms that the cheap BI methodology can be used to produce robust temperature-sensitive BI parameters for living black spruce trees in the eastern Canadian taiga. LBI, DBI, and MXD data contain much stronger MJJA temperature signals than TRW for wider frequency and spatial domains. However, LBI is less temperature-sensitive than DBI and can be distorted at low frequencies by some potential discoloration problems and low measurement resolution. Since LBI and DBI can be measured simultaneously, attention should be paid equally to the two parameters in future works with living-tree materials in order to select the most suitable proxy for paleoclimate reconstructions, even where no apparent discoloration occurs. In addition, although discoloration issues are challenging the BI method, DBI of black spruce is unaffected by iron stains on the subfossil stems buried in lake sediments (Wang et al., 2020). DBI data from living-tree and subfossil black spruce trees can thus potentially be combined to perform long-term temperature reconstructions.

Our results add to many previous studies showing that MXD is the most robust temperature proxy that expresses a strong and more stable temperature signal across frequencies and space. The measurement of MXD data is expensive, while not necessarily

much time-consuming compared to BI method according to our experiences with disc samples. If facilities and funding are available, the most temperature-sensitive and robust MXD is recommended for temperature reconstructions using black spruce. Even though, the BI technique provides a cheaper solution to obtain climate-sensitive proxies (e.g., LBI and DBI) similar to the MXD and more robust than the TRW parameter for dendroclimatology.

1.8 Acknowledgements

This work was supported by the “PERSISTENCE” project funded by the Natural Sciences and Engineering Research Council of Canada (the NSERC-CRD program), Hydro-Québec, Manitoba Hydro and the Ouranos Consortium. FW also received funding from the China Scholarship Council (CSC). SY received funding from the project of Key Laboratory Opening Subject of Xinjiang Uigur Autonomous Region (2016D03005) and the project of Basic Research Operating Expenses of the Central-level Non-profit Research Institutes (IDM201202). We greatly thank Florent Vignola for his assistance in cutting wood blocks from tree discs, Ann Delwaide at Laval University for access to the twin-blade saw, professor Feng Chen and Tongwen Zhang for their permissions to perform tree-ring density measurements at Institute of Desert and Meteorology, China Meteorological Administration. FW thanks Zahed Shakeri for his advises to improve the manuscript.

1.9 References

Anchukaitis, K.J., Wilson, R., Briffa, K.R., Büntgen, U., Cook, E.R., D'Arrigo, R., Davi, N., Esper, J., Frank, D., Gunnarson, B.E., Hegerl, G., Helama, S., Klesse, S., Krusic, P.J., Linderholm, H.W., Myglan, V., Osborn, T.J., Zhang, P., Rydval, M., Schneider, L., Schurer, A., Wiles, G., Zorita, E., 2017. Last millennium Northern Hemisphere summer temperatures from tree rings: Part II, spatially resolved reconstructions. Quat. Sci. Rev. 163, 1–22. https://doi.org/10.1016/j.quascirev.2017.02.020

Arbellay, E., Jarvis, I., Chavardès, R.D., Daniels, L.D., Stoffel, M., 2018. Tree-ring proxies of larch bud moth defoliation: latewood width and blue intensity are more precise than tree-ring width. Tree Physiol. 38, 1237–1245. https://doi.org/10.1093/treephys/tpy057

Björklund, J., Gunnarson, B.E., Seftigen, K., Esper, J., Linderholm, H.W., 2014. Blue intensity and density from northern Fennoscandian tree rings, exploring the potential to improve summer temperature reconstructions with earlywood information. Clim. Past 10, 877–885. https://doi.org/10.5194/cp-10-877-2014

Björklund, J., Gunnarson, B.E., Seftigen, K., Zhang, P., Linderholm, H.W., 2015. Using adjusted Blue Intensity data to attain high-quality summer temperature information: A case study from Central Scandinavia. The Holocene 25, 547–556. https://doi.org/10.1177/0959683614562434

Björklund, J., Seftigen, K., Schweingruber, F., Fonti, P., von Arx, G., Bryukhanova, M.V., Cuny, H.E., Carrer, M., Castagneri, D., Frank, D.C., 2017. Cell size and wall dimensions drive distinct variability of earlywood and latewood density in Northern Hemisphere conifers. New Phytol. 216, 728–740. https://doi.org/10.1111/nph.14639

Björklund, J., von Arx, G., Nievergelt, D., Wilson, R., Van den Bulcke, J., Günther, B., Loader, N.J., Rydval, M., Fonti, P., Scharnweber, T., Andreu-Hayles, L., Büntgen, U., D'Arrigo, R., Davi, N., De Mil, T., Esper, J., Gärtner, H., Geary, J., Gunnarson, B.E., Hartl, C., Hevia, A., Song, H., Janecka, K., Kaczka, R.J., Kirdyanov, A.V., Kochbeck, M., Liu, Y., Meko, M., Mundo, I., Nicolussi, K., Oelkers, R., Pichler, T., Sánchez-Salguero, R., Schneider, L., Schweingruber, F., Timonen, M., Trouet, V., Van Acker, J., Verstege, A., Villalba, R., Wilmking, M., Frank, D., 2019. Scientific merits and analytical challenges of tree-ring densitometry. Rev. Geophys. 57, 1224–1264. https://doi.org/10.1029/2019RG000642

Björklund, J., Seftigen, K., Fonti, P., Nievergelt, D., von Arx, G., 2020. Dendroclimatic potential of dendroanatomy in temperature-sensitive Pinus sylvestris. Dendrochronologia 60, 125673. https://doi.org/10.1016/j.dendro.2020.125673

Blake, S.A.P., Palmer, J.G., Björklund, J., Harper, J.B., Turney, C.S.M., 2020. Palaeoclimate potential of New Zealand *Manoao colensoi* (silver pine) tree rings using Blue-Intensity (BI). Dendrochronologia 60, 125664. https://doi.org/10.1016/j.dendro.2020.125664

Boucher, E., Nicault, A., Arseneault, D., Bégin, Y., Karami, M.P., 2017. Decadal Variations in eastern Canada's taiga wood biomass production forced by ocean-atmosphere interactions. Sci. Rep. 7, 2457. https://doi.org/10.1038/s41598-017-02580-9

Bunn, A.G., 2008. A dendrochronology program library in R (dplR). Dendrochronologia 26, 115–124. https://doi.org/10.1016/j.dendro.2008.01.002

Campbell, R., McCarroll, D., Loader, N.J., Grudd, H., Robertson, I., Jalkanen, R., 2007. Blue intensity in *Pinus sylvestris* tree-rings: developing a new palaeoclimate proxy. The Holocene 17, 821–828. https://doi.org/10.1177/0959683607080523

Conkey, L.E., 1986. Red spruce tree-ring widths and densities in eastern North America as indicators of past climate. Quat. Res. 26, 232–243. https://doi.org/10.1016/0033-5894(86)90107-9

Cook, E.R., Peters, K., 1997. Calculating unbiased tree-ring indices for the study of climatic and environmental change. The Holocene 7, 361–370. https://doi.org/10.1177/095968369700700314

Cook, E.R., Kairiukstis, L.A., 2013. Methods of dendrochronology: applications in the environmental sciences. Springer Science & Business Media.

Cook, E. R., Krusic, P. J., Melvin, T. M., 2014. "Program RCSsigFree: Version 45_v2b." Lamont-Doherty Earth Obs. Columbia University. https://www.ldeo.columbia.edu/tree-ring-laboratory/resources/software

Dolgova, E., 2016. June–September temperature reconstruction in the Northern Caucasus based on blue intensity data. Dendrochronologia. 39, 17–23. https://doi.org/10.1016/j.dendro.2016.03.002

Environment Canada, 2020. Canadian climate normals or averages 1981-2010. http://climate.weather.gc.ca/climate_normals/index_e.html. last access: 25 August, 2020.

Esper, J., Düthorn, E., Krusic, P.J., Timonen, M., Büntgen, U., 2014. Northern European summer temperature variations over the Common Era from integrated tree-ring density records. J. Quat. Sci. 29, 487–494. https://doi.org/10.1002/jqs.2726

Esper, J., Schneider, L., Smerdon, J.E., Schöne, B.R., Büntgen, U., 2015. Signals and memory in tree-ring width and density data. Dendrochronologia 35, 62–70. https://doi.org/10.1016/j.dendro.2015.07.001

Esper, J., Büntgen, U., Hartl-Meier, C., Oppenheimer, C., Schneider, L., 2017a. Northern Hemisphere temperature anomalies during the 1450s period of ambiguous volcanic forcing. Bull. Volcanol. 79, 41. https://doi.org/10.1007/s00445-017-1125-9

Esper, J., Carnelli, A.L., Kamenik, C., Filot, M., Leuenberger, M., Treydte, K., 2017b. Spruce tree-ring proxy signals during cold and warm periods. Dendrobiology 77. https://doi.org/10.12657/denbio.077.001

Frank, D., Esper, J., 2005. Characterization and climate response patterns of a high-elevation, multi-species tree-ring network in the European Alps. Dendrochronologia 22, 107–121. https://doi.org/10.1016/j.dendro.2005.02.004

Fuentes, M., Salo, R., Björklund, J., Seftigen, K., Zhang, P., Gunnarson, B., Aravena, J.-C., Linderholm, H.W., 2017. A 970-year-long summer temperature reconstruction from Rogen, west-central Sweden, based on blue intensity from tree rings. The Holocene 28, 254–266. https://doi.org/10.1177/0959683617721322

Gindl, W., Grabner, M., Wimmer, R., 2000. The influence of temperature on latewood lignin content in treeline Norway spruce compared with maximum density and ring width. Trees 14, 409–414. https://doi.org/10.1007/s004680000057

Harris, I., Jones, P.D., Osborn, T.J., Lister, D.H., 2014. Updated high-resolution grids of monthly climatic observations – the CRU TS3.10 Dataset. Int. J. Climatol. 34, 623–642. https://doi.org/10.1002/joc.3711

Heeter, K.J., Harley, G.L., Van De Gevel, S.L., White, P.B., 2019. Blue intensity as a temperature proxy in the eastern United States: a pilot study from a southern disjunct population of Picea rubens (Sarg.). Dendrochronologia 55, 105–109. https://doi.org/10.1016/j.dendro.2019.04.010

Helama, S., Vartiainen, M., Kolström, T., Peltola, H., Meriläinen, J., 2008. X-ray microdensitometry applied to subfossil tree-rings: growth characteristics of ancient pines from the southern boreal forest zone in Finland at intra-annual to centennial time-scales. Veg. Hist. Archaeobotany 17, 675–686. https://doi.org/10.1007/s00334-008-0147-9

Huybers, P., 2020. Multi-taper coherence method with bias correction. (https://www.mathworks.com/matlabcentral/fileexchange/22551-multi-taper-coherence-method-with-bias-correction), MATLAB Central File Exchange. Retrieved August 6, 2020.

Kaczka, R.J., Spyt, B., Janecka, K., Beil, I., Büntgen, U., Scharnweber, T., Nievergelt, D., Wilmking, M., 2018. Different maximum latewood density and blue intensity measurements techniques reveal similar results. Dendrochronologia 49, 94–101. https://doi.org/10.1016/j.dendro.2018.03.005

Lu, Q., Liu, X., Anhäuser, T., Keppler, F., Wang, Y., Zeng, X., Zhang, Q., Zhang, L., Wang, K., Zhang, Y., 2020. Tree-ring lignin proxies in *Larix gmelinii* forest growing in a permafrost area of northeastern China: temporal variation and potential for climate reconstructions. Ecol. Indic. 118, 106750. https://doi.org/10.1016/j.ecolind.2020.106750

McCarroll, D., Pettigrew, E., Luckman, A., Guibal, F., Edouard, J.-L., 2002. Blue reflectance provides a surrogate for latewood density of high-latitude pine tree rings. Arct. Antarct. Alp. Res. 34, 450–453. https://doi.org/10.1080/15230430.2002.12003516

McCarroll, D., Loader, N. J., Jalkanen, R., Gagen, M. H., Grudd, H., Gunnarson, B. E., Kirchhefer, A. J., Friedrich, M., Linderholm, H. W., Lindholm, M., Boettger, T., Los, S. O., Remmele, S., Kononov, Y. M., Yamazaki, Y. H., Young, G. H. and Zorita, E., 2013. A 1200-year multiproxy record of tree growth and summer temperature at the northern pine forest limit of Europe, The Holocene, 23(4), 471–484. doi:10.1177/0959683612467483

Melvin, T.M., Briffa, K.R., Nicolussi, K., Grabner, M., 2007. Time-varying-response smoothing. Dendrochronologia 25, 65–69. https://doi.org/10.1016/j.dendro.2007.01.004

Miina, J., 2000. Dependence of tree-ring, earlywood and latewood indices of Scots pine and Norway spruce on climatic factors in eastern Finland. Ecol. Model. 132, 259–273. https://doi.org/10.1016/S0304-3800(00)00296-9

Österreicher, A., Weber, G., Leuenberger, M., Nicolussi, K., 2015. Exploring blue intensity-comparison of blue intensity and MXD data from Alpine spruce trees. TRACE–Tree Rings Archaeol. Climatol. Ecol. 13, 56–61.

Parfitt, R., Ummenhofer, C.C., Buckley, B.M., Hansen, K.G., D'Arrigo, R.D., 2020. Distinct seasonal climate drivers revealed in a network of tree-ring records from Labrador, Canada. Clim. Dyn. 54, 1897–1911. https://doi.org/10.1007/s00382-019-05092-6

Payette, S., 1993. The range limit of boreal tree species in Québec-Labrador: an ecological and palaeoecological interpretation. Rev. Palaeobot. Palynol. 79, 7–30. https://doi.org/10.1016/0034-6667(93)90036-T

Piermattei, A., Crivellaro, A., Carrer, M., Urbinati, C., 2015. The "blue ring": anatomy and formation hypothesis of a new tree-ring anomaly in conifers. Trees 29, 613–620. https://doi.org/10.1007/s00468-014-1107-x

Rayner, N.A., Parker, D.E., Horton, E.B., Folland, C.K., Alexander, L.V., Rowell, D.P., Kent, E.C., Kaplan, A., 2003. Global analyses of sea surface temperature, sea ice, and night marine air temperature since the late nineteenth century. J. Geophys. Res. Atmos. 108. https://doi.org/10.1029/2002JD002670

Rydval, M., Larsson, L.-Å., McGlynn, L., Gunnarson, B.E., Loader, N.J., Young, G.H.F., Wilson, R., 2014. Blue intensity for dendroclimatology: should we have the blues? Experiments from Scotland. Dendrochronologia 32, 191–204. https://doi.org/10.1016/j.dendro.2014.04.003

Rydval, M., Druckenbrod, D.L., Svoboda, M., Trotsiuk, V., Janda, P., Mikoláš, M., Čada, V., Bače, R., Teodosiu, M., Wilson, R., 2018. Influence of sampling and disturbance history on climatic sensitivity of temperature-limited conifers. The Holocene 28, 1574–1587. https://doi.org/10.1177/0959683618782605

Schweingruber, F.H., 2012. Tree Rings: Basics and Applications of Dendrochronology. Springer Science & Business Media.

Seftigen, K., Fuentes, M., Ljungqvist, F.C., Björklund, J., 2020. Using Blue Intensity from drought-sensitive Pinus sylvestris in Fennoscandia to improve reconstruction of past hydroclimate variability. Clim. Dyn. 55, 579–594. https://doi.org/10.1007/s00382-020-05287-2

St. George, S., Esper, J., 2019. Concord and discord among Northern Hemisphere paleotemperature reconstructions from tree rings. Quat. Sci. Rev. 203, 278–281. https://doi.org/10.1016/j.quascirev.2018.11.013

Thomson, D.J., 1982. Spectrum estimation and harmonic analysis. Proc. IEEE 70, 1055–1096. https://doi.org/10.1109/PROC.1982.12433

Tuovinen, M., McCarroll, D., Grudd, H., Jalkanen, R., Los, S., 2009. Spatial and temporal stability of the climatic signal in northern Fennoscandian pine tree-ring width and maximum density. Boreas 38, 1–12. https://doi.org/10.1111/j.1502-3885.2008.00046.x

Wang, F., Arseneault, D., Pan, B., Liao, Q., Sugiyama, J., 2019. Pre-1930 unstable relationship between climate and tree-ring width of *Pinus taiwanensis* hayata in southeastern China. Dendrochronologia 57, 125629. https://doi.org/10.1016/j.dendro.2019.125629

Wang, F., Arseneault, D., Boucher, É., Yu, S., Ouellet, S., Chaillou, G., Delwaide, A., Wang, L., 2020. Chemical destaining and the delta correction for blue intensity measurements of stained lake subfossil trees. Biogeosci. 17, 4559–4570. https://doi.org/10.5194/bg-17-4559-2020

Wang, L., Payette, S., Bégin, Y., 2001. 1300-year tree-ring width and density series based on living, dead and subfossil black spruce at tree-line in Subarctic Quebec, Canada. The Holocene 11, 333–341. https://doi.org/10.1191/095968301674769686

Wang, L., Payette, S., Bégin, Y., 2002. Relationships between anatomical and densitometric characteristics of black spruce and summer temperature at tree line in northern Quebec. Can. J. For. Res. 32, 477–486. https://doi.org/10.1139/x01-208

Wigley, T.M.L., Briffa, K.R., Jones, P.D., 1984. On the average value of correlated time series, with applications in dendroclimatology and hydrometeorology. J. Clim. Appl. Meteorol. 23, 201–213. https://doi.org/10.1175/1520-0450(1984)023<0201:OTAVOC>2.0.CO;2

Wiles, G.C., Charlton, J., Wilson, R.J.S., D'Arrigo, R.D., Buma, B., Krapek, J., Gaglioti, B.V., Wiesenberg, N., Oelkers, R., 2019. Yellow-cedar blue intensity tree-ring chronologies as records of climate in Juneau, Alaska, USA. Can. J. For. Res. 49, 1483–1492. https://doi.org/10.1139/cjfr-2018-0525

Wilson, R., Rao, R., Rydval, M., Wood, C., Larsson, L.-Å., Luckman, B.H., 2014. Blue Intensity for dendroclimatology: The BC blues: A case study from British Columbia, Canada. The Holocene 24, 1428–1438. https://doi.org/10.1177/0959683614544051

Wilson, R., D'Arrigo, R., Andreu-Hayles, L., Oelkers, R., Wiles, G., Anchukaitis, K., Davi, N., 2017a. Experiments based on blue intensity for reconstructing North Pacific temperatures along the Gulf of Alaska. Clim. Past. 13, 1007–1022. https://doi.org/10.5194/cp-13-1007-2017

Wilson, R., Wilson, D., Rydval, M., Crone, A., Büntgen, U., Clark, S., Ehmer, J., Forbes, E., Fuentes, M., Gunnarson, B.E., Linderholm, H.W., Nicolussi, K., Wood, C., Mills, C., 2017b. Facilitating tree-ring dating of historic conifer timbers using Blue Intensity. J. Archaeol. Sci. 78, 99–111. https://doi.org/10.1016/j.jas.2016.11.011

Wilson, R., Anchukaitis, K., Andreu-Hayles, L., Cook, E., D'Arrigo, R., Davi, N., Haberbauer, L., Krusic, P., Luckman, B., Morimoto, D., Oelkers, R., Wiles, G., Wood, C., 2019. Improved dendroclimatic calibration using blue intensity in the southern Yukon. The Holocene 29, 1817–1830. https://doi.org/10.1177/0959683619862037

Yang, K.C., 2007. Growth ring contrast enhancement and the differentiation of sapwood and heartwood zones. Wood Fiber Sci. 19, 339–342.

Zang, C., Biondi, F., 2015. treeclim: an R package for the numerical calibration of proxy-climate relationships. Ecography 38, 431–436. https://doi.org/10.1111/ecog.01335

1.10 Tables

Table 1-1: Description of the standardized tree-ring chronologies at the 17 studied sites.

Site Name	Latitude	Longitude	No. of Trees	Timespan	EPS			
					MXD	LBI	DBI	TRW
CANE*	54.44	-68.37	9	1901–2003	0.87	0.88	0.89	0.81
CEA*	55.56	-68.12	7	1901–2003	0.75	0.67	0.72	0.74
DA1*	53.86	-72.41	8	1901–2004	0.92	0.90	0.85	0.74
HM2*	54.24	-70.79	19	1901–2002	0.93	0.95	0.94	0.90
L105	50.81	-68.80	22	1901–2016	0.91	0.91	0.91	0.94
L134	56.38	-73.97	28	1901–2007	0.94	0.93	0.91	0.90
L20	54.56	-71.24	14	1901–2010	0.93	0.95	0.93	0.94
LAB17*	53.97	-62.98	7	1901–2008	0.85	0.87	0.87	0.71
LAB32*	53.61	-60.89	5	1901–2008	0.79	0.77	0.87	0.92
LAB35*	53.07	-61.63	7	1901–2007	0.90	0.81	0.85	0.68
LAB50*	52.89	-67.07	8	1901–2008	0.84	0.91	0.92	0.91
LAB56*	51.29	-68.12	7	1901–2007	0.92	0.81	0.80	0.62
LECA*	55.79	-73.44	7	1901–2006	0.93	0.92	0.90	0.79
NIT*	53.29	-70.94	8	1901–2003	0.91	0.89	0.89	0.83
POOL*	55.72	-66.89	5	1901–2003	0.80	0.83	0.85	0.56
ROZX*	54.79	-72.99	6	1901–2001	0.75	0.84	0.91	0.84
T1*	53.89	-73.89	11	1901–2003	0.88	0.93	0.94	0.94
Regional	-	-	178	1901–2000	0.99	0.99	0.99	0.96

EPS values smaller than 0.8 are underlined. *: MXD data were originally measured by Boucher et al. (2017). Chronologies of the four proxies share the same timespan at each site.

Table 1-2: Correlation coefficients between pairs of regional tree-ring parameters over the 1901–2000 period.

Parameter	LBI	DBI	MXD	TRW
DBI	0.95**/0.95**	-	-	-
MXD	0.97**/0.98**	0.92**/0.92**	-	-
TRW	0.54**/0.55**	0.67**/0.70**	0.47**/0.48**	-
EBI	0.48**/0.41**	0.32**/0.13	0.55**/0.43**	0.17/-0.25*

Values before and after the slash symbol refer to correlation coefficients calculated using raw chronologies and their first differences, respectively. * and ** refer to statistical significance at 0.95 and 0.99 levels, respectively.

1.11 Figures

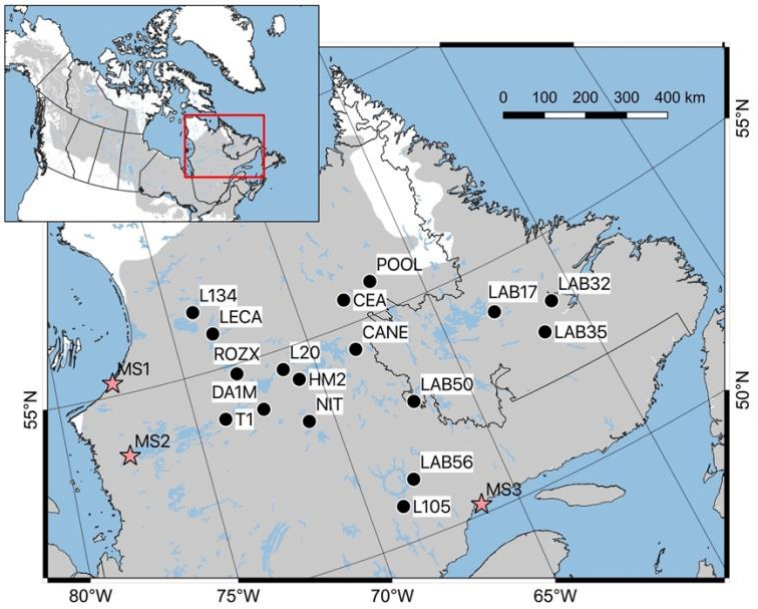

Figure 1-1: Locations of the 17 sampling sites (circles) across the eastern Canadian taiga and three nearby meteorological stations (stars). MS1: Kuujjuarapik A; MS2: La Grande Rivière A; MS3: Sept-Iles A. The gray shade shows the distribution range of black spruce, available at https://www.fs.fed.us/database/feis/pdfs/Little/aa_SupportingFiles/LittleMaps.html.

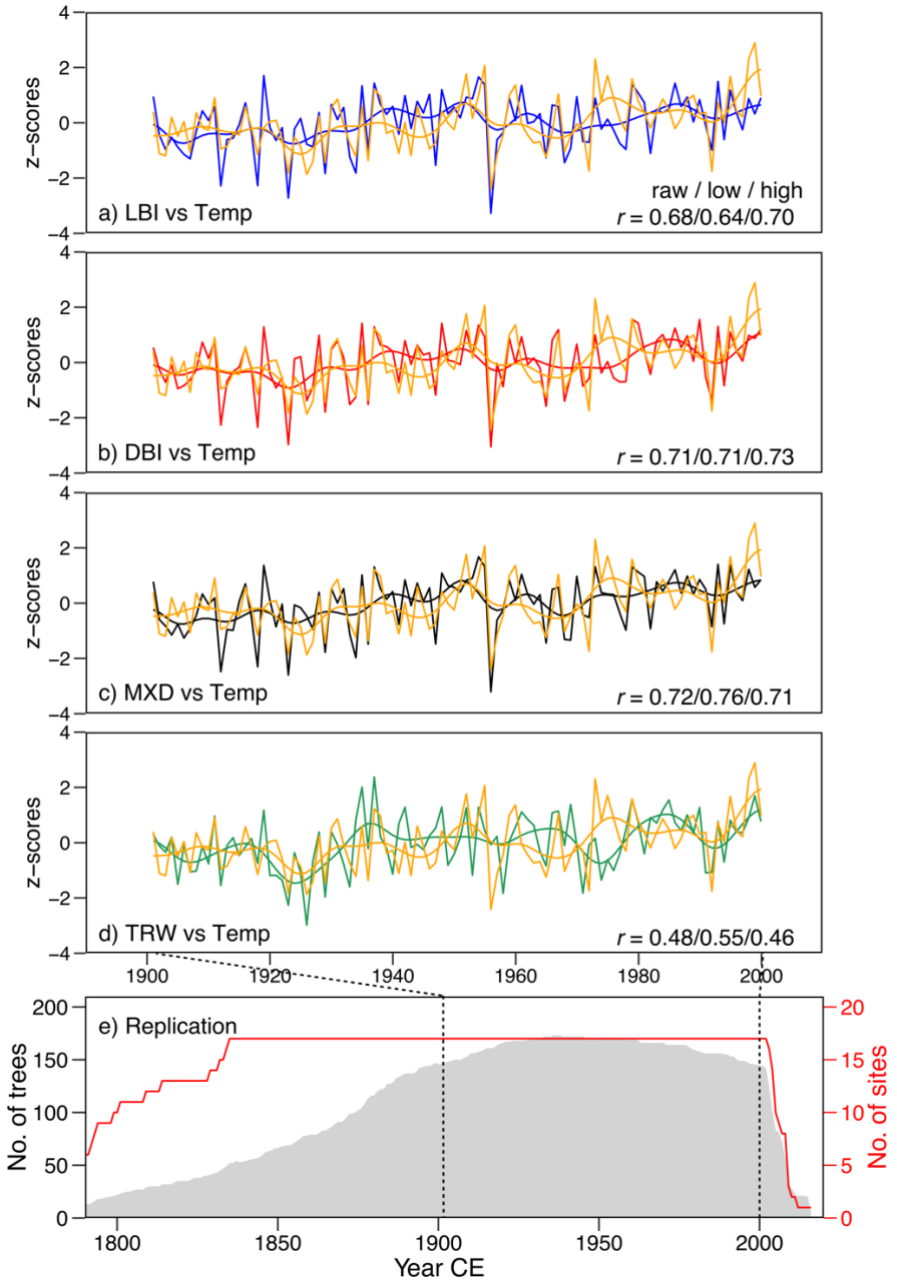

Figure 1-2: Comparison of regional chronologies with MJJA regional mean temperatures (orange) over the 1901–2000 time interval (a–d), and the total number of trees sampled across the 17 sites (e).Smoothed curves in (a–d) are 10-year filtered using the Butterworth filter. Correlation coefficients with MJJA mean temperatures refer to unfiltered (raw), 10-year low-pass (low), and 10-year high-pass time series (high), respectively. All series are scaled with respect to the z-scores of the MJJA regional mean temperatures.

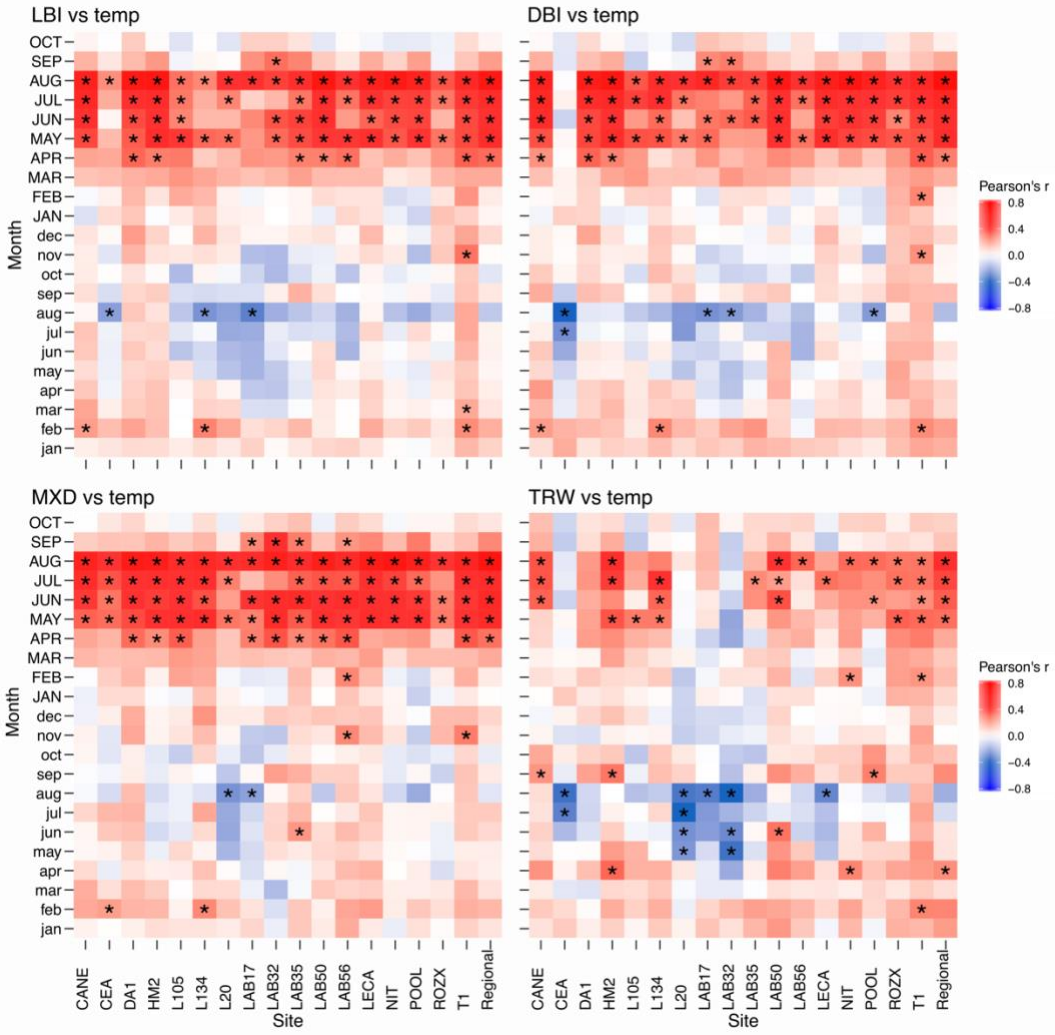

Figure 1-3: Correlation of LBI, DBI, MXD, and TRW chronologies with corresponding monthly land temperature targets over the 1901–2000 time interval. Asterisks refer to statistical significance at the 0.99 confidence level calculated using bootstrap resampling with 1000 iterations.

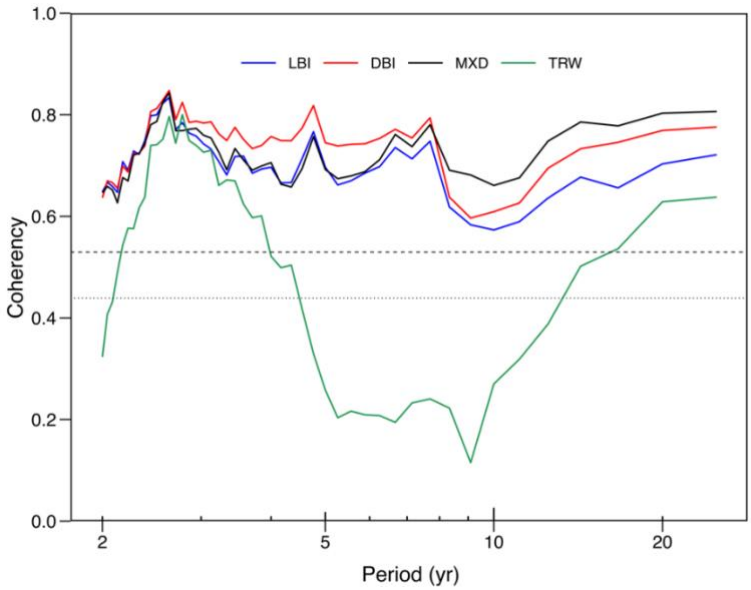

Figure 1-4: Coherence analysis of the regional LBI, DBI, MXD, and TRW chronologies with MJJA regional mean temperature over the 1901–2000 time interval. Periods are the reciprocals of frequencies, e.g., a period of 5 represents a frequency of 0.2. Horizontal dotted and dashed lines refer to the 0.95 and 0.99 confidence levels, respectively.

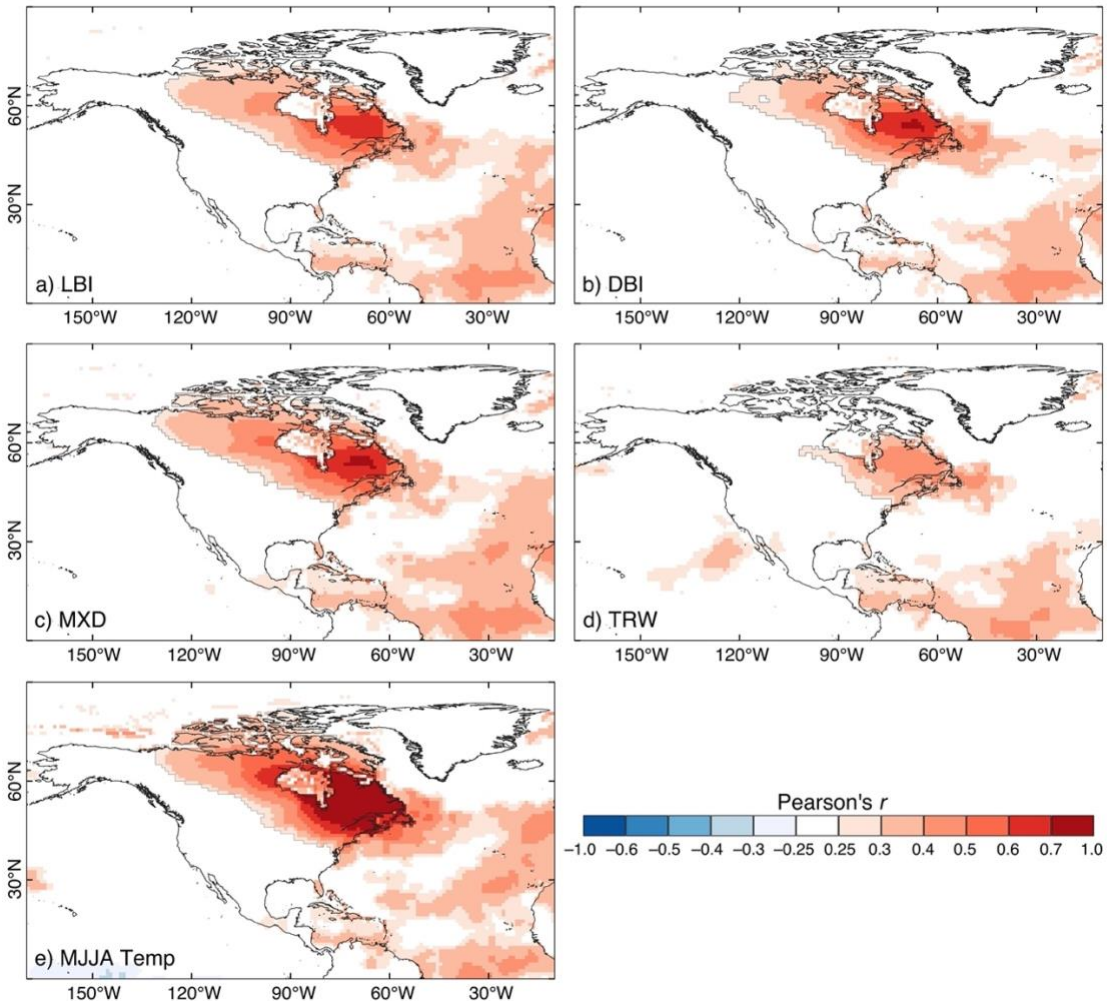

Figure 1-5: Spatial correlations of LBI, DBI, MXD, and TRW regional chronologies (a–d), and MJJA regional mean temperatures (averaged from 75ºW–60º W and 50ºN–60º N) (e) against land (CRU TS 4.03) and oceanic (HadISST1) MJJA 1º gridded temperatures for the 1901–2000 time interval. Only Pearson's r ≥ 0.25 and ≤ -0.25, approximately referring to statistical significance at the 0.99 confidence level, are shown in colors.

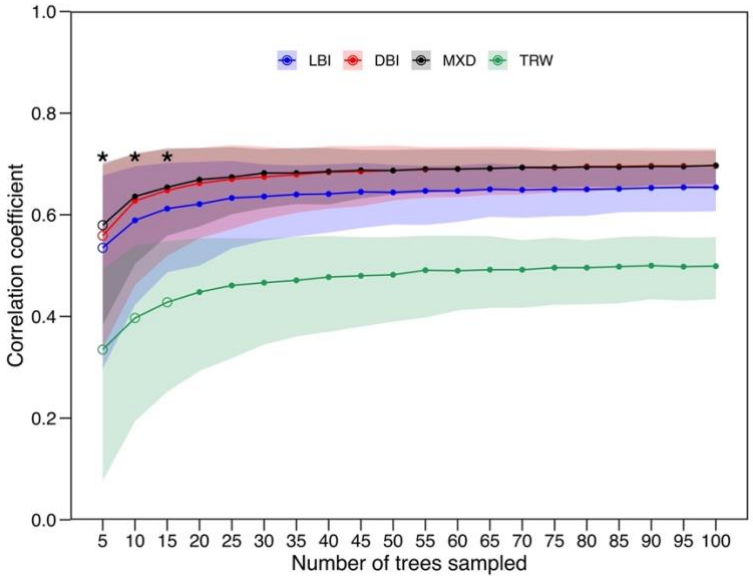

Figure 1-6: Influence of tree replication on the MJJA temperature signals of the LBI, DBI, MXD, and TRW regional chronologies over the 1901–2000 time interval. The median correlation coefficients along with 95% confidence intervals are indicated by dots and shades, respectively. A replication retaining <90% of the optimal temperature signal (given by the results of 100 trees) is marked with an empty circle (one-sided Wilcoxon rank sum test; $p < 0.01$). Asterisks indicate significant differences in temperature correlation coefficients between DBI and MXD proxies (difference > 0.005; one-sided Wilcoxon rank sum test; $p < 0.01$).

1.12 Supplementary Materials

Supplementary Figures

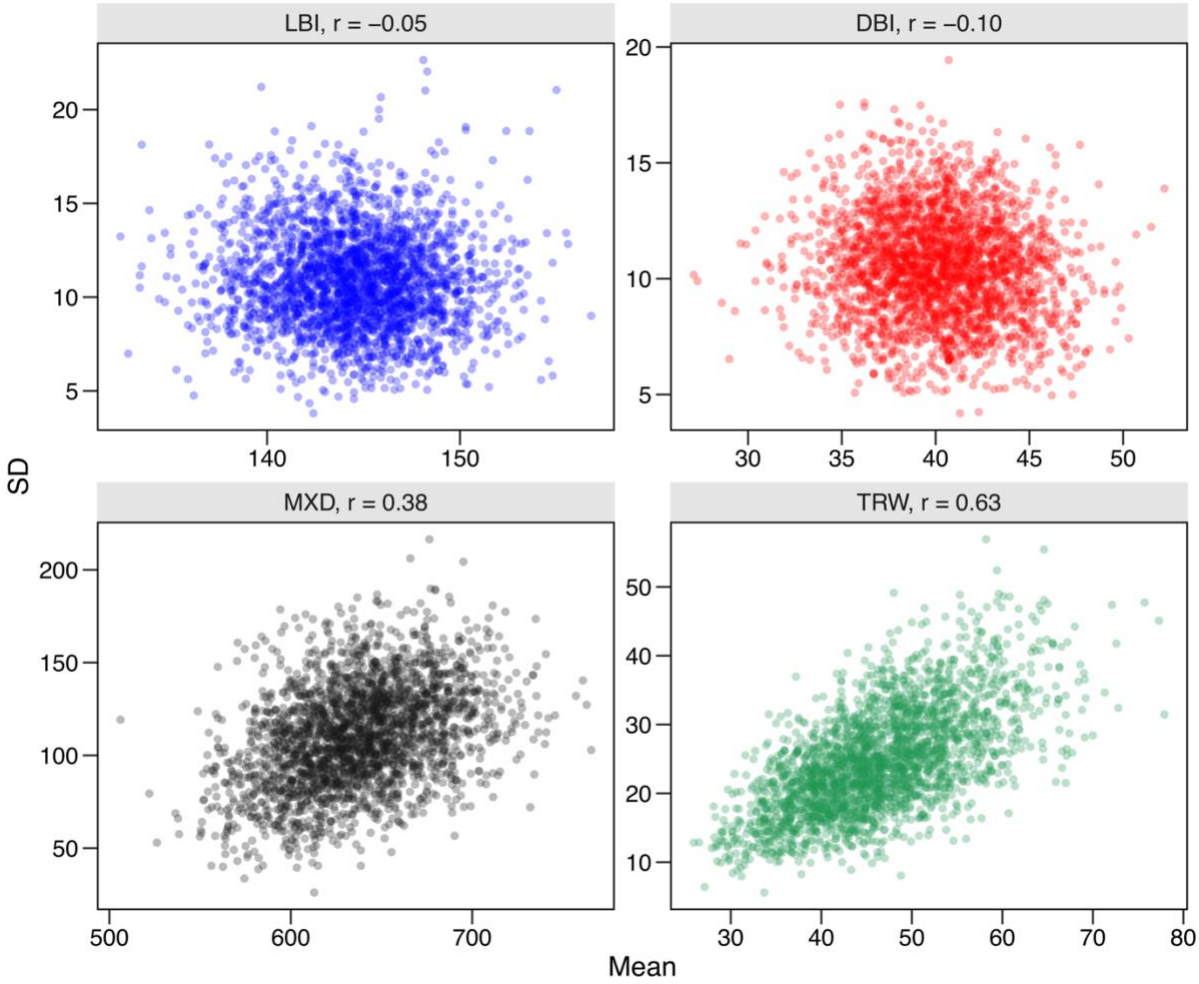

Figure 1-S1: Relationships between the mean and standard deviation (SD) of LBI, DBI, MXD, and TRW raw measurements before standardization. Each point represents the mean and SD calculated using randomly sampled 10 tree rings without replacement from a collection of 24810 tree rings. An evident linearity suggests heteroscedastic variance, as for MXD and TRW of black spruce.

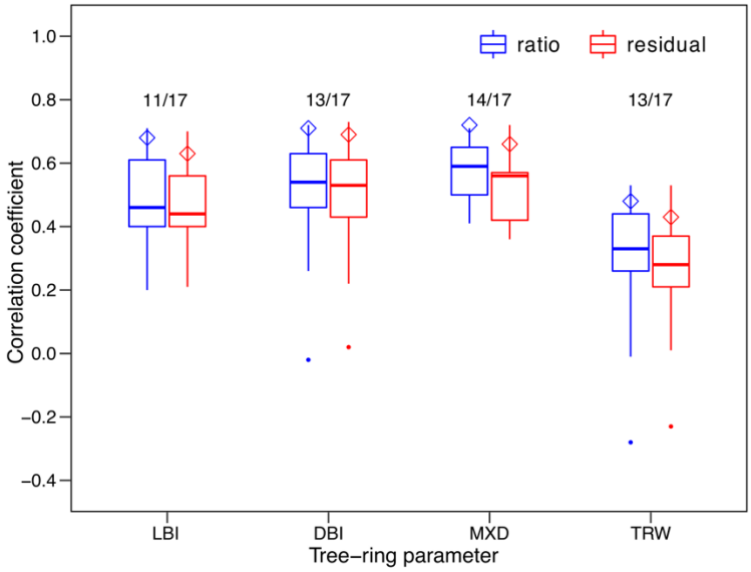

Figure 1-S2: MJJA temperature signal strength of tree-ring chronologies generated using ratios (blue) and power-transformation plus residuals (red) indexation during the signal-free age-dependent spline standardization. The signal strength was assessed using the Pearson's *r* between local tree-ring and temperature series over the full timespans of each chronology since the year 1901 (Table 1-1; boxes and whiskers), and between the regional tree-ring and temperature series over the 1901–2000 time interval (diamonds). Horizontal bars, boxes, and whiskers show the median, the interquartile range, and values outside the interquartile ranges, respectively. Outliers are shown as dots. Values above the boxes give the proportion of sites where ratio chronologies are more strongly correlated with MJJA temperatures than residual chronologies.

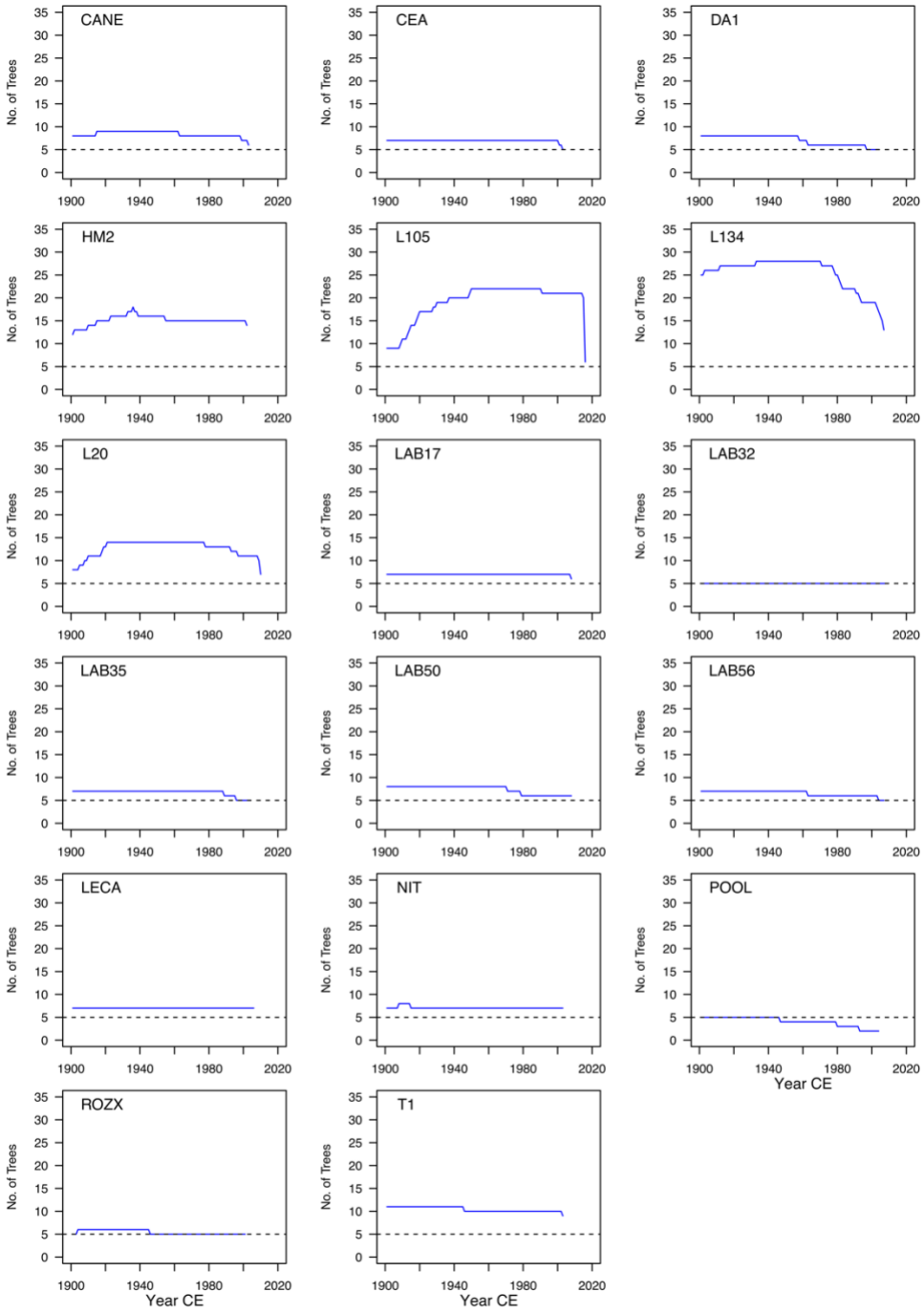

Figure 1-S3: Replication of local tree-ring chronologies at the 17 sites since 1901. Dashed horizontal lines refer to a minimum replication of 5 trees used to truncate each local chronology, except for the site POOL.

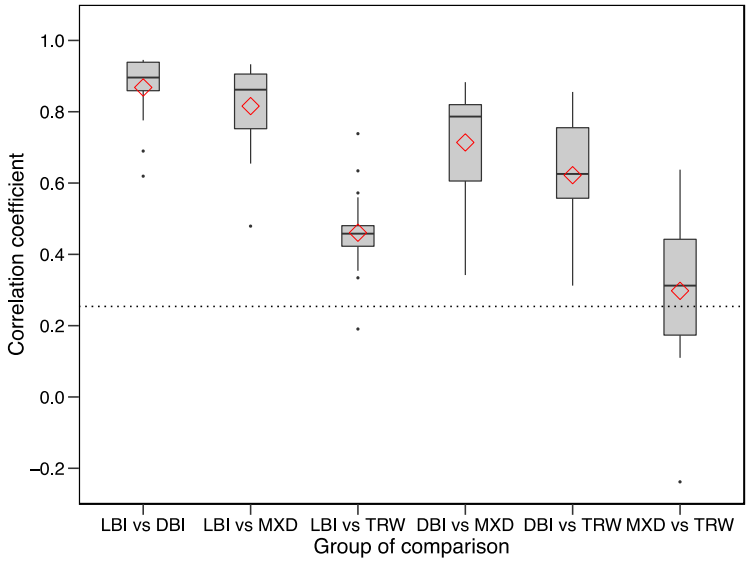

Figure 1-S4: Inter-parameter (LBI, DBI, MXD, and TRW) correlation analysis among the 17 local chronologies. Horizontal bars, boxes, and whiskers show the median, the interquartile range, and values outside the interquartile ranges, respectively. Outliers are shown as dots. The red diamonds refer to the mean correlation coefficients among the 17 sites for each pair of parameters.

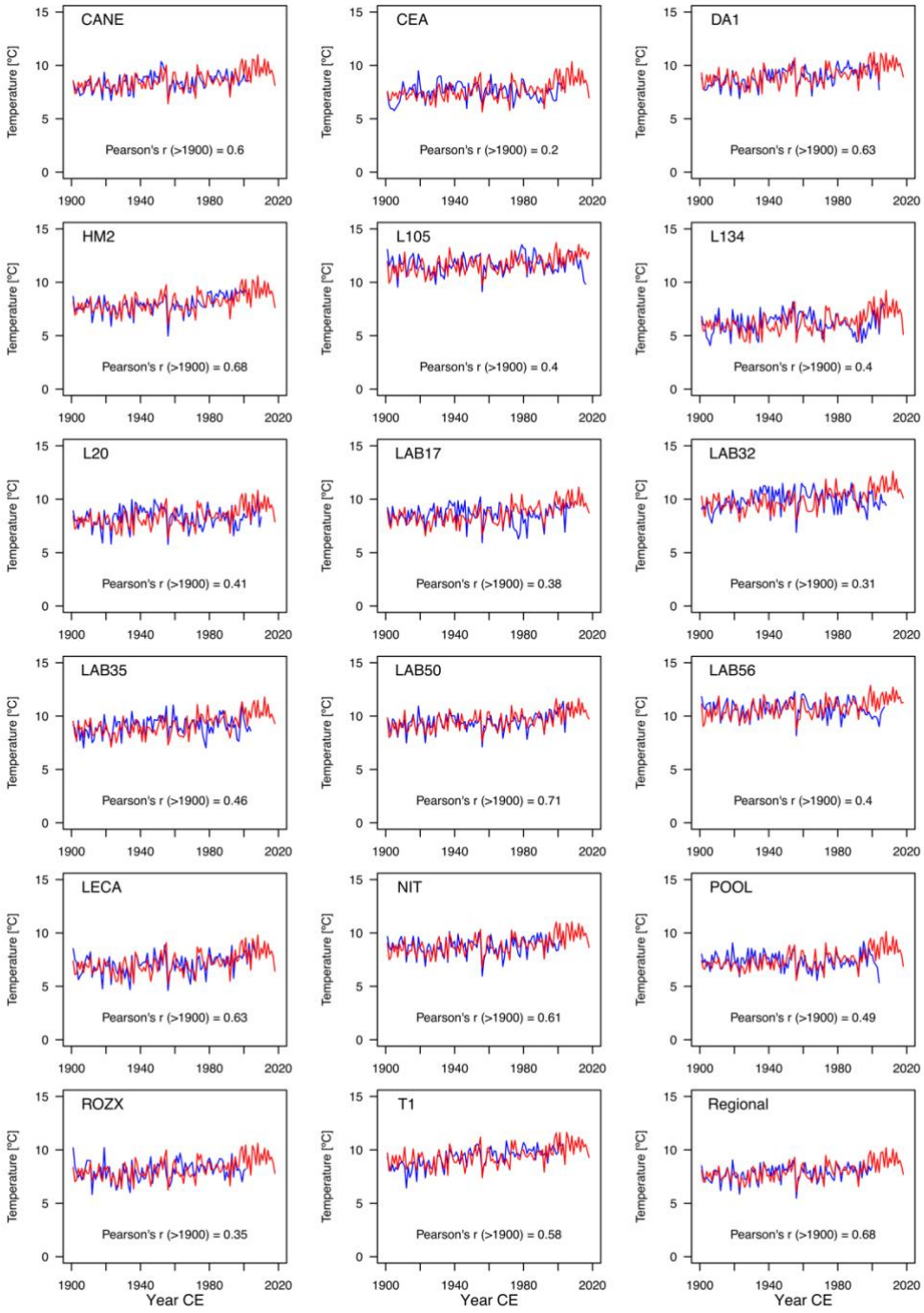

Figure 1-S5: Comparisons of local and regional LBI standardized chronologies (blue) against local and regional MJJA temperature targets (red).

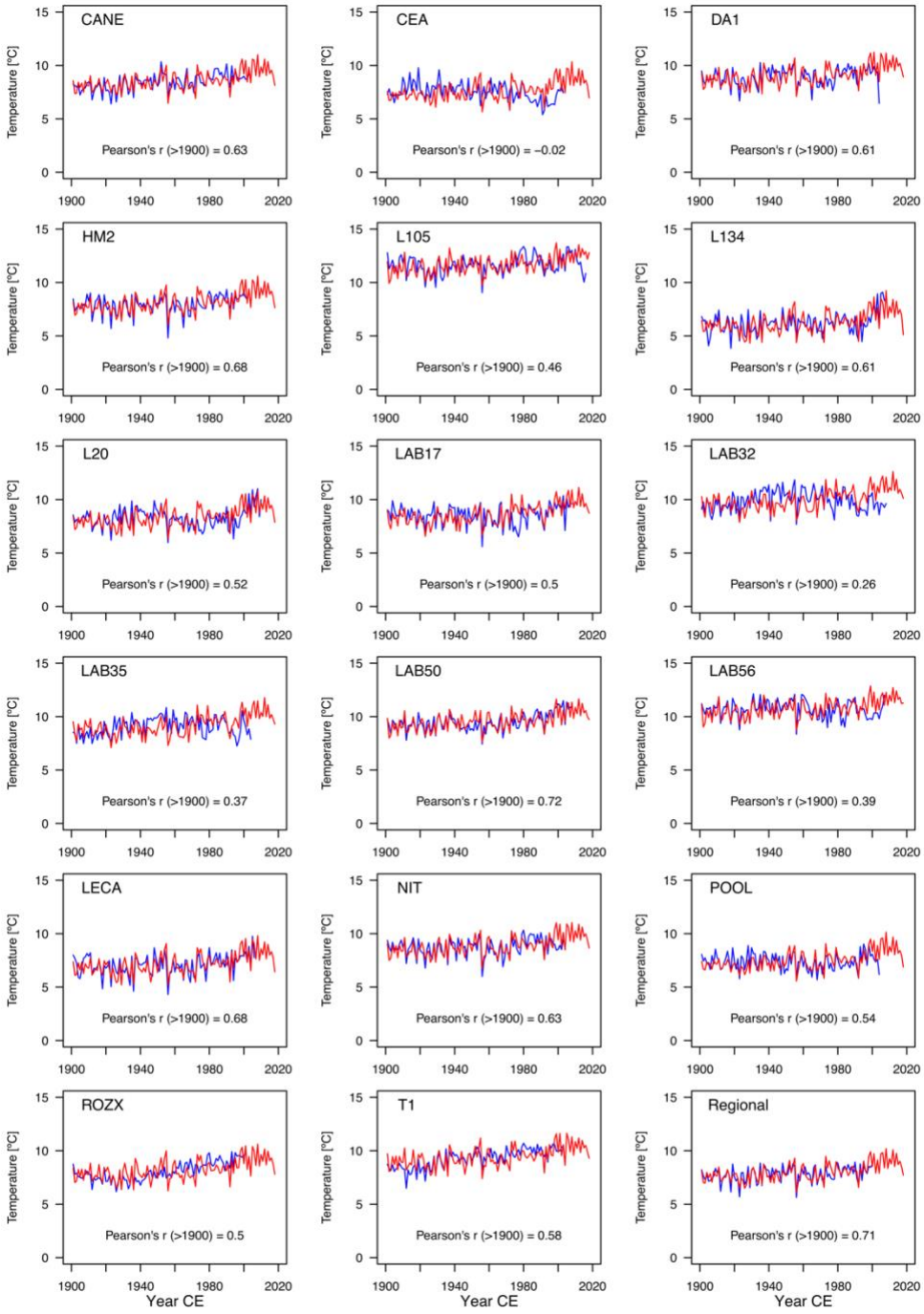

Figure 1-S6: Comparisons of local and regional DBI standardized chronologies (blue) against local and regional MJJA temperature targets (red).

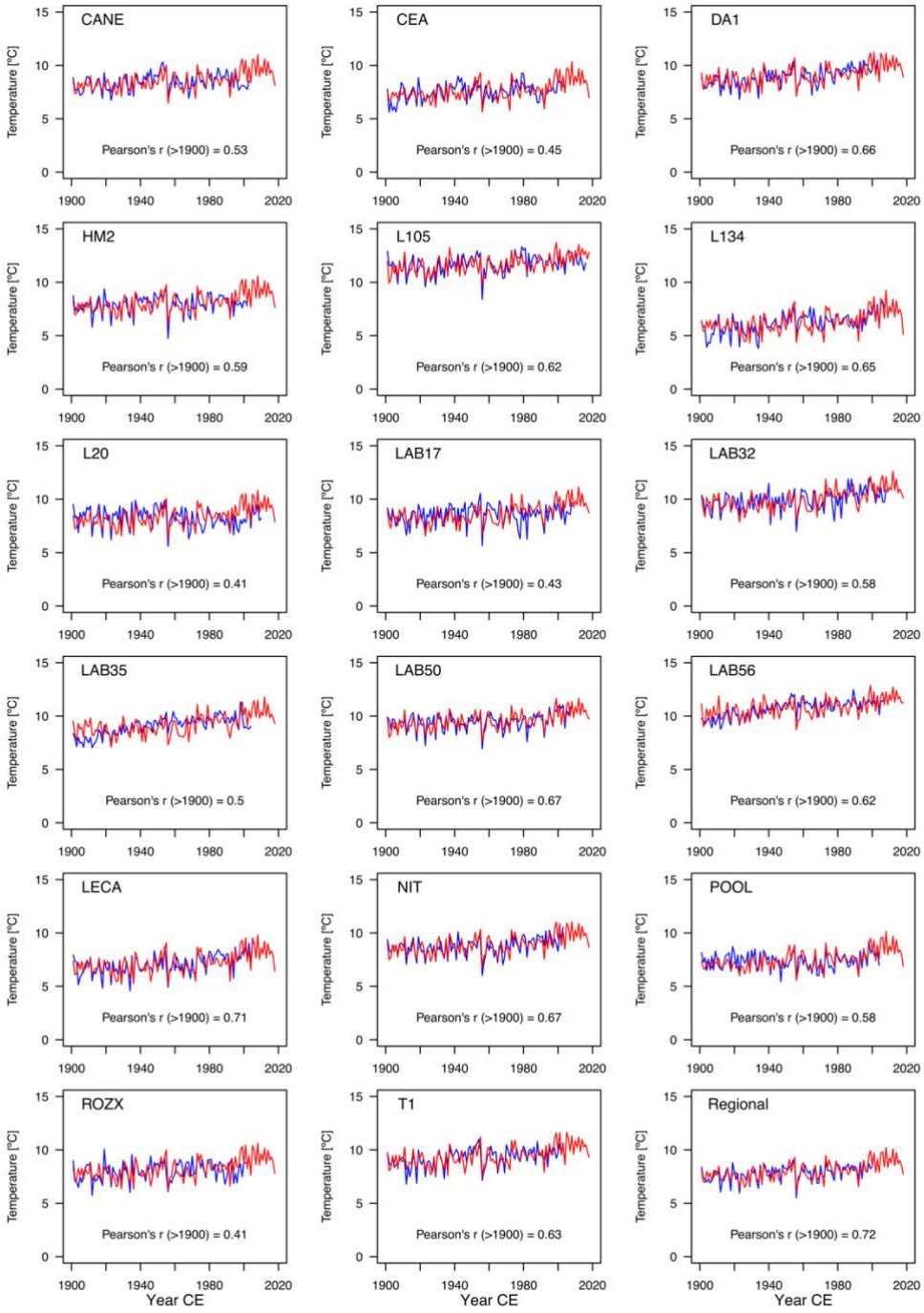

Figure 1-S7: Comparisons of local and regional MXD standardized chronologies (blue) against local and regional MJJA temperature targets (red).

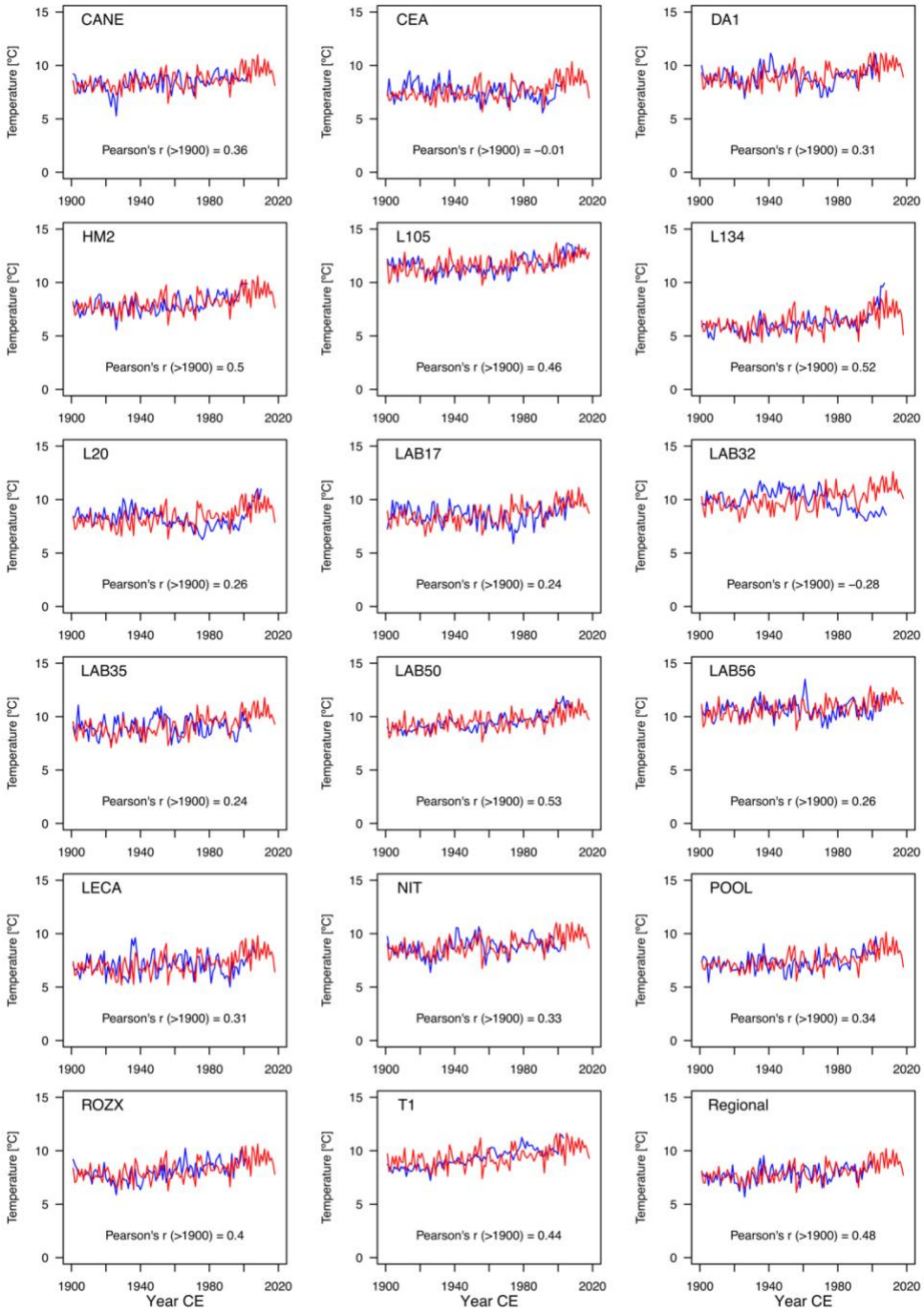

Figure 1-S8: Comparisons of local and regional TRW standardized chronologies (blue) against local and regional MJJA temperature targets (red).

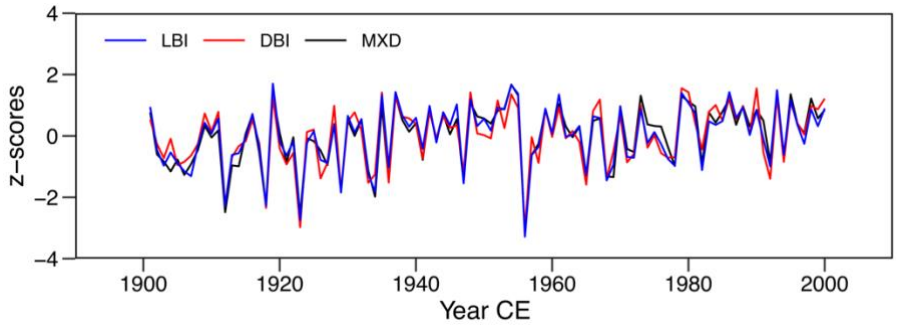

Figure 1-S9: Comparison of LBI, DBI, and MXD regional chronologies.

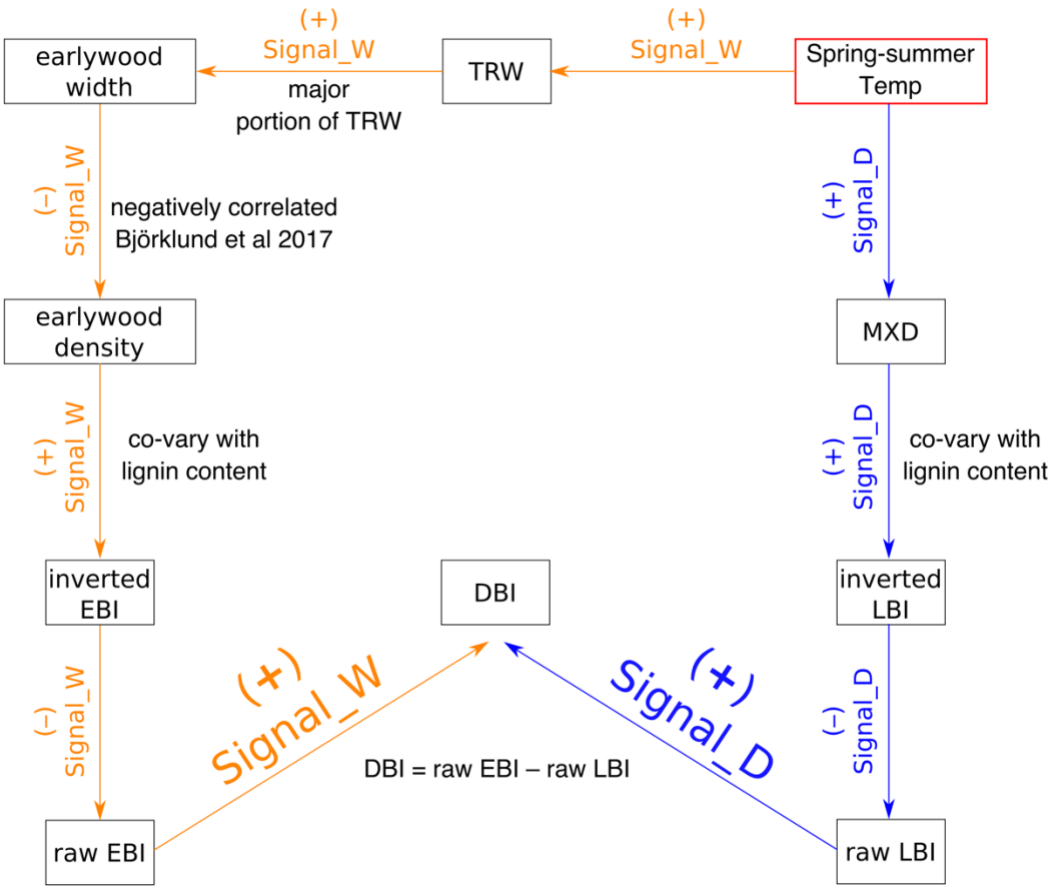

Figure 1-S10: Diagram of assumed relationships and transfer of temperature signal among tree-ring parameters. Signal_D and Signal_W represent the spring–summer temperature signals that control MXD and TRW values, respectively. (+) and (–) refer to positive and negative correlations, respectively.

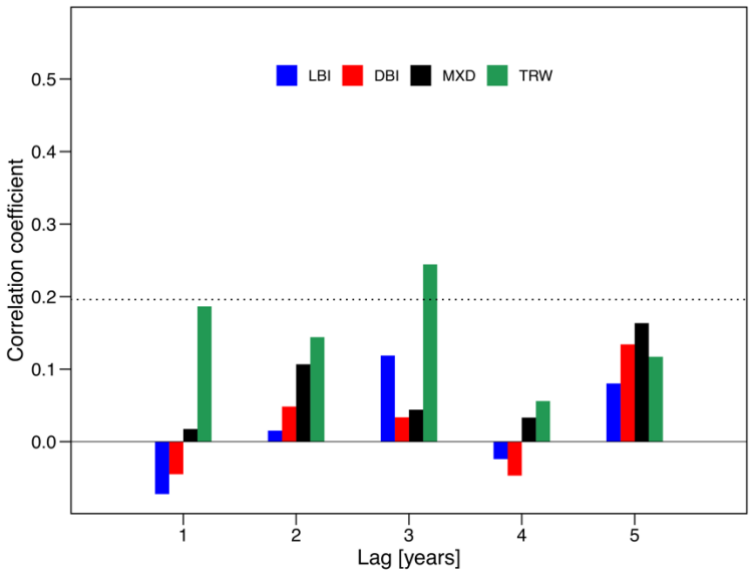

Figure 1-S11: Lagged autocorrelations of the LBI, DBI, MXD and TRW chronologies with MJJA regional land temperature target over the 1901–2000 time interval. The horizontal dashed line refers to statistical significance at the 0.95 confidence level.

CHAPITRE II

CHEMICAL DESTAINING AND THE DELTA CORRECTION FOR BLUE INTENSITY MEASUREMENTS OF STAINED LAKE SUBFOSSIL TREES

Feng Wang[a, b*], Dominique Arseneault[a, b], Étienne Boucher[c], Shulong Yu[d], Steeven Ouellet[a], Gwenaëlle Chaillou[e], Ann Delwaide[f], Lily Wang[g]

a. Département de Biologie, Chimie et Géographie, Université du Québec à Rimouski, Rimouski, G5L 3A1, Canada

b. Centre d'Études Nordiques, Université du Québec à Rimouski, Rimouski, G5L 3A1, Canada

c. Département de Géographie, GEOTOP and Centre d'Études Nordiques, Université du Québec à Montréal, Montréal, H3A 0B9, Canada

d. Key Laboratory of Tree-ring Ecology of Uigur Autonomous Region and Key Laboratory of Tree-ring Physical and Chemical Research, Institute of Desert Meteorology, China Meteorological Administration, Urumqi, 830002, China

e. Canada Research Chair in Geochemistry of Coastal Hydrogeosystems, Québec-Océan, UQAR/ISMER, Rimouski, G5L 3A1, Canada

f. Département de Géographie, Université Laval, Quebec City, G1V 0A6, Canada

g. Institute of Geographic Sciences and Natural Resources Research, Chinese Academy of Science, Beijing, 100101, China

Published in Biogeosciences 2020

2.1 Résumé

Le deuxième chapitre de ma thèse, intitulé « *Décoloration chimique et correction delta des mesures d'intensité du bleu des arbres subfossiles* », a été co-écrit par Feng Wang, Dominique Arseneault, Étienne Boucher, Shulong Yu, Steeven Ouellet, Gwenaëlle Chaillou, Ann Delwaide et Lily Wang. Comme auteur principal, j'ai réalisé les traitements et analyses chimiques, les mesures des cernes, l'analyse des données, la production des figures et l'écriture du manuscrit. Les professeurs Dominique Arseneault, Étienne Boucher et Gwenaëlle Chaillou ont supervisé et révisé cette recherche. Shulong Yu, Steeven Ouellet, Ann Delwaide et Lily Wang ont contribué à la préparation des échantillons et à la production des données. Dans ce chapitre, nos recherches sur la méthode BI ont été étendues aux spécimens subfossiles d'épinette noire qui présentent un bois coloré en raison d'un séjour prolongé dans les sédiments lacustres. Les arbres enfouis dans les sédiments de deux lacs ont été interdatés par dendorchronologie et ont servi à étudier l'effet de la coloration du bois sur les mesures de BI, en comparant des approches chimiques et mathématiques pour réduire l'effet de la coloration du bois.

La coloration des échantillons de bois des arbres subfossiles compromet l'application à grande échelle de la technique de l'intensité du bleu (BI) pour les reconstitutions dendroclimatiques millénaires. Dans cette étude, nous avons utilisé sept réactifs chimiques pour décolorer des échantillons d'épinettes noires subfossiles (*Picea mariana* (Mill.) B.S.P.) provenant de deux lacs de la forêt boréale de l'est du Canada. Nous avons par la suite comparé les séries chronologiques de BI pour le bois final (LBI) et de BI delta (DBI) avec la densité maximale conventionnelle du bois final (MXD), mesurée à partir des échantillons colorés et décolorés. Les résultats ont montré que la coloration des subfossiles est très probablement causée par l'oxydation post-échantillonnage du fer ferreux imprégné dans le bois à partir des sédiments lacustres. Trois réactifs (acide ascorbique, ascorbate de sodium et dithionite de sodium, tous mélangés à de l'acide éthylènediaminetétraacétique) éliminent plus de 90 % du Fe. Cependant, même pour le meilleur réactif, un écart d'environ +2°C par rapport aux

données MXD persiste dans la reconstitution de la température basée sur LBI, probablement à cause d'une décoloration incomplète. Au contraire, la simple correction mathématique de type delta, le DBI, permet de supprimer l'effet de la coloration du Fe, et montre des résultats très similaires aux données MXD (r > 0,82) pour les échelles de temps annuelles à centennales au cours des 360 dernières années. Cette étude souligne la difficulté de supprimer complètement l'effet de la coloration du Fe dans les arbres subfossiles et confirme la robustesse de l'approche DBI. Les données DBI mesurées à partir des arbres subfossiles peuvent être utilisées pour effectuer des reconstitutions fiables des températures du dernier millénaire.

2.2 Abstract

The second chapter of my thesis, entitled *Chemical destaining and the delta correction for blue intensity measurements of stained lake subfossil trees*, was co-authored by Feng Wang, Dominique Arseneault, Étienne Boucher, Shulong Yu, Steeven Ouellet, Gwenaëlle Chaillou, Ann Delwaide, and Lily Wang. As the main author, I carried out chemical treatments and analyses, measurements of tree rings, data analysis, production of figures and writing. Professors Dominique Arseneault, Étienne Boucher, and Gwenaëlle Chaillou supervised and revised this research. Shulong Yu, Steeven Ouellet, Ann Delwaide, and Lily Wang contributed to sample preparation and data production. In the second chapter, our investigation on the BI method was extended to the subfossil samples of black spruce which are discolored due to long stay in lake sediments. Trees buried in the sediments of two lakes were cross-dated using dendrochronological method and were used to study the effect of wood stain on BI measurements, by comparing chemical and mathematical approaches.

The stain of wood samples from lake subfossil trees (LSTs) is challenging the wide application of the blue intensity (BI) technique for millennial dendroclimatic reconstructions. In this study, we used seven chemical destaining reagents to treat samples of subfossil black spruce (*Picea mariana* (Mill.) B.S.P.) trees from two lakes in the eastern Canadian boreal

forest. We subsequently compared latewood BI (LBI) and delta BI (DBI) time series along with conventional maximum latewood density (MXD) measured from the stained and destained samples. Results showed that the stain of our samples is most likely caused by postsampling oxidation of dissolved ferrous iron in lake sediments that penetrated into wood. Three reagents (ascorbic acid, sodium ascorbate, and sodium dithionite all mixed with ethylenediaminetetraacetic acid) could remove >90% of Fe. However, even for the best chemical protocol, a discrepancy of about +2°C compared to MXD data remained in the LBI-based temperature reconstruction due to incomplete destaining. On the contrary, the simple mathematical delta correction, DBI, was unaffected by Fe stain and showed very similar results compared to MXD data ($r > 0.82$) from annual to centennial timescales over the past ~360 years. This study underlines the difficulty of completely destaining lake subfossil samples while confirming the robustness of the DBI approach. DBI data measured from stained LSTs can be used to perform robust millennial temperature reconstructions.

2.3 Introduction

The blue intensity (BI) technique is an alternative to the more expensive X-ray densitometric methodology in producing proxy parameters such as maximum latewood density (MXD) for dendroclimatology (Björklund et al., 2019; McCarroll et al., 2002). MXD is the most suitable tree-ring parameter for summer temperature reconstructions in northern and high-altitude regions (Esper et al., 2014; Frank and Esper, 2005). However, compared to the less-climate-sensitive ring-width data, millennial MXD series have been much less frequently developed worldwide, mainly due to the high cost of densitometric equipment (Anchukaitis et al., 2017; St. George and Esper, 2019; Wilson et al., 2016). In contrast, BI is more affordable because it uses commercial flatbed scanners and image analysis software to measure the blue light reflectance of tree rings (Rydval et al., 2014). Excellent coherence was reported between the latewood BI (LBI) and MXD data measured from living-tree materials of a number of coniferous tree species across the northern hemisphere (Campbell et al., 2007; Kaczka et al., 2018; Österreicher et al., 2015; Rydval et al., 2014; Wilson et al.,

2014), suggesting the potentials to use BI method in dendrocliamtic reconstructions (McCarrol et al., 2013; Rydval et al., 2017; Wilson et al., 2019).

However, the BI technique is also facing challenges due to heterogeneous colors of various wood materials. The best-known issue is the sapwood-heartwood color difference of several tree species such as pine and larch, which does not co-vary with density (Björklund et al., 2014; Rydval et al., 2014; Wilson et al., 2019). Some wood types, such as dead trees and historical materials, may also be discolored by decay or weathering (Wilson et al., 2014). Another less documented color issue occurs with lake subfossil trees (LSTs), which often have darker wood than living trees (Wilson et al., 2019). LSTs are a very interesting source of material to extend tree-ring chronologies from centuries to several millennia and can greatly improve the replication of reconstructions, especially in regions where only short-lived tree species occur (Arseneault et al., 2013; Grudd et al., 2002). All the above color issues may potentially alter the accuracy of BI data (e.g., LBI) and introduce biases in BI-based climate reconstructions, particularly for the low-frequency domain (Björklund et al., 2014; Wilson et al., 2019). Therefore, it is critical to develop unbiased BI data from a variety of wood materials, in particular from LSTs, to make the promising BI technique widely applicable in future dendroclimatic reconstructions.

Some solutions have been proposed to overcome the sapwood-heartwood color issue. Sheppard and Wiedenhoeft (2007) used hydrogen peroxide to bleach wood colors and attenuate the sapwood-heartwood difference, although an earlier study claimed that chemical bleaching likely degraded the climate signal (Sheppard, 1999). A later and seemingly more promising approach consists of a simple mathematical correction computed as the BI difference between the earlywood and latewood, (i.e., the delta BI; hereafter DBI) of each tree ring. DBI corrects for the low-frequency (decadal–centennial) variations distorted by the sapwood-heartwood color issues (Björklund et al., 2014, 2015). Only a few studies attempted to use BI data measured from LSTs to develop long-term temperature reconstructions, but the staining issue was not addressed and these BI series were not directly compared to MXD

data. For example, Rydval et al. (2017) combined the high-frequency temperature signals extracted from LBI with the low frequency from ring-width data of LSTs in order to reconstruct temperatures, without using the low-frequency information of the more temperature-sensitive BI data.

In this study, we explore the potential of generating unbiased BI series from stained black spruce LSTs from two eastern Canadian lakes (Fig. 2-1a). More specifically, we compared chemical destaining with the DBI approach as well as with conventional MXD data. The following hypotheses were formulated: (1) the stain of LSTs is mainly caused by oxidation of Fe (Hyacinthe et al., 2006; Kostka and Luther, 1994; Pelé et al., 2015; Zhang and Xi, 2003), which can be removed using some anti-oxidant reagents; (2) chemical destaining and DBI can greatly improve BI-based temperature reconstructions that are comparable to MXD-based reconstructions. We first treated thin wood laths of stained LSTs using seven potential chemical reagents and quantified the proportion of Fe extracted by chemicals. Subsequently, we performed dendroclimatic assessments by comparing LBI and DBI chronologies of the destained and stained LST samples with MXD data over the past ~360 years.

2.4 Materials and methods

2.4.1 Study sites and staining issue

The two studied lakes (L20 and L105) are located approximately 450 km apart in the eastern Canadian boreal forest of the Quebec-Labrador Peninsula (Fig. 2-1a). The climate of this region is characterized by short, mild summers and long, cold winters (Environment Canada, 2020). Regional forests are strongly dominated by black spruce, mixed with balsam fir (*Abies balsamea* L.) and eastern larch (*Larix laricina* (Du Roi) K. koch) (Payette, 1993). Lakes are extremely abundant and cover up to about 25% of the landscape. Numerous black spruce trees in the lakeshore forests thus become LSTs after falling in water and eventually becoming buried in lake sediments (Arseneault et al., 2013; Gennaretti et al., 2014a, 2014b).

Black spruce LSTs from L20 (54.56º N, 71.24º W) were previously included in a millennial temperature reconstruction (Gennaretti et al., 2014c). L105 (50.81º N, 67.80º W) is a newly sampled lake where more than a thousand black spruce LSTs were extracted, and many of them were successfully cross-dated to develop a millennial ring-width chronology (unpublished data).

LSTs in the eastern Canadian boreal forest are frequently stained to various blue-gray intensities (Fig. 2-S1). When dry, these stains correspond well to the Munsell Soil Color Chart 2009-5Y-Chroma I. In total, 78% and 79% of the cross-dated LSTs at L20 and L105 were stained to some degrees of gray, respectively (Fig. 2-1b, c). Very few LSTs displayed additional colors, for example due to fungal discoloration. Stained LSTs are distributed throughout the time span of the two millennial chronologies with increasing proportions back in time, particularly before the year 1800 CE (Fig. 2-1b, c), suggesting that staining issues are unavoidable when using BI measurements from this material.

2.4.2 Destaining experiment

We selected stem cross sections from five (evenly and heavily) stained LSTs and five unstained lakeshore living trees from each of the two studied lakes. Using a twin-blade saw (DendroCut, Walesch Electronic), we transversally cut sixteen 1 mm-thick laths along the radius of each subfossil tree (total of 160 laths), and 2 laths from each living tree (total of 20 laths). All laths were pretreated using 95% ethanol in Soxhlet extractors for 48 hours to remove resins and then air-dried and weighed. Sixteen pretreated laths from each LST were divided into eight pairs. Seven pairs were immersed in 50 mL of one of the seven chemical solutions (Table 2-1) in Falcon® 50mL tubes (see an example in Fig. 2-2), then placed on an electronic shaker (SK-600, Montreal Biotech Inc.) with a speed of 133 rpm at room temperature (c.a. 20 ºC) for 24 h (MixC) and 48 h (other reagents). Treated laths were rinsed 4–5 times, immersed in de-ionized water for 2 h to remove dissolved elements absorbed by wood tissues, and then air-dried for subsequent analysis. The eighth pair of subfossil laths

and all the living-tree laths were not treated with destaining reagents and considered as control samples. Design of the experiments is illustrated in Fig. 2-S2.

During the destaining treatments, we sequentially sampled reaction solutions to construct temporal Fe dissolution curves (the most abundant metal element detected in preliminary tests) for MixA, MixB, and MixC, which were the most effective destaining reagents. A total of 1 mL of solution was sampled at 0, 1, 3, 6, 12, and 24 h for MixA and MixB, and at 0, 0.5, 1, 3, 6, and 12 h for MixC (Fig. 2-2). Treatment and sampling times were set shorter for MixC since it was the most active reagent. The 1 mL extracted solutions were then diluted in 5 mL of 5% (v/v) hydrochloric acid in Falcon® 15 mL tubes in order to avoid Fe(II) precipitation prior to the chemical analysis of Fe concentrations. After destaining, one lath from each pair of laths was used to quantify the amount of residual Fe and was digested using 5 mL nitric acid and 1 mL hydrogen peroxide in a MARS-Xpress microwave digestion system (CEM Corporation) at 150 ºC for 30 minutes (Fig. 2-2). Digested solutions were diluted to 25 mL in volumetric flasks using de-ionized water. Fe concentrations were measured using the microwave plasma-atomic emission spectrometer (MP-AES, Agilent 4200; the limit of detection is ~4.6 ppb for dissolved Fe), and data were adjusted to milligram of Fe per gram of wood according to the dilution and weight of the corresponding wood lath. Fe concentrations in this study represent the total amount of ferrous and ferric Fe, because MP-AES does not distinguish the type of Fe ions.

The second lath of each pair was air-dried, finely sanded (to 1000 grit), and scanned using the SilverFast 8.0 software (LaserSoft Imaging) and an Epson V800 flatbed scanner. In order to obtain optimal calibration results, the sanded laths were scanned to RGB images of 3200 dpi along with a color IT8.7/2 calibration target (LaserSoft Imaging). The scanner was covered by a black plastic box to avoid interference of external light (Rydval et al., 2014). It should be noted that the actual image resolution is approximately 2580 dpi (horizontal) by 1825 dpi (vertical) according to the USAF-1951 resolution target. Wood RGB intensities (definition 1–3 in Table 2-2), were then measured using the CooRecorder 8.1

software (Cybis Dendrochronology). Because high RGB values represent light colors (i.e., high brightness), they were subtracted from a value of 256 such that smaller RGB values are associated with lighter colors. RGB intensities were compared among treatments (seven treatments plus two controls) to assess the efficiency of the destaining reagents.

2.4.3 Dendroclimatic assessment

In order to perform dendroclimatic assessments of the most effective destaining treatments, in a separate experiment we selected 57 trees of different types (stained and unstained LSTs as well as living trees) which were cross-dated after the year 1600 CE from L20 and L105 (28 and 29 trees, respectively; Fig. 2-S3). We cut eight 1 mm-thick laths from two radii of each tree to acquire four pairs of laths (Fig. 2-S4). Laths were pretreated using 95% ethanol in Soxhlet extractors for 48 h. We then treated three pairs of laths per tree using the MixA, MixB, and MixC, respectively, while keeping the fourth lath as an untreated control. The conditions of destaining treatments were the same as explained above, except that the treatments lasted for 6 h, which is the time required for optimal destaining according to the Fe dissolution curves (Fig. 2-S5). Treated laths were then air-dried for LBI, DBI, and MXD measurements.

Measured tree-ring parameters are explained in Table 2-2. The wood laths for dendrochronological assessments were firstly X-rayed to generate MXD data prior to being sanded and scanned for BI measurements. X-ray densitometry experiments were conducted in a controlled environment with relative humidity of 50% and room temperature of 20ºC. X-ray films were developed using the DendroXray2 system (Walesch Electronic) and MXD series were measured using the Dendro2003 system (Walesch Electronic) with a resolution of 10μm along the measured density profile. LBI and DBI were measured using the same procedure as the measurement of wood RGB intensities. We subtracted the raw LBI values from a value of 256 in order to make the LBI positively correlated with MXD data, according to Rydval et al. (2014) and Wilson et al. (2019). Before data analysis, LBI, DBI, and MXD

data were averaged by tree (i.e., each lath pair) for each treatment (MixA, MixB, MixC, and Control).

We used regional curve standardization (RCS) to remove the biological trends from tree-ring series in order to retain low-frequency (decadal–centennial) climatic variations (Briffa and Melvin, 2011; Helama et al., 2017). An age-dependent spline with an initial stiffness of 2 years was used to estimate the regional curve. Standardized tree-ring series were computed as ratios between the raw data and the smoothed regional curve. In total, we standardized 24 groups of tree-ring data by site (L105 and L20), parameter (LBI, DBI, and MXD) and treatment (MixA, MixB, MixC, and Control). We excluded data from chemically treated, unstained trees (unstained LSTs plus living trees) because BI data of unstained trees tended to be altered by reagents, mostly the MixC (Fig. 2-S7). Consequently, we pooled the data of stained LSTs that were chemically treated, plus the data of the untreated, unstained trees for each standardization. In addition, living-tree data of L20 after the year 1950 CE were excluded as BI diverged from the MXD data (Fig. 2-S3 and 2-S8), which was likely due to the sapwood-heartwood color issue and narrow rings caused by poor tree health (see discussions below).

Regional chronologies for each tree-ring parameter (LBI, DBI, and MXD) and treatment (MixA, MixB, MixC, and Control) were generated by pooling standardized series from both sites using the Tukey's bi-weight robust mean. This approach was used because of the limited tree replication per site (Fig. 2-S3). Regional MXD chronologies from the four treatments were similar (Fig. 2-S9) and thus averaged into one reference chronology. All regional chronologies were truncated at the year 1655 CE to ensure a minimum replication of five trees (Fig. 2-S3c).

We performed temperature reconstructions using the regional LBI, DBI, and MXD chronologies to further quantify the influence of the destaining protocols. Instrumental summer (May to August) temperature data were obtained from the CRU TS 4.02 0.5° gridded monthly mean temperature dataset (Harris et al., 2014) and averaged from the four grid cells

closest to each lake in order to generate a regional temperature target. The reconstructions were based on the scaling method (Esper et al., 2005; Rydval et al., 2017) by adjusting means and standard deviations of the chronologies to those of the temperature target over the 1901–2015 time interval.

2.4.4 Data analysis

Data were analyzed using the R program (R Core Team, 2018). We conducted linear regressions between wood RGB intensities and logarithmic residual Fe of both treated and untreated LSTs in order to assess the roles of Fe in the staining issue. For chronology assessments, we generated several high-pass and low-pass LBI, DBI, and MXD series using the Butterworth filter available in the "dplR" R package (Bunn, 2008). Pearson correlation coefficients were used to assess the degrees of agreement among all the time series. Performance of reconstructions was assessed following a regression-based calibration–verification procedure using the "treeclim" R package (Zang and Biondi, 2015). Since our chronologies showed higher replication during 1901–1960 (Fig. 2-S3), this time interval was used for calibration, while the 1961–2015 period was used for verification. We also calculated 1-year lagged 31-year moving expressed population signal (EPS; Wigley et a., 1984) to assess the temporal robustness of chronologies used for reconstruction.

2.5 Results

2.5.1 Effects of chemical destaining

LSTs displayed a variety of color changes after the seven destaining treatments (Fig. 2-3a). NaAsc resulted in very similar colors to that of the untreated stained samples, representing the weakest destaining effect. Conversely, MixA, MixB, and MixC showed dramatic effects and almost completely removed the gray stain. MixC was the most effective destaining solution based on wood RGB intensities, although the resultant colors still slightly differed from the living-tree standards (Fig. 2-3a, b). BI was less variable with varying degrees of posttreatment stains in comparison to red and green intensities (Fig. 2-3b),

suggesting a potentially weaker influence of wood stain on the BI data. MixC, the only reagent with bleaching function (Table 2-1), could have an additional bleaching effect on the wood, resulting in smaller LBI and DBI values in living and unstained trees compared to untreated control (Fig. 2-S7). However, DBI of the stained LSTs was only slightly modified by the MixC treatment (Fig. 2-S7), indicating that the bleaching effect of MixC is weak for the stained samples.

2.5.2 Stain versus iron

Chemical analyses showed strong links between Fe concentrations and color intensities of wood, especially for green and red intensities (Fig. 2-3a, c). Total Fe concentration was the highest for untreated stained LSTs and near zero for living trees (Fig. 2-3c). MixA, MixB, and MixC could remove 94.1%, 92.5%, and 96.2% of Fe relative to the amount measured in the untreated stained LSTs, respectively. Although Fe dissolution curves stabilized after 6–12 h (Fig. 2-S5), minor quantities of residual Fe after the treatments (24–48 h) indicated that all destaining reactions are incomplete. Significant ($p < 0.001$) linear relationships existed between the log of residual Fe and posttreatment color (RGB) intensities of treated earlywood and latewood (Fig. 2-3d, e). However, such linearity markedly weakened for the delta RGB intensities, especially for the delta BI (p=0.087, Fig. 2-3f), indicating that DBI of LSTs is insignificantly affected by the staining issue. Note that wood delta BI and DBI were not calculated exactly in the same way (see Table 2-2; delta BI is the averaged difference between BI of entire latewood and earlywood from all tree rings in a sample, while DBI is a tree-ring parameter which presents the difference between LBI and BI of entire earlywood for each tree ring).

2.5.3 Comparison of LBI and DBI against MXD chronology

LBI chronologies of the four retained treatments (MixA, MixB, MixC, and Control) diverged relative to the reference MXD chronology (Fig. 2-4a) prior to the year 1900 CE when the stained LSTs dominated the chronologies (Fig. 2-S3c). Correlation analyses showed that coherence between LBI and MXD chronologies was only robust for the 10-year

high-pass filtered data ($r > 0.89$) and decreased at longer timescales (Fig. 2-4c). In contrast, DBI chronologies were very similar to the reference MXD chronology for all the four treatments (Fig. 2-4b). Correlations with MXD data were strong and stable among all frequencies tested ($r > 0.82$) (Fig. 2-4d). In addition, few differences were found between the control DBI series and the chemically treated DBI data, although the colors of wood samples were visually distinct (Fig. 2-3a).

2.6 Discussion

2.6.1 Causes of stain

The significant relationships between posttreatment wood RGB intensities and residual Fe (Fig. 2-3), along with the rapid postsampling staining (Fig. 2-5b), support our hypothesis that oxidation of Fe is a major cause of stain in our lake subfossil material. Fe is abundant in natural aquatic systems as dissolved and particulate fractions (Bortleson and Lee, 1974; Davison, 1993; Nürnberg and Dillon, 1993). Briefly, dissolved Fe, mainly in Fe(II) state, is reduced and mobilized in porewater in the anoxic sediments. Dissolved Fe can migrate upward to oxic bottom water to form particulate Fe(III) oxides (Davison, 1993; Davison et al., 1982). This cycle results in much higher concentrations of dissolved Fe in the anoxic sediments compared to the oxygenated freshwaters (Zaw and Chiswell, 1999). Soluble forms of Fe in the anoxic sediments can readily penetrate into the buried wood tissues. When buried LSTs are extracted from lakes, cut and exposed to air, dissolved Fe is rapidly oxidized to colored Fe-oxides (oxyhydroxides, hydroxides and more crystalline Fe(III) oxides) which may bind to wood (Pelé et al., 2015). This process is also supported by the fact that fresh cuts from buried portions were heavily stained while exposed (but submerged) portions of the same LST were not (Fig. 2-5a). Photooxidation is assumed to be less likely, yet not improbable, because the stain contaminated both surface and inner portions of LSTs.

Furthermore, we found that amorphous and crystalline Fe oxides are likely produced during the oxidation of dissolved Fe. About 63.4% of Fe was removed by the NaAsc reagent,

although posttreatment colors of LSTs only slightly lightened (Fig. 2-3a, c). The neutral NaAsc, similar to buffered ascorbates, only extracts the most-reactive amorphous Fe-oxides (Anschutz et al., 2005; Hyacinthe et al., 2006; Kostka and Luther, 1994). The less-reactive crystalline phases can be removed by EDTA, HAsc, MixA, MixB, and MixC, each of which removed at least 25% more Fe than NaAsc. In fact, EDTA, ascorbic acid, and sodium dithionite, which are the active chemicals in these solutions, are known as useful extractants of both crystalline and amorphous Fe oxides (Borggaard, 1982; Hyacinthe et al., 2006; Kostka and Luther, 1994; Tessier et al., 1979). The notable destaining effect of these solutions (Fig. 2-3a) also implies that crystalline Fe oxides are more color-reflective than amorphous ones. In our experiment, HAc extracted less Fe than NaAsc but with a better destaining effect (Fig. 2-3). A probable explanation is that acid-soluble Fe oxides extracted by HAc (Chester and Hughes, 1969; Gupta and Chen, 1975; Tessier et al., 1979) are in amorphous and crystalline phases which have stronger color reflectivity, whereas NaAsc only extracted less-color-reflective amorphous Fe oxides.

Other metal elements most likely have a negligible staining effect on LSTs compared to Fe. Our preliminary analyses demonstrated that, among 15 potential metal elements (including iron, manganese, chromium, cobalt, copper, lead, etc.), Fe was the only element present at high concentrations. Although manganese was relatively abundant in the samples (several times higher than other metals), its concentration was still approximately 20 times lower than Fe. In addition, we did not detect any copper and lead in our samples. On the other hand, Fe complexes bound to sulfur and phosphorus might also be responsible for the staining of LSTs in addition to the Fe oxides. However, the MP-AES instrument is not sufficiently sensitive to verify our hypothesis regarding those Fe complexes (detection limits are ~6500 ppb and 125 ppb for dissolved sulfur and phosphorus, respectively, compared to ~4.6 ppb for dissolved Fe).

2.6.2 Chemical destaining versus delta correction

The divergent trends of the three chemically treated LBI chronologies (MixA, MixB, and MixC) compared to the reference MXD chronology demonstrate that none of the destaining treatments can generate satisfactory and robust LBI data (Fig. 2-4a). Although MixC is the most effective protocol resulting in very little residual Fe (<5% relative to the stained LSTs), the corresponding LBI chronology still displayed a significant long-term bias before the year 1830 CE (Fig. 2-4a), leading to a discrepancy of about +2 ºC compared to the MXD-based reconstruction (Fig. 2-6a). If no chemical treatment had been applied, the temperature discrepancy would be amplified to about +4 ºC (not shown). These errors are caused by the extreme color sensitivity of LBI values as direct measures of blue light reflectance. Therefore, any stain contributing to the wood color will strongly contaminate the LBI data, especially in the low-frequency domain (Björklund et al., 2014). These results discourage the use of LBI when staining is present in subfossils woods. By contrast, the high-frequency variability of LBI data seems unaffected by the Fe stain (Fig. 2-4b).

Unlike LBI data, DBI is unaffected by the Fe stain from annual to centennial timescales, which is shown by the high and stable coherence between DBI and MXD chronologies (Fig. 2-4b, d) and the non-significant linear relationships between the log of residual Fe concentrations and delta BI data (Fig. 2-3f). The linearity between DBI and MXD remained almost unaffected by destaining treatments, for example as with the most efficient MixC protocol (Fig. 2-S10). Furthermore, compared to the Control DBI chronology, no chemical treatments substantially improved the correlation of DBI with MXD data (Fig. 2-4d), resulting in nearly identical trends in the corresponding temperature reconstructions in comparison with MXD, except for some periods where tree replication is less than 10 (Fig. 2-6c, d). This evidence suggests that DBI is not only excellent to resolve the sapwood-heartwood color biases, but also efficiently resolves the low-frequency biases caused by the Fe stain in black spruce LSTs from the eastern Canadian boreal forest.

We observed that LBI as well as DBI diverged from the MXD data after the year 1950 CE at L20 (Fig. 2-S8). The divergence of LBI is due to slight color differences between heartwood and sapwood of selected living trees although this issue is generally not serious for black spruce compared to pine or larch species (Rydval et al., 2014; Sheppard, 1999; Yang, 2007). Although DBI is theoretically sufficient to solve the sapwood-heartwood color issue (Björklund et al., 2014), in our case it could only partially correct this problem (Fig. 2-S8). Old living trees were collected from lakeshore forests at the L20 site and they often displayed declining ring widths compared to healthy trees sampled later at the same site (not shown). DBI of L20 is likely influenced by these narrow tree rings (Björklund et al., 2019) because DBI of black spruce is not only correlated to MXD but also to the ring-width data (Wang et al., 2020). We thus speculate the divergence of DBI reflects mostly a specific issue related to the declining growth of unhealthy trees.

This study confirms the robustness of DBI data from stained black spruce LSTs. Yet, two points need to be considered for future DBI-based climate reconstructions. Firstly, a higher tree replication is often needed for DBI than MXD data in order to obtain a robust chronology (Rydval et al., 2014; Wilson et al., 2019). Thus, it is not surprising that the control DBI-based reconstruction showed weaker verification statistics against instrumental temperature (Table 2-S1) and some slight instability during poorly replicated periods with more variable EPS values (Fig. 2-6e). When replication was above 15 trees during 1901–1960 (Fig. 2-S3c), the calibration r^2 was similar for DBI and MXD data against temperature (Table 2-S1). Secondly, Björklund et al. (2014, 2015) suggested some multi-centennial biases in DBI data due to the heterogeneous wood color. Although this phenomenon is not obvious in our case regardless of the Fe stain, our reconstruction only spanned the last three centuries and further attention is needed to verify this potential bias.

2.7 Conclusion

Our study indicates that the simple delta correction of differentiating latewood and earlywood BI values is more effective to resolve the staining biases of BI data from LSTs than the much more complex and time-consuming chemical destaining protocols tested here. DBI of black spruce LSTs is unaffected by the Fe stain from annual to centennial timescales and allows robust temperature reconstructions similar to MXD data. Consequently, DBI from stained black spruce LSTs is a promising proxy for developing millennial temperature reconstructions in the eastern Canadian boreal forests, a region with very few long MXD series (Wang et al., 2001). On the contrary, LBI is very color sensitive and appears problematic in retaining the low-frequency climatic signal.

The chemical destaining experiments, though not satisfactory regarding the robustness of LBI data, suggest that postsampling chemical Fe oxidation most likely result in the staining issue. Since Fe is so abundant in the Earth's systems, our results may be representative of much wider regions. On the other hand, the excellent Fe extraction abilities (removal of >90% Fe) of three chemical mixtures also suggest that they, in particular the MixC, can be further used as part of Fe extraction protocols for waterlogged archeological artifacts which also face Fe-staining issues (Fors et al., 2014, 2012; Pelé et al., 2015; Zhang and Xi, 2003).

2.8 Acknowledgements

This work was supported by the "PERSISTENCE" project funded by the Natural Sciences and Engineering Research Council of Canada (the NSERC-CRD program), Hydro-Québec, Manitoba Hydro, and the Ouranos consortium. FW was also funded by the China Scholarship Council. SY was supported by Key Laboratory Opening Subject of Xinjiang Uighur Autonomous Region (2016D03005) and Basic Research Operating Expenses of the Central-level Non-profit Research Institutes (IDM201202). LW was supported by National Natural Science Foundation of China (41571094). We greatly thank Florent Vignola for his

assistance in cutting wood blocks. Leila Jolicoeur, Nadège Trou-Kechout, and Pauline Balducci helped during laboratory and fieldworks. We also thank professor Feng Chen and Tongwen Zhang for their permissions to perform tree-ring density measurements at Institute of Desert and Meteorology, China Meteorological Administration.

2.9 References

Anchukaitis, K. J., Wilson, R., Briffa, K. R., Büntgen, U., Cook, E. R., D'Arrigo, R., Davi, N., Esper, J., Frank, D., Gunnarson, B. E., Hegerl, G., Helama, S., Klesse, S., Krusic, P. J., Linderholm, H. W., Myglan, V., Osborn, T. J., Zhang, P., Rydval, M., Schneider, L., Schurer, A., Wiles, G. and Zorita, E.: Last millennium Northern Hemisphere summer temperatures from tree rings: Part II, spatially resolved reconstructions, Quat. Sci. Rev., 163, 1–22, doi:10.1016/j.quascirev.2017.02.020, 2017.

Anschutz, P., Dedieu, K., Desmazes, F. and Chaillou, G.: Speciation, oxidation state, and reactivity of particulate manganese in marine sediments, Chem. Geol., 218, 265–279, doi:10.1016/j.chemgeo.2005.01.008, 2005.

Arseneault, D., Dy, B., Gennaretti, F., Autin, J. and Bégin, Y.: Developing millennial tree ring chronologies in the fire-prone North American boreal forest, J. Quat. Sci., 28, 283–292, doi:10.1002/jqs.2612, 2013.

Björklund, J., Gunnarson, B. E., Seftigen, K., Zhang, P. and Linderholm, H. W.: Using adjusted Blue Intensity data to attain high-quality summer temperature information: A case study from Central Scandinavia, The Holocene, 25, 547–556, doi:10.1177/0959683614562434, 2015.

Björklund, J., von Arx, G., Nievergelt, D., Wilson, R., Van den Bulcke, J., Günther, B., Loader, N. J., Rydval, M., Fonti, P., Scharnweber, T., Andreu-Hayles, L., Büntgen, U., D'Arrigo, R., Davi, N., De Mil, T., Esper, J., Gärtner, H., Geary, J., Gunnarson, B. E., Hartl, C., Hevia, A., Song, H., Janecka, K., Kaczka, R. J., Kirdyanov, A. V., Kochbeck, M., Liu, Y., Meko, M., Mundo, I., Nicolussi, K., Oelkers, R., Pichler, T., Sánchez-Salguero, R., Schneider, L., Schweingruber, F., Timonen, M., Trouet, V., Van Acker, J., Verstege, A., Villalba, R., Wilmking, M. and Frank, D.: Scientific merits and analytical challenges of tree-ring densitometry, Rev. Geophys., 57, 1224–1264, doi:10.1029/2019RG000642, 2019.

Björklund, J. A., Gunnarson, B. E., Seftigen, K., Esper, J. and Linderholm, H. W.: Blue intensity and density from northern Fennoscandian tree rings, exploring the potential to improve summer temperature reconstructions with earlywood information, Clim. Past, 10, 877–885, doi:10.5194/cp-10-877-2014, 2014.

Borggaard, O. K.: Selective extraction of amorphous iron oxides by EDTA from selected silicates and mixtures of amorphous and crystallline iron oxides, Clay Miner., 17, 365–368, doi:10.1180/claymin.1982.017.3.09, 1982.

Bortleson, G. C. and Lee, G. F.: Phosphorus, iron, and manganese distribution in sediment cores of six Wisconsin lakes, Limnol. Oceanogr., 19, 794–801, doi:10.4319/lo.1974.19.5.0794, 1974.

Briffa, K. R. and Melvin, T. M.: A Closer Look at Regional Curve Standardization of Tree-Ring Records: Justification of the Need, a Warning of Some Pitfalls, and Suggested Improvements in Its Application, in Dendroclimatology: Progress and Prospects, edited by M. K. Hughes, T. W. Swetnam, and H. F. Diaz, pp. 113–145, Springer Netherlands, Dordrecht., 2011.

Bunn, A. G.: A dendrochronology program library in R (dplR), Dendrochronologia, 26, 115–124, doi:10.1016/j.dendro.2008.01.002, 2008.

Campbell, R., McCarroll, D., Loader, N. J., Grudd, H., Robertson, I. and Jalkanen, R.: Blue intensity in *Pinus sylvestris* tree-rings: developing a new palaeoclimate proxy, The Holocene, 17, 821–828, doi:10.1177/0959683607080523, 2007.

Chester, R. and Hughes, M. J.: The trace element geochemistry of a North Pacific pelagic clay core, Deep Sea Res. Oceanogr. Abstr., 16, 639–654, doi:10.1016/0011-7471(69)90064-3, 1969.

Davison, W.: Iron and manganese in lakes, Earth-Sci. Rev., 34, 119–163, doi:10.1016/0012-8252(93)90029-7, 1993.

Davison, W., Woof, C. and Rigg, E.: The dynamics of iron and manganese in a seasonally anoxic lake; direct measurement of fluxes using sediment traps, Limnol. Oceanogr., 27, 987–1003, doi:10.4319/lo.1982.27.6.0987, 1982.

Environment Canada: Canadian climate normals or averages 1981-2010, available at http://climate.weather.gc.ca/climate_normals/index_e.html, last access: 14 March, 2020.

Esper, J., Frank, D. C., Wilson, R. J. S. and Briffa, K. R.: Effect of scaling and regression on reconstructed temperature amplitude for the past millennium, Geophys. Res. Lett., 32, doi:10.1029/2004GL021236, 2005.

Esper, J., Düthorn, E., Krusic, P. J., Timonen, M. and Büntgen, U.: Northern European summer temperature variations over the Common Era from integrated tree-ring density records, J. Quat. Sci., 29, 487–494, doi:10.1002/jqs.2726, 2014.

Fors, Y., Jalilehvand, F., Damian Risberg, E., Björdal, C., Phillips, E. and Sandström, M.: Sulfur and iron analyses of marine archaeological wood in shipwrecks from the Baltic Sea and Scandinavian waters, J. Archaeol. Sci., 39, 2521–2532, doi:10.1016/j.jas.2012.03.006, 2012.

Fors, Y., Grudd, H., Rindby, A., Jalilehvand, F., Sandström, M., Cato, I. and Bornmalm, L.: Sulfur and iron accumulation in three marine-archaeological shipwrecks in the Baltic Sea: The Ghost, the Crown and the Sword, Sci. Rep., 4, 4222, doi:10.1038/srep04222, 2014.

Frank, D. and Esper, J.: Characterization and climate response patterns of a high-elevation, multi-species tree-ring network in the European Alps, Dendrochronologia, 22, 107–121, doi:10.1016/j.dendro.2005.02.004, 2005.

Gennaretti, F., Arseneault, D. and Bégin, Y.: Millennial disturbance-driven forest stand dynamics in the Eastern Canadian taiga reconstructed from subfossil logs, J. Ecol., 102, 1612–1622, doi:10.1111/1365-2745.12315, 2014a.

Gennaretti, F., Arseneault, D. and Bégin, Y.: Millennial stocks and fluxes of large woody debris in lakes of the North American taiga, J. Ecol., 102, 367–380, doi:10.1111/1365-2745.12198, 2014b.

Gennaretti, F., Arseneault, D., Nicault, A., Perreault, L. and Bégin, Y.: Volcano-induced regime shifts in millennial tree-ring chronologies from northeastern North America, Proc. Natl. Acad. Sci., 111, 10077, doi:10.1073/pnas.1324220111, 2014c.

Grudd, H., Briffa, K. R., Karlén, W., Bartholin, T. S., Jones, P. D. and Kromer, B.: A 7400-year tree-ring chronology in northern Swedish Lapland: natural climatic variability expressed on annual to millennial timescales, The Holocene, 12, 657–665, doi:10.1191/0959683602hl578rp, 2002.

Gupta, S. K. and Chen, K. Y.: Partitioning of trace metals in selective chemical fractions of nearshore sediments, Environ. Lett., 10, 129–158, doi:10.1080/00139307509435816, 1975.

Harris, I., Jones, P. D., Osborn, T. J. and Lister, D. H.: Updated high-resolution grids of monthly climatic observations – the CRU TS3.10 Dataset, Int. J. Climatol., 34, 623–642, doi:10.1002/joc.3711, 2014.

Helama, S., Melvin, T. M. and Briffa, K. R.: Regional curve standardization: State of the art, The Holocene, 27, 172–177, doi:10.1177/0959683616652709, 2017.

Hyacinthe, C., Bonneville, S. and Van Cappellen, P.: Reactive iron(III) in sediments: Chemical versus microbial extractions, Geochim. Cosmochim. Acta, 70, 4166–4180, doi:10.1016/j.gca.2006.05.018, 2006.

Kaczka, R. J., Spyt, B., Janecka, K., Beil, I., Büntgen, U., Scharnweber, T., Nievergelt, D. and Wilmking, M.: Different maximum latewood density and blue intensity measurements techniques reveal similar results, Dendrochronologia, 49, 94–101, doi:10.1016/j.dendro.2018.03.005, 2018.

Kostka, J. E. and Luther, G. W.: Partitioning and speciation of solid phase iron in saltmarsh sediments, Geochim. Cosmochim. Acta, 58, 1701–1710, doi:10.1016/0016-7037(94)90531-2, 1994.

McCarroll, D., Loader, N. J., Jalkanen, R., Gagen, M. H., Grudd, H., Gunnarson, B. E., Kirchhefer, A. J., Friedrich, M., Linderholm, H. W., Lindholm, M., Boettger, T., Los, S. O., Remmele, S., Kononov, Y. M., Yamazaki, Y. H., Young, G. H. and Zorita, E.: A 1200-year multiproxy record of tree growth and summer temperature at the northern pine forest limit of Europe, The Holocene, 23(4), 471–484, doi:10.1177/0959683612467483, 2013.

McCarroll, D., Pettigrew, E., Luckman, A., Guibal, F. and Edouard, J.-L.: Blue reflectance provides a surrogate for latewood density of high-latitude pine tree rings, Arct. Antarct. Alp. Res., 34, 450–453, doi:10.1080/15230430.2002.12003516, 2002.

Nürnberg, G. K. and Dillon, P. J.: Iron budgets in temperate lakes, Can. J. Fish. Aquat. Sci., 50, 1728–1737, https://doi.org/10.1139/f93-194, 1993.

Österreicher, A., Weber, G., Leuenberger, M. and Nicolussi, K.: Exploring blue intensity-comparison of blue intensity and MXD data from Alpine spruce trees, TRACE–Tree Rings Archaeol. Climatol. Ecol., 13, 56–61, doi: 10.2312/GFZ.b103-15069, 2015.

Payette, S.: The range limit of boreal tree species in Québec-Labrador: an ecological and palaeoecological interpretation, Rev. Palaeobot. Palynol., 79, 7–30, doi:10.1016/0034-6667(93)90036-T, 1993.

Pelé, C., Guilminot, E., Labroche, S., Lemoine, G. and Baron, G.: Iron removal from waterlogged wood: Extraction by electrophoresis and chemical treatments, Stud. Conserv., 60, 155–171, doi:10.1179/2047058413Y.0000000110, 2015.

R Core Team: R: A language and environment for statistical computing, available online at https://www.R-project.org/, 2018.

Rydval, M., Larsson, L.-Å., McGlynn, L., Gunnarson, B. E., Loader, N. J., Young, G. H. F. and Wilson, R.: Blue intensity for dendroclimatology: Should we have the blues? Experiments from Scotland, Dendrochronologia, 32, 191–204, doi:10.1016/j.dendro.2014.04.003, 2014.

Rydval, M., Loader, N. J., Gunnarson, B. E., Druckenbrod, D. L., Linderholm, H. W., Moreton, S. G., Wood, C. V. and Wilson, R.: Reconstructing 800 years of summer temperatures in Scotland from tree rings, Clim. Dyn., 49, 2951–2974, doi:10.1007/s00382-016-3478-8, 2017.

Sheppard, P. R.: Overcoming extraneous wood color variation during low-magnification reflected-light image analysis of conifer tree rings, Wood Fiber Sci., 31, 106–115, 1999.

Sheppard, P. R. and Wiedenhoeft, A.: An advancement in removing extraneous color from wood for low-magnification reflected-light image analysis of conifer tree rings, Wood Fiber Sci., 39, 173–183, 2007.

St. George, S. and Esper, J.: Concord and discord among Northern Hemisphere paleotemperature reconstructions from tree rings, Quat. Sci. Rev., 203, 278–281, doi:10.1016/j.quascirev.2018.11.013, 2019.

Tessier, A., Campbell, P. G. C. and Bisson, M.: Sequential extraction procedure for the speciation of particulate trace metals, Anal. Chem., 51, 844–851, doi:10.1021/ac50043a017, 1979.

Wang, F., Arseneault, D., Boucher, É., Galipaud Gloaguen, G., Deharte, A., Yu, S., Troukechout, N.: Temperature sensitivity of blue intensity, maximum latewood density, and ring width data of black spruce tree rings in the eastern Canadian taiga, Dendrochronologia, 64, 12577, https://doi.org/10.1016/j.dendro.2020.12577, 2020

Wang, L., Payette, S. and Bégin, Y.: 1300-year tree-ring width and density series based on living, dead and subfossil black spruce at tree-line in Subarctic Quebec, Canada, The Holocene, 11(3), 333–341, doi:10.1191/095968301674769686, 2001.

Wigley, T. M. L., Briffa, K. R. and Jones, P. D.: On the average value of correlated time series, with applications in dendroclimatology and hydrometeorology, J. Clim. Appl. Meteorol., 23(2), 201–213, doi:10.1175/1520-0450(1984)023<0201:OTAVOC>2.0.CO;2, 1984.

Wilson, R., Rao, R., Rydval, M., Wood, C., Larsson, L.-Å. and Luckman, B. H.: Blue Intensity for dendroclimatology: The BC blues: A case study from British Columbia, Canada, The Holocene, 24, 1428–1438, doi:10.1177/0959683614544051, 2014.

Wilson, R., Anchukaitis, K., Andreu-Hayles, L., Cook, E., D'Arrigo, R., Davi, N., Haberbauer, L., Krusic, P., Luckman, B., Morimoto, D., Oelkers, R., Wiles, G. and Wood, C.: Improved dendroclimatic calibration using blue intensity in the southern Yukon, The Holocene, 29, 1817–1830, doi:10.1177/0959683619862037, 2019.

Wilson, R., Anchukaitis, K., Briffa, K., Büntgen, U., Cook, E., D'Arrigo, R., Davi, N., Esper, J., Frank, D., Gunnarson, B., Hegerl, G., Klesse, S., Krusic, P., Linderholm, H., Myglan, V., Peng, Z., Rydval, M., Schneider, L., Schurer, A., Wiles, G., Zorita, E.: Last millennium northern hemisphere summer temperatures from tree rings: Part I: The long term context, Quat. Sci. Rev. 134, 1–18, https://doi.org/10.1016/j.quascirev.2015.12.005, 2016.

Yang, K. C.: Growth ring contrast enhancement and the differentiation of sapwood and heartwood zones, Wood Fiber Sci., 19, 339–342, 2007.

Zang, C. and Biondi, F.: treeclim: an R package for the numerical calibration of proxy-climate relationships, Ecography, 38, 431–436, doi:10.1111/ecog.01335, 2015.

Zaw, M. and Chiswell, B.: Iron and manganese dynamics in lake water, Water Res., 33, 1900–1910, doi:10.1016/S0043-1354(98)00360-1, 1999.

Zhang, J., Xi, S.: Research on the decoloration of waterlogged bamboo slips. Sci. Conserv. Archaeol. 15, 37–42, 2003. In Chinese with English abstract.

2.10 Tables

Table 2-1: Basic chemical properties of the seven chemical solutions.

Code	Chemical components	Chemical property	pH
NaAsc	2% sodium ascorbate	reduction	7
HAc	2% acetic acid	acidity	3
EDTA	2% disodium EDTA	chelation & acidity	5
HAsc	2% ascorbic acid	reduction & acidity	3
MixA	2% ascorbic acid + 2% disodium EDTA	reduction, chelation & acidity	4
MixB	2% sodium ascorbate + 2% disodium EDTA	reduction & chelation	7
MixC	2% sodium dithionite + 2% disodium EDTA	reduction, bleaching & chelation	7

All solutions were diluted using de-ionized water with no trace of Fe concentration. Concentrations are in v/v for HAc and in w/v for other solutions. EDTA: Ethylenediaminetetraacetic acid. Values of pH were estimated using pH test papers.

Table 2-2: Definitions of wood color intensities and tree-ring parameters used in this study.

No.	Parameter	Definition
1	earlywood & latewood RGB intensities*	Mean R, G, and B intensities from all pixels of earlywood or latewood (see Fig. 2-S6), averaged from all tree rings of each wood lath.
2	wood RGB intensities*	Mean RGB intensities averaged from earlywood and latewood RGB intensities.
3	delta RGB intensities	Earlywood RGB intensities subtracted from corresponding latewood RGB intensities.
4	LBI*	Mean blue intensity of 30% of the darkest pixels in latewood (Fig. 2-S6).
5	DBI	Raw LBI (measured from 30% of the darkest pixels) subtracted from raw earlywood BI (measured from 100% of pixels), automatically derived from CooRecorder 8.0 for each tree ring.
6	MXD	The maximum value of measured tree-ring latewood density.

The RGB intensities refer to the color intensities measured separately for the red (R), green (G), and blue (B) channels. The parameters No.1–3 are used to quantify wood colors, while the parameters No. 4–6 are conventional dendrochronological parameters. *: data were inverted by subtracting the raw data from a value of 256.

2.11 Figures

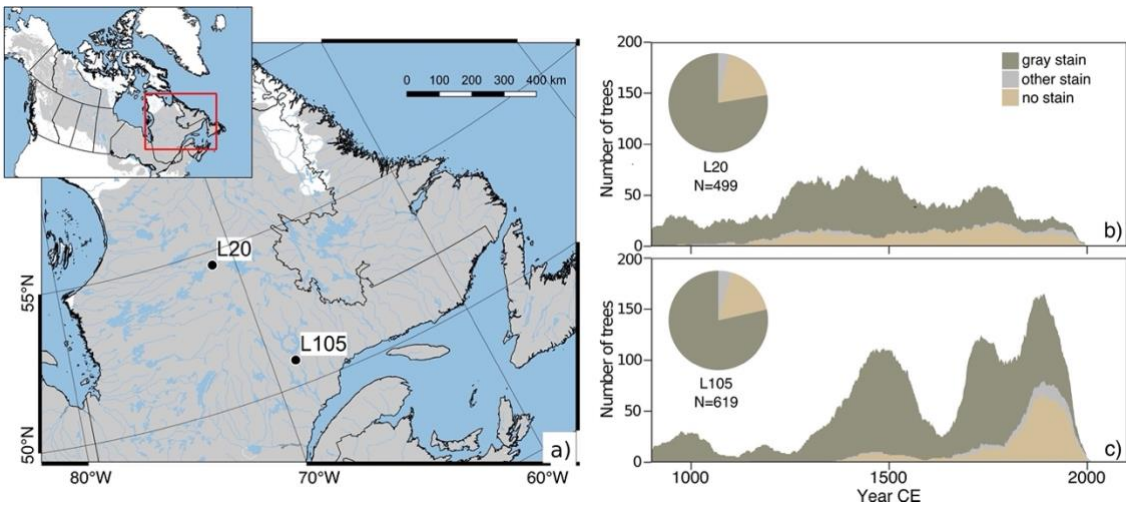

Figure 2-1: Location of the two studied lakes (a), and frequency of cross-dated LSTs according to staining at L20 (b) and L105 (c). The gray shading in (a) corresponds to the distribution range of black spruce, map source available at https://www.fs.fed.us/database/feis/pdfs/Little/aa_SupportingFiles/LittleMaps.html, last access: 15 September 2020. The "other stain" category includes a variety of additional colors such as red or dark brown.

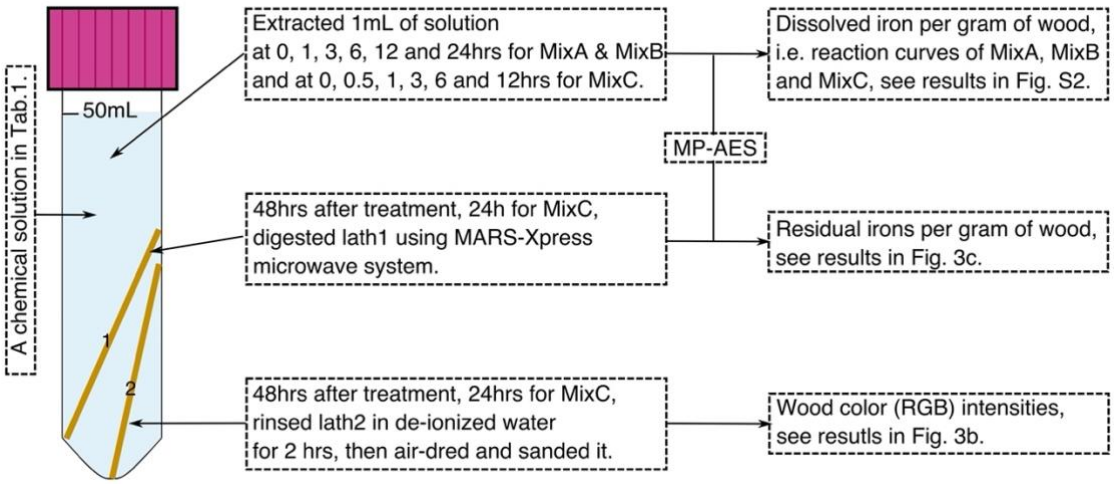

Figure 2-2: Diagram of one chemical destaining experiment for one pair of wood laths from the same subfossil tree in a Falcon® 50mL tube. MP-AES: microwave plasma-atomic emission spectrometer, Agilent 4200.

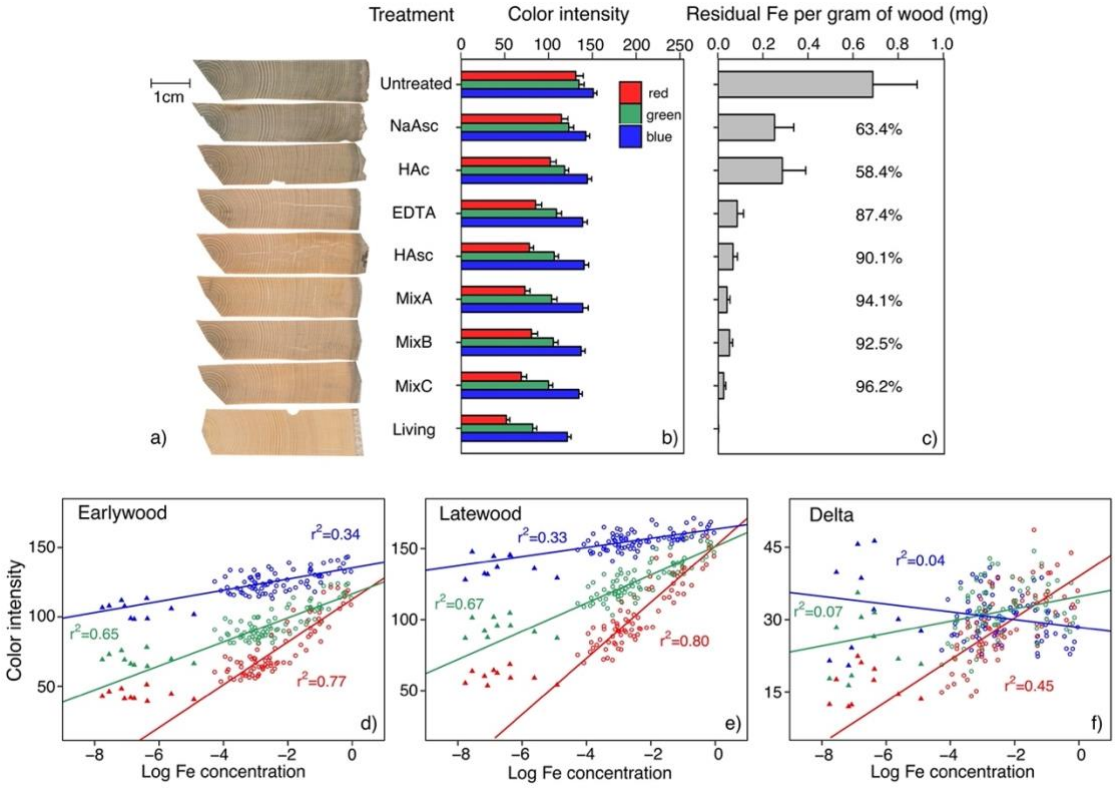

Figure 2-3: Residual iron (Fe) and wood RGB intensities (see definitions in Table 2-2) of LST laths treated with seven chemical reagents. Panel (a) shows examples of treated laths from one LST sample and one living tree sample (last row). The gray outer part of the example LST is discolored due to decay. Panel (b) shows the mean wood RGB intensities according to treatment. Panel (c) shows the mean concentrations of residual Fe according to treatment. Error bars in (b) and (c) refer to standard deviations of corresponding group. Percentages in (c) refer to the Fe removed by destaining treatments relative to the Fe concentrations of untreated stained LSTs. Panels (d)–(f) show the linear regressions of earlywood, latewood and delta RGB intensities against the log of residual Fe. Regressions are based only on the LST data (circles). Living-tree data are plotted as triangles but are excluded from the regressions.

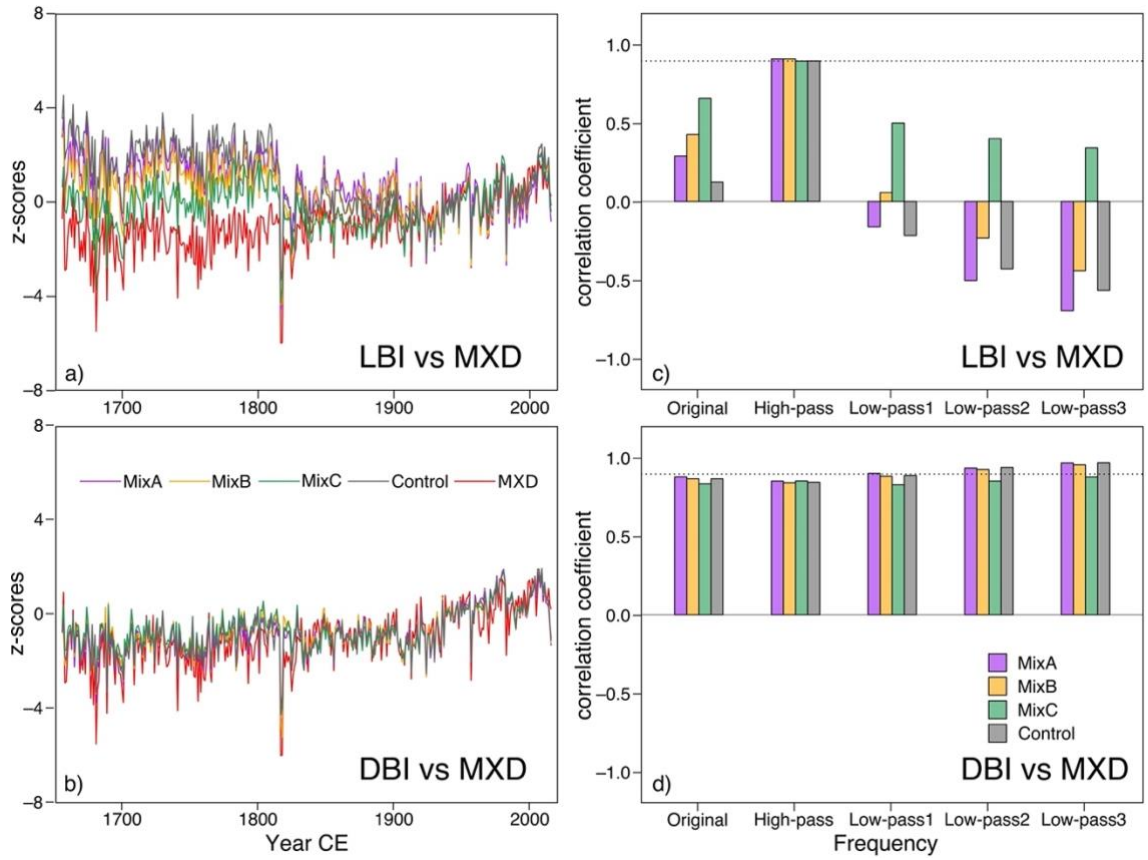

Figure 2-4: Comparisons of LBI (a, c) and DBI chronologies (b, d) for the MixA, MixB, MixC and Control treatments against the reference MXD chronology. In (a) and (b), chronologies are transformed to z-scores relative to the 1901–2015 time interval. Panels (c) and (d) show correlations of LBI and DBI chronologies against MXD chronology at different timescales. Original: the original RCS standardized chronologies; high-pass: 10-year high-pass filtered series; low-pass1, 2 and 3: 10-year, 50-year and 100-year low-pass series filtered using the Butterworth filter. Dotted horizontal lines in the right panel show the correlation (r = 0.89) between the high-pass filtered LBI and MXD chronology.

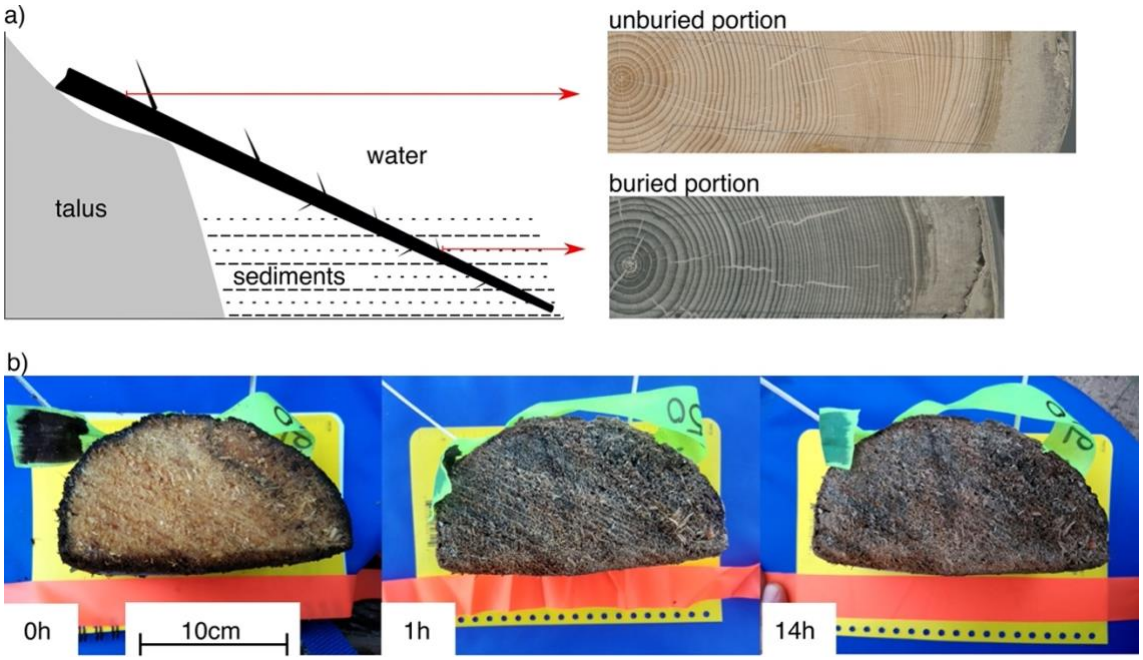

Figure 2-5: Schema of different cross-sectional colors from the buried and exposed cross sections of the same partially buried tree (a), and field observations of cross-sectional color changes after a fresh disc was cut from a buried tree and exposed to air (b).

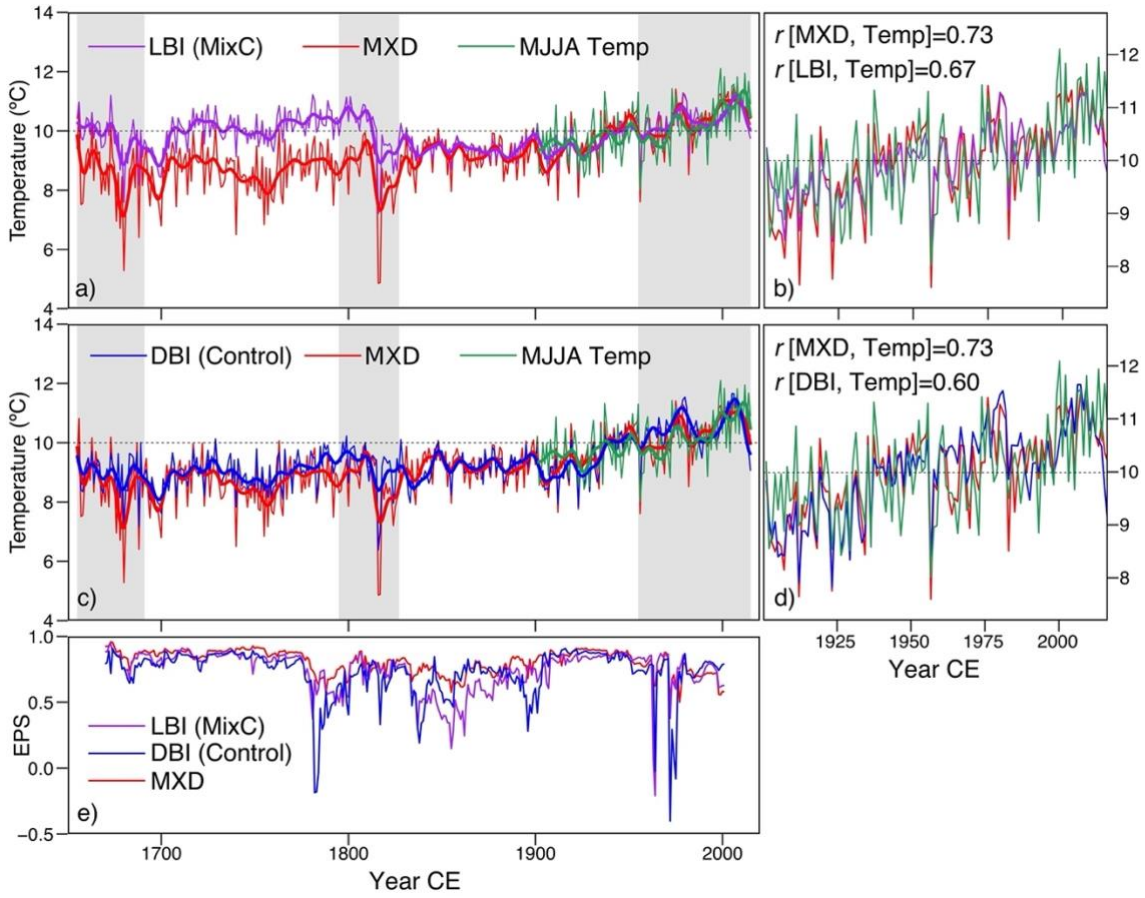

Figure 2-6: Temperature reconstructions using the LBI chronology for the MixC protocol (purple), the Control DBI chronology (blue), and the reference MXD chronology (red) for the 1655–2015 (a, c) and 1901–2015 (b, d) time intervals. Panel (e) shows the 1-year-lag moving EPS computed in 31-year windows. EPS of the reference MXD was averaged from MXD chronologies of four different treatments (Fig. 2-S9). Thick smooth lines denote the 10-year low-pass series filtered using the Butterworth filter. Vertical gray bars show the periods where tree replication is less than 10 (Fig. 2-S3c).

2.12 Supplementary Materials

Supplementary Table

Table 2-S1: Statistics of calibration (1901–1960) and verification (1960–2015) for LBI, DBI and MXD against the May–August temperature target.

	LBI vs Temp	**DBI vs Temp**	**MXD vs Temp**
Full r^2	0.431	0.358	0.528
Calibration r^2	0.427	0.429	0.464
Verification r^2	0.246	0.088	0.443
Verification RE	0.529	0.425	0.632
Verification CE	0.216	0.043	0.388
RMSE	0.112	0.096	0.144

All statistics in the table are significant $p < 0.05$, reduction of error (RE) and coefficient of efficiency (CE) > 0. RMSE: root-mean-square error.

Figure 2-S1: A general view of the staining issue of wet LSTs at the site L105. Note the blue-gray colors of many cross-sections sampled on lake subfossils.

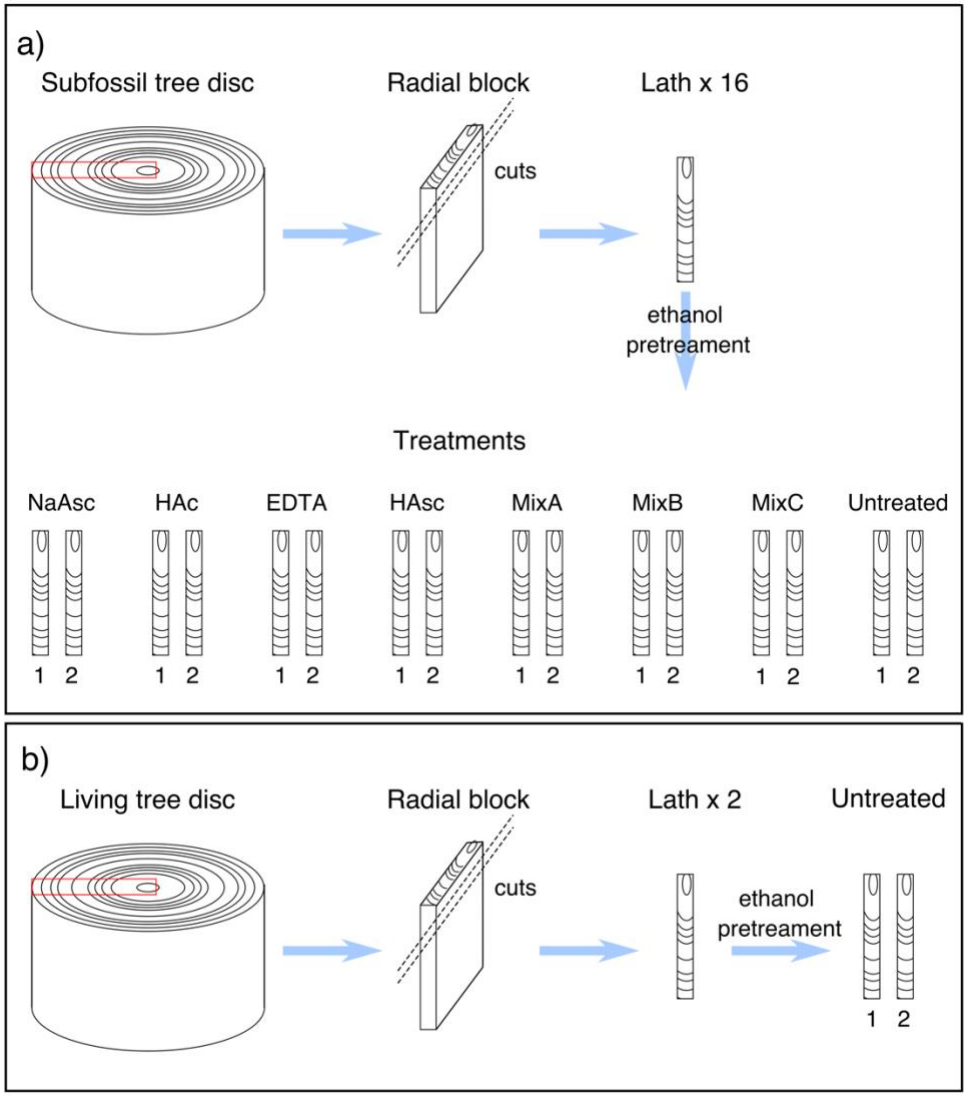

Figure 2-S2: Design of destaining experiments following Section 2.4.2 showing how a subfossil tree replicate (a) and a living-tree replicate (b) were cut into 1mm-thick laths and how these laths were treated using different chemical reagents. Lath 1 and 2 of each pair were used to analyze the residual Fe and wood RGB intensities, respectively. In total, ten subfossil tree replicates and ten living-tree replicates were processed following the corresponding procedure.

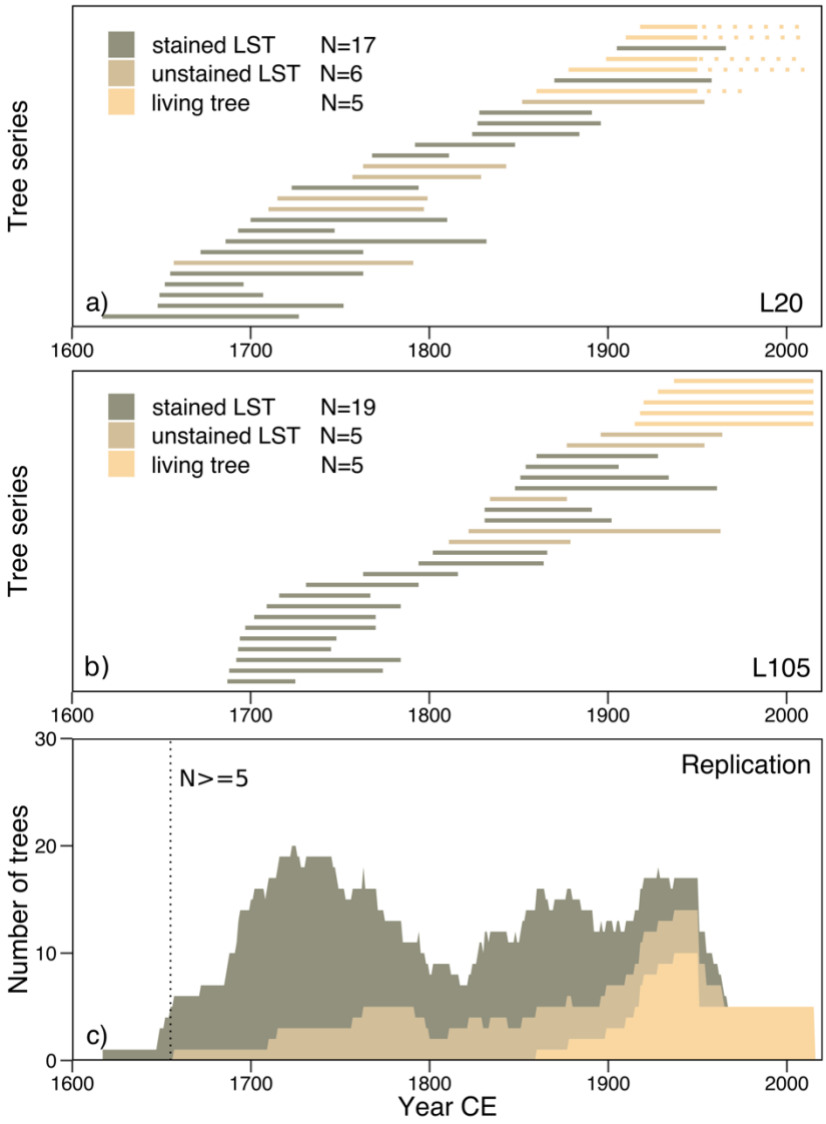

Figure 2-S3: Timespans of tree-ring series used for developing LBI, DBI, and MXD chronologies (a–b), and tree replication of the regional chronology (c). Dotted lines in (a) denote the post-1950 period at L20, for which living-tree data were excluded due to the likely sapwood-heartwood color differences and unhealthy growth of trees. Note that LBI, DBI, and MXD series share the same timespans and chronologies share the same tree replication because we kept only tree rings with measured values for all the three parameters (i.e., LBI, DBI, and MXD).

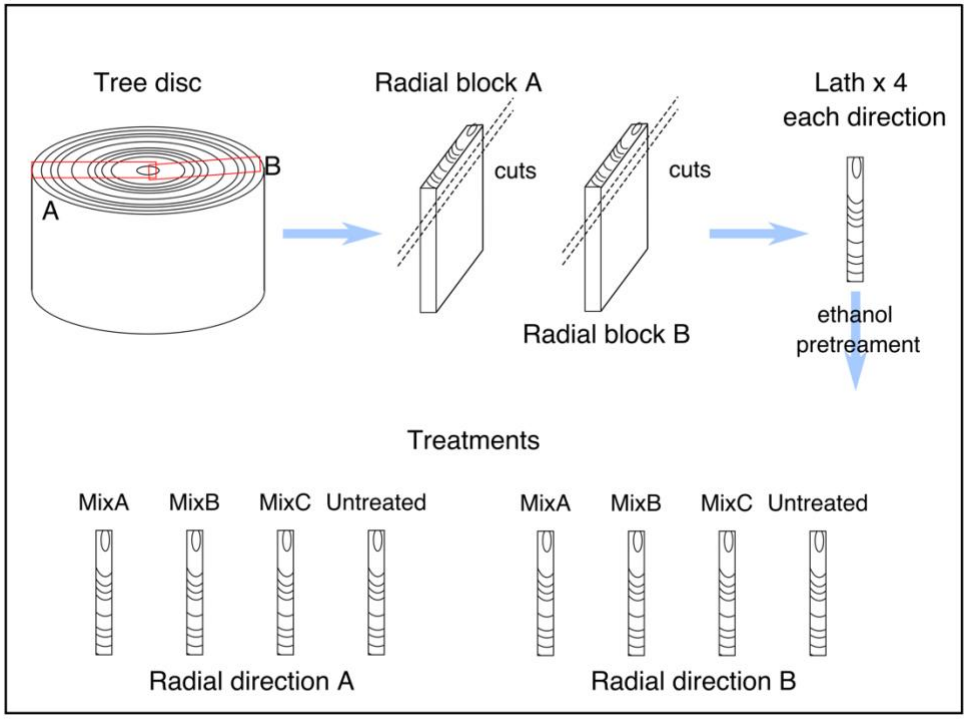

Figure 2-S4: Destaining treatments of selected samples used for dendrochronological assessments following Section 2.4.3 showing how a tree replicate was cut into 1mm-thick laths and how these laths were treated using different chemical reagents. LBI, DBI, and MXD series were measured from each lath after treatments. In total, 57 tree samples from L20 and L105 were processed following this procedure.

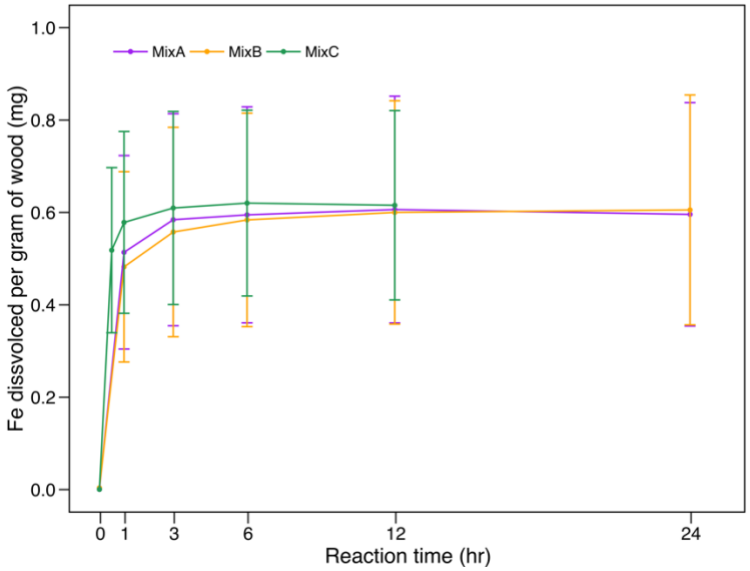

Figure 2-S5: Fe dissolution curves during the MixA, MixB, and MixC treatments. Dots and error bars refer to the mean and standard deviation values, respectively. Note that the reaction curve of MixC was computed from data of 9 LST replicates (10 for MixA and MixB).

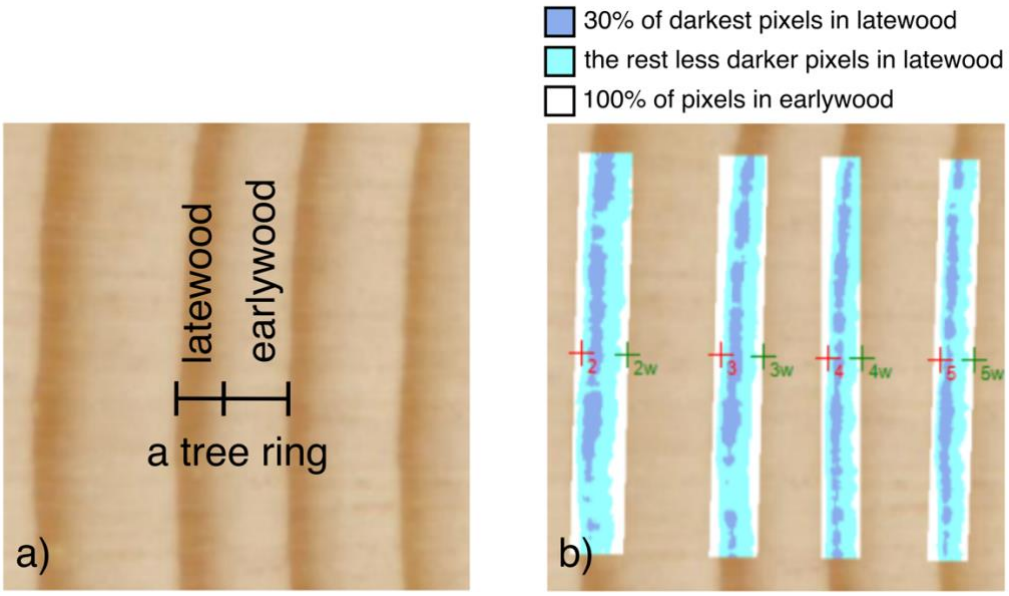

Figure 2-S6: Tree-ring structure (a) and an example of tree-ring color intensity measurement using CooRecorder 8.1 (Cybis Dendrochronology) (b).

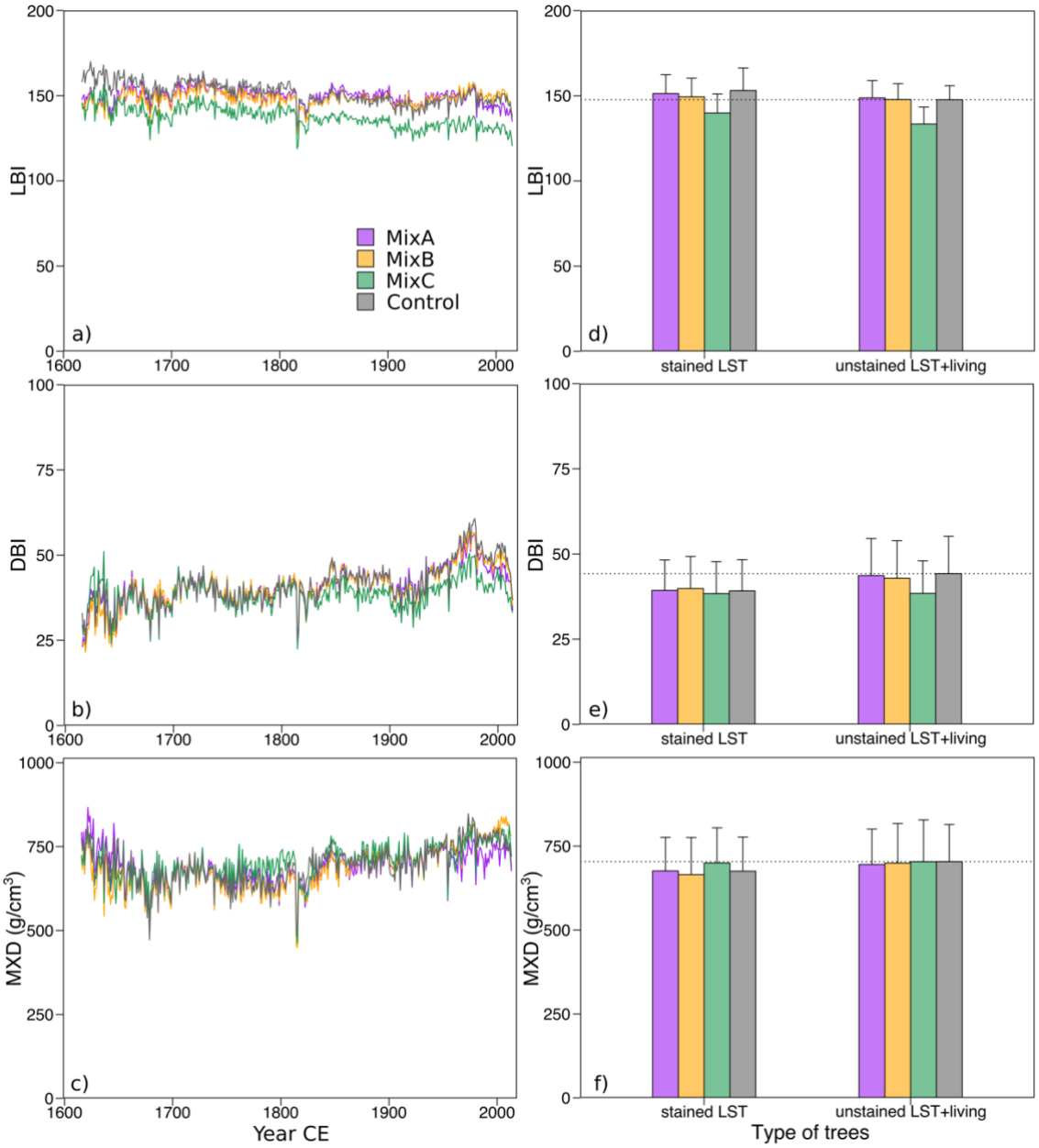

Figure 2-S7: Raw data of LBI, DBI, and MXD of treated (MixA, MixB, and MixC) and untreated (Control) LSTs and living trees. Panels (a)–(c) show the averaged mean value of the series according to calendar years. Panels (d)–(f) show the averaged data (bars) of stained LSTs and unstained LSTs+living trees, along with their standard deviations (error bars). Dotted horizontal lines denote the averaged data of untreated, unstained LSTs+living trees.

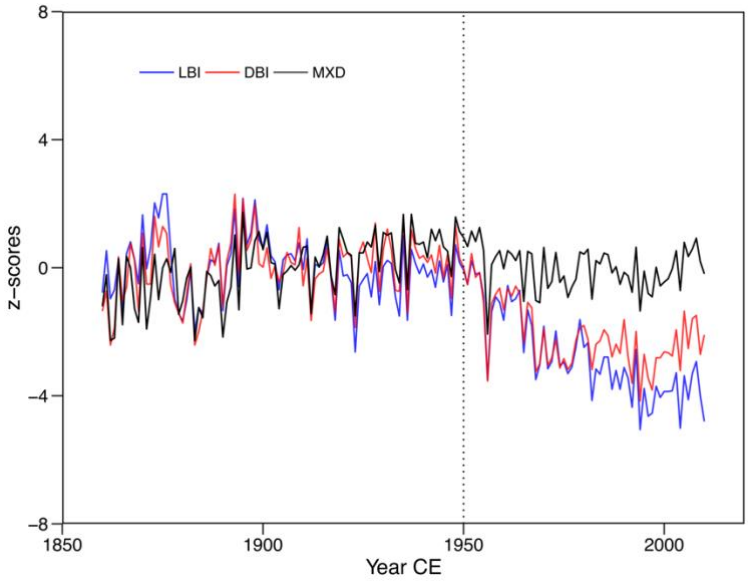

Figure 2-S8: Averaged raw measurements of LBI, DBI, and MXD from five living trees at L20 (untreated with destaining chemicals). Data are transformed to z-scores relative to the 1860–1950 time interval. Dotted vertical line denotes the approximate onset (1950) of BI divergence relative to MXD data.

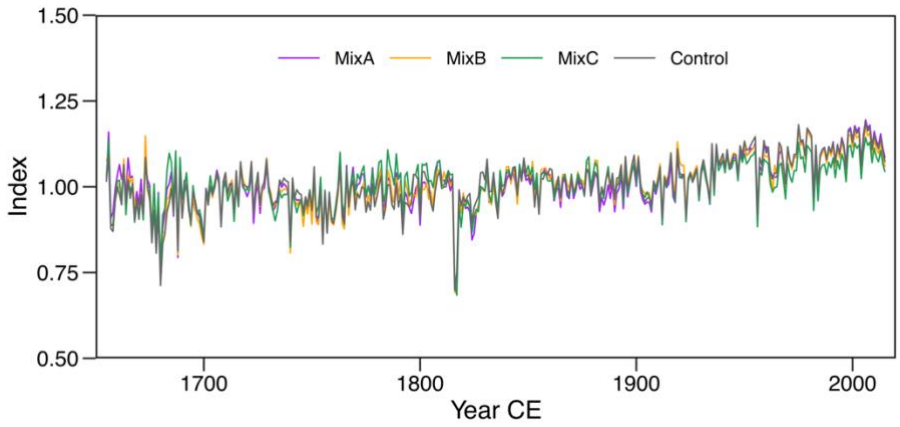

Figure 2-S9: MXD regional chronologies for the MixA, MixB, MixC, and Control treatments.

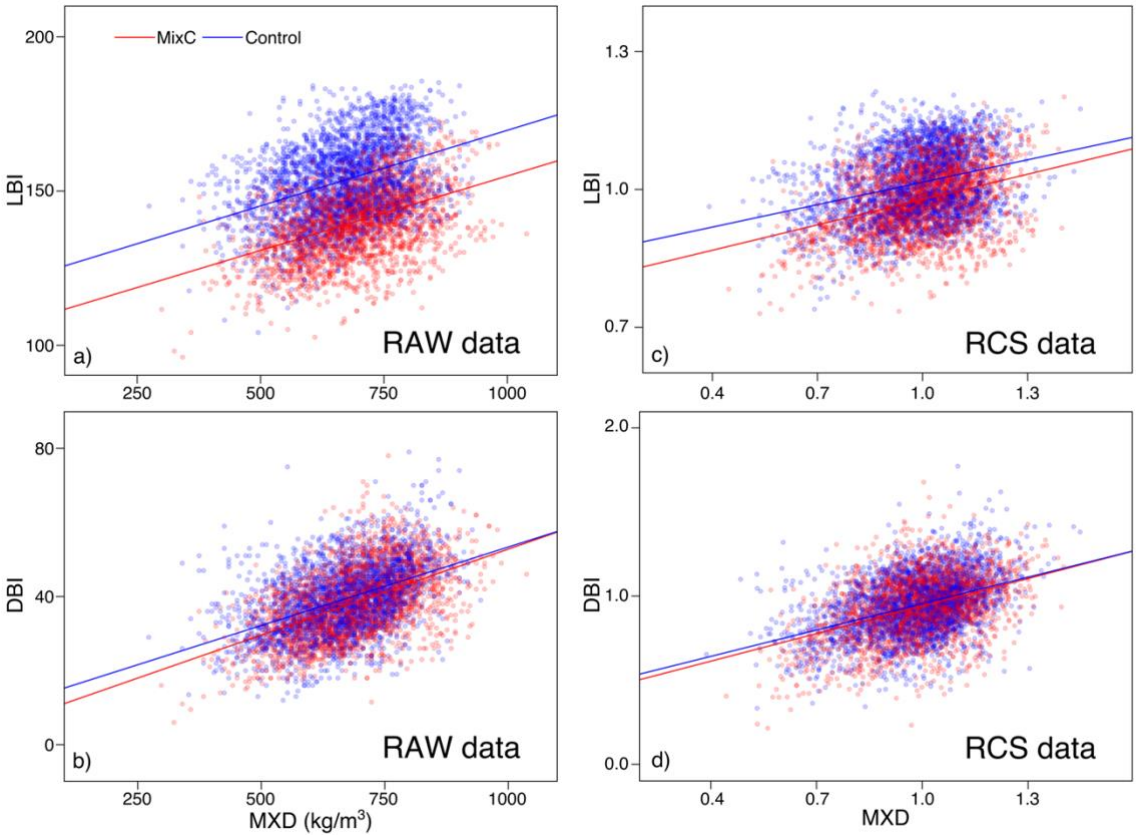

Figure 2-S10: Comparisons of LBI (a, c) and DBI (b, d) against MXD data for the MixC treated and Control stained LSTs. Comparisons are based on raw data (left panel) and RCS standardized data (right panel). Straight lines are linear regressions between BI and MXD data.

CHAPITRE III

NORTH AMERICAN MILLENNIAL TEMPERATURES FROM TREE-RING DENSITY DATA

Feng Wang[a*], Dominique Arseneault[a], Étienne Boucher[b], Fabio Gennaretti[c], Shulong Yu[d], Tongwen Zhang[d]

a. Département de Biologie, Chimie et Géographie, Centre d'Études Nordiques, Université du Québec à Rimouski, Rimouski, G5L 3A1, Canada
b. Département de Géoscience, GEOTOP, and Centre d'Études Nordiques, Université du Québec à Montréal, Montréal, H3A 0B9, Canada
c. Groupe de Recherche en Écologie de la MRC-Abitibi, Institut de Recherche sur les Forêts, Centre d'Étude de la Forêt, Université du Québec en Abitibi-Témiscamingue, Amos, J9T 2L8, Canada
d. Key Laboratory of Tree-ring Ecology of Uigur Autonomous Region and Key Laboratory of Tree-ring Physical and Chemical Research, Institute of Desert Meteorology, China Meteorological Administration, Urumqi, 830002, China

To be submitted

3.1 Résumé

Le troisième chapitre de ma thèse, intitulé « *Températures millénaires nord-américaines à partir de données de densité des cernes des arbres* » a été co-écrit par Feng Wang, Dominique Arseneault, Étienne Boucher, Fabio Gennaretti, Shulong Yu et Tongwen Zhang. En tant qu'auteur principal du manuscrit, j'ai participé à la collecte des échantillons de bois et des données de densité des cernes, à l'analyse statistique et à la production des figures et du manuscrit. Les professeurs Dominique Arseneault et Étienne Boucher ont conçu, supervisé et révisé cette recherche. Le professeur Fabio Gennarreti a guidé les reconstructions bayésiennes de température et a aidé à interpréter les résultats de ce chapitre. Shulong Yu et Tongwen Zhang ont contribué à la collecte et à la préparation des échantillons ainsi qu'à la mesure des données. En fonction des résultats des deux chapitres précédents, nous avons choisi dans le troisième chapitre la densité maximale du bois final pour reconstituer les températures estivales millénaires dans la péninsule du Québec-Labrador. Nous avons cherché à mieux comprendre la variabilité régionale des températures estivales et les mécanismes de forçage externes au cours du dernier millénaire.

Bien que la densité maximale du bois final soit le proxy le plus sensible pour reconstituer les températures estivales avec une résolution annuelle, seulement 12 de ces reconstitutions recouvrent le dernier millénaire, et 11 d'entre elles sont regroupées en Eurasie. Nous utilisons les mesures de densité de 1294 arbres subfossiles et vivants pour reconstituer les températures estivales du dernier millénaire pour un grand domaine spatial du nord-est de l'Amérique du Nord. Notre étude indique un optimum climatique médiéval et un Petit Âge Glaciaire bien définis, suivi par un taux de réchauffement centenaire sans précédent au cours des 100 dernières années. Un total de 29 épisodes extrêmement froids peut être attribués à de fortes éruptions volcaniques avec une persistance plus longue pour les éruptions tropicales qu'extratropicales. Ces variations climatiques forcées ont dépassé la variation climatique interne à l'échelle régionale.

3.2 Abstract

The third chapter of my thesis, entitled *North American millennial temperatures from tree-ring density data*, was co-authored by Feng Wang, Dominique Arseneault, Étienne Boucher, Fabio Gennaretti, Shulong Yu, and Tongwen Zhang. As the principal author of the manuscript, I participated in collection of wood samples and tree-ring density data, statistical analysis, and production of figures and the manuscript. Professors Dominique Arseneault and Étienne Boucher conceived, supervised, and reviewed this research. Professor Fabio Gennarreti guided the Bayesian temperature reconstructions and helped to interpret the outputs of this chapter. Shulong Yu, and Tongwen Zhang contributed to sample collection and preparation, and data measurements. According to the results of the previous two chapters, in the third chapter we chose maximum latewood density to reconstruct millennial summer temperatures in the Québec-Labrador Peninsula. We aimed to better understand the regional summer temperature variability and the associated external forcing mechanisms over the last millennium.

Although maximum latewood density is the most sensitive tree-ring proxy for reconstructing summer temperatures with annual resolution, only 12 such reconstructions span the last millennium, with 11 of them clustered in Eurasia. Here, we use density measurements from 1, 294 subfossil and living trees to reconstruct last millennium summer temperatures for a large spatial domain in Northeastern North America. Our study indicates well-defined Medieval Warm Period and Little Ice Age, followed by an unprecedented centennial warming rate during the last 100 years. A total of 29 extremely cold episodes could be attributed to strong volcanic eruptions with a longer persistence for tropical than extratropical eruptions. These forced climate variations overwhelmed the internal climate variability at the regional scale.

3.3 Introduction

Millennial temperatures reconstructed from climate proxies provide crucial historical insights into Earth's climate variability, as well as benchmarks for quantifying the recent warming and evaluating the realism of climate model simulations (*1–3*). Annually resolved tree rings are the backbone of temperature reconstructions at the scale of the Common Era (*4*), and maximum latewood density (MXD) is the most sensitive proxy for reconstructing summer temperatures (*5–8*). However, only 12 MXD chronologies have so far allowed reconstructing summer temperatures back to 1000 CE, with 11 of them clustered in Eurasia (Table 3-S1), leading to a well-known gap of MXD-based temperature reconstruction in North America (*8–10*) (Fig 3-1A). Due to this data gap, large uncertainties persist in the millennial history of summer temperatures across the Northern Hemisphere, as well as on the impact of explosive volcanism—a primary driver of Earth's climate variability (*11, 12*). For example, it is recently suggested that Northern Hemisphere extratropical (NHET; 30–90ºN) eruptions may trigger a stronger peak of hemispheric summer cooling compared to tropical eruptions with similar stratospheric sulfur injection (*13*). However, the duration of the post-eruption cooling effect, and how it varies across the Northern Hemisphere as a function of eruption types, remain largely unknown.

3.4 Results and discussion

We performed an unprecedented number of MXD measurements, from 1,249 black spruce (*Picea mariana* (Mill.) B.S.P.) lake subfossil logs and adjacent lakeshore living trees, to build three well-replicated millennial chronologies (Fig. 3-S1) in the boreal forest of Northeastern North America (hereafter the NENA region; Fig. 3-1A; Table 3-S2). The existing, but shorter (1363–1989 CE) and less replicated Quex dataset (45 trees) was added to our network (Fig. 3-1A; Supplementary Materials). Overall, this large and unique dataset is robust, with a yearly replication >30 trees since 900 CE (Fig. 3-2A; Fig. 3-S2). We first developed an MXD-based summer (May–August, MJJA) temperature reconstruction for the

772–2017 CE period (hereafter D-STREC; Fig. 3-2B; see Materials and Methods). Correlation with the MJJA temperature target (CRU TS4.03 (*14*), hereafter CRU) reaches 0.75 (Pearson's *r*, $P < 0.001$) over 1905–2006 CE and remains stable in two subintervals (Fig. 3-2D). A two-century historical record in southern Québec (Materials and Methods) extends the period of verification, correlating at 0.39 and 0.62 ($P < 0.001$; 1837–2006 CE) with D-STREC at interannual and decadal timescales, respectively, even if this record was developed ~450–1400 km away from the sites of our network (Fig. 3-1A). The spatial domain of D-STREC ($r \geq 0.3$ with CRU MJJA temperatures) covers the northeastern half of North America and has a striking resemblance with the correlation field of the regional MJJA temperature target, even outside North America (Fig. 3-1B, E). Compared to a previous temperature reconstruction (*15*) using tree-ring widths plus $\delta^{13}C$ and $\delta^{18}O$ time series from tree-ring cellulose (3P-STREC), the D-STREC reconstruction skill is substantially improved (Table 3-S3), with a much larger spatial domain (Fig. 3-1), due to the enhanced sensitivity of MXD data to high-frequency temperature variability ($r_{\text{D-STREC}} = 0.72$ vs. $r_{\text{3P-STREC}} = 0.40$ versus the 10-yr high-pass temperature target) (*5*, *6*). Furthermore, D-STREC agrees almost perfectly with the historical record at 1816 CE following the 1815 CE Tambora eruption (Fig. 3-S3), while 3P-STREC underestimates this cooling by ~2.5ºC, indicating that volcanic cooling can be reliably recorded by our MXD data.

We then combined these two independent reconstructions to yield a four-proxy summer temperature reconstruction spanning 997–2006 CE (hereafter 4P-STREC; Fig. 3-2C). Compared to D-STREC, 4P-STREC accounts for a higher fraction of the regional MJJA temperature variance (60%; $r = 0.77$ during 1905–2006 CE), with 96% of the CRU observational target constrained within the 95% confidence interval (the 95% CI in Fig. 3-2C). 4P-STREC is less prone to proxy-level uncertainties than 3P-STREC and D-STREC (Fig. 3-S4), and provides the most informative summer temperature variability for NENA over the past 1000 years.

4P-STREC shows that the strongest centennial warming of the last millennium occurred during the twentieth century (1904–2003 CE; with a linear trend of 0.16 ± 0.02 ºC per decade), with a temperature rise more than twice as fast as any other non-overlapping 100-year period (Table 3-S4). Furthermore, 1997–2006 CE was the warmest decade of the last millennium (1.0ºC above the 1905–2006 average). Relatively warm summers also occurred during the Medieval Climate Anomaly (~997–1250 CE), with seven out of the 10 warmest decades clustered between 997 and 1250 CE (Table 3-S4). Medieval summers were, on average, 0.25ºC warmer than the 1905–2006 average. Conversely, the Little Ice Age (~1251–1930 CE) was relatively cold (−0.27 ºC with respect to (w.r.t.) 1905–2006 CE), especially during 1601–1930 CE (−0.44 ºC). Nine out of the 10 coldest decades and half of the 32 coldest summers (≤ mean−2 standard deviation (SD)) were clustered in the second half of the Little Ice Age after ~1601 CE (Tables 3-S5, S6; Fig. 3-2C).

Short-term cold episodes were closely related to tropical explosive volcanic eruptions. The 1815 CE Tambora eruption resulted in the coldest summer (1816 CE, −3.83ºC w.r.t. 1905–2006 CE), and the coldest decade (1816–1825 CE, −1.51ºC) of the last millennium. Other large tropical eruptions, such as the Kuwae (1457 CE?), Huaynaputina (1600 CE), Parker (1640 CE), Cosiguina (1835 CE), and Santa Maria (1902 CE) events, were each followed by very cold decades (Table 3-S6). Conversely, the 1257 eruption of Samalas, the most sulfur-rich eruption of the Common Era (*12*) and often associated with a pronounced summer cooling in Europe (*16*), only produced a weak cooling anomaly of −0.65ºC (w.r.t. 1905–2006 CE) at 1258 CE. As suggested by Guillet *et al*. (*17*), the cooling effect of Samalas might have been dampened by a positive phase of El Niño-Southern Oscillation, in this particular region.

Out of the 32 coldest summers reconstructed by 4P-STREC, 13 and 16 years could be attributed to tropical and NHET eruption events, respectively (Fig. 3-2C; Table 3-S5). However, tropical eruptions induced longer cooling episodes than did NHET eruptions. Superposed epoch analysis (see Materials and Methods) indicates that, on average, tropical

eruptions caused a ~10-year significant cooling, followed by an additional ~2-year recovery to the pre-eruption level (Fig. 3-3A). The cooling peak generally lagged the tropical eruptions by one year (Fig. 3-3A; Fig. 3-S5A). In contrast, the cooling effect of NHET eruptions lasted only ~1–3 years and was most frequently significant at the year of the eruption (Fig. 3-3B; Fig. 3-S5B). Analyses on NHET reconstructions and simulations (Fig. 3-S6) confirm the consistency of these results across the Northern Hemisphere. Stratospheric aerosols injected by tropical volcanoes spread poleward with a residence time of 1–3 years (*18*, *19*), while aerosols of NHET eruptions are mainly constrained to 30–90ºN with a shorter lifetime (*20*, *21*). Because tropical eruptions influence a larger oceanic domain with high thermal capacity (*19*, *22*), ocean–atmosphere heat exchanges can cool continental summers (*23*) beyond the direct aerosol forcing, in a more persistent way, compared to NHET eruptions (Fig. 3-3). Both D-STREC and 4P-STREC reveal similar responses to the two eruption types (Fig. 3-S7). Conversely, 3P-STREC shows a cooling peak that lags the tropical eruption by about 9 years and no significant cooling following NHET eruptions. This behavior most likely results from the strong biological memory of ring-width data (*5*), the only high-frequency component of 3P-STREC.

Although 4P-STREC was developed from a limited sector of NENA, it behaves like a large-scale, NHET temperature reconstruction at the multidecadal (20-yr) time scale. The smoothed 4P-STREC correlates significantly with five NHET tree-ring-based summer temperature reconstructions (r = 0.32–0.63, P < 0.005), which are mostly dominated by Eurasian tree-ring data (*6*, *24–26*) (Fig. 3-4A). Furthermore, the warm and cold epochs of 4P-STREC correspond well with an ensemble of 25 full-forcing simulations of MJJA temperatures (averaged over land 30–90ºN) from global climate models (the Coupled Model Intercomparison Project Phase 5/Paleoclimate Model Intercomparison Project Phase 3 protocol (*27*); hereafter referred to as CMIP5; Fig. 3-4B). The correlation with the hemispheric CMIP5 multi-model mean during 997–2000 CE (r = 0.58, P < 0.001) exceeds those between 4P-STREC and four out of the five NHET reconstructions, and even surpasses the correlations between two NHET reconstructions and the multi-model mean (Fig. 3-4C).

By averaging 25 members, the CMIP5 multi-model mean largely masks out the unforced internal variability (*28, 29*). Thus, the relatively high correlations among 4P-STREC and NHET reconstructions and simulations imply that externally forced climate variations produce a strong imprint at both hemispheric and regional scales, and that the internal climate variability does not blur these forced climate variations in the NENA sector. Comparison of 4P-STREC with single-forcing simulations of NHET land summer temperatures points toward volcanism as the main forcing synchronizing NENA and hemispheric summer temperatures (Fig. 3-S8). Consequently, in conformity with Mann *et al.* (*30*) and several detection and attribution studies on hemispheric and global millennial temperatures (*2*, *31*), our study considerably downgrades the importance of self-oscillatory mechanisms and raises the role of volcanism in shaping NENA's multi-decadal summer temperature variability.

3.5 Materials and methods

3.5.1 MXD network and chronology development

Our MXD network consists of series from 1,668 radii of 1,294 black spruce (*Picea mariana* (Mill.) B.S.P.) trees from four sites across the eastern Canadian boreal forest (Fig. 3-1A; Table 3-S2), an extratropical region with typically cold/long winters, and warm/short summers. L105, L20, and L135 are three newly sampled sites. To ensure data homogeneity (*32, 33*), we sampled living trees from the lakeshore forests of corresponding lakes where subfossils were collected. New MXD data from these sites were measured from 1–2 radii of each sample using the X-ray densitometric technique (see Wang *et al.* (*34*) for details). Dating of millennial chronologies at these three sites were validated using a sample showing globally coherent cosmogenic ^{14}C signature at 774 CE (*35*). The existing Quex dataset was obtained from the NOAA International Tree Ring Data Bank (Table 3-S2) and was corrected for its erroneous location in the metadata and for the cross-dating of one sample (Supplementary Text S1). All MXD measurements were averaged by tree before subsequent analysis.

After comparing three standardization methods, including the widely applied regional curve standardization (*36*), the regionally constrained individual signal-free standardization (RSFi) (*37*) method was selected to detrend the MXD series at each site (see Supplementary Texts S2, S3). The RSFi method efficiently removed non-climatic signals (e.g., local competition and disturbances) introduced by trees established in different eras, while preserving the long-term variability. In addition, because the MXD series of black spruce trees are known to exhibit heteroscedastic variance (*38*), we compared chronologies calculated from ratios and residuals plus power-transformation (*39*) via a simple linear-scaling approach (*40*). The RSFi ratio chronologies were chosen for final temperature reconstructions, due to better overall performance (Supplementary Text S2). Chronology characteristics were assessed by the expressed population signal (*41*), rbar, and mean cambial age (Fig. 3-S2).

3.5.2 MJJA temperature reconstruction

Two MXD-based summer temperature reconstructions (D-STREC and 4P-STREC) were developed using a Bayesian linear regression approach (see details in Supplementary Text S4) (*15*). Compared to conventional reconstruction methods, the Bayesian approach provides posterior distributions of the climate variable taking into account individual proxy likelihoods, thus enabling comprehensive uncertainty assessments and improving the reconstruction skills (Fig. 3-S9). MXD and other proxies (ring width (*33*), $\delta^{18}O$ (*42*), and $\delta^{13}C$ (*15*)) showed optimal temperature responses over the MJJA season (Fig. 3-S10). Therefore, regional MJJA temperatures were averaged over an area covering our data network (50º–60º N, 65º–77º W) from the CRU TS4.03 dataset (*14*) (Fig. 3-1A; data obtained from KNMI Climate Explorer: https://climexp.knmi.nl/), and the full calibration period was set to 1905–2006 CE. D-STREC is based on four local MXD chronologies and was limited to the 772–2017 period to ensure the reconstruction robustness, based on EPS > 0.85 and replication > 15 trees (Fig. 3-S2; Fig. 3-S2A). Calibration of the local MXD chronology at the site Quex was limited to the 1905–1989 period, due to the shorter time coverage.

In order to develop the 4P-STREC reconstruction, we combined the median of D-STREC reconstruction posteriors, with millennial ring width, $\delta^{18}O$, and $\delta^{13}C$ series available over 997–2006 CE. Specifically, the input ring-width data are the medians of local chronologies (1,932 trees) from six sites, including L20 (*33*), while isotope data are available only for the L20 site (*15*, *42*). Because individual isotope values were obtained from multi-year wood samples grouped by cohorts, $\delta^{18}O$ and $\delta^{13}C$ chronologies correspond to yearly values smoothed with a 9-year-triangular filter (*15*). Thus, in order to be integrated into the same multiproxy reconstruction, the D-STREC median, ring width, and regional MJJA temperatures were decomposed to low-frequency and high-frequency components using a similar filter. The high-frequency component of ring-width data was not used for the final 4P-STREC because it did not add additional skill to the reconstruction. In the multiproxy Bayesian framework, we first separately developed one multiproxy low-frequency (using four proxies) and one MXD-based high-frequency reconstructions, and then combined them to generate the 4P-STREC. In addition, we reproduced the 3P-STREC reconstruction of Gennaretti *et al.* (*15*), but using the aforementioned new regional MJJA temperature target in order to obtain comparable results. Although 3P-STREC and D-STREC are completely independent by proxy types (no proxy in common) and almost independent by sampling sites (one out of 9 sites in common), the two reconstructions share a relatively high fraction of common low-frequency variability over 997–2006 CE ($r = 0.50$, $P < 0.001$ for the 10-year smoothed series; Fig. 3-2B).

Two types of confidence intervals were calculated for the three reconstructions. The first type (referred to as "95% CI") assesses the uncertainties of the Bayesian model and was derived directly from the 2.5th and 97.5th percentiles of the posterior temperatures for each reconstructed year. The second type (referred to as "95% CI + data uncertainty") additionally considers the time-varying uncertainties in the proxy chronologies. We produced 100 chronologies per proxy with a sampling procedure based on available data points (individual MXD data per site, 6 ring-width chronologies, and a cohort of 5 trees for isotopes). Assuming that data points are normally distributed for each year, the chronologies were built sampling

at each year from a normal distribution $N \sim (\mu, \sigma)$, where μ is the mean of the available data points and σ is the standard error of mean. Fig. 3-S1 illustrates the range of $\pm 1.96 \times$ standard error of mean for the four local MXD chronologies. The 100 chronologies were then included in the Bayesian models for generating alternative D-STREC, 3P-STREC, and 4P-STREC reconstructions. The final "95% CI + data uncertainty" was derived from the 2.5th and 97.5th percentiles of the mixed posteriors from the 100 runs. Differencing the "95% CI + data uncertainty" from the "95% CI" thus allows assessing the sensitivity due to proxy-level uncertainties (Fig. 3-S4).

3.5.3 Historical temperature record

We generated a long MJJA temperature record from a compilation of historical daily temperature observations from the Saint-Lawrence Valley in southern Québec (*43*) (data obtained from http://ncdc.noaa.gov/paleo/study/16336). The historical record was constructed based on multiple observers at Québec City, Montréal, and the Ottawa River region, which are ~450–800km away from our closest site, L105 (Fig. 3-1A). Maximum and minimum temperature data were averaged to represent the daily mean temperatures, which were later aggregated to monthly data. In order to minimize uncertainties due to a high frequency of missing values in the early 19th century, a monthly aggregate for each year was retained only if there were less than eight missing daily values in the corresponding month. The valid temperatures of four months from May to August were then averaged to yield a seasonal (MJJA) temperature record starting from 1805 CE with continuous values since 1837 CE (Fig. 3-2D).

3.5.4 Last millennium temperature simulations

We used 25 full-forcing and 23 single-forcing last-millennium simulations of monthly near-surface air temperatures. The full-forcing CMIP5 simulations include 16 members from the CESM Last Millennium Ensemble (*44*) (CESM-LME; including 3 members of isotope-enabled CESM (*45*)) and 9 members from the CMIP5 Past1000 experiments. The single-forcing simulations were obtained from the CESM-LME runs singly forced by greenhouse

gases, land use, orbital, solar, and volcanic forcing only. In addition, the pre-industrial 850 control run of CESM-LME was used as an unforced baseline to evaluate the correlations between 4P-STREC and the single-forcing simulations. Corresponding climate models and experiments are detailed in Table 3-S8. In order to allow for direct comparisons among models, all model outputs were interpolated to a T21 (~5.6º×5.6º) resolution using the first-order conservative remapping function provided by the Climate Data Operators (*46*). Gridded data were then averaged over land between 30ºN and 90ºN according to area weights, to generate a full-forcing and a single-forcing ensemble of simulated NHET land temperatures for the MJJA season. Although CMIP5 simulations tend to underestimate the impact of NHET eruptions (Fig. 3-S6), this result probably reflects the fact that CMIP5 volcanic forcing differs from the updated datasets we used to select volcanic events (Tables 3-S7, S8).

3.5.5 Correlation analysis and significance test

We used Pearson's correlation to assess the relations among reconstruction, simulation, and climate timeseries. Because strong autocorrelation reduces effective degrees of freedom of timeseries and could bias conventional Student's t-tests (*47*), we adopted the method of PAGES 2k (*2*) to test statistical significance for Pearson's *r*, with a null hypothesis that original timeseries are unrelated. First, we generated 1000 random red-noise timeseries for each original series with the same lag-1 autocorrelation coefficient using the "colorednoise" R package (*48*). The random series were smoothed, if needed, and then correlated against each other, as we did for the original data, to form a distribution of 5×10^5 correlation coefficients for each pair of comparisons. Finally, these distributions were compared with the true Pearson's *r* to calculate probabilities (*P*-values) to test the null hypothesis under a two-sided test. Correlation coefficients are considered significant when *P*-values are smaller than 0.05.

3.5.6 Attribution of cold extremes to volcanic eruptions

The cold extremes of 4P-STREC were attributed to volcanic eruptions according to the Global Volcanism Program (*49*) (GVP; volcanic explosivity index (VEI) ≥ 4) and three ice-

core-based volcanic forcing reconstructions (eVolv2k (*50*), IVI2 (*51*), and ICI (*52*)). A successful match was identified when a cold extreme corresponded to a volcanic event from at least one of the above datasets, allowing a maximum 2-year lag (Table 3-S5). Tropical and NHET eruptions were identified from the corresponding volcanoes provided by GVP (tropical: 30 ºS–30 ºN, NHET: 30–90 ºN) or the ice-core datasets (unidentified events).

3.5.7 Superposed epoch analysis (SEA)

We used a regular SEA approach provided by the algorithm of Rao *et al.* (*53*) to investigate the composite responses to the target volcanic events. First, we constructed a list of tropical and NHET volcanic eruptions (Table 3-S7) according to the stratospheric aerosol optical depth at 550 nm (SAOD) estimated from the eVolv2k reconstruction (1000–1900 CE) (*50*), combined with the CMIP6 dataset (1901–2016 CE) (*54*). The $SAOD_{NHET}$ (area-weighted average over extratropical 30ºN to 90ºN) ≥ 0.03 (~1/3 of the Pinatubo 1991 CE eruption) was used as criteria by which to select tropical and NHET eruptions that have potentially affected the extratropical Northern Hemisphere. We kept all 32 events that corresponded to identified eruptions (VEI ≥ 4) according to the GVP (*49*). The unidentified events were further screened, and were included when also listed in both IVI2 (*51*) and ICI (*52*), by permitting a 3-year lag (*55*). Four events that fulfilled the criteria (Aira 1471 CE, Serua 1693 CE, Unidentified 1808 CE, and Pinatubo 1991 CE) were discarded because of case-specific reasons (see Table 3-S7). In total, 24 tropical and 19 NHET events were retained for the SEA.

The key eruptions years used for the SEA were re-evaluated to minimize potential uncertainties. For unidentified events, we adopted the years adjusted by the latest application of eVolv2k (*13*), which accounted for the time lags between eruptions and ice sheet deposition. The adjustments on 10 tropical events led to a more similar SEA result, compared to that using identified tropical eruptions (Figs. 3-S11A, S12A). In addition, key years were set one year after the year of eruption for events that occurred after August (otherwise assumed in the same year), a strategy adapted from Guevara-Murua *et al.* (*56*). Not

considering this lag could introduce biases to SEA because tree ring is a seasonal proxy. For example, an eruption in December cannot affect the tree-ring formation of black spruce in the same year because black spruce grows in spring–summer (*57*). This adjustment was applied to limited events with known eruption months, yet, it could result in a more evident cooling in response to NHET eruptions (Fig. 3-S11B). We performed SEA on multiple time series (reconstructions and simulations) based on the constructed key eruption years. We considered the temperature anomalies of 15 post-eruption years relative to the 5-year pre-eruption mean. The statistical significance of volcanic cooling was assessed using the block reshuffling method (*58*) with 10,000 iterations. The robustness and consistency of SEA results were validated using multiple subsets of retained volcanic events, as well as using the instrumental temperature series (Fig. 3-3A, B; Fig. 3-S12).

3.6 Acknowledgments

F. Vignola, A. Delwaide, N. Trou-Kechout, P. Balducci, and J. Larose contributed to collecting and processing black spruce samples. A. Schurer and B. Nasri kindly commented on the earlier version of this article. R. Liu helped with the tree-ring density measurements. S. Payette and J. Esper provided the Boniface and Greece tree-ring data, respectively. M. Toohey provided the combined eVolv2k and CMIP6 volcanic forcing dataset. M.P. Rao provided and interpreted the SEA algorithm. This work was financially supported by the Natural Sciences and Engineering Research Council of Canada in collaboration with Hydro-Québec, Manitoba Hydro, and Ouranos under the PERSISTENCE project (grant no. RDC 485475-15). F.W. also received support from the China Scholarship Council. S.Y. and T.Z. were supported by Science and Technology Department of the Xinjiang Autonomous Region (grant no. 2020D04040, 2018D04028).

3.7 References

1. PAGES 2k Consortium, Continental-scale temperature variability during the past two millennia. *Nat. Geosci.* **6**, 339–346 (2013).

2. PAGES 2k Consortium, Consistent multidecadal variability in global temperature reconstructions and simulations over the Common Era. *Nat. Geosci.* **12**, 643–649 (2019).

3. B. Christiansen, F. C. Ljungqvist, Challenges and perspectives for large-scale temperature reconstructions of the past two millennia. *Rev. Geophys.* **55**, 40–96 (2017).

4. U. Büntgen, T. Kyncl, C. Ginzler, D. S. Jacks, J. Esper, W. Tegel, K.-U. Heussner, J. Kyncl, Filling the Eastern European gap in millennium-long temperature reconstructions. *Proc. Natl. Acad. Sci.* **110**, 1773 (2013).

5. J. Esper, L. Schneider, J. E. Smerdon, B. R. Schöne, U. Büntgen, Signals and memory in tree-ring width and density data. *Dendrochronologia*. **35**, 62–70 (2015).

6. R. Wilson, K. Anchukaitis, K. R. Briffa, U. Büntgen, E. Cook, R. D'Arrigo, N. Davi, J. Esper, D. Frank, B. Gunnarson, G. Hegerl, S. Helama, S. Klesse, P. J. Krusic, H. W. Linderholm, V. Myglan, T. J. Osborn, M. Rydval, L. Schneider, A. Schurer, G. Wiles, P. Zhang, E. Zorita, Last millennium northern hemisphere summer temperatures from tree rings: Part I: The long term context. *Quat. Sci. Rev.* **134**, 1–18 (2016).

7. J. Björklund, G. von Arx, D. Nievergelt, R. Wilson, J. Van den Bulcke, B. Günther, N. J. Loader, M. Rydval, P. Fonti, T. Scharnweber, L. Andreu-Hayles, U. Büntgen, R. D'Arrigo, N. Davi, T. De Mil, J. Esper, H. Gärtner, J. Geary, B. E. Gunnarson, C. Hartl, A. Hevia, H. Song, K. Janecka, R. J. Kaczka, A. V. Kirdyanov, M. Kochbeck, Y. Liu, M. Meko, I. Mundo, K. Nicolussi, R. Oelkers, T. Pichler, R. Sánchez-Salguero, L. Schneider, F. Schweingruber, M. Timonen, V. Trouet, J. Van Acker, A. Verstege, R. Villalba, M. Wilmking, D. Frank, Scientific merits and analytical challenges of tree-ring densitometry. *Rev. Geophys.* **57**, 1224–1264 (2019).

8. F. Zhu, J. Emile-Geay, G. J. Hakim, J. King, K. J. Anchukaitis, Resolving the differences in the simulated and reconstructed temperature response to volcanism. *Geophys. Res. Lett.*, **47**, e2019GL086908 (2020).

9. K. J. Anchukaitis, R. Wilson, K. R. Briffa, U. Büntgen, E. R. Cook, R. D'Arrigo, N. Davi, J. Esper, D. Frank, B. E. Gunnarson, G. Hegerl, S. Helama, S. Klesse, P. J. Krusic, H. W. Linderholm, V. Myglan, T. J. Osborn, P. Zhang, M. Rydval, L. Schneider, A. Schurer, G. Wiles, E. Zorita, Last millennium Northern Hemisphere summer temperatures from tree rings: Part II, spatially resolved reconstructions. *Quat. Sci. Rev.* **163**, 1–22 (2017).

10. S. St. George, J. Esper, Concord and discord among Northern Hemisphere paleotemperature reconstructions from tree rings. *Quat. Sci. Rev.* **203**, 278–281 (2019).

11. A. Robock, Volcanic eruptions and climate. *Rev. Geophys.* **38**, 191–219 (2000).

12. M. Sigl, M. Winstrup, J. R. McConnell, K. C. Welten, G. Plunkett, F. Ludlow, U. Büntgen, M. Caffee, N. Chellman, D. Dahl-Jensen, H. Fischer, S. Kipfstuhl, C. Kostick, O. J. Maselli, F. Mekhaldi, R. Mulvaney, R. Muscheler, D. R. Pasteris, J. R. Pilcher, M. Salzer, S. Schüpbach, J. P. Steffensen, B. M. Vinther, T. E. Woodruff, Timing and climate forcing of volcanic eruptions for the past 2,500 years. *Nature*. **523**, 543–549 (2015).

13. M. Toohey, K. Krüger, H. Schmidt, C. Timmreck, M. Sigl, M. Stoffel, R. Wilson, Disproportionately strong climate forcing from extratropical explosive volcanic eruptions. *Nat. Geosci.* **12**, 100–107 (2019).

14. I. Harris, P. D. Jones, T. J. Osborn, D. H. Lister, Updated high-resolution grids of monthly climatic observations – the CRU TS3.10 Dataset. *Int. J. Climatol.* **34**, 623–642 (2014).

15. F. Gennaretti, D. Huard, M. Naulier, M. Savard, C. Bégin, D. Arseneault, J. Guiot, Bayesian multiproxy temperature reconstruction with black spruce ring widths and stable isotopes from the northern Quebec taiga. *Clim. Dyn.* **49**, 4107–4119 (2017).

16. J. Luterbacher, J. P. Werner, J. E. Smerdon, L. Fernández-Donado, F. J. González-Rouco, D. Barriopedro, F. C. Ljungqvist, U. Büntgen, E. Zorita, S. Wagner, J. Esper, D. McCarroll, A. Toreti, D. Frank, J. H. Jungclaus, M. Barriendos, C. Bertolin, O. Bothe, R. Brázdil, D. Camuffo, P. Dobrovolný, M. Gagen, E. García-Bustamante, Q. Ge, J. J. Gómez-Navarro, J. Guiot, Z. Hao, G. C. Hegerl, K. Holmgren, V. V. Klimenko, J. Martín-Chivelet, C. Pfister, N. Roberts, A. Schindler, A. Schurer, O. Solomina, L. von Gunten, E. Wahl, H. Wanner, O. Wetter, E. Xoplaki, N. Yuan, D. Zanchettin, H. Zhang, C. Zerefos, European summer temperatures since Roman times. *Environ. Res. Lett.* **11**, 024001 (2016).

17. S. Guillet, C. Corona, M. Stoffel, M. Khodri, F. Lavigne, P. Ortega, N. Eckert, P. D. Sielenou, V. Daux, O. V. Churakova (Sidorova), N. Davi, J.-L. Edouard, Y. Zhang, B. H. Luckman, V. S. Myglan, J. Guiot, M. Beniston, V. Masson-Delmotte, C. Oppenheimer, Climate response to the Samalas volcanic eruption in 1257 revealed by proxy records. *Nat. Geosci.* **10**, 123–128 (2017).

18. D. P. Schneider, C. M. Ammann, B. L. Otto-Bliesner, D. S. Kaufman, Climate response to large, high-latitude and low-latitude volcanic eruptions in the Community Climate System Model. *J. Geophys. Res. Atmospheres*. **114**, D15101 (2009).

19. G. Stenchikov, T. L. Delworth, V. Ramaswamy, R. J. Stouffer, A. Wittenberg, F. Zeng, Volcanic signals in oceans. *J. Geophys. Res. Atmospheres*. **114**, D16104 (2009).

20. L. Oman, A. Robock, G. Stenchikov, G. A. Schmidt, R. Ruedy, Climatic response to high-latitude volcanic eruptions. *J. Geophys. Res. Atmospheres*. **110**, D13103 (2005).

21. B. Kravitz, A. Robock, Climate effects of high-latitude volcanic eruptions: Role of the time of year. *J. Geophys. Res. Atmospheres*. **116**, D01105 (2011).

22. D. Zanchettin, C. Timmreck, H.-F. Graf, A. Rubino, S. Lorenz, K. Lohmann, K. Krüger, J. H. Jungclaus, Bi-decadal variability excited in the coupled ocean–atmosphere system by strong tropical volcanic eruptions. *Clim. Dyn.* **39**, 419–444 (2012).

23. S. Brönnimann, J. Franke, S. U. Nussbaumer, H. J. Zumbühl, D. Steiner, M. Trachsel, G. C. Hegerl, A. Schurer, M. Worni, A. Malik, J. Flückiger, C. C. Raible, Last phase of the Little Ice Age forced by volcanic eruptions. *Nat. Geosci.* **12**, 650–656 (2019).

24. M. Stoffel, M. Khodri, C. Corona, S. Guillet, V. Poulain, S. Bekki, J. Guiot, B. H. Luckman, C. Oppenheimer, N. Lebas, M. Beniston, V. Masson-Delmotte, Estimates of volcanic-induced cooling in the Northern Hemisphere over the past 1,500 years. *Nat. Geosci.* **8**, 784–788 (2015).

25. L. Schneider, J. E. Smerdon, U. Büntgen, R. J. S. Wilson, V. S. Myglan, A. V. Kirdyanov, J. Esper, Revising midlatitude summer temperatures back to A.D. 600 based on a wood density network. *Geophys. Res. Lett.* **42**, 4556–4562 (2015).

26. S. Guillet, C. Corona, F. Ludlow, C. Oppenheimer, M. Stoffel, Climatic and societal impacts of a “forgotten” cluster of volcanic eruptions in 1108-1110 CE. *Sci. Rep.* **10**, 6715 (2020).

27. G. A. Schmidt, J. H. Jungclaus, C. M. Ammann, E. Bard, P. Braconnot, T. J. Crowley, G. Delaygue, F. Joos, N. A. Krivova, R. Muscheler, B. L. Otto-Bliesner, J. Pongratz, D. T. Shindell, S. K. Solanki, F. Steinhilber, L. E. A. Vieira, Climate forcing reconstructions for use in PMIP simulations of the last millennium (v1.0). *Geosci. Model Dev.* **4**, 33–45 (2011).

28. G. Hegerl, F. Zwiers, Use of models in detection and attribution of climate change. *WIREs Clim. Change*. **2**, 570–591 (2011).

29. M. E. Mann, B. A. Steinman, S. K. Miller, On forced temperature changes, internal variability, and the AMO. *Geophys. Res. Lett.* **41**, 3211–3219 (2014).

30. M. E. Mann, B. A. Steinman, D. J. Brouillette, S. K. Miller, Multidecadal climate oscillations during the past millennium driven by volcanic forcing. *Science*. **371**, 1014 (2021).

31. G. C. Hegerl, T. J. Crowley, M. Allen, W. T. Hyde, H. N. Pollack, J. Smerdon, E. Zorita, Detection of human influence on a new, validated 1500-year temperature reconstruction. *J. Clim.* **20**, 650–666 (2007).

32. J. Esper, D. C. Frank, M. Timonen, E. Zorita, R. J. S. Wilson, J. Luterbacher, S. Holzkämper, N. Fischer, S. Wagner, D. Nievergelt, A. Verstege, U. Büntgen, Orbital forcing of tree-ring data. *Nat. Clim. Change*. **2**, 862–866 (2012).

33. F. Gennaretti, D. Arseneault, A. Nicault, L. Perreault, Y. Bégin, Volcano-induced regime shifts in millennial tree-ring chronologies from northeastern North America. *Proc. Natl. Acad. Sci.* **111**, 10077 (2014).

34. F. Wang, D. Arseneault, É. Boucher, S. Yu, S. Ouellet, G. Chaillou, A. Delwaide, L. Wang, Chemical destaining and the delta correction for blue intensity measurements of stained lake subfossil trees. *Biogeosciences*. **17**, 4559–4570 (2020).

35. U. Büntgen, L. Wacker, J. D. Galván, S. Arnold, D. Arseneault, M. Baillie, J. Beer, M. Bernabei, N. Bleicher, G. Boswijk, A. Bräuning, M. Carrer, F. C. Ljungqvist, P. Cherubini, M. Christl, D. A. Christie, P. W. Clark, E. R. Cook, R. D'Arrigo, N. Davi, Ó. Eggertsson, J. Esper, A. M. Fowler, Z. Gedalof, F. Gennaretti, J. Grießinger, H. Grissino-Mayer, H. Grudd, B. E. Gunnarson, R. Hantemirov, F. Herzig, A. Hessl, K.-U. Heussner, A. J. T. Jull, V. Kukarskih, A. Kirdyanov, T. Kolář, P. J. Krusic, T. Kyncl, A. Lara, C. LeQuesne, H. W. Linderholm, N. J. Loader, B. Luckman, F. Miyake, V. S. Myglan, K. Nicolussi, C. Oppenheimer, J. Palmer, I. Panyushkina, N. Pederson, M. Rybníček, F. H. Schweingruber, A. Seim, M. Sigl, O. Churakova (Sidorova), J. H. Speer, H.-A. Synal, W. Tegel, K. Treydte, R. Villalba, G. Wiles, R. Wilson, L. J. Winship, J. Wunder, B. Yang, G. H. F. Young, Tree rings reveal globally coherent signature of cosmogenic radiocarbon events in 774 and 993 CE. *Nat. Commun.* **9**, 3605 (2018).

36. K. R. Briffa, P. D. Jones, T. S. Bartholin, D. Eckstein, F. H. Schweingruber, W. Karlén, P. Zetterberg, M. Eronen, Fennoscandian summers from ad 500: temperature changes on short and long timescales. *Clim. Dyn.* **7**, 111–119 (1992).

37. J. A. Björklund, B. E. Gunnarson, P. J. Krusic, H. Grudd, T. Josefsson, L. Östlund, H. W. Linderholm, Advances towards improved low-frequency tree-ring reconstructions, using an updated Pinus sylvestris L. MXD network from the Scandinavian Mountains. *Theor. Appl. Climatol.* **113**, 697–710 (2013).

38. F. Wang, D. Arseneault, É. Boucher, G. Galipaud Gloaguen, A. Deharte, S. Yu, N. Trou-kechout, Temperature sensitivity of blue intensity, maximum latewood density, and ring width data of living black spruce trees in the eastern Canadian taiga. *Dendrochronologia*. **64**, 125771 (2020).

39. E. R. Cook, K. Peters, Calculating unbiased tree-ring indices for the study of climatic and environmental change. *The Holocene*. **7**, 361–370 (1997).

40. J. Esper, D. C. Frank, R. J. S. Wilson, K. R. Briffa, Effect of scaling and regression on reconstructed temperature amplitude for the past millennium. *Geophys. Res. Lett.* **32**, L07711 (2005).

41. T. M. L. Wigley, K. R. Briffa, P. D. Jones, On the average value of correlated time series, with applications in dendroclimatology and hydrometeorology. *J. Clim. Appl. Meteorol.* **23**, 201–213 (1984).

42. M. Naulier, M. M. Savard, C. Bégin, F. Gennaretti, D. Arseneault, J. Marion, A. Nicault, Y. Bégin, A millennial summer temperature reconstruction for northeastern Canada using oxygen isotopes in subfossil trees. *Clim Past.* **11**, 1153–1164 (2015).

43. V. C. Slonosky, Daily minimum and maximum temperature in the St-Lawrence Valley, Quebec: two centuries of climatic observations from Canada. *Int. J. Climatol.* **35**, 1662–1681 (2015).

44. B. L. Otto-Bliesner, E. C. Brady, J. Fasullo, A. Jahn, L. Landrum, S. Stevenson, N. Rosenbloom, A. Mai, G. Strand, Climate variability and change since 850 CE: an ensemble approach with the Community Earth System Model. *Bull. Am. Meteorol. Soc.* **97**, 735–754 (2016).

45. E. Brady, S. Stevenson, D. Bailey, Z. Liu, D. Noone, J. Nusbaumer, B. L. Otto-Bliesner, C. Tabor, R. Tomas, T. Wong, J. Zhang, J. Zhu, The connected isotopic water cycle in the Community Earth System Model version 1. *J. Adv. Model. Earth Syst.* **11**, 2547–2566 (2019).

46. U. Schulzweida, CDO User Guide (Version 1.9.8). http://doi.org/10.5281/zenodo.3539275 (2019).

47. J. Hu, J. Emile-Geay, J. Partin, Correlation-based interpretations of paleoclimate data–where statistics meet past climates. *Earth Planet. Sci. Lett.* **459**, 362–371 (2017).

48. J. Pilowsky, colorednoise: Simulate temporally autocorrelated populations. (2020; https://CRAN.R-project.org/package=colorednoise).

49. Global Volcanism Program, Volcanoes of the World, v. 4.8.8, E. Venzke, Ed. (Smithsonian Institution, 2013), downloaded 14 May, 2020. https://doi.org/10.5479/si.GVP.VOTW4-2013s

50. M. Toohey, M. Sigl, Volcanic stratospheric sulfur injections and aerosol optical depth from 500 BCE to 1900 CE. *Earth Syst. Sci. Data*. **9**, 809–831 (2017).

51. C. Gao, A. Robock, C. Ammann, Volcanic forcing of climate over the past 1500 years: An improved ice core-based index for climate models. *J. Geophys. Res. Atmospheres*. **113**， D2311 (2008).

52. T. J. Crowley, M. B. Unterman, Technical details concerning development of a 1200 yr proxy index for global volcanism. *Earth Syst. Sci. Data*. **5**, 187–197 (2013).

53. M. P. Rao, E. R. Cook, B. I. Cook, K. J. Anchukaitis, R. D. D'Arrigo, P. J. Krusic, A. N. LeGrande, A double bootstrap approach to Superposed Epoch Analysis to evaluate response uncertainty. *Dendrochronologia*. **55**, 119–124 (2019).

54. B. Luo, Stratospheric aerosol radiative forcing and SAD version v4.0.0 1850–2016 for use in CMIP6 models (2018; ftp://iacftp.ethz.ch/pub_read/luo/CMIP6_SAD_radForcing_v4.0.0/). [Last access: 7 July, 2021]

55. L. J. Lücke, G. C. Hegerl, A. P. Schurer, R. Wilson, Effects of memory biases on variability of temperature reconstructions. *J. Clim.* **32**, 8713–8731 (2019).

56. A. Guevara-Murua, E. J. Hendy, A. C. Rust, K. V. Cashman, Consistent decrease in North Atlantic Tropical Cyclone frequency following major volcanic eruptions in the last three centuries. *Geophys. Res. Lett.* **42**, 9425–9432 (2015).

57. C. Lupi, H. Morin, A. Deslauriers, S. Rossi, Xylogenesis in black spruce: does soil temperature matter? *Tree Physiol.* **32**, 74–82 (2012).

58. J. B. Adams, M. E. Mann, C. M. Ammann, Proxy evidence for an El Niño-like response to volcanic forcing. *Nature*. **426**, 274–278 (2003).

59. S. Payette, L. Filion, L. Gauthier, Y. Boutin, Secular climate change in old-growth tree-line vegetation of northern Quebec. *Nature*. **315**, 135–138 (1985).

60. S. Payette, L. Filion, A. Delwaide, C. Bégin, Reconstruction of tree-line vegetation response to long-term climate change. *Nature*. **341**, 429–432 (1989).

61. D. Frank, J. Esper, Characterization and climate response patterns of a high-elevation, multi-species tree-ring network in the European Alps. *Dendrochronologia*. **22**, 107–121 (2005).

62. T. M. Melvin, K. R. Briffa, CRUST: Software for the implementation of regional chronology standardisation: Part 1. Signal-Free RCS. *Dendrochronologia*. **32**, 7–20 (2014).

63. T. M. Melvin, K. R. Briffa, K. Nicolussi, M. Grabner, Time-varying-response smoothing. *Dendrochronologia*. **25**, 65–69 (2007).

64. T. J. Osborn, K. Briffa, P. Jones, Adjusting variance for sample-size in tree-ring chronologies and other regional-mean timeseries. *Dendrochronologia*. **15**, 89–99 (1997).

65. D. C. Frank, J. Esper, E. R. Cook, On variance adjustments in tree-ring chronology development. *TRACE*. **4**, 56–66 (2007).

66. É. Boucher, A. Nicault, D. Arseneault, Y. Bégin, M. P. Karami, Decadal variations in eastern Canada's taiga wood biomass production forced by ocean-atmosphere interactions. *Sci. Rep.* **7**, 2457 (2017).

67. S. Vallée, S. Payette, Contrasted growth of black spruce (*Picea mariana*) forest trees at treeline associated with climate change over the last 400 years. *Arct. Antarct. Alp. Res.* **36**, 400–406 (2004).

68. D. McCarroll, N. J. Loader, R. Jalkanen, M. H. Gagen, H. Grudd, B. E. Gunnarson, A. J. Kirchhefer, M. Friedrich, H. W. Linderholm, M. Lindholm, T. Boettger, S. O. Los, S. Remmele, Y. M. Kononov, Y. H. Yamazaki, G. H. Young, E. Zorita, A 1200-year multiproxy record of tree growth and summer temperature at the northern pine forest limit of Europe. *The Holocene*. **23**, 471–484 (2013).

69. P. Zhang, H. W. Linderholm, B. E. Gunnarson, J. Björklund, D. Chen, 1200 years of warm-season temperature variability in central Scandinavia inferred from tree-ring density. *Clim Past.* **12**, 1297–1312 (2016).

70. U. Büntgen, D. C. Frank, D. Nievergelt, J. Esper, Summer temperature variations in the European Alps, A.D. 755–2004. *J. Clim.* **19**, 5606–5623 (2006).

71. J. Esper, L. Klippel, P. J. Krusic, O. Konter, C. C. Raible, E. Xoplaki, J. Luterbacher, U. Büntgen, Eastern Mediterranean summer temperatures since 730 CE from Mt. Smolikas tree-ring densities. *Clim. Dyn*. **54**, 1367–1382 (2020).

72. S. Helama, M. Vartiainen, J. Holopainen, H. M. Mäkelä, T. Kolström, J. Meriläinen, A palaeotemperature record for the Finnish Lakeland based on microdensitometric variations in tree rings. *Geochronometria*. **41**, 265–277 (2014).

73. T. M. Melvin, H. Grudd, K. R. Briffa, Potential bias in 'updating' tree-ring chronologies using regional curve standardisation: Re-processing 1500 years of Torneträsk density and ring-width data. *The Holocene*. **23**, 364–373 (2013).

74. K. R. Briffa, T. M. Melvin, T. J. Osborn, R. M. Hantemirov, A. V. Kirdyanov, V. S. Mazepa, S. G. Shiyatov, J. Esper, Reassessing the evidence for tree-growth and inferred temperature change during the Common Era in Yamalia, northwest Siberia. *Quat. Sci. Rev.* **72**, 83–107 (2013).

75. B. H. Luckman, R. J. S. Wilson, Summer temperatures in the Canadian Rockies during the last millennium: a revised record. *Clim. Dyn.* **24**, 131–144 (2005).

76. T. J. Crowley, G. Zielinski, B. Vinther, R. Udisti, K. Kreutz, J. Cole-Dai, E. Castellano, Volcanism and the Little Ice Age. *PAGES News* **16**, 22–23 (2008).

77. X. Xin, T. Wu, J. Zhang, Introduction of CMIP5 Experiments carried out with the Climate System Models of Beijing Climate Center. *Adv. Clim. Change Res.* **4**, 41–49 (2013).

78. L. Landrum, B. L. Otto-Bliesner, E. R. Wahl, A. Conley, P. J. Lawrence, N. Rosenbloom, H. Teng, Last millennium climate and its variability in CCSM4. *J. Clim.* **26**, 1085–1111 (2013).

79. S. J. Phipps, H. V. McGregor, J. Gergis, A. J. E. Gallant, R. Neukom, S. Stevenson, D. Ackerley, J. R. Brown, M. J. Fischer, T. D. van Ommen, Paleoclimate data–model comparison and the role of climate forcings over the past 1500 years. *J. Clim.* **26**, 6915–6936 (2013).

80. G. A. Schmidt, R. Ruedy, J. E. Hansen, I. Aleinov, N. Bell, M. Bauer, S. Bauer, B. Cairns, V. Canuto, Y. Cheng, A. Del Genio, G. Faluvegi, A. D. Friend, T. M. Hall, Y. Hu, M. Kelley, N. Y. Kiang, D. Koch, A. A. Lacis, J. Lerner, K. K. Lo, R. L. Miller, L. Nazarenko, V. Oinas, J. Perlwitz, J. Perlwitz, D. Rind, A. Romanou, G. L. Russell, M. Sato, D. T. Shindell, P. H. Stone, S. Sun, N. Tausnev, D. Thresher, M.-S. Yao, Present-day atmospheric simulations using GISS modelE: comparison to in situ, satellite, and reanalysis data. *J. Clim.* **19**, 153–192 (2006).

81. J.-L. Dufresne, M.-A. Foujols, S. Denvil, A. Caubel, O. Marti, O. Aumont, Y. Balkanski, S. Bekki, H. Bellenger, R. Benshila, S. Bony, L. Bopp, P. Braconnot, P. Brockmann, P. Cadule, F. Cheruy, F. Codron, A. Cozic, D. Cugnet, N. de Noblet, J.-P. Duvel, C. Ethé, L. Fairhead, T. Fichefet, S. Flavoni, P. Friedlingstein, J.-Y. Grandpeix, L. Guez, E. Guilyardi, D. Hauglustaine, F. Hourdin, A. Idelkadi, J. Ghattas, S. Joussaume, M. Kageyama, G. Krinner, S. Labetoulle, A. Lahellec, M.-P. Lefebvre, F. Lefevre, C. Levy, Z. X. Li, J. Lloyd, F. Lott, G. Madec, M. Mancip, M. Marchand, S. Masson, Y. Meurdesoif, J. Mignot, I. Musat, S. Parouty, J. Polcher, C. Rio, M. Schulz, D. Swingedouw, S. Szopa, C. Talandier, P. Terray, N. Viovy, N. Vuichard, Climate change projections using the IPSL-CM5 Earth System Model: from CMIP3 to CMIP5. *Clim. Dyn.* **40**, 2123–2165 (2013).

82. J. H. Jungclaus, S. J. Lorenz, C. Timmreck, C. H. Reick, V. Brovkin, K. Six, J. Segschneider, M. A. Giorgetta, T. J. Crowley, J. Pongratz, N. A. Krivova, L. E. Vieira, S. K. Solanki, D. Klocke, M. Botzet, M. Esch, V. Gayler, H. Haak, T. J. Raddatz, E. Roeckner, R. Schnur, H. Widmann, M. Claussen, B. Stevens, J. Marotzke, Climate and carbon-cycle variability over the last millennium. *Clim Past*. **6**, 723–737 (2010).

83. S. Yukimoto, Y. Adachi, M. Hosaka, T. Sakami, H. Yoshimura, M. Hirabara, T. Y. Tanaka, E. Shindo, H. Tsujino, M. Deushi, R. Mizuta, S. Yabu, A. Obata, H. Nakano, T. Koshiro, T. Ose, A. Kitoh, A new global climate model of the Meteorological Research Institute: MRI-CGCM3 —model description and basic performance. *J. Meteorol. Soc. Jpn. Ser II*. **90A**, 23–64 (2012).

84. A. P. Schurer, G. C. Hegerl, M. E. Mann, S. F. B. Tett, S. J. Phipps, Separating forced from chaotic climate variability over the past millennium. *J. Clim.* **26**, 6954–6973 (2013).

3.8 Figures

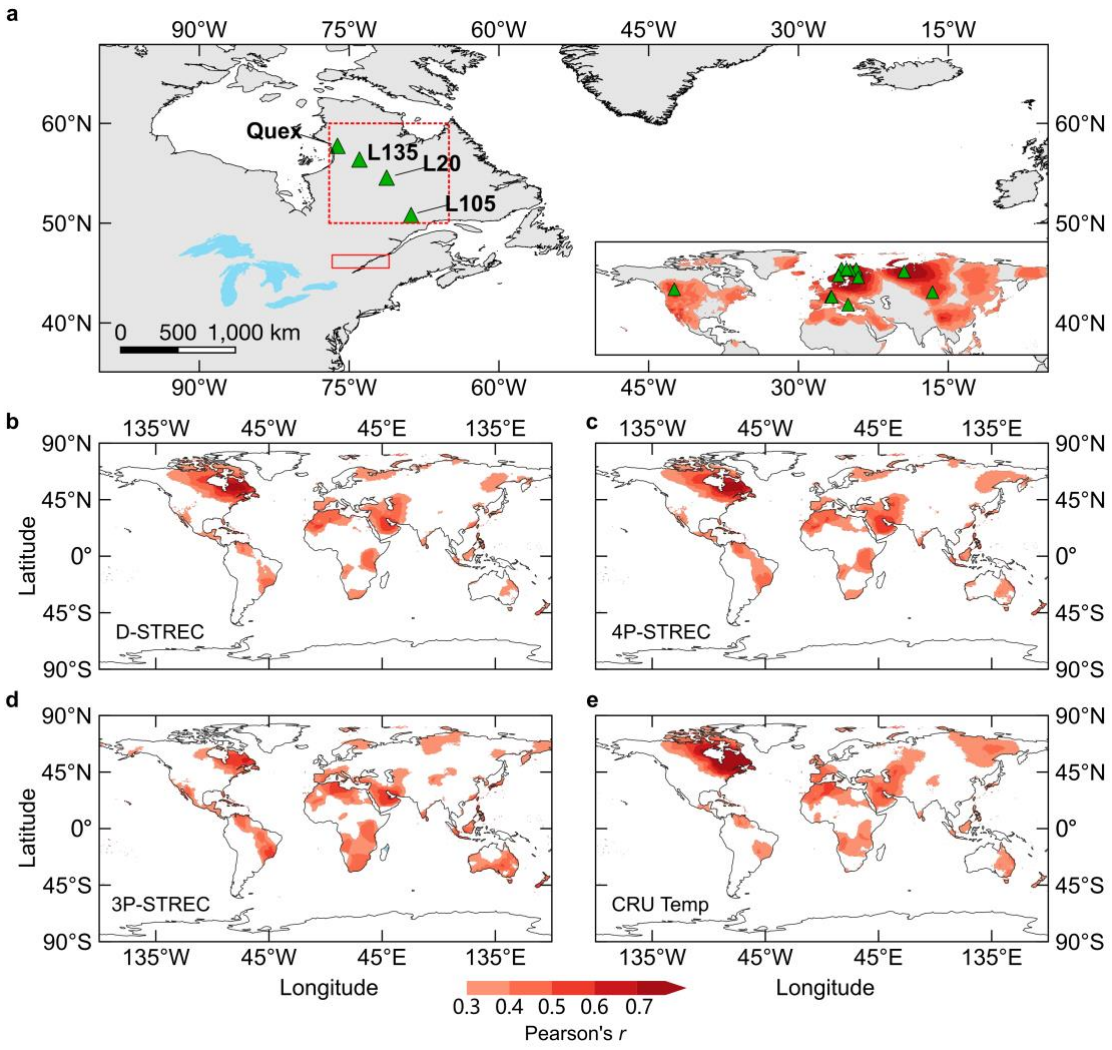

Figure 3-1: Millennial MXD network and correlation fields with gridded MJJA temperature of the CRU dataset. (**A**) Locations of the MXD network with an inset showing the existing millennial MXD chronologies previously used for summer temperature reconstructions across the Northern Hemisphere (see details in Table 3-S1) as well as their correlations with MJJA temperatures (1901–1976 CE), thus indicating the North American data gap. The red dotted square (50º–60º N, 65º–77º W) encloses the area used to calculate the temperature target from the CRU dataset. The red solid square refers to the area where the historical southern Québec temperatures were recorded (Materials and Methods). (**B**)–(**E**) Spatial domains of reconstructed and observed (CRU) temperatures over the 1905–2006 period.

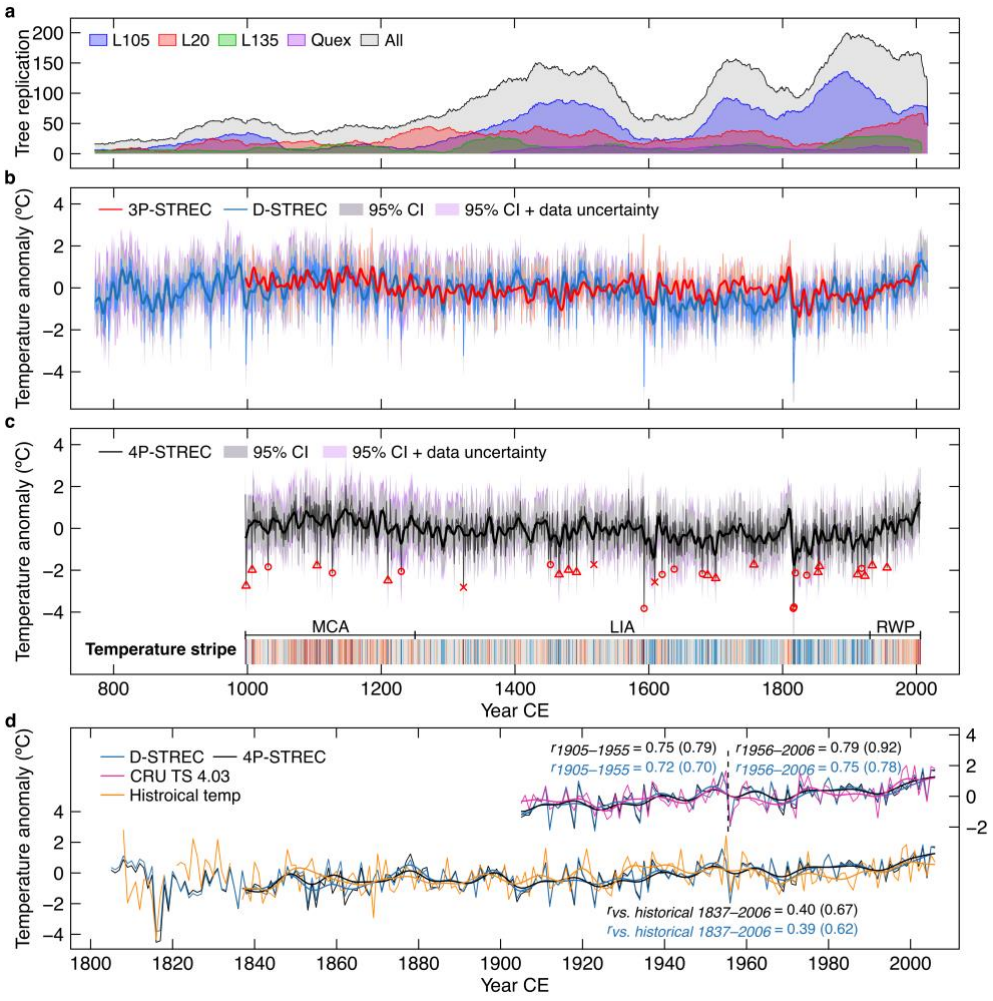

Figure 3-2: Reconstructed MJJA temperature anomalies w.r.t. 1905–2006 CE in NENA. (**A**) Replication of MXD series on the tree basis. (**B**) D-STREC and 3P-STREC superimposed on the two 95% confidence intervals (CIs) of D-STREC. Smoothed curves are produced using a 10-year low-pass Butterworth filter. The "95% CI" is the uncertainty of the Bayesian model. The "95% CI + data uncertainty" additionally considers the proxy-level uncertainty (see Materials and Methods). (**C**) Same as (**B**), but for 4P-STREC along with a temperature stripe graphic (expressed in 10 colors from cold-blue to warm-red) highlighting the Medieval Climate Anomaly (MCA; ~997–1250 CE), the Little Ice Age (LIA; ~1251–1930 CE), and the recent warming period (RWP; ~1931–2006 CE). Circles, triangles, and crosses denote cold extremes (≤ mean−2SD) matched to tropical and NHET volcanic eruptions, and the unattributed extremes, respectively (Table 3-S5). (**D**) Comparison of D-STREC and 4P-STREC with observed MJJA temperatures (CRU dataset and historical southern Québec record). Pearson's *r* values for D-STREC and 4P-STREC versus temperature observations are shown in blue and black, respectively; *r* values in brackets are for 10-year low-pass filtered series produced by a Butterworth filter ($P < 0.05$ in all cases).

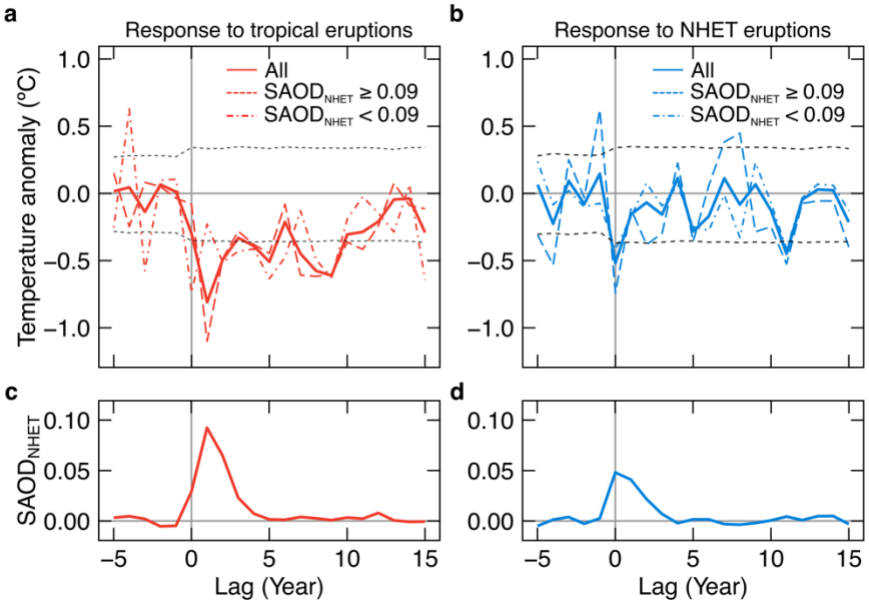

Figure 3-3: Superposed epoch analysis for 4P-STREC according to volcanic aerosol forcing. (**A**) 4P-STREC responses to tropical eruptions with stratospheric aerosol optical depth at 550 nm area-weighted averaged over 30–90ºN ($SAOD_{NHET}$) ≥ 0.03 ("All"), $SAOD_{NHET}$ ≥ 0.09, and 0.03 ≤ $SAOD_{NHET}$ < 0.09. (**B**) Same as (**A**) but for NHET eruptions. (**C**) Superposed volcanic aerosol forcing (expressed as $SAOD_{NHET}$) of tropical eruptions with $SAOD_{NHET}$ ≥ 0.03. (**D**) Same as (**C**), but for NHET eruptions. Responses and forcing are calculated relative to the 5-year pre-eruption mean. Horizontal dashed lines in (**A**) and (**B**) represent the 0.95 statistical significance level (Materials and Methods). The eruptions used for analyses are listed in Table 3-S7.

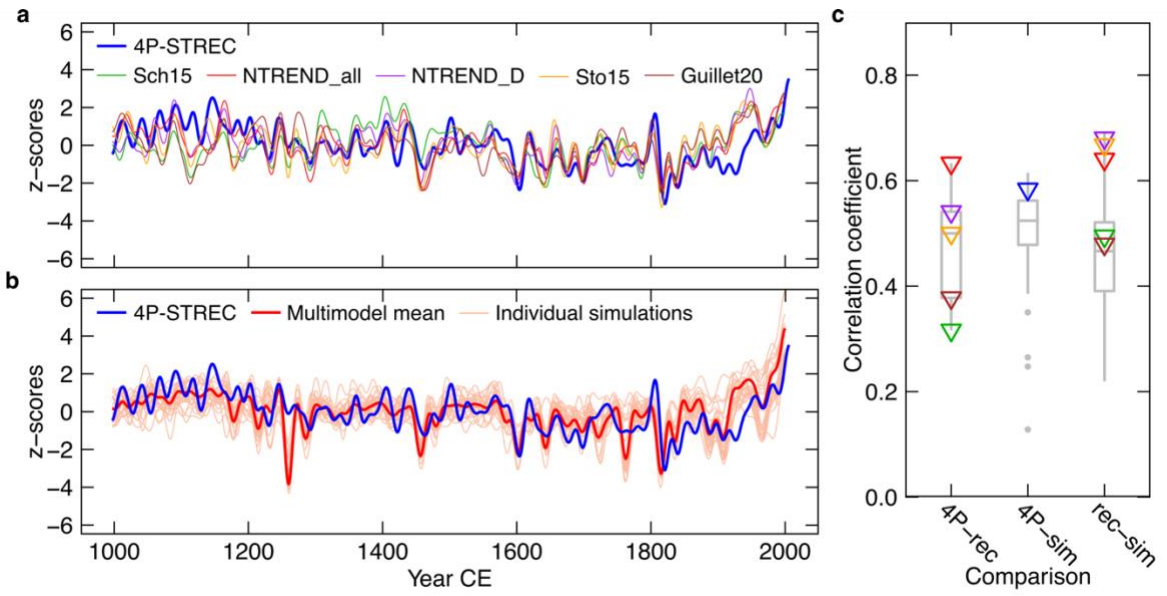

Figure 3-4: Comparison of 4P-STREC with NHET summer temperature reconstructions and simulations. (**A**) 4P-STREC compared to five tree-ring-based reconstructions. Sch15, Schneider *et al*. (*25*); NTREND_all and NTREND_D, the final and the MXD-only reconstructions in Wilson *et al*. (*6*); Sto15, Stoffel *et al*. (*24*); Guillet20, Guillet *et al*. (*26*). (**B**) 4P-STREC compared to an ensemble of 25 CMIP5 full-forcing near-surface MJJA temperature simulations averaged over land 30–90ºN. (**C**) Pearson's *r* among the time series displayed in (**A**) and (**B**) over 997–2000 CE. 4P-rec, 4P-STREC versus reconstructions (box and triangles); 4P-sim, 4P-STREC versus individual simulations (box) and the multi-model mean (blue triangle); rec-sim, NHET reconstructions versus individual simulations (box) and the multi-model mean (triangles; colors refer to the legend of (**A**)). Boxes show the median and the 25%–75% range, whiskers the 1.5 times interquartile range, points the outliers. In (**A**) and (**B**), all the time series are smoothed using a 20-year low-pass Butterworth filter and transformed to z-scores w.r.t. the 1000–2000 time period.

3.9 Supplementary Text

S1. Validation of Quex MXD data

The Quex MXD dataset was validated before being included in our density network and some problems were found. Firstly, the site location must be corrected by ~300 km from the town of Kuujjuarapik (55.33ºN, 77.83ºW) to the region of the Boniface River (57.75ºN, 76.17ºW). The Boniface River area is a region of relict forests and the only known location in northern Quebec where >500 years of long black spruce tree-ring chronologies can be developed from dried spruce trunk at the soil surface (*59*, *60*). An additional indication of the erroneous location is that the site Quex is labeled as "Bonif historic" in the NOAA International Tree Ring Data Bank, coinciding with Boniface River. In order to confirm the origin of Quex, the dataset was correlated over the period 1901–1988 CE against a black spruce ring-width network comprising 60 sites across the Quebec-Labrador Peninsula. Ring-width data were used because they are more abundant and display a smaller spatial domain than does MXD (*61*). Considering that tree replications varied among sites, we standardized ring width as ratios using individual age-dependent spline with the signal-free approach (a suitable method for standardizing living black spruce ring-width series (*38*)) at each site and used the first-differenced data to amplify interannual variability. The Pearson's correlation coefficients clearly show a strengthening relation with the Quex ring width toward the Boniface River region, away from the wrong location of Kuujjuarapik (Fig. 3-S13A). A similar eccentric location is also evidenced by the correlation field of the raw (not first-differenced) Quex ring-width chronology against gridded CRU data (Fig. 3-S13B).

Furthermore, there are several zero values in some of the MXD series of Quex that were likely due to very narrow rings or measurement errors, because missing rings are extremely rare in black spruce in northern Québec. We accordingly replaced these zero values with the available density data from a second radius of the same tree ID in the corresponding year. A missing value was only kept if there was no density measurement from

the second radius. In addition, cross-dating of one core series (ID: 858181) was corrected because of a dating error. Core series were then averaged by tree for further analyses. We also estimated a pith offset of 2 rings (missing metadata; the modal value in our own data) for each tree series for the subsequent standardization.

S2. Comparison of standardization methods

To optimize temperature signals in our final reconstructions, we compared three methods to standardize MXD data at the four sites, including the conventional regional curve standardization (RCS) (*36*), RCS with signal-free approach (sfRCS) (*62*), and regionally constrained individual signal-free standardization (RSFi) (*37*). Chronologies were calculated based on ratios and residuals plus power-transformation (hereafter named ratio chronology and residual chronology, respectively) for the three methods using the RCSigfree program (https://www.ldeo.columbia.edu/tree-ring-laboratory/resources/software). For all methods, we used age-dependent spline smoothing (*63*) with an initial stiffness of 2 years to estimate the growth trends of the MXD series, and chronologies were calculated using Tukey's bi-weight robust mean along with the variance stabilization procedure (*64, 65*).

We calculated Pearson's correlation coefficients among local chronologies, and between each chronology and local MJJA temperatures averaged from monthly data of the four gridded cells closest to each site (CRU dataset). This analysis shows that the RSFi method in general resulted in stronger correlations among sites and with the local temperature target (Table 3-S9), and could correct for the "divergent trends" in recent decades that are evident with other methods, in particular for the site L135 (Fig. 3-S14). In general, the ratio chronologies showed slightly higher correlations (among sites and with MJJA temperatures) than the residual chronologies across standardization methods, although this trend was not evident for the RSFi method (Table 3-S9).

The skills of the RSFi ratio and residual chronologies were further assessed via temperature reconstructions using a time-efficient linear scaling approach (*40*) that yields

similar results to the linear Bayesian method (*15*) (Fig. 3-S9). For this assessment, we used RSFi chronologies at the four sites. The scaling method forced each local series to have the same mean and variance as those of the regional MJJA temperature target over the 1905–2006 time period (1905–1989 CE for site Quex). The scaled chronologies were then arithmetically averaged and scaled again with respect to the temperature target to form a scaled reconstruction. In agreement with comparisons of most sites (Table 3-S9), the regional MJJA temperatures were also better correlated when using the ratio-based reconstruction (Fig. 3-S9). Consequently, RSFi ratio chronologies were chosen for our final temperature reconstructions.

S3. RSFi standardization

The RSFi method (*37*) combines the individual signal-free standardization with the signal-free RCS method. At each site, we first used the RCSigfree program to standardize MXD data using the individual signal-free age-dependent spline smoothing to generate individual growth trends (curves) for each individual series. The sfRCS was also applied to generate a signal-free regional curve. Briefly, each individual growth curve was aligned with the regional curve according to cambial age, and was adjusted to the same mean value as that of the regional curve for the same cambial age interval. The mean-adjusted individual growth curves were then used to re-standardize raw MXD series. This procedure is efficient for removing irregular growth trends due to atypic growth rates and disturbances in different time periods, while also preserving the low-frequency domain that would be lost when using only individual-based standardization. Chronologies were finally calculated using Tukey's bi-weight robust mean along with the variance stabilization procedure (*64*, *65*).

S4. Bayesian reconstruction

The linear Bayesian approach used for our summer temperature reconstructions was originally designed to perform a multi-proxy reconstruction (*15*). Here, we use this approach with multiple proxy series. The posterior density of the reconstructed climate (c_i) at year *i*,

given by N proxy series $\boldsymbol{D}_i = [d_{1,i}, d_{2,i}..., d_{N,i}]$ and observed climate data (C_{cal}) of the same timescale, can be written as:

$$p(c_i|\boldsymbol{D}_i, \boldsymbol{D}_{cal}, C_{cal}) \propto \left[\prod_{k=1}^{N} \int p\left(d_{k,i}|c_i, \tau\right) p\left(d_{k,cal}|C_{cal}, \tau\right) p(\tau)\, d\tau\right] p(c_i). \quad \text{(Eq.1)}$$

where $d_{k,cal}$ is the data of the kth series over the calibration period, and τ is a set of parameters $[\alpha, \beta, \sigma]$ defining the linear relationship between each proxy series and the climate data with normally distributed errors:

$$p\left(d_{k,i}|c_i, \tau\right) \equiv N\left(d_{k,i}; \mu = \alpha c_i + \beta, \sigma\right). \quad \text{(Eq.2)}$$

Equation (2) can be solved using $d_{k,cal}$ and C_{cal} ($p\left(d_{k,cal}|C_{cal}, \tau\right)$), the proxy and climate data during the calibration period, and Markov Chain Monte Carlo sampling with Metropolis–Hastings steps.

In equation (1) the term $p(c_i)$ is a prior of climate (i.e., given by the linear scaling MXD-based reconstructions in our cases, see below) and was assumed to be normally distributed:

$$p(c_i) \equiv N\left(c_i; \mu_c, \sigma_c\right). \quad \text{(Eq.3)}$$

For D-STREC, 4P-STREC, and 3P-STREC, α, β, and σ were assumed to be a uniform prior in $sin(tan^{-1}(\alpha))$, a uniform prior, and a Jeffreys prior, respectively. We ran three parallel chains and obtained a total of 90,000 draws (after discarding 5000 burn-in times for each chain) to generate posteriors for these three parameters. Parameters for $p(c_i)$ were derived from the MXD-based temperature reconstruction using the linear scaling method (Fig. 3-S9). In order to reconstruct the HF components of 4P-STREC and 3P-STREC, the scaled temperature reconstruction was also decomposed using a 9-year-triangular filter to generate high-frequency (HF) priors.

3.10 Supplementary Materials

Supplementary Tables

Table 3-S1. Published millennial MXD chronologies previously used for climate reconstructions. ITRDB: the NOAA International Tree Ring Data Bank.

Site name	Continent	Lat. / Long. (º)	Species	Timespan CE	Reference
Forfjorddalen	Europe	68.8 / 15.7	*Pinus sylvestris*	978–2005	McCarroll *et al*. (*68*)
Jämtland		63.3 / 13.3	*Pinus sylvestris*	850–2011	Zhang *et al*. (*69*)
Laanila		68.5 / 27.3	*Pinus sylvestris*	800–2005	McCarroll *et al*. (*68*)
Lauenen		46.4 / 7.3	*Picea abies*	982–1976	Schweingruber, ITRDB
Lötschental		46.3 / 7.8	*Larix decidua*	735–2004	Büntgen *et al*. (*70*)
N-Greece		40.1 / 20.9	*Pinus heldreichii*	730–2015	Esper *et al*. (*71*)
Nscan		67.5 / 22.5	*Pinus sylvestris*	-215–2006	Esper *et al*. (*32*)
S-Finland		61.9 / 29.0	*Pinus sylvestris*	674–2000	Helama *et al*. (*72*)
Torneträsk		68.2 / 19.5	*Pinus sylvestris*	441–2010	Melvin *et al*. (*73*)
Altai	Asia	50.0 / 88.0	*Larix sibirica*	462–2007	Schneider *et al.* (*25*)
Polar Ural		66.5 / 65.4	*Larix sibirica*	778–2006	Briffa *et al*. (*74*)
Athabasca	N. America	52.3 / −117.3	*Picea engelmannii*	867–1994	Luckman and Wilson (*75*)

Table 3-S2. Properties of the MXD network. No. radii / tree: number of measured radii and corresponding trees. MSL: mean segment length of individual MXD series. AR1: mean first-order autocorrelation of raw MXD series. Timespans show periods of the four local MXD chronologies used in D-STREC, whereas bracketed years refer to the start of each chronology. L105, L20, and L135 are three newly sampled sites and site L135 is composed of three adjacent lakes (L13, L14, and L15, distance < 3km). Quex was developed by Fritz H. Schweingruber, and is available on the NOAA International Tree Ring Data Bank: https://www.ncdc.noaa.gov/paleo-search/study/4349. Note that the location of Quex has been corrected (Supplementary Text S1).

Site	Lat. (°)	Long. (°)	Elev.(m)	No. radii / tree	MSL	AR1	Timespan CE
L105	50.8	−68.8	531	788 / 647	87	0.56	772 (715) –2017
L20	54.6	−71.2	483	583 / 438	76	0.41	772 (658) –2016
L135	56.7	−74.0	251	214 / 164	90	0.40	772 (647)–2008
Quex	57.8	−76.2	50	83 / 45	134	0.33	1363 (1352)–1989

Table 3-S3. Calibration statistics of Bayesian summer temperature reconstructions over the 1905–2006 time period. For r and R^2, the raw, low, and high represent the results of unfiltered, 10-year low-pass and high-pass filtered series, respectively (Butterworth filter). The continuous potential ranked probability score (CRPSpot) and the reliability score (Reli) were calculated from 1000 members randomly drawn from posteriors of each reconstruction. Other statistics were calculated based on the median, 2.5, and 97.5 percentiles of reconstruction posteriors. RMSE: root-mean-square error. CI: confidence interval.

Statistics	**D-STREC**	**4P-STREC**	**3P-STREC**
r (raw/low/high)	0.75/0.80/0.72	0.77/0.87/0.71	0.59/0.85/0.40
R^2 (raw/low/high)	0.56/0.64/0.52	0.60/0.77/0.51	0.35/0.72/0.16
RMSE	0.58	0.56	0.70
CRPSpot	0.33	0.31	0.39
Reli	$19.9e^{-3}$	$7.2e^{-3}$	$8.0e^{-3}$
95% CI coverage	0.87	0.96	0.98
95% CI width	1.84	2.26	3.33

Table 3-S4. Non-overlapping warmest decades and strongest centennial warming trends reconstructed by 4P-STREC. Temperatures are shown in anomalies w.r.t. 1905–2006 period. Periods later than 1900 CE are in bold. Only positive non-overlapping trends are shown.

Rank	Warmest decades		100-year warming trends	
	Period	**Temp. ºC**	**Period**	**ºC /10 y ± SE**
1	**1997–2006**	**1.00**	**1904–2003**	**0.16 ± 0.02**
2	1147–1156	0.91	998–1097	0.06 ± 0.03
3	1086–1095	0.77	1644–1743	0.05 ± 0.02
4	1116–1125	0.69	1453–1552	0.05 ± 0.02
5	1137–1146	0.69	1316–1415	0.04 ± 0.02
6	1065–1074	0.66	1804–1902	0.02 ± 0.03
7	1199–1208	0.65	-	-
8	1804–1813	0.57	-	-
9	1181–1190	0.53	-	-
10	**1979–1988**	**0.51**	-	-

Table 3-S5. Extremely cold years (≤ mean−2SD) in the 4P-STREC and D-STREC reconstructions, and correspondence to volcanic eruptions according to the GVP (*49*) (VEI ≥ 4), eVolv2k (*50*), IVI2 (*51*), and ICI (*52*) (Materials and Method). Temperatures are shown in anomalies (ºC) w.r.t. the 1905–2006 time period. Question marks refer to uncertain results. Dates with # are the matches provided by Toohey *et al*. (*13*).

Year	Temp. ºC	Extreme in	Match to volcanic eruptions				Location
CE	4P-STREC	D-STREC	GVP	eVolv2k	IVI2	ICI	
998	-2.74	Yes	-	998	-	-	NHET
1007	-1.98	Yes	-	-	-	1006	NHET
1031	-1.84	Yes	1030	1028	1030?	-	Tropical
1104	-1.77	No	1104	-	-	-	NHET
1127	-2.13	Yes	-	1127	-	1128	Tropical
1210	-2.49	Yes	1210	1210	-	-	NHET
1230	-2.06	Yes	-	1230	1227#	1228#	Tropical
1323	-2.81	Yes	-	-	-	-	-
1453	-1.73	No	-	1453	1452	1454	Tropical
1466	-2.20	Yes	-	-	-	1467	NHET
1480	-1.98	Yes	1480	1480	1480	1480	NHET
1492	-2.09	Yes	-	-	-	1493	NHET
1518	-1.73	No	-	-	-	-	-
1593	-3.83	Yes	1593	1595?	1593	1593	Tropical
1609	-2.56	Yes	-	-	-	-	-
1620	-2.20	Yes	-	-	1619	1620	Tropical
1638	-1.95	Yes	1638	1637?	-	-	Tropical
1680	-2.17	Yes	1680	-	-	1680	Tropical
1688	-2.24	Yes	-	-	-	1688	NHET
1700	-2.38	Yes	-	-	-	1700	NHET
1757	-1.73	Yes	1755	1755	1755	-	NHET
1816	-3.83	Yes	1815	1815	1815	1815	Tropical
1817	-3.75	Yes	1815	1815	1815	1815	Tropical
1819	-2.13	Yes	1818	-	-	-	Tropical
1836	-2.24	Yes	1835	1835	1835	1835	Tropical
1853	-2.09	Yes	1853	1853	-	1854?	NHET
1855	-1.80	Yes	1854	1856?	-	1854?	NHET
1912	-2.20	Yes	1912	No data	1912	1912	NHET
1918	-1.91	Yes	1917	No data	-	-	Tropical
1923	-2.27	Yes	-	No data	-	1924	NHET
1934	-1.77	No	1933	No data	-	-	NHET
1956	-1.88	Yes	1956	No data	-	1956	NHET

Table 3-S6. Non-overlapping coldest decades reconstructed by 4P-STREC and correspondence to volcanic eruptions. All the ten coldest decades are associated with large tropical eruptions with VEI ≥ 4 provided by the GVP (*49*), except for the Kuwae? eruption with uncertain VEI.

Rank	Period CE	Temp. ºC	Match to volcanic eruptions
1	1816–1825	-1.51	Tambora (1815, VEI = 7)
2	1836–1845	-1.15	Cosiguina (1835, VEI = 5)
3	1601–1610	-1.09	Huaynaputina (1600, VEI = 6)
4	1693–1702	-0.98	Serua (1693, VEI = 4)
5	1904–1913	-0.83	Santa Maria (1902, VEI = 6)
6	1679–1688	-0.78	Tangkoko-Duasudara (1680, VEI = 5?)
7	1921–1930	-0.76	Manam (1919, VEI = 4); Kelut (1919, VEI = 4)?
8	1460–1469	-0.71	Kuwae? (1457, VEI = ?)
9	1640–1649	-0.70	Parker (1640, VEI = 5)
10	1862–1871	-0.67	Makian (1861, VEI = 4)

Table 3-S7. Tropical and NHET volcanic eruptions with peak $SAOD_{NHET} \geq 0.03$ derived from eVolv2k (*50*) combined with CMIP6 (*54*) datasets. VEI is provided by the GVP (*49*). Ice years from IVI2 (*51*) and ICI (*52*) were used to screen unidentified eruptions (Materials and Method). Question marks refer to uncertain values. [a]: eruption years adjusted by Toohey *et al.* (*13*). [b]: eruption years adjusted by authors. [c]: events matched by Toohey *et al.* (*50*). [*]: categorized to unidentified events.

Key Year CE	Eruption Year	Volcano	VEI	Peak $SAOD_{NHET}$ (Year)	Ice year			Location
					eVolv2k	IVI2	ICI	
1020	1020	Unidentified	-	0.051 (1020)	1020	1018	1021	NHET
1170	1170[a]	Unidentified	-	0.157 (1172)	1171	1167[c]	1169	Tropical
1180	1180[a]	Unidentified	-	0.246 (1182)	1182	1176[c]	1184	NHET
1190	1190[a]	Unidentified	-	0.063 (1192)	1191	1188	1193	Tropical
1210	1210	Katla	4	0.083 (1210)	1210	-	-	NHET
1229	1229[a]	Unidentified	-	0.212 (1231)	1230	1227	1228	Tropical
1257	1257.7(±2)	Samalas	7?	0.482 (1258)	1257	1258	1257	Tropical
1275	1275[a]	Unidentified	-	0.047 (1277)	1276	1275	1275	Tropical
1285	1285[a]	Unidentified	-	0.121 (1287)	1286	1284	1286	Tropical
1328	1328[a]	Unidentified	-	0.092 (1329)	1329	1328	1329	NHET
1343	1343[a]	Unidentified	-	0.125 (1346)	1345	1341[c]	1344	Tropical
1452	1452[a]	Kuwae?[*]	-	0.102 (1454)	1453	1452	1454	Tropical
1457	1457[a]	Kuwae?[*]	-	0.211 (1459)	1458	1459	1459	Tropical
1477	1477.2	Bardarbunga	6	0.118 (1477)	1477	1476	1474	NHET
1480	1480.1(±2)	St. Helens	5+	0.052 (1480)	1480	1480	1480	NHET
1510	1510.7	Hekla	4	0.051 (1511)	1510	1512	1508	NHET
1586	1586	Kelut	5?	0.092 (1586)	1585	1584	1585	Tropical
1593	1593	Raung	5?	0.075 (1596)	1595	1593	1593	Tropical
1600	1600.2	Huaynaputina	6	0.182 (1601)	1600	1600	1600	Tropical
1641	1640.12	Parker	5?	0.163 (1640)	1640	1641	1640	Tropical
1668	1667.9	Shikotsu	5	0.085 (1668)	1667	-	1667	NHET
1673	1673.5	Gamkonora	5?	0.043 (1674)	1673	1673	1673	Tropical
1694	1694[a]	Unidentified	-	0.126 (1696)	1695	1693	1695	Tropical
1708	1707.12	Fujisan	5	0.031 (1708)	1707	-	1704	NHET
1730	1730[a]	Unidentified	-	0.119 (1729)	1729	1729	1731	NHET
1740	1739.8	Shikotsu	5	0.080 (1740)	1739	-	1739	NHET
1756	1755.10	Katla	5?	0.032 (1756)	1755	1755	-	NHET
1762	1762[a]	Unidentified	-	0.044 (1763)	1762	1761	1762	Tropical
1766	1766.4	Hekla	4	0.050 (1766)	1766	-	-	NHET
1783	1783.5	Grimsvotn	4+	0.378 (1784)	1783	1783	1783	NHET
1796	1796[b]	Unidentified	-	0.030 (1797)	1797	1796	1796	NHET
1815	1815.4	Tambora	7	0.250 (1816)	1815	1815	1815	Tropical
1831	1831	Babuyan Claro	4	0.137 (1832)	1831	1831	1831	Tropical
1835	1835.1	Cosiguina	5	0.087 (1836)	1835	1835	1835	Tropical
1857	1856.9	Hokkaido	5	0.034 (1856)	1855	-	1854	NHET
1862	1861.12	Makian	4	0.041 (1862)	1861	1861	1861	Tropical
1873	1873.1	Grimsvotn	4	0.031 (1873)	1873	-	1872	NHET
1883	1883.5	Krakatau	6	0.116 (1884)	1883	1883	1883	Tropical
1903	1902.10	Santa Maria	5?	0.108 (1903)	No data	1902	1902	Tropical
1907	1907.3	Ksudach	5	0.034 (1907)	No data	-	1907	NHET
1912	1912.6	Novarupta	6	0.103 (1912)	No data	1912	1912	NHET
1963	1963.2	Agung	5	0.030 (1965)	No data	1963	1963	Tropical
1982	1982.3	Chichon, El	5	0.096 (1983)	No data	1982	1982	Tropical

Four events were discarded for superposed epoch analysis based on case-specific reasons. Aira (1471 CE): the eruption likely lasted for several years. Serua (1693 CE): there is only a one-year lag to the stronger 1694 eruption. Unidentified (1808 CE): strong interference with the Tambora eruption (1815 CE; Fig. 3-S11C). Pinatubo (1991 CE): too strong of an influence of the recent warming against the volcanic cooling trend.

Table 3-S8. CMIP5 last-millennium ensemble models and volcanic forcing datasets used. GRA, Gao *et al*. (*51*); CEA, Crowley *et al*. (*76*). FULL, full-forcing; GHG, greenhouse gases only; LU, land use only; ORB, orbital only; SOL, solar only; VOL, volcanic only simulations; CNTL, unforced control run. Note that the full-forcing members of CESM-LME and CMIP5 Past1000 were named CMIP5 simulations in the main text.

Sub-ensemble	Model	Type	Volcanic forcing	Member	Reference
CESM-LME	CESM-CAM5	FULL	GRA	1–13	Otto-Bliesner *et al*. (*44*)
		GHG	-	1–3	
		LU	-	1–3	
		ORB	-	1–3	
		SOL	-	1, 3–5	
		VOL	GRA	1–5	
		CNTL	-	1	
	iCESM1	FULL	GRA	1–3	Brady *et al*. (*45*)
		GHG	-	1	
		ORB	-	1	
		SOL	-	1	
		VOL	GRA	1–2	
CMIP5 Past1000	BCC-CSM1.1	FULL	GRA	1	Xin *et al*. (*77*)
	CCSM4	FULL	GRA	1	Landrum *et al*. (*78*)
	CSIRO-Mk-3L-1-2	FULL	CEA	1	Phipps *et al*. (*79*)
	GISS-E2-R	FULL	CEA & CRA	r121 & r128	Schmidt *et al*. (*80*)
	IPSL-CM5A-LR	FULL	GRA	1	Dufresne *et al*. (*81*)
	MPI-ESM-P	FULL	CEA	1	Jungclaus *et al*. (*82*)
	MRI-CGCM3	FULL	GRA	1	Yukimoto *et al*. (*83*)
	HadCM3	FULL	CEA	1	Schurer *et al*. (*84*)

Table 3-S9. Correlations among sites and MJJA temperatures according to standardization methods. PT: power transformation. Correlation coefficients were calculated over the common time periods of each pair of time series. Temp refers to the corresponding local CRU MJJA mean temperatures starting from 1901 CE. The highest correlations for corresponding pairs are highlighted in bold.

Standardization Method		**Ratios**				**Residuals + PT**			
		L105	L20	L135	Quex	L105	L20	L135	Quex
RCS	L20	0.45	-	-	-	0.45	-	-	-
	L135	0.14	**0.53**	-	-	0.14	0.52	-	-
	Quex	0.18	0.49	**0.64**	-	0.23	0.52	0.64	-
	Temp	0.59	0.48	0.22	0.59	0.59	0.47	0.21	0.59
sfRCS	L20	0.45	-	-		0.45	-	-	-
	L135	0.14	0.52	-		0.14	0.52	-	-
	Quex	0.17	0.48	0.65		0.21	0.52	0.66	-
	Temp	0.59	0.48	0.22	0.57	0.59	0.47	0.21	0.55
RSFi	L20	0.50	-	-	-	**0.55**	-	-	-
	L135	**0.19**	**0.53**	-	-	0.18	0.50	-	-
	Quex	0.17	0.50	0.62	-	**0.19**	0.50	0.63	-
	Temp	**0.65**	0.59	**0.68**	0.62	**0.65**	**0.60**	0.63	**0.63**

Supplementary Figures

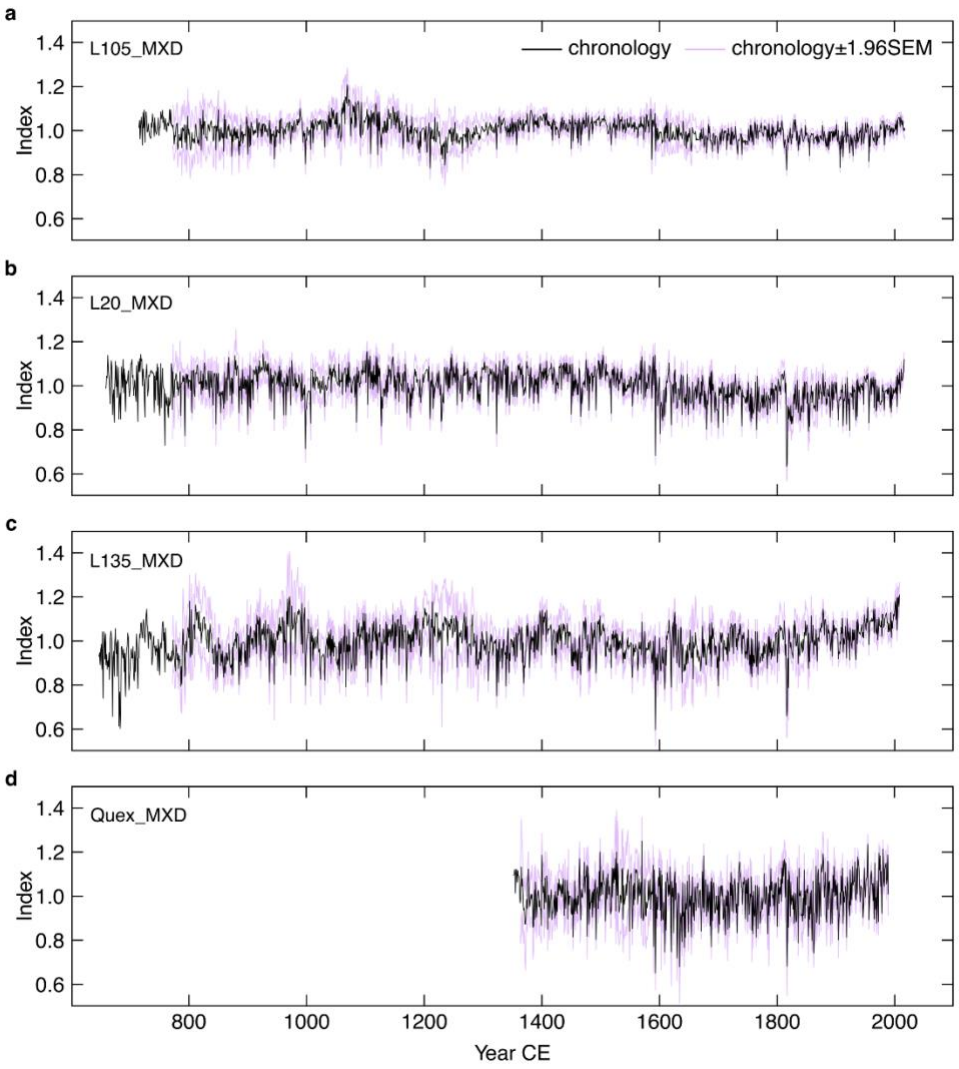

Figure 3-S1: Local MXD chronologies (standardized using the RSFi method; Supplementary Text S3).Purple curves represent the ± 1.96×standard error of mean (SEM) of available MXD data.

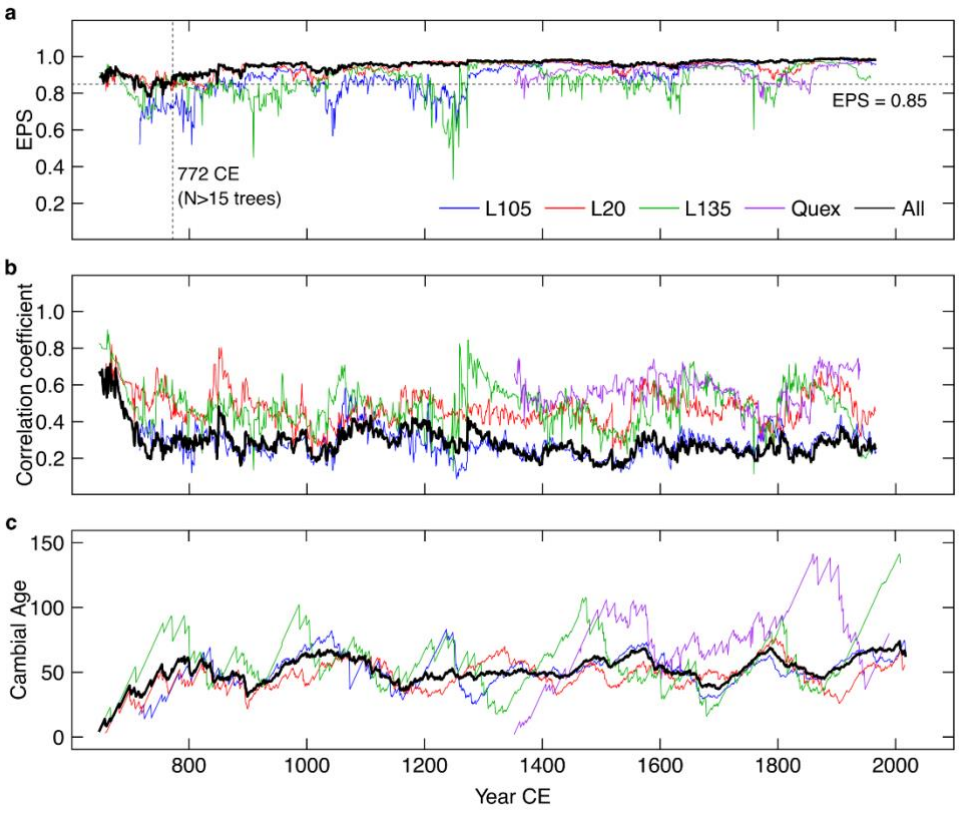

Figure 3-S2: Summary statistics of local and regional MXD series. (**A**) 51-year moving EPS values (*41*) aligned by the first year of each window. The regional EPS is consistently above 0.85 since 772 CE. (**B**) 51-year moving rbar statistics. (**C**) Mean cambial age. Mean cambial age of Quex dataset was estimated using a pith offset of 2 years for each tree series. Thick black curves show the regional statistics calculated using all MXD data.

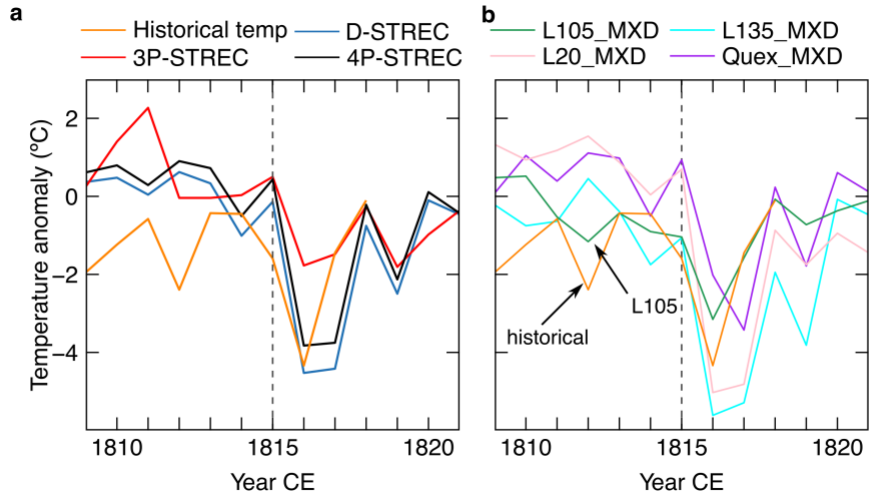

Figure 3-S3: Tambora (1815 CE) cooling recorded in historical MJJA temperatures, three temperature reconstructions, and the MXD chronologies at four sites. L105 is southernmost and closest to the Saint Lawrence Valley where the historical record was developed. L105 MXD chronology shows a consistent pattern from 1815–1817 CE compared to the historical data. The historical and reconstructed temperature series are shown in anomalies w.r.t. 1905–2006 CE. Local MXD chronologies are scaled relative to the historical temperature data over the 1905–2006 period (1905–1989 for the Quex site chronology).

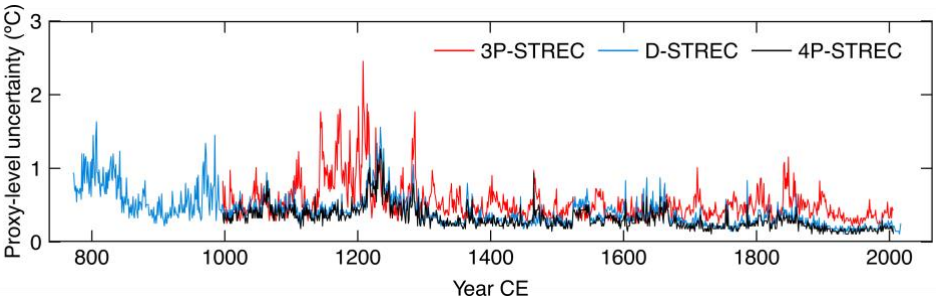

Figure 3-S4: Proxy-level uncertainties of three temperature reconstructions. This is calculated based on differencing the "95% CI + uncertainty" and the "95% CI" of corresponding reconstructions (Materials and Methods). In general, 4P-STREC shows the smallest values, representing that its reconstructed values are the most insensitive to proxy-level uncertainties, such as the measurement errors and individual sample biases.

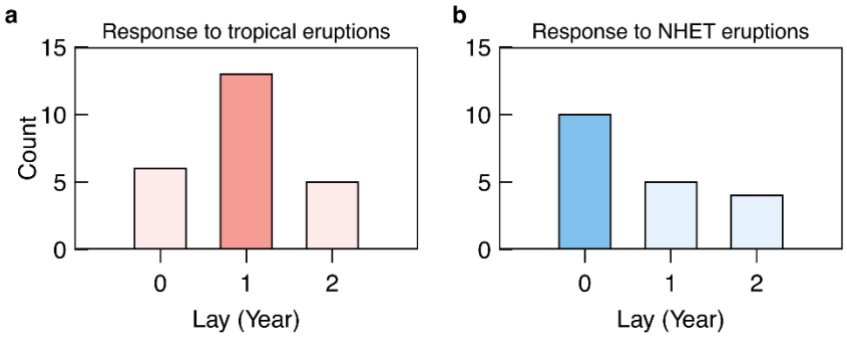

Figure 3-S5: Timing of cooling maxima occurred within 2 years after tropical (**A**) and NHET (**B**) eruptions in 4P-STREC. In line with superposed epoch analysis, the cooling maxima most frequently occurs one year after tropical eruptions and the same year as NHET eruptions, respectively.

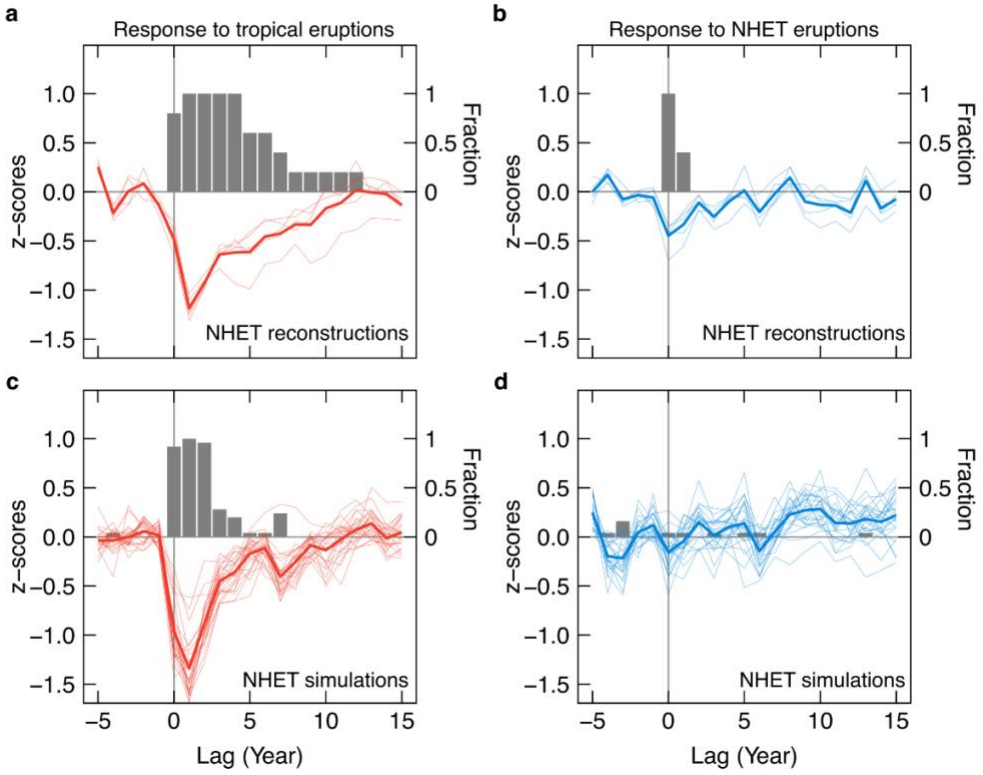

Figure 3-S6: Volcanic responses of NHET tree-ring summer temperature reconstructions (**A**, **B**) and climate model simulations (**C**, **D**). The reconstruction and (CMIP5) simulation time series are the same as those used in Fig. 3-4 and are transformed to z-scores w.r.t. the 1000–2000 period prior to superposed epoch analysis (SEA). SEAs are based on all the tropical (left panel) and NHET eruptions (right panel) listed in Table 3-S7. Thick and thin curves refer to the mean and individual responses, respectively. Bars denote fractions of significant cooling (above the 0.95 statistical level) of individual reconstructions or simulations. A fraction of 1 means that all the time series show significant cooling. Similar to SEA based on 4P-STREC, both NHET summer temperature reconstructions and simulations suggest distinct cooling persistence in response to tropical and NHET eruptions.

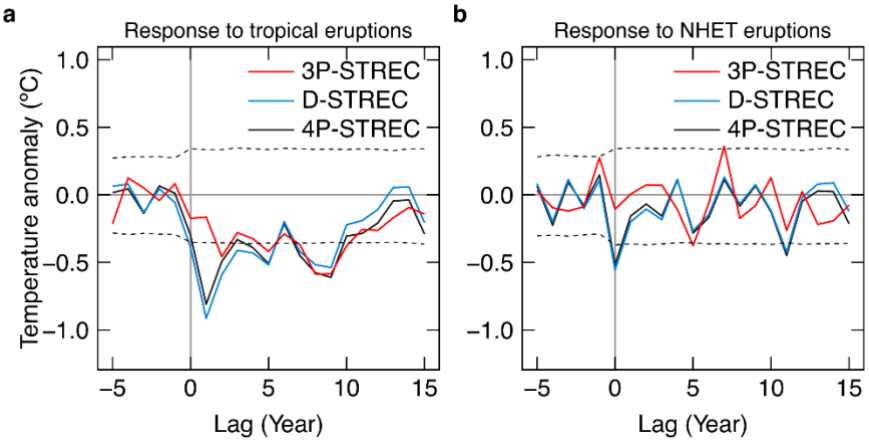

Figure 3-S7: Comparison of volcanic responses among three summer temperature reconstructions in NENA. Superposed epoch analyses are based on all the tropical (**A**) and NHET (**B**) eruptions listed in Table 3-S7. Horizontal dashed lines refer to the 0.95 statistical significance level for 4P-STREC.

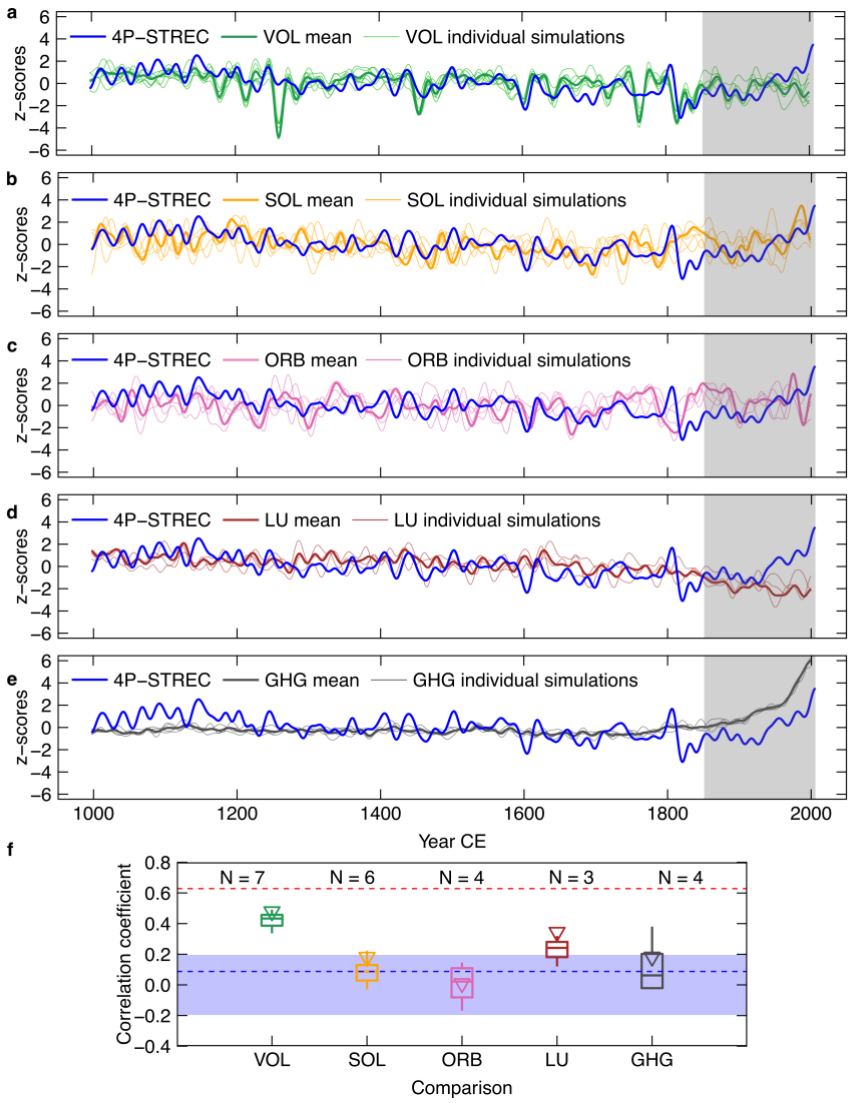

Figure 3-S8: Comparison of 4P-STREC with the single-forcing simulations of NHET land summer temperatures from CESM-LME. (**A**)–(**E**) 4P-STREC versus volcanic (VOL), solar (SOL), orbital (ORB), land use (LU), and greenhouse gases only (GHG) simulations. All the time series are smoothed using a 20-year low-pass Butterworth filter and transformed to z-scores w.r.t. the 1000–2000 time period. (**F**) Pearson's *r* between the smoothed 4P-STREC and the single-forcing simulations during 997–1850 CE. Red and blue dashed lines denote the correlations with the full-forcing multi-model mean and the unforced 850 control, respectively. Boxes show the median and the 25%–75% range, whiskers the 1.5 times interquartile range of correlations with (N) individual simulations. Triangles refer to the correlations with the mean of simulations. Blue shading shows the 95% confidence interval of correlations among 1000 random red-noise series of 4P-STREC and the control run (see Materials and Methods). The post-1850 (shaded) period was excluded for analysis in order to focus on the pre-industrial period.

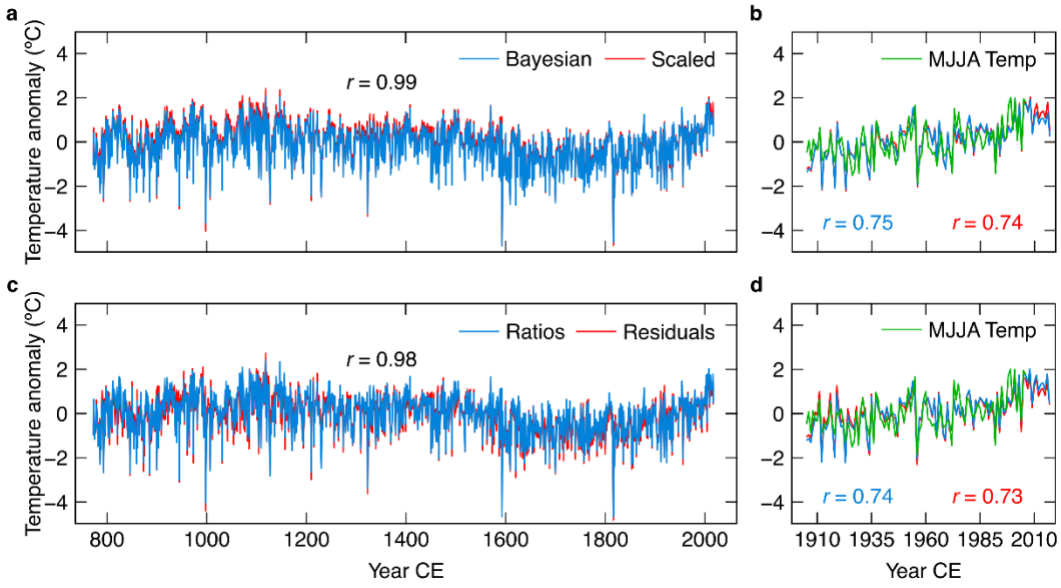

Figure 3-S9: Comparison of temperature reconstruction methods. (**A**, **B**) Reconstructions using RSFi ratio chronologies based on the Bayesian and linear scaling methods. (**C**, **D**) Reconstructions using RSFi ratio and residual chronologies based on the scaling method. *r* values in (**B**) and (**D**) refer to the correlations between reconstructions and the regional MJJA temperature target over the 1905–2006 time period.

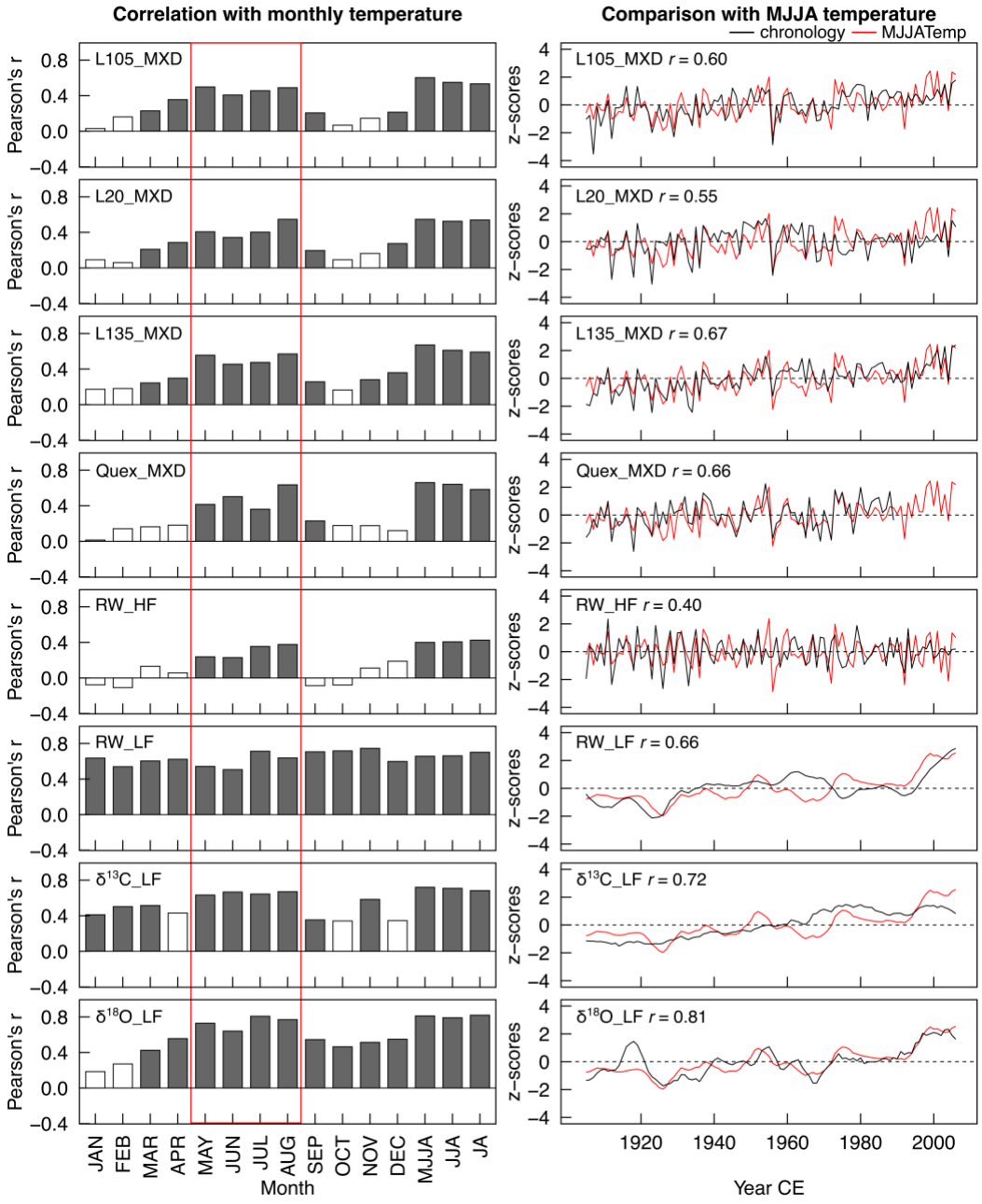

Figure 3-S10: Tree-ring responses to regional mean temperatures from the CRU TS4.03 dataset over the 1905–2006 time period (1905–1989 CE for MXD at Quex). Left panel: monthly temperature correlations where gray bars denote significant Pearson's correlation coefficients ($P < 0.05$; see Materials and Methods). Right panel: comparisons between tree-ring series and MJJA regional mean temperatures. RW: tree-ring width. RW_LF and RW_HF refer to the high- and low-frequency RW components filtered using a 9-year triangular filter, respectively.

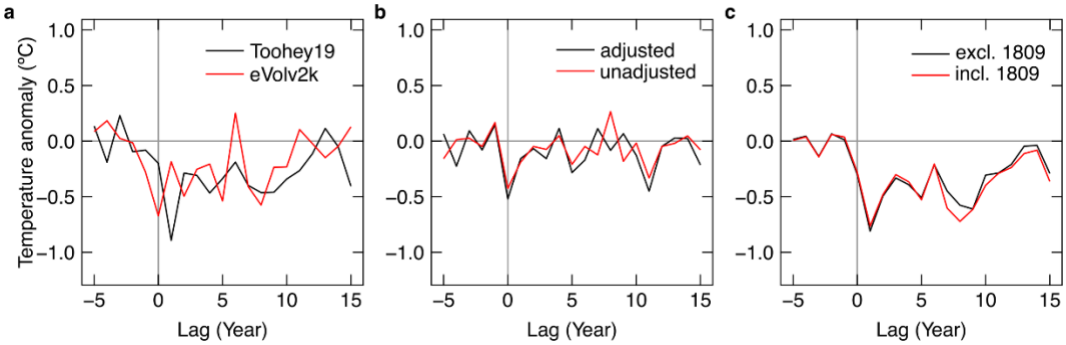

Figure 3-S11: Tests of 4P-STREC responses to volcanic eruptions. (**A**) Superposed epoch analyses (SEA) using 10 tropical events with the key years were derived from Toohey19 (*13*) (1170, 1190, 1229, 1275, 1285, 1343, 1452, 1457, 1586, and 1694 CE) and eVolv2k (*50*) (1171, 1191, 1230, 1276, 1286, 1345, 1453, 1458, 1585, and 1695 CE). (**B**) SEA using 19 NHET events with adjusted and unadjusted eruption years. A few key years were adjusted according to available eruption months (see the first two columns in Table S7). (**C**) SEA using 24 tropical eruptions with (incl. 1809) and without (excl. 1809) the 1809 CE event.

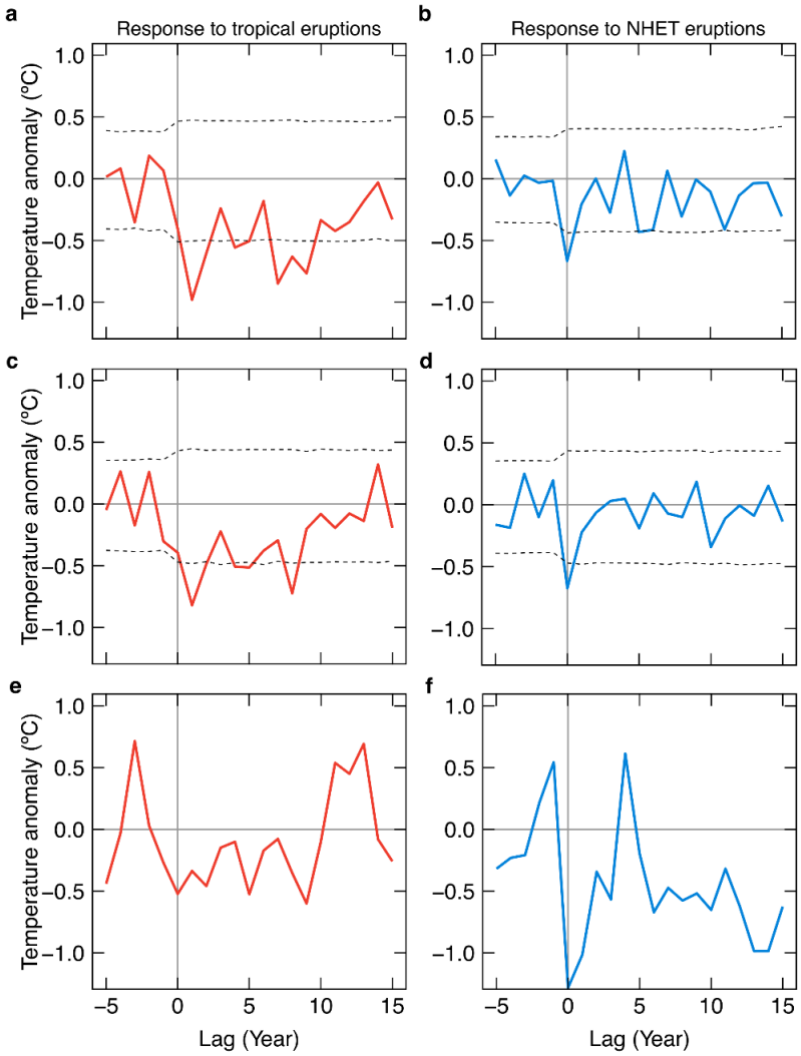

Figure 3-S12: Validation of volcanic responses. (**A**) Superposed epoch analysis (SEA) of 4P-STREC using identified tropical eruptions (1257, 1586, 1593, 1600, 1641, 1673, 1815, 1831, 1835, 1862, 1883, 1903, 1963, and 1982 CE). (**B**) Same as (**A**), but using identified NHET eruptions (1210, 1477, 1480, 1510, 1668, 1708, 1740, 1756, 1766, 1783, 1857, 1873, 1907, and 1912 CE). (**C**) Same as (**A**), but using tropical eruptions not overlapped with other events ($SAOD_{NHET}$ ≥0.03) within ±10 years (1170, 1190, 1229, 1257, 1275, 1285, 1641, 1883, and 1963 CE). (**D**) Same as (**C**), but using NHET eruptions not overlapped with other events ($SAOD_{NHET}$ ≥0.03) within ±10 years (1180, 1210, 1328, 1510, 1708, 1730, 1740, 1783, 1796, and 1873 CE). (**E**) SEA on the MJJA observation target (CRU dataset) using large tropical eruptions (1963 and 1982 CE). (**F**) Same as in (**E**), but using NHET eruptions (1912, 1933, and 1956 CE). The 1933 and 1956 CE eruptions (VEI = 5) were used to increase number of events, although they had peak $SAOD_{NHET}$ smaller than 0.03. The 0.95 statistical significance level is shown in the horizontal dashed lines in (**A**)–(**D**). All tests confirm the distinct responses to tropical and NHET eruptions.

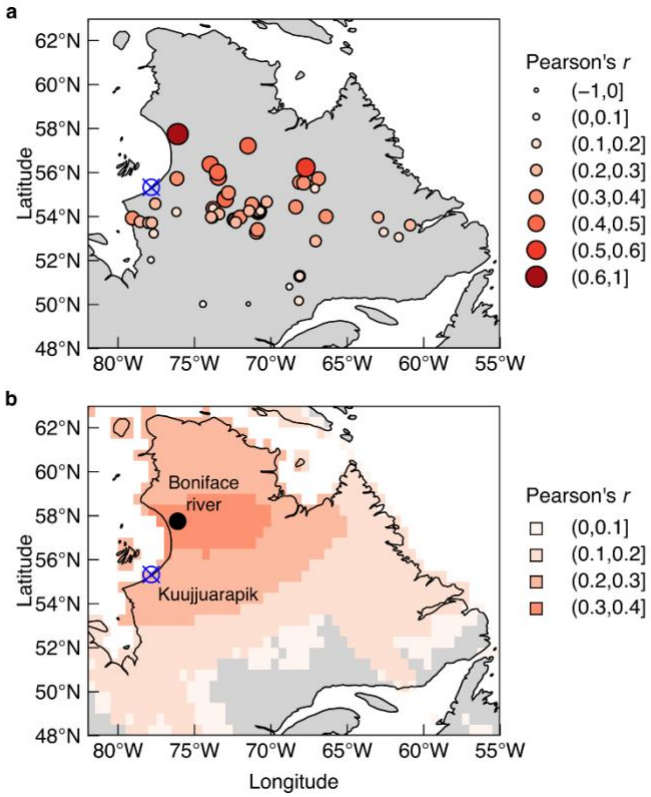

Figure 3-S13: Validation of the location of the Quex tree-ring dataset. (**A**) Spatial pattern of correlation coefficients between the Quex ring-width chronology and 60 black spruce sites over the 1901–1988 period. Ring-width data were obtained from Wang *et al*. (*38*), Boucher *et al*. (*66*), Vallée and Payette (*67*), and the NOAA International Tree Ring Data Bank. (**B**) Correlation field of the Quex ring-width chronology against April–July 0.5º gridded mean temperatures of the CRU TS4.03 dataset over the 1901–1988 period.

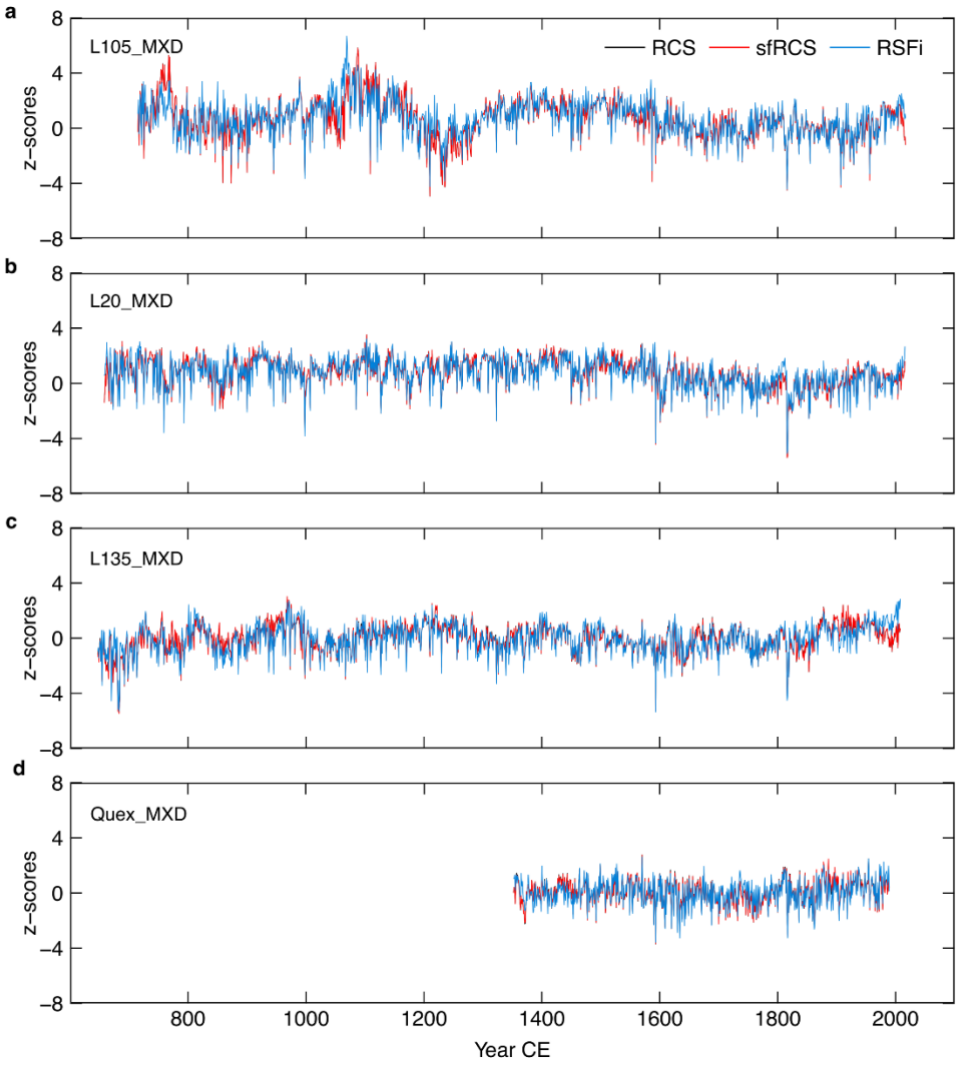

Figure 3-S14: Comparison of standardization methods for MXD ratio chronologies. RCS, regional curve standardization; sfRCS, signal-free regional curve standardization; RSFi, regionally constrained individual signal-free standardization. All chronologies are transformed to z-scores w.r.t. the 1601–2000 time period.

GENERAL CONCLUSION

The primary objective of this research was to develop a robust millennial summer temperature reconstruction for the eastern Canadian boreal forest using temperature-sensitive MXD data or the BI surrogates (i.e., LBI or DBI) measured from living and subfossil samples of black spruce. First, I evaluated the potential of the relatively affordable, simpler, but immature BI technique using living trees from 17 sites (Chapter I) and the stained subfossil trees buried in sediments of two boreal lakes (Chapter II). These two chapters provided comprehensive assessments of the temperature reconstruction performance of BI relative to MXD data over the last few centuries. Second, in Chapter III, I produced the first MXD-based millennial summer temperature reconstructions for northeastern North America. The final reconstruction products include: 1) a 1300-year density-based reconstruction (D-STREC) using three new millennial MXD chronologies (developed from 1,249 trees along a ~800 km south-north transect across the boreal forest of the Québec-Labrador Peninsula) plus an existing, but less replicated (45 trees) 600-year-long chronology previously developed at treeline; and 2) a 1000-year multiproxy reconstruction (4P-STREC) using D-STREC plus low-frequency components from published TRW, $\delta^{18}O$, and $\delta^{13}C$ data (Gennaretti et al., 2014a, 2017; Naulier et al., 2015). Compared to the previous reconstructions using TRW only (Gennaretti et al., 2014a) and TRW plus isotopes (Gennaretti et al., 2017), the two new reconstructions led to an improved knowledge of the regional summer temperature variability and its associated forcing mechanisms during the last millennium.

In Chapter I, I demonstrated that BI measurements from living black spruce trees are promising surrogates for X-ray-based MXD measurements. At the regional scale (the eastern Canadian taiga), both LBI and DBI chronologies built from unstained, living trees highly

resemble the MXD series from the same trees over the 1901–2000 time period. Summer temperature signals contained in the LBI and DBI chronologies are similar to the one contained in the corresponding MXD chronologies, and are much stronger than in TRW data. These results will improve our confidence in the future to use BI measurements of black spruce as robust proxies for dendroclimatic reconstructions. This thesis thus adds to previous studies reporting the strong coherence of BI (LBI and DBI) with MXD data, demonstrating that the BI method is likely applicable and valid for a number of coniferous species across different continents (North America, Eurasia, and even Oceania; McCarroll et al., 2002; Campbell et al., 2007; Rydval et al., 2014; Wilson et al., 2014; Österreicher et al., 2015; Kaczka et al., 2018; Brookhouse and Graham, 2016; Blake et al., 2020). This interesting property of BI data stems out from the fact that both X-ray-based density and blue reflectance chronologies quantify the cell-wall ratio of tree rings (Björklund et al., 2020b).

In chapter I, I also found that LBI and DBI possess their specific properties. LBI is a direct measure of wood surface colors under the blue channel and consistently showed attenuated low-frequency temperature signal compared to MXD across several statistical analyses. Although the tested samples were carefully selected to avoid potential color contamination, this "loss" of relevant climate information appears inherent to LBI measurements due to the high sensitivity to minor color biases (for example, due to incomplete resin extraction) in addition to the lower resolutions of BI measurements compared to the X-ray densitometric method (Björklund et al., 2019). By contrast, DBI of black spruce contains the variance in common between LBI (or MXD) and climate plus some climate information related to TRW. This feature, along with the fact that DBI effectively reduces color biases of wood surface (Björklund et al., 2014, 2015), has led to an enhanced temperature signal in the resultant DBI chronology, at a level comparable to that of MXD. Producing several BI parameters in parallel (e.g., LBI and DBI) is thus recommended in order to develop more robust tree-ring climate reconstructions in the future.

At the same time, application of the promising BI method is largely challenged by discoloration problems appearing on various types of wood materials. In the eastern Canadian boreal forest, subfossil trees buried in lakes and sediments (i.e., LSTs) are an important source of material to extend living-tree chronologies from centuries to millennia with high replications (Arseneault et al., 2013; Gennaretti et al., 2014). In Chapter II, I showed that LSTs buried in lake sediments are frequently stained (~78%) to blue–gray. According to destaining experiments and chemical element analysis, we determined that the stain of LSTs were mainly caused by crystalline iron oxides produced by postsampling oxidation of dissolved ferrous iron that transferred from sediments to buried wood tissues. I also used seven potential chemical destaining reagents (reducing, acidic, chelating and/or bleaching) chemical reagents and found that producing unbiased LBI data is difficult due to incomplete destaining. Nevertheless, three chemical mixtures were capable of extracting > 90% iron absorbed by the wood tissues, indicating the usefulness of these chemicals to remove iron from wood materials in fields of archaeology and geology. Regarding dendroclimatology, the residual stains introduce substantial biases when raw LBI measurements are used to reconstruct temperatures, leading to a discrepancy of ~4^{o} C relative to a reconstruction based on MXD data from the same samples. However, the mathematical correction of LBI, i.e., DBI, appears to be insensitive to the iron stain and displays similar inter-annual to centennial trends compared to the MXD-based reconstruction. These results, along with the slightly stronger temperature sensitivity of DBI observed from living black spruce trees in Chapter I, suggest that DBI of stained LSTs and living-tree samples can be combined to perform high-quality millennial summer temperature reconstructions from black spruce, the most dominant tree species in the North American boreal forest, and probably for other regions and species where iron-stained LSTs have been/will be discovered.

Although in Chapters I and II, I verified the dendroclimatic potential of BI measurements from black spruce, I also found that maximum latewood density remains the most sensitive temperature proxy among the four examined tree-ring parameters (LBI, DBI, MXD, and TRW). Compared to BI parameters and TRW, MXD is not affected by iron stains

and is less sensitive to low tree replication. Thus, MXD still represents one of the most powerful proxies for reconstructing summer temperatures in cool regions if the costly X-ray equipment is available. Meanwhile, the BI method can serve as a reliable complement to the X-ray densitometric technique to produce surrogates of MXD. With the maturation of the BI technique, it will certainly help understand past climate trends beyond as is revealed using TRW data.

Therefore, in Chapter III, I used a new network consisting of an unprecedented number of MXD series from the eastern Canadian boreal forests in order to reconstruct the regional millennial summer temperatures. The high replication, multiple sites, and the inherent advantages of MXD data have made D-STREC and 4P-STREC the two most robust millennial summer temperature reconstructions ever published for the northeastern half of the North American continent. D-STREC and 4P-STREC calibrated more strongly against the regional MJJA temperature observations than the 3P-STREC reconstruction based on TRW, $\delta^{18}O$, and $\delta^{13}C$ data, and display much larger spatial domains, which are almost identical to the correlation filed of the temperature observations. Moreover, comparison with a long instrumental record from southern Québec (Slonovsky et al., 2015) indicates that the two MXD-derived reconstructions more precisely record the volcanic-induced cooling following the Tambora eruption (1815 CE), compared to the substantial (~2.5 ^{o} C) underestimation of 3P-STREC. In addition, 4P-STREC and D-STREC perfectly express the decadal and interannual volcanic cooling persistence. These improvements arise mostly from the superiority of MXD data which can precisely capture the inter-annual temperature variability due to relatively weak biological memory (Esper et al., 2015), highlighting the critical importance of MXD in investigating the volcanic forcing mechanism within the climate system. In fact, 4P-STREC even displays better reconstruction performance than the D-STREC reconstruction because its low-frequency domain is complemented by four types of tree-ring proxies (i.e., MXD, TRW, $\delta^{18}O$, and $\delta^{13}C$), indicating the advantage of the multiproxy approach to optimize climate reconstructions.

The 4P-STREC record provided major scientific advances. First, it showed that Northeastern North America (NENA) has experienced unprecedented warmth since the beginning of the 20th century, including the strongest centennial warming trend (1903–2004 CE) and the warmest decade (1997–2006 CE). Second, it showed that the summers of the Medieval Climate Anomaly (~997–1250 CE) were relatively warm, in line with several paleoclimatic studies in pan-North-Atlantic regions. The average summer temperatures during the medieval times equalled recent temperatures of the 1931–2006 period. In contrast, the Little Ice Age (1251–1930 CE) was relative cold (−0.27ºC relative to 1905–2006 CE), especially around ~1601–1930 CE, when several of the coldest decades in the last millennium occurred. Third, it showed that the multidecadal regional temperature variability has been highly correlated with tree-ring-based reconstructions and climate model simulations performed at the much larger scale of the Northern Hemisphere extratropics (NHET). I attributed this regional-hemispheric coherence to the dominant role of volcanic forcing, emphasized by a relatively high correlation between 4P-STREC and the only volcano-forced simulation of NHET summer temperatures for the pre-industrial era. Fourth, it showed that both tropical and NHET volcanic eruptions have played important roles in cooling summer temperatures in NENA. At the regional and Northern Hemispheric scales, cooling induced by tropical eruptions peaks the first year and tends to last ~12 years. In contrast, the climatic effect of NHET eruptions is much shorter (1–3 years) and similar to the period of volcanic aerosol forcing. It often peaked in the same year of the eruptions. These results indicate tropical eruptions have a played more prominent role than NHET eruptions, in synchronizing the regional and hemispheric multidecadal summer temperature variability. The distinct cooling persistence of tropical and NHET eruptions likely reflects different propagation of radiative forcing across the ocean and atmosphere (i.e., aerosols of tropical eruptions spread across the globe while aerosols of NHET eruptions are mainly constrained in the NHET region).

In conclusion, this thesis provides strong evidence that the BI method is a promising alternative to obtain tree-ring density data. In addition, it has filled a critical data gap of

Northern Hemisphere MXD-based reconstructions and improved our understanding of the millennial summer temperature variability and its volcanic forcing mechanisms in northeastern North America. These results will encourage the production of more tree-ring density (or blue intensity) records from coniferous species across the Northern Hemisphere and even the Southern Hemisphere. The two summer temperature reconstructions developed in this research are important archives of climate variability in the eastern Canadian boreal forest. These reconstructions provide more accurate assessment of the timing and amplitudes of important historical climate epochs to place the recent warming in a more rigorous historical context. They will help to assess the long-term dynamics of the associated climate factors (such as the hydroclimate which is an important energy source of Québec), the boreal forest productivity, and even the fire history. Furthermore, the new reconstructions can contribute to data-model comparisons as well as detection and attribution studies to disentangle the impacts of natural and anthropogenic forcings from the internal climate variability. Future efforts can be made to validate the usefulness of delta blue intensity parameter on the millennial timescale, to develop more and longer regional MXD chronologies over the entire Common Era, and to apply more sophisticated methods such as the BARCAST climate field reconstruction (Tingley and Huybers, 2010) and the inverse modeling approach based on physiological models (Boucher et al., 2017), in order to produce more comprehensive regional climate variability in the eastern Canadian boreal forest.

REFERENCES

Anchukaitis, K.J., Wilson, R., Briffa, K.R., Büntgen, U., Cook, E.R., D'Arrigo, R., Davi, N., Esper, J., Frank, D., Gunnarson, B.E., Hegerl, G., Helama, S., Klesse, S., Krusic, P.J., Linderholm, H.W., Myglan, V., Osborn, T.J., Zhang, P., Rydval, M., Schneider, L., Schurer, A., Wiles, G., Zorita, E., 2017. Last millennium Northern Hemisphere summer temperatures from tree rings: Part II, spatially resolved reconstructions. Quat. Sci. Rev. 163, 1–22. https://doi.org/10.1016/j.quascirev.2017.02.020

Arbellay, E., Jarvis, I., Chavardès, R.D., Daniels, L.D., Stoffel, M., 2018. Tree-ring proxies of larch bud moth defoliation: latewood width and blue intensity are more precise than tree-ring width. Tree Physiol. 38, 1237–1245. https://doi.org/10.1093/treephys/tpy057

Arosio, T., Ziehmer, M.M., Nicolussi, K., Schlüchter, C., Leuenberger, M., 2020. Alpine Holocene tree-ring dataset: age-related trends in the stable isotopes of cellulose show species-specific patterns. Biogeosciences 17, 4871–4882. https://doi.org/10.5194/bg-17-4871-2020

Arseneault, D., Payette, S., 1997. Reconstruction of millennial forest dynamics from tree remains in a subarctic tree line peatland. Ecology 78, 1873–1883. https://doi.org/10.1890/0012-9658(1997)078[1873:ROMFDF]2.0.CO;2

Arseneault, D., Dy, B., Gennaretti, F., Autin, J., Bégin, Y., 2013. Developing millennial tree ring chronologies in the fire-prone North American boreal forest. J. Quat. Sci. 28, 283–292. https://doi.org/10.1002/jqs.2612

Autin, J., Gennaretti, F., Arseneault, D., Bégin, Y., 2015. Biases in RCS tree ring chronologies due to sampling heights of trees. Dendrochronologia 36, 13–22. https://doi.org/10.1016/j.dendro.2015.08.002

Bajolle, L., Larocque-Tobler, I., Gandouin, E., Lavoie, M., Bergeron, Y., Ali, A.A., 2018. Major postglacial summer temperature changes in the central coniferous boreal forest of Quebec (Canada) inferred using chironomid assemblages. J. Quat. Sci. 33, 409–420. https://doi.org/10.1002/jqs.3022

Bergeron, Y., Fenton, N.J., 2012. Boreal forests of eastern Canada revisited: old growth, nonfire disturbances, forest succession, and biodiversity. Botany 90, 509–523. https://doi.org/10.1139/b2012-034

Björklund, J.A., Gunnarson, B.E., Krusic, P.J., Grudd, H., Josefsson, T., Östlund, L., Linderholm, H.W., 2013. Advances towards improved low-frequency tree-ring reconstructions, using an updated Pinus sylvestris L. MXD network from the Scandinavian Mountains. Theor. Appl. Climatol. 113, 697–710. https://doi.org/10.1007/s00704-012-0787-7

Björklund, J., Gunnarson, B.E., Seftigen, K., Esper, J., Linderholm, H.W., 2014. Blue intensity and density from northern Fennoscandian tree rings, exploring the potential to improve summer temperature reconstructions with earlywood information. Clim. Past 10, 877–885. https://doi.org/10.5194/cp-10-877-2014

Björklund, J., Gunnarson, B.E., Seftigen, K., Zhang, P., Linderholm, H.W., 2015. Using adjusted Blue Intensity data to attain high-quality summer temperature information: A case study from Central Scandinavia. The Holocene 25, 547–556. https://doi.org/10.1177/0959683614562434

Björklund, J., Seftigen, K., Schweingruber, F., Fonti, P., von Arx, G., Bryukhanova, M.V., Cuny, H.E., Carrer, M., Castagneri, D., Frank, D.C., 2017. Cell size and wall dimensions drive distinct variability of earlywood and latewood density in Northern Hemisphere conifers. New Phytol. 216, 728–740. https://doi.org/10.1111/nph.14639

Björklund, J., von Arx, G., Nievergelt, D., Wilson, R., Van den Bulcke, J., Günther, B., Loader, N.J., Rydval, M., Fonti, P., Scharnweber, T., Andreu-Hayles, L., Büntgen, U., D'Arrigo, R., Davi, N., De Mil, T., Esper, J., Gärtner, H., Geary, J., Gunnarson, B.E., Hartl, C., Hevia, A., Song, H., Janecka, K., Kaczka, R.J., Kirdyanov, A.V., Kochbeck, M., Liu, Y., Meko, M., Mundo, I., Nicolussi, K., Oelkers, R., Pichler, T., Sánchez-Salguero, R., Schneider, L., Schweingruber, F., Timonen, M., Trouet, V., Van Acker, J., Verstege, A., Villalba, R., Wilmking, M., Frank, D., 2019. Scientific merits and analytical challenges of tree-ring densitometry. Rev. Geophys. 57, 1224–1264. https://doi.org/10.1029/2019RG000642

Björklund, J., Seftigen, K., Fonti, P., Nievergelt, D., von Arx, G., 2020a. Dendroclimatic potential of dendroanatomy in temperature-sensitive *Pinus sylvestris*. Dendrochronologia 60, 125673. https://doi.org/10.1016/j.dendro.2020.125673

Björklund, J., Fonti, M.V., Fonti, P., den Bulcke, J.V., von Arx, G., 2020b. Cell wall dimensions reign supreme: cell wall composition is irrelevant for the temperature signal of latewood density/blue intensity in Scots pine. Dendrochronologia 125785. https://doi.org/10.1016/j.dendro.2020.125785

Blake, S.A.P., Palmer, J.G., Björklund, J., Harper, J.B., Turney, C.S.M., 2020. Palaeoclimate potential of New Zealand *Manoao colensoi* (silver pine) tree rings using Blue-Intensity (BI). Dendrochronologia 60, 125664. https://doi.org/10.1016/j.dendro.2020.125664

Boucher, E., Nicault, A., Arseneault, D., Bégin, Y., Karami, M.P., 2017. Decadal variations in eastern Canada's taiga wood biomass production forced by ocean-atmosphere interactions. Sci. Rep. 7, 2457. https://doi.org/10.1038/s41598-017-02580-9

Briffa, K.R., Jones, P.D., Bartholin, T.S., Eckstein, D., Schweingruber, F.H., Karlén, W., Zetterberg, P., Eronen, M., 1992. Fennoscandian summers from ad 500: temperature changes on short and long timescales. Clim. Dyn. 7, 111–119. https://doi.org/10.1007/BF00211153

Briffa, K.R., Osborn, T.J., Schweingruber, F.H., Jones, P.D., Shiyatov, S.G., Vaganov, E.A., 2002. Tree-ring width and density data around the Northern Hemisphere: Part 1, local and regional climate signals. The Holocene 12, 737–757. https://doi.org/10.1191/0959683602hl587rp

Briffa, K.R., Melvin, T.M., 2011. A closer look at regional curve standardization of tree-ring records: justification of the need, a warning of some pitfalls, and suggested improvements in its application, in: Hughes, M.K., Swetnam, T.W., Diaz, H.F. (Eds.), Dendroclimatology: Progress and Prospects. Springer Netherlands, Dordrecht, pp. 113–145. https://doi.org/10.1007/978-1-4020-5725-0_5

Brookhouse, M., Graham, R., 2016. Application of the minimum blue-intensity technique to a southern-hemisphere conifer. Tree-Ring Res. 72, 103–107. https://doi.org/10.3959/1536-1098-72.02.103

Buckley, B.M., Hansen, K.G., Griffin, K.L., Schmiege, S., Oelkers, R., D'Arrigo, R.D., Stahle, D.K., Davi, N., Nguyen, T.Q.T., Le, C.N., Wilson, R.J.S., 2018. Blue intensity from a tropical conifer's annual rings for climate reconstruction: An ecophysiological perspective. Dendrochronologia 50, 10–22. https://doi.org/10.1016/j.dendro.2018.04.003

Büntgen, U., Kyncl, T., Ginzler, C., Jacks, D.S., Esper, J., Tegel, W., Heussner, K.-U., Kyncl, J., 2013. Filling the Eastern European gap in millennium-long temperature reconstructions. Proc. Natl. Acad. Sci. 110, 1773. https://doi.org/10.1073/pnas.1211485110

Büntgen, U., Arseneault, D., Boucher, É., Churakova (Sidorova), O.V., Gennaretti, F., Crivellaro, A., Hughes, M.K., Kirdyanov, A.V., Klippel, L., Krusic, P.J., Linderholm, H.W., Ljungqvist, F.C., Ludescher, J., McCormick, M., Myglan, V.S., Nicolussi, K., Piermattei, A., Oppenheimer, C., Reinig, F., Sigl, M., Vaganov, E.A., Esper, J., 2020. Prominent role of volcanism in Common Era climate variability and human history. Dendrochronologia 64, 125757. https://doi.org/10.1016/j.dendro.2020.125757

Campbell, R., McCarroll, D., Loader, N.J., Grudd, H., Robertson, I., Jalkanen, R., 2007. Blue intensity in *Pinus sylvestris* tree-rings: developing a new palaeoclimate proxy. The Holocene 17, 821–828. https://doi.org/10.1177/0959683607080523

Campbell, R., McCarroll, D., Robertson, I., Loader, N.J., Grudd, H., Gunnarson, B., 2011. Blue intensity in *Pinus sylvestris* tree rings: a manual for a new palaeoclimate proxy. Tree-Ring Res. 67, 127–134. https://doi.org/10.3959/2010-13.1

Cao, X., Fang, K., Chen, P., Zhang, P., Björklund, J., Pumijumnong, N., Guo, Z., 2020. Microdensitometric records from humid subtropical China show distinct climate signals in earlywood and latewood. Dendrochronologia 64, 125764. https://doi.org/10.1016/j.dendro.2020.125764

Chen, F., Yuan, Y., Wei, W., Yu, S., Zhang, T., 2012. Reconstructed temperature for Yong'an, Fujian, Southeast China: Linkages to the Pacific Ocean climate variability. Glob. Planet. Change 86–87, 11–19. https://doi.org/10.1016/j.gloplacha.2012.01.005

Christiansen, B., Ljungqvist, F.C., 2017. Challenges and perspectives for large-scale temperature reconstructions of the past two millennia. Rev. Geophys. 55, 40–96. https://doi.org/10.1002/2016RG000521

Cook, E.R., Briffa, K.R., Meko, D.M., Graybill, D.A., Funkhouser, G., 1995. The "segment length curse" in long tree-ring chronology development for palaeoclimatic studies. The Holocene 5, 229–237. https://doi.org/10.1177/095968369500500211

Cyr, D., Gauthier, S., Bergeron, Y., Carcaillet, C., 2009. Forest management is driving the eastern North American boreal forest outside its natural range of variability. Front. Ecol. Environ. 7, 519–524. https://doi.org/10.1890/080088

Delwaide, A., Asselin, H., Arseneault, D., Lavoie, C., Payette, S., 2021. A 2233-year tree-ring chronology of subarctic black spruce (*Picea mariana*): growth forms response to long-term climate change. Écoscience, DOI: 10.1080/11956860.2021.1952014

Dinis, L., Bégin, C., Savard, M.M., Marion, J., Brigode, P., Alvarez, C., 2019. Tree-ring stable isotopes for regional discharge reconstruction in eastern Labrador and teleconnection with the Arctic Oscillation. Clim. Dyn. 53, 3625–3640. https://doi.org/10.1007/s00382-019-04731-2

Dolgova, E., 2016. June–September temperature reconstruction in the Northern Caucasus based on blue intensity data. Dendrochronologia 39, 17–23. https://doi.org/10.1016/j.dendro.2016.03.002

D'Orangeville, L., Duchesne, L., Houle, D., Kneeshaw, D., Côté, B., Pederson, N., 2016. Northeastern North America as a potential refugium for boreal forests in a warming climate. Science 352, 1452. https://doi.org/10.1126/science.aaf4951

Duffy, J.E., McCarroll, D., Loader, N.J., Young, G.H.F., Davies, D., Miles, D., Bronk Ramsey, C., 2019. Absence of age-related trends in stable oxygen isotope ratios from oak tree rings. Glob. Biogeochem. Cycles 33, 841–848. https://doi.org/10.1029/2019GB006195

Environment and Climate Change Canada, 2020. Canadian Climate Normals or Averages 1981-2010. http://climate.weather.gc.ca/climate_normals/index_e.html. Last access: 14 March 2020.

Esper, J., Frank, D., Büntgen, U., Kirdyanov, A., 2008. Influence of pith offset on tree-ring chronology trend. TRACE–Tree Rings Archaeol. Climatol. Ecol. 7, 205–210.

Esper, J., Frank, D.C., Timonen, M., Zorita, E., Wilson, R.J.S., Luterbacher, J., Holzkämper, S., Fischer, N., Wagner, S., Nievergelt, D., Verstege, A., Büntgen, U., 2012. Orbital forcing of tree-ring data. Nat. Clim. Change 2, 862–866. 10.1038/NCLIMATE1589

Esper, J., Schneider, L., Krusic, P.J., Luterbacher, J., Büntgen, U., Timonen, M., Sirocko, F., Zorita, E., 2013. European summer temperature response to annually dated volcanic eruptions over the past nine centuries. Bull. Volcanol. 75, 736. https://doi.org/10.1007/s00445-013-0736-z

Esper, J., Düthorn, E., Krusic, P.J., Timonen, M., Büntgen, U., 2014. Northern European summer temperature variations over the Common Era from integrated tree-ring density records. J. Quat. Sci. 29, 487–494. https://doi.org/10.1002/jqs.2726

Esper, J., Schneider, L., Smerdon, J.E., Schöne, B.R., Büntgen, U., 2015. Signals and memory in tree-ring width and density data. Dendrochronologia 35, 62–70. https://doi.org/10.1016/j.dendro.2015.07.001

Esper, J., Krusic, P.J., Ljungqvist, F.C., Luterbacher, J., Carrer, M., Cook, E., Davi, N.K., Hartl-Meier, C., Kirdyanov, A., Konter, O., Myglan, V., Timonen, M., Treydte, K., Trouet, V., Villalba, R., Yang, B., Büntgen, U., 2016. Ranking of tree-ring based temperature reconstructions of the past millennium. Quat. Sci. Rev. 145, 134–151. https://doi.org/10.1016/j.quascirev.2016.05.009

Esper, J., St. George, S., Anchukaitis, K., D'Arrigo, R., Ljungqvist, F.C., Luterbacher, J., Schneider, L., Stoffel, M., Wilson, R., Büntgen, U., 2018. Large-scale, millennial-length temperature reconstructions from tree-rings. Dendrochronologia 50, 81–90. https://doi.org/10.1016/j.dendro.2018.06.001

Esper, J., Klippel, L., Krusic, P.J., Konter, O., Raible, C.C., Xoplaki, E., Luterbacher, J., Büntgen, U., 2020. Eastern Mediterranean summer temperatures since 730 CE from Mt. Smolikas tree-ring densities. Clim. Dyn. 54, 1367–1382. https://doi.org/10.1007/s00382-019-05063-x

Filion, L., Payette, S., Gauthier, L., Boutin, Y., 1986. Light rings in subarctic conifers as a dendrochronological tool. Quat. Res. 26, 272–279. https://doi.org/10.1016/0033-5894(86)90111-0

Frank, D., Esper, J., 2005. Characterization and climate response patterns of a high-elevation, multi-species tree-ring network in the European Alps. Dendrochronologia 22, 107–121. https://doi.org/10.1016/j.dendro.2005.02.004

Frank, D., Büntgen, U., Böhm, R., Maugeri, M., Esper, J., 2007. Warmer early instrumental measurements versus colder reconstructed temperatures: shooting at a moving target. Quat. Sci. Rev. 26, 3298–3310. https://doi.org/10.1016/j.quascirev.2007.08.002

Franke, J., Frank, D., Raible, C.C., Esper, J., Brönnimann, S., 2013. Spectral biases in tree-ring climate proxies. Nat. Clim. Change 3, 360–364. https://doi.org/10.1038/nclimate1816

Fritts, H., 1976. Tree Rings and Climate, 1st ed. Academic Press, London.

Fuentes, M., Salo, R., Björklund, J., Seftigen, K., Zhang, P., Gunnarson, B., Aravena, J.-C., Linderholm, H.W., 2017. A 970-year-long summer temperature reconstruction from Rogen, west-central Sweden, based on blue intensity from tree rings. The Holocene 28, 254–266. https://doi.org/10.1177/0959683617721322

Gagen, M., McCarroll, D., Loader, N.J., Robertson, I., Jalkanen, R., Anchukaitis, K.J., 2007. Exorcising the `segment length curse': summer temperature reconstruction since AD 1640 using non-detrended stable carbon isotope ratios from pine trees in northern Finland. The Holocene 17, 435–446. https://doi.org/10.1177/0959683607077012

Gagnon-Poiré, A., Brigode, P., Francus, P., Fortin, D., Lajeunesse, P., Dorion, H., Trottier, A.-P., 2020. Reconstructing past hydrology of eastern Canadian boreal catchments using clastic varved sediments and hydro-climatic modeling: 160 years of fluvial inflows. Clim. Past Discuss. 2020, 1–40. https://doi.org/10.5194/cp-2020-87

Gennaretti, F., Arseneault, D., Nicault, A., Perreault, L., Bégin, Y., 2014a. Volcano-induced regime shifts in millennial tree-ring chronologies from northeastern North America. Proc. Natl. Acad. Sci. 111, 10077. https://doi.org/10.1073/pnas.1324220111

Gennaretti, F., Arseneault, D., Bégin, Y., 2014b. Millennial stocks and fluxes of large woody debris in lakes of the North American taiga. J. Ecol. 102, 367–380. https://doi.org/10.1111/1365-2745.12198

Gennaretti, F., Arseneault, D., Bégin, Y., 2014c. Millennial disturbance-driven forest stand dynamics in the Eastern Canadian taiga reconstructed from subfossil logs. J. Ecol. 102, 1612–1622. https://doi.org/10.1111/1365-2745.12315

Gennaretti, F., Huard, D., Naulier, M., Savard, M., Bégin, C., Arseneault, D., Guiot, J., 2017. Bayesian multiproxy temperature reconstruction with black spruce ring widths and stable isotopes from the northern Quebec taiga. Clim. Dyn. 49, 4107–4119. https://doi.org/10.1007/s00382-017-3565-5

Girardin, M.-P., Tardif, J., Flannigan, M.D., Bergeron, Y., 2004. Multicentury reconstruction of the Canadian Drought Code from eastern Canada and its relationship with paleoclimatic indices of atmospheric circulation. Clim. Dyn. 23, 99–115. https://doi.org/10.1007/s00382-004-0417-x

Guillet, S., Corona, C., Ludlow, F., Oppenheimer, C., Stoffel, M., 2020. Climatic and societal impacts of a "forgotten" cluster of volcanic eruptions in 1108-1110 CE. Sci. Rep. 10, 6715. https://doi.org/10.1038/s41598-020-63339-3

Harley, G.L., Heeter, K.J., Maxwell, J.T., Rayback, S.A., Maxwell, R.S., Reinemann, T.E.P., H. Taylor, A., 2020. Towards broad-scale temperature reconstructions for Eastern North America using blue light intensity from tree rings. Int. J. Climatol. https://doi.org/10.1002/joc.6910

Heeter, K.J., Harley, G.L., Maxwell, J.T., McGee, J.H., Matheus, T.J., 2020. Late summer temperature variability for the Southern Rocky Mountains (USA) since 1735 CE: applying blue light intensity to low-latitude *Picea engelmannii* Parry ex Engelm. Clim. Change 162, 965–988. https://doi.org/10.1007/s10584-020-02772-9

Heeter, K.J., Rochner, M.L., Harley, G.L., 2021a. Summer air temperature for the greater Yellowstone ecoregion (770–2019 CE) over 1,250 years. Geophys. Res. Lett. 48, e2020GL092269. https://doi.org/10.1029/2020GL092269

Heeter, K.J., Harley, G.L., Maxwell, J.T., Wilson, R.J., Abatzoglou, J.T., Rayback, S.A., Rochner, M.L., Kitchens, K.A., 2021b. Summer temperature variabilsity since 1730 CE across the low-to-mid latitudes of western North America from a tree ring blue intensity network. Quat. Sci. Rev. 267, 107064. https://doi.org/10.1016/j.quascirev.2021.107064

Hegerl, G.C., Crowley, T.J., Allen, M., Hyde, W.T., Pollack, H.N., Smerdon, J., Zorita, E., 2007. Detection of human influence on a new, validated 1500-year temperature reconstruction. J. Clim. 20, 650–666. https://doi.org/10.1175/JCLI4011.1

Helama, S., Melvin, T.M., Briffa, K.R., 2017. Regional curve standardization: State of the art. The Holocene 27, 172–177. https://doi.org/10.1177/0959683616652709

Hély, C., Girardin, M.P., Ali, A.A., Carcaillet, C., Brewer, S., Bergeron, Y., 2010. Eastern boreal North American wildfire risk of the past 7000 years: A model-data comparison. Geophys. Res. Lett. 37, L14709. https://doi.org/10.1029/2010GL043706

IPCC, 2013. Summary for Policymakers, in: Climate Change 2013: The Physical Science Basis. Contribution of Working Group I to the Fifth Assessment Report of the Intergovernmental Panel on Climate Change [Stocker, T.F., D. Qin, G.-K. Plattner, M. Tignor, S.K. Allen, J. Boschung, A. Nauels, Y. Xia, V. Bex and P.M. Midgley (eds.)]. Cambridge University Press, Cambridge, pp. 1–30. https://doi.org/10.1017/CBO9781107415324.004

Jacquin, P., Longuetaud, F., Leban, J.-M., Mothe, F., 2017. X-ray microdensitometry of wood: A review of existing principles and devices. Dendrochronologia 42, 42–50. https://doi.org/10.1016/j.dendro.2017.01.004

Jones, P.D., Briffa, K.R., Osborn, T.J., Lough, J.M., van Ommen, T.D., Vinther, B.M., Luterbacher, J., Wahl, E.R., Zwiers, F.W., Mann, M.E., Schmidt, G.A., Ammann, C.M., Buckley, B.M., Cobb, K.M., Esper, J., Goosse, H., Graham, N., Jansen, E., Kiefer, T., Kull, C., Küttel, M., Mosley-Thompson, E., Overpeck, J.T., Riedwyl, N., Schulz, M., Tudhope, A.W., Villalba, R., Wanner, H., Wolff, E., Xoplaki, E., 2009. High-resolution palaeoclimatology of the last millennium: a review of current status and future prospects. The Holocene 19, 3–49. https://doi.org/10.1177/0959683608098952

Kaczka, R.J., Spyt, B., Janecka, K., Beil, I., Büntgen, U., Scharnweber, T., Nievergelt, D., Wilmking, M., 2018. Different maximum latewood density and blue intensity measurements techniques reveal similar results. Dendrochronologia 49, 94–101. https://doi.org/10.1016/j.dendro.2018.03.005

Kampe, A., Magel, E., 2013. New insights into heartwood and heartwood formation, in: Fromm, J. (Ed.), Cellular aspects of wood formation, plant cell monographs. Springer Berlin Heidelberg, Berlin, Heidelberg, pp. 71–95. https://doi.org/10.1007/978-3-642-36491-4_3

Kerwin, M.W., Overpeck, J.T., Webb, R.S., Anderson, K.H., 2004. Pollen-based summer temperature reconstructions for the eastern Canadian boreal forest, subarctic, and Arctic. Quat. Sci. Rev. 23, 1901–1924. https://doi.org/10.1016/j.quascirev.2004.03.013

Lavoie, C., Payette, S., 1997. Late-Holocene light-ring chronologies from subfossil black spruce stems in mires of subarctic Québec. The Holocene 7, 129–137. https://doi.org/10.1177/095968369700700201

Linderholm, H.W., Björklund, J., Seftigen, K., Gunnarson, B.E., Fuentes, M., 2015. Fennoscandia revisited: a spatially improved tree-ring reconstruction of summer temperatures for the last 900 years. Clim. Dyn. 45, 933–947. https://doi.org/10.1007/s00382-014-2328-9

Liu, Y., Wang, Y., Li, Q., Song, H., Linderholm, H.W., Leavitt, S.W., Wang, R., An, Z., 2014. Tree-ring stable carbon isotope-based May–July temperature reconstruction over Nanwutai, China, for the past century and its record of 20th century warming. Quat. Sci. Rev. 93, 67–76. https://doi.org/10.1016/j.quascirev.2014.03.023

Lücke, L.J., Hegerl, G.C., Schurer, A.P., Wilson, R., 2019. Effects of memory biases on variability of temperature reconstructions. J. Clim. 32, 8713–8731. https://doi.org/10.1175/JCLI-D-19-0184.1

Mann, M.E., Zhang, Z., Hughes, M.K., Bradley, R.S., Miller, S.K., Rutherford, S., Ni, F., 2008. Proxy-based reconstructions of hemispheric and global surface temperature variations over the past two millennia. Proc. Natl. Acad. Sci. 105, 13252. https://doi.org/10.1073/pnas.0805721105

Mann, M.E., Zhang, Z., Rutherford, S., Bradley, R.S., Hughes, M.K., Shindell, D., Ammann, C., Faluvegi, G., Ni, F., 2009. Global signatures and dynamical origins of the Little Ice Age and Medieval Climate Anomaly. Science 326, 1256. https://doi.org/10.1126/science.1177303

Masson-Delmotte, V., Schulz, M., Abe-Ouchi, A., Beer, J., Ganopolski, A., Rouco, J.G., Jansen, E., Lambeck, K., Luterbacher, J., Naish, T., 2013. Information from Paleoclimate Archives, in: Climate Change 2013: The Physical Science Basis. Contribution of Working Group I to the Fifth Assessment Report of the Intergovernmental Panel on Climate Change [Stocker, T.F., D. Qin, G.-K. Plattner, M. Tignor, S.K. Allen, J. Boschung, A. Nauels, Y. Xia, V. Bex and P.M. Midgley (eds.)]. Cambridge University Press, Cambridge, pp. 383–464. https://doi.org/10.1017/CBO9781107415324.013

McCarroll, D., Pettigrew, E., Luckman, A., Guibal, F., Edouard, J.L., 2002. Blue reflectance provides a surrogate for latewood density of high-latitude pine tree rings. Arct. Antarct. Alp. Res. 34, 450–453. https://doi.org/10.1080/15230430.2002.12003516

McCarroll, D., Loader, N.J., Jalkanen, R., Gagen, M.H., Grudd, H., Gunnarson, B.E., Kirchhefer, A.J., Friedrich, M., Linderholm, H.W., Lindholm, M., Boettger, T., Los, S.O., Remmele, S., Kononov, Y.M., Yamazaki, Y.H., Young, G.H., Zorita, E., 2013. A 1200-year multiproxy record of tree growth and summer temperature at the northern pine forest limit of Europe. The Holocene 23, 471–484. https://doi.org/10.1177/0959683612467483

Melvin, T.M., Briffa, K.R., 2008. A “signal-free” approach to dendroclimatic standardisation. Dendrochronologia 26, 71–86. https://doi.org/10.1016/j.dendro.2007.12.001

Melvin, T.M., Briffa, K.R., 2014. CRUST: Software for the implementation of regional chronology standardisation: Part 2. Further RCS options and recommendations. Dendrochronologia 32, 343–356. https://doi.org/10.1016/j.dendro.2014.07.008

Nakatsuka, T., Sano, M., Li, Z., Xu, C., Tsushima, A., Shigeoka, Y., Sho, K., Ohnishi, K., Sakamoto, M., Ozaki, H., Higami, N., Nakao, N., Yokoyama, M., Mitsutani, T., 2020. A 2600-year summer climate reconstruction in central Japan by integrating tree-ring stable oxygen and hydrogen isotopes. Clim. Past 16, 2153–2172. https://doi.org/10.5194/cp-16-2153-2020

Nasri, B.R., Boucher, É., Perreault, L., Rémillard, B.N., Huard, D., Nicault, A., Members of the ARCHIVES-PERSISTENCE projects, 2020. Modeling hydrological inflow persistence using paleoclimate reconstructions on the Québec-Labrador (Canada) Peninsula. Water Resour. Res. 56, e2019WR025122. https://doi.org/10.1029/2019WR025122

Naulier, M., Savard, M.M., Bégin, C., Gennaretti, F., Arseneault, D., Marion, J., Nicault, A., Bégin, Y., 2015. A millennial summer temperature reconstruction for northeastern Canada using oxygen isotopes in subfossil trees. Clim. Past 11, 1153–1164. https://doi.org/10.5194/cp-11-1153-2015

Neukom, R., Schurer, A.P., Steiger, Nathan.J., Hegerl, G.C., 2018. Possible causes of data model discrepancy in the temperature history of the last millennium. Sci. Rep. 8, 7572. https://doi.org/10.1038/s41598-018-25862-2

Neukom, R., Steiger, N., Gómez-Navarro, J.J., Wang, J., Werner, J.P., 2019. No evidence for globally coherent warm and cold periods over the preindustrial Common Era. Nature 571, 550–554. https://doi.org/10.1038/s41586-019-1401-2

Österreicher, A., Weber, G., Leuenberger, M., Nicolussi, K., 2015. Exploring blue intensity-comparison of blue intensity and MXD data from Alpine spruce trees. TRACE–Tree Rings Archaeol. Climatol. Ecol. 13, 56–61.

PAGES 2k Consortium, 2013. Continental-scale temperature variability during the past two millennia. Nat. Geosci. 6, 339–346. https://doi.org/10.1038/ngeo1797

PAGES 2k Consortium, 2017. A global multiproxy database for temperature reconstructions of the Common Era. Sci. Data 4, 170088. https://doi.org/10.1038/sdata.2017.88

PAGES 2k Consortium, 2019. Consistent multidecadal variability in global temperature reconstructions and simulations over the Common Era. Nat. Geosci. 12, 643–649. https://doi.org/10.1038/s41561-019-0400-0

Parfitt, R., Ummenhofer, C.C., Buckley, B.M., Hansen, K.G., D'Arrigo, R.D., 2020. Distinct seasonal climate drivers revealed in a network of tree-ring records from Labrador, Canada. Clim. Dyn. 54, 1897–1911. https://doi.org/10.1007/s00382-019-05092-6

Payette, S., Filion, L., Gauthier, L., Boutin, Y., 1985. Secular climate change in old-growth tree-line vegetation of northern Quebec. Nature 315, 135–138. https://doi.org/10.1038/315135a0

Payette, S., Filion, L., Delwaide, A., Bégin, C., 1989. Reconstruction of tree-line vegetation response to long-term climate change. Nature 341, 429–432. https://doi.org/10.1038/341429a0

Payette, S., 1993. The range limit of boreal tree species in Québec-Labrador: an ecological and palaeoecological interpretation. Rev. Palaeobot. Palynol. 79, 7–30. https://doi.org/10.1016/0034-6667(93)90036-T

Payette, S., Delwaide, A., 2004. Dynamics of subarctic wetland forests over the past 1500 years. Ecol. Monogr. 74, 373–391. https://doi.org/10.1890/03-4033

Phipps, S.J., McGregor, H.V., Gergis, J., Gallant, A.J.E., Neukom, R., Stevenson, S., Ackerley, D., Brown, J.R., Fischer, M.J., van Ommen, T.D., 2013. Paleoclimate data–model comparison and the role of climate forcings over the past 1500 years. J. Clim. 26, 6915–6936. https://doi.org/10.1175/JCLI-D-12-00108.1

Porter, T.J., Pisaric, M.F.J., Field, R.D., Kokelj, S.V., Edwards, T.W.D., deMontigny, P., Healy, R., LeGrande, A.N., 2014. Spring-summer temperatures since AD 1780 reconstructed from stable oxygen isotope ratios in white spruce tree-rings from the Mackenzie Delta, northwestern Canada. Clim. Dyn. 42, 771–785. https://doi.org/10.1007/s00382-013-1674-3

Québec: Ministère de l'Environnement (Ed.), 2002. L'eau, la vie, l'avenir: politique nationale de l'eau. Environnement Québec, Québec.

Rennie, J.J., Lawrimore, J.H., Gleason, B.E., Thorne, P.W., Morice, C.P., Menne, M.J., Williams, C.N., de Almeida, W.G., Christy, J.R., Flannery, M., Ishihara, M., Kamiguchi, K., Klein-Tank, A.M.G., Mhanda, A., Lister, D.H., Razuvaev, V., Renom, M., Rusticucci, M., Tandy, J., Worley, S.J., Venema, V., Angel, W., Brunet, M., Dattore, B., Diamond, H., Lazzara, M.A., Le Blancq, F., Luterbacher, J., Mächel, H., Revadekar, J., Vose, R.S., Yin, X., 2014. The international surface temperature initiative global land surface databank: monthly temperature data release description and methods. Geosci. Data J. 1, 75–102. https://doi.org/10.1002/gdj3.8

Robock, A., 2000. Volcanic eruptions and climate. Rev. Geophys. 38, 191–219. https://doi.org/10.1029/1998RG000054

Rydval, M., Larsson, L.-Å., McGlynn, L., Gunnarson, B.E., Loader, N.J., Young, G.H.F., Wilson, R., 2014. Blue intensity for dendroclimatology: Should we have the blues? Experiments from Scotland. Dendrochronologia 32, 191–204. https://doi.org/10.1016/j.dendro.2014.04.003

Rydval, M., Loader, N.J., Gunnarson, B.E., Druckenbrod, D.L., Linderholm, H.W., Moreton, S.G., Wood, C.V., Wilson, R., 2017a. Reconstructing 800 years of summer temperatures in Scotland from tree rings. Clim. Dyn. 49, 2951–2974. https://doi.org/10.1007/s00382-016-3478-8

Rydval, M., Gunnarson, B.E., Loader, N.J., Cook, E.R., Druckenbrod, D.L., Wilson, R., 2017b. Spatial reconstruction of Scottish summer temperatures from tree rings. Int. J. Climatol. 37, 1540–1556. https://doi.org/10.1002/joc.4796

Rydval, M., Druckenbrod, D.L., Svoboda, M., Trotsiuk, V., Janda, P., Mikoláš, M., Čada, V., Bače, R., Teodosiu, M., Wilson, R., 2018. Influence of sampling and disturbance history on climatic sensitivity of temperature-limited conifers. The Holocene 28, 1574–1587. https://doi.org/10.1177/0959683618782605

Saucier, J.-P., Grondin, P., Robitaille, A., Bergeron, J.-F. (2003) Zones de végétation et domaines bioclimatiques du Québec. Gouvernement du Québec, Ministère des Ressources naturelles, de la Faune et des Parcs, Québec.

Schneider, L., Smerdon, J.E., Büntgen, U., Wilson, R.J.S., Myglan, V.S., Kirdyanov, A.V., Esper, J., 2015. Revising midlatitude summer temperatures back to A.D. 600 based on a wood density network. Geophys. Res. Lett. 42, 4556–4562. https://doi.org/10.1002/2015GL063956

Schurer, A.P., Hegerl, G.C., Mann, M.E., Tett, S.F.B., Phipps, S.J., 2013. Separating forced from chaotic climate variability over the past millennium. J. Clim. 26, 6954–6973. https://doi.org/10.1175/JCLI-D-12-00826.1

Schurer, A.P., Tett, S.F.B., Hegerl, G.C., 2014. Small influence of solar variability on climate over the past millennium. Nat. Geosci. 7, 104–108. https://doi.org/10.1038/ngeo2040

Schweingruber, F.H., 2012. Tree rings: basics and applications of dendrochronology. Springer Science & Business Media.

Seftigen, K., Fuentes, M., Ljungqvist, F.C., Björklund, J., 2020. Using Blue Intensity from drought-sensitive *Pinus sylvestris* in Fennoscandia to improve reconstruction of past hydroclimate variability. Clim. Dyn. 55, 579–594. https://doi.org/10.1007/s00382-020-05287-2

Sheppard, P.R., Graumlich, L.J., Conkey, L.E., 1996. Reflected-light image analysis of conifer tree rings for reconstructing climate. The Holocene 6, 62–68. https://doi.org/10.1177/095968369600600107

Sheppard, P.R., 1999. Overcoming extraneous wood color variation during low-magnification reflected-light image analysis of conifer tree rings. Wood Fiber Sci. 31, 106–115.

Sheppard, P.R., Wiedenhoeft, A., 2007. An advancement in removing extraneous color from wood for low-magnification reflected-light image analysis of conifer tree rings. Wood Fiber Sci. 39, 173–183.

Sigl, M., Winstrup, M., McConnell, J.R., Welten, K.C., Plunkett, G., Ludlow, F., Büntgen, U., Caffee, M., Chellman, N., Dahl-Jensen, D., Fischer, H., Kipfstuhl, S., Kostick, C., Maselli, O.J., Mekhaldi, F., Mulvaney, R., Muscheler, R., Pasteris, D.R., Pilcher, J.R., Salzer, M., Schüpbach, S., Steffensen, J.P., Vinther, B.M., Woodruff, T.E., 2015. Timing and climate forcing of volcanic eruptions for the past 2,500 years. Nature 523, 543–549. https://doi.org/10.1038/nature14565

Slonosky, V.C., 2015. Daily minimum and maximum temperature in the St-Lawrence Valley, Quebec: two centuries of climatic observations from Canada. Int. J. Climatol. 35, 1662–1681. https://doi.org/10.1002/joc.4085

St. George, S., Esper, J., 2019. Concord and discord among Northern Hemisphere paleotemperature reconstructions from tree rings. Quat. Sci. Rev. 203, 278–281. https://doi.org/10.1016/j.quascirev.2018.11.013

Stine, A.R., Huybers, P., 2014. Arctic tree rings as recorders of variations in light availability. Nat. Commun. 5, 3836. https://doi.org/10.1038/ncomms4836

Stoffel, M., Khodri, M., Corona, C., Guillet, S., Poulain, V., Bekki, S., Guiot, J., Luckman, B.H., Oppenheimer, C., Lebas, N., Beniston, M., Masson-Delmotte, V., 2015. Estimates of volcanic-induced cooling in the Northern Hemisphere over the past 1,500 years. Nat. Geosci. 8, 784–788. https://doi.org/10.1038/ngeo2526

Stralberg, D., Arseneault, D., Baltzer, J.L., Barber, Q.E., Bayne, E.M., Boulanger, Y., Brown, C.D., Cooke, H.A., Devito, K., Edwards, J., Estevo, C.A., Flynn, N., Frelich, L.E., Hogg, E.H., Johnston, M., Logan, T., Matsuoka, S.M., Moore, P., Morelli, T.L., Morissette, J.L., Nelson, E.A., Nenzén, H., Nielsen, S.E., Parisien, M.-A., Pedlar, J.H., Price, D.T., Schmiegelow, F.K., Slattery, S.M., Sonnentag, O., Thompson, D.K., Whitman, E., 2020. Climate-change refugia in boreal North America: what, where, and for how long? Front. Ecol. Environ. 18, 261–270. https://doi.org/10.1002/fee.2188

Tingley, M.P., Stine, A.R., Huybers, P., 2014. Temperature reconstructions from tree-ring densities overestimate volcanic cooling. Geophys. Res. Lett. 41, 7838–7845. https://doi.org/10.1002/2014GL061268

Trachsel, M., Kamenik, C., Grosjean, M., McCarroll, D., Moberg, A., Brázdil, R., Büntgen, U., Dobrovolný, P., Esper, J., Frank, D.C., Friedrich, M., Glaser, R., Larocque-Tobler, I., Nicolussi, K., Riemann, D., 2012. Multi-archive summer temperature reconstruction for the European Alps, AD 1053–1996. Quat. Sci. Rev. 46, 66–79. https://doi.org/10.1016/j.quascirev.2012.04.021

Viau, A.E., Gajewski, K., 2009. Reconstructing millennial-scale, regional paleoclimates of boreal Canada during the Holocene. J. Clim. 22, 316–330. https://doi.org/10.1175/2008JCLI2342.1

Viau, A.E., Ladd, M., Gajewski, K., 2012. The climate of North America during the past 2000 years reconstructed from pollen data. Glob. Planet. Change 84–85, 75–83. https://doi.org/10.1016/j.gloplacha.2011.09.010

Wang, F., Arseneault, D., Pan, B., Liao, Q., Sugiyama, J., 2019. Pre-1930 unstable relationship between climate and tree-ring width of *Pinus taiwanensis* hayata in southeastern China. Dendrochronologia 57, 125629. https://doi.org/10.1016/j.dendro.2019.125629

Wang, F., Arseneault, D., Boucher, É., Galipaud Gloaguen, G., Deharte, A., Yu, S., Troukechout, N., 2020. Temperature sensitivity of blue intensity, maximum latewood density, and ring width data of living black spruce trees in the eastern Canadian taiga. Dendrochronologia 64, 125771. https://doi.org/10.1016/j.dendro.2020.125771

Wang, L., Payette, S., Bégin, Y., 2001. 1300-year tree-ring width and density series based on living, dead and subfossil black spruce at tree-line in Subarctic Quebec, Canada. The Holocene 11, 333–341. https://doi.org/10.1191/095968301674769686

Wang, L., Payette, S., Bégin, Y., 2002. Relationships between anatomical and densitometric characteristics of black spruce and summer temperature at tree line in northern Quebec. Can. J. For. Res. 32, 477–486. https://doi.org/10.1139/x01-208

White, J.C., Wulder, M.A., Hermosilla, T., Coops, N.C., Hobart, G.W., 2017. A nationwide annual characterization of 25years of forest disturbance and recovery for Canada using Landsat time series. Remote Sens. Environ. 194, 303–321. https://doi.org/10.1016/j.rse.2017.03.035

Wiles, G.C., Charlton, J., Wilson, R.J.S., D'Arrigo, R.D., Buma, B., Krapek, J., Gaglioti, B.V., Wiesenberg, N., Oelkers, R., 2019. Yellow-cedar blue intensity tree-ring chronologies as records of climate in Juneau, Alaska, USA. Can. J. For. Res. 49, 1483–1492. https://doi.org/10.1139/cjfr-2018-0525

Wilson, R., Rao, R., Rydval, M., Wood, C., Larsson, L.-Å., Luckman, B.H., 2014. Blue Intensity for dendroclimatology: The BC blues: A case study from British Columbia, Canada. The Holocene 24, 1428–1438. https://doi.org/10.1177/0959683614544051

Wilson, R., Anchukaitis, K., Briffa, K.R., Büntgen, U., Cook, E., D'Arrigo, R., Davi, N., Esper, J., Frank, D., Gunnarson, B., Hegerl, G., Helama, S., Klesse, S., Krusic, P.J., Linderholm, H.W., Myglan, V., Osborn, T.J., Rydval, M., Schneider, L., Schurer, A., Wiles, G., Zhang, P., Zorita, E., 2016. Last millennium northern hemisphere summer temperatures from tree rings: Part I: The long term context. Quat. Sci. Rev. 134, 1–18. https://doi.org/10.1016/j.quascirev.2015.12.005

Wilson, R., Wilson, D., Rydval, M., Crone, A., Büntgen, U., Clark, S., Ehmer, J., Forbes, E., Fuentes, M., Gunnarson, B.E., Linderholm, H.W., Nicolussi, K., Wood, C., Mills, C., 2017a. Facilitating tree-ring dating of historic conifer timbers using Blue Intensity. J. Archaeol. Sci. 78, 99–111. https://doi.org/10.1016/j.jas.2016.11.011

Wilson, R., D'Arrigo, R., Andreu-Hayles, L., Oelkers, R., Wiles, G., Anchukaitis, K., Davi, N., 2017b. Experiments based on blue intensity for reconstructing North Pacific temperatures along the Gulf of Alaska. Clim. Past 13, 1007–1022. https://doi.org/10.5194/cp-13-1007-2017

Wilson, R., Anchukaitis, K., Andreu-Hayles, L., Cook, E., D'Arrigo, R., Davi, N., Haberbauer, L., Krusic, P., Luckman, B., Morimoto, D., Oelkers, R., Wiles, G., Wood, C., 2019. Improved dendroclimatic calibration using blue intensity in the southern Yukon. The Holocene 29, 1817–1830. https://doi.org/10.1177/0959683619862037

Young, G.H.F., Demmler, J.C., Gunnarson, B.E., Kirchhefer, A.J., Loader, N.J., McCarroll, D., 2011. Age trends in tree ring growth and isotopic archives: A case study of *Pinus sylvestris* L. from northwestern Norway: Brief Report. Glob. Biogeochem. Cycles 25, n/a-n/a. https://doi.org/10.1029/2010GB003913

Zhu, F., Emile-Geay, J., Hakim, G.J., King, J., Anchukaitis, K.J., 2020. Resolving the differences in the simulated and reconstructed temperature response to volcanism. Geophys. Res. Lett. 47, e2019GL086908. https://doi.org/10.1029/2019GL08690